Universitat de Girona

ON THE GENERATION OF DESIGN ALLOWABLES OF COMPOSITE COUPONS ACCOUNTING FOR DEFECTS USING A MULTI-FIDELITY APPROACH

Oriol Vallmajó Martín

ADVERTIMENT. L'accés als continguts d'aquesta tesi doctoral i la seva utilització ha de respectar els drets de la persona autora. Pot ser utilitzada per a consulta o estudi personal, així com en activitats o materials d'investigació i docència en els termes establerts a l'art. 32 del Text Refós de la Llei de Propietat Intel·lectual (RDL 1/1996). Per altres utilitzacions es requereix l'autorització prèvia i expressa de la persona autora. En qualsevol cas, en la utilització dels seus continguts caldrà indicar de forma clara el nom i cognoms de la persona autora i el títol de la tesi doctoral. No s'autoritza la seva reproducció o altres formes d'explotació efectuades amb finalitats de lucre ni la seva comunicació pública des d'un lloc aliè al servei TDX. Tampoc s'autoritza la presentació del seu contingut en una finestra o marc aliè a TDX (framing). Aquesta reserva de drets afecta tant als continguts de la tesi com als seus resums i índexs.

ADVERTENCIA. El acceso a los contenidos de esta tesis doctoral y su utilización debe respetar los derechos de la persona autora. Puede ser utilizada para consulta o estudio personal, así como en actividades o materiales de investigación y docencia en los términos establecidos en el art. 32 del Texto Refundido de la Ley de Propiedad Intelectual (RDL 1/1996). Para otros usos se requiere la autorización previa y expresa de la persona autora. En cualquier caso, en la utilización de sus contenidos se deberá indicar de forma clara el nombre y apellidos de la persona autora y el título de la tesis doctoral. No se autoriza su reproducción u otras formas de explotación efectuadas con fines lucrativos ni su comunicación pública desde un sitio ajeno al servicio TDR. Tampoco se autoriza la presentación de su contenido en una ventana o marco ajeno a TDR (framing). Esta reserva de derechos afecta tanto al contenido de la tesis como a sus resúmenes e índices.

WARNING. Access to the contents of this doctoral thesis and its use must respect the rights of the author. It can be used for reference or private study, as well as research and learning activities or materials in the terms established by the 32nd article of the Spanish Consolidated Copyright Act (RDL 1/1996). Express and previous authorization of the author is required for any other uses. In any case, when using its content, full name of the author and title of the thesis must be clearly indicated. Reproduction or other forms of for profit use or public communication from outside TDX service is not allowed. Presentation of its content in a window or frame external to TDX (framing) is not authorized either. These rights affect both the content of the thesis and its abstracts and indexes.

Universitat de Girona

Doctoral Thesis

On the generation of design allowables of composite coupons accounting for defects using a multi-fidelity approach

Oriol Vallmajó Martín

2024

Universitat de Girona

Doctoral Thesis

On the generation of design allowables of composite coupons accounting for defects using a multi-fidelity approach

Oriol Vallmajó Martín

2024

Doctoral Program in Technology

Advisors:

Dr. Albert Turon Travesa
Universitat de Girona
Dr. Albertino José Castanho Arteiro
Universidade do Porto

Thesis submitted to the Universitat de Girona for the degree of Doctor of Philosophy

Oriol Vallmajó Martín

On the generation of design allowables of composite coupons accounting for defects using a multi-fidelity approach

Doctoral Thesis, 2024
Doctoral Program in Technology
Advisors: Dr. Albert Turon Travesa and Dr. Albertino José Castanho Arteiro

Universitat de Girona
AMADE Research Group
Escola Politècnica Superior
Dept. d'Enginyeria Mecànica i de la Construcció Industrial
Carrer Universitat de Girona, 4. Campus de Montilivi
17003 Girona

To my family, my friends and Mireia.
Comencem!

There is no time for losers.

— Queen
Singer

Impossible means that you haven't found a solution yet.

— Henry Ford
Founder of Ford Motor Company

Si ens aixequem ben d'hora, i sense retrets, som un país imparable.

— Pep Guardiola
Jugador i entrenador de futbol

Quality means doing it right when no one is looking.

— Henry Ford
Founder of Ford Motor Company

Entre el miracle i el desastre és on vivim.

— Oques Grasses
La gent que estimo

When people are determined, they can overcome anything.

— Nelson Mandela
Politician

Preface

The work contained in this Ph.D. thesis was conducted in the AMADE Research Group (Escola Politècnica Superior, Dept. d'Enginyeria Mecànica i de la Construcció Industrial, Universitat de Girona, Spain). The thesis was carried out with predoctoral Grant 2020FI B2 00110 from the Catalan government. The author also acknowledges the funding of the project RTI, United States 2018-099373-B-100, with also the financial support from the Spanish Ministerio de Economía, Industria y Competitividad (MINECO) and the European Social Fund. In addition, this work has been conducted within the framework of CAELESTIS project, funded buy the European Climate, Infrastucture and Environment Executive Agency (CINEA) under grant agreement No. 101056886.

Girona, February 2024

Oriol Vallmajó Martín

Acknowledgements

The important thing is not to arrive; the important thing is the journey! Completing a thesis was not my initial dream, but over these last few years, it has become my passion. However, I could never have accomplished this alone. This thesis has become a reality thanks to all the people who have helped and motivated me.

Firstly, I would like to profoundly thank my advisors, Dr. Albert Turon Travesa and Dr. Albertino Arteiro. Albert has always known how to say the right words to motivate me during the challenging moments, and I am truly thankful for his continuous encouragement and belief in me. Despite the physical distance, Albertino always found a way to meet me and guide the research derived from this thesis in the right direction. This work would not have been possible without their invaluable support. Thank you all for our insightful discussions and for always being there. I am sure I wouldn't have completed this remarkable work without your guidance and support. You are not only brilliant professors but, overall, incredible people.

I would also like to extend my thanks to all the people from around the world and from different institutions who contributed to this thesis and helped me write all the articles that form this doctoral thesis.

També m'agradaria molt agrair a tots els membres del grup de recerca AMADE, tant els meus companys estudiants com tots els professors que el formen. Heu contribuït a crear un ambient de treball immillorable durant tots aquests anys, permetent-nos discutir i debatre sobre els temes que em preocupaven. Alhora, hem trobat moments per distreure'ns junts. Gràcies, companys! En aquest punt, m'agradaria fer una menció especial pel Dr. Joan Andreu Mayugo, membre del grup qui em va motivar a emprendre aquest projecte fa 6 anys. Sense ell, ni tan sols m'hauria plantejat començar una tesi doctoral. En segon lloc, també vull expressar un agraïment particular a l'Ivan Ruiz Cózar. Des del primer dia que vaig entrar a AMADE et vas convertir en el meu mentor, em vas ajudar a integrar-me, a aprendre i, sobretot, a buscar la perfecció. Les nostres interminables discussions han permès que avui pugui estar escrivint aquesta tesi. Moltes gràcies per tota la teva ajuda i suport. I per últim, a en Martí Descamps

amb qui estic compartint un projecte de gran rellevància: Hyper-Kamiokande. Un plaer poder treballar colze a colze amb tu.

Agraït als companys de carrera que em van permetre formar-me com a enginyer industrial. En especial, en Max, en Deca, en Pol, l'Òscar i l'Ariadna que vau fer tot l'estudi molt més amè, alegre, fàcil i divertit.

Una menció especial a tots els meus amics. Els VUIT, en Jordi, en Martí i l'Àlex, i a les noves benvingudes, Estel, Paula i Laura, que sempre m'heu mantingut de peus a terra i m'heu sabut donar les millors estones per esbargir-me durant aquests darrers anys. Heu hagut d'aguantar les meves xapes sobre els materials compostos i m'heu animat a que em pugui convertir en el Dr. Vallmajó. Moltes gràcies per tot el vostre escalf! Sou els millors amics que un pot tenir. També agrair a tota la resta d'amics. Sense els nostres tibers, les llargues nits de festa amb la Tusa i tots els moments junts aquesta tesi s'hagués fet molt més feixuga. A l'Aleix, en Raül, l'Andreu, en Pol, l'Arnald, l'Isaac, en Sisu, en Ferran, en Casas, l'Àlvaro, la Júlia, l'Elena, la Laura, la Nona i la Maria, moltes gràcies per la diversió i alegria que transmeteu.

Una menció especial pels companys de la Penya Bons Aires. En especial, a l'Àngel i l'Aniol. Heu permès que hagi pogut assolir les meves passions, l'enginyeria, la formació i el futbol, al mateix temps que hem rigut i hem viscut l'esport en passió. Aniol, moltes gràcies per tot el treball que has hagut de fer tu sol aquests darrers mesos per deixar-me convertir en doctor. Sou els millors! Som-hi Penya!

També vull agrair als meus nous companys del Saint George School. No ha sigut fàcil començar aquest repte al mateix temps que escriure una tesi doctoral, però vosaltres m'ho heu posat molt fàcil. En especial, gràcies a en Pep, la Conchi, la Montse, la Sara, la Mavi, la Marta i l'Andrès.

Finalment, agrair a la meva família "Vallmajó-Martín". Per tots els moments viscuts, per tots els viatges, per totes les celebracions i, sobretot, per tenir-vos sempre al costat. Tieta, moltes gràcies per la teva constant mostra de vitalitat, alegria i entusiasme. Sempre preguntant i mostrant interès pel teu nebot. Tiet, Rosa i Pol gràcies pel vostre suport i per la diversió assegurada que és estar amb vosaltres. Iaia, muchisimas gracias por tus abrazos, por todo lo que has hecho por nosotros juntamente con el avi. Anna, Joan, Biel i Jan, les estones amb vosaltres

són immillorables i sempre amanides amb allò que tant ens agrada. Anna, ets una persona increïble, plena d'energia i alegria i la teva gran vocació m'ha ajudat a voler ser com tu. Mama i Papa heu sigut, sou i sereu imprescindibles per mi. M'heu ajudat moltíssim a orientar la meva carrera, m'heu animat sempre a fer allò que volia i gràcies a com m'heu educat i tot l'esforç que hi heu dedicat, avui puc estar publicant una tesi doctoral. My brother-in-law, Chris, many thank for your contributions, our discussions despite working in different fields, and for letting me experience some awesome moments. I a tu Queralt, la primera Dra. Vallmajó-Martín de la família. M'has obert les portes a tot, m'has animat al mateix temps que aconsellat i, malgrat que no estiguem tan a prop com ens agradaria, sempre estàs al meu costat. Ets la millors germana del món i sense haver viscut la teva empenta, energia i perfeccionament, estic segur que no ho hauria aconseguit. Us estimo molt!

I és clar, a tu Mireia. Ens vam conèixer i poc després jo vaig decidir començar aquest viatge. M'has animat als moments més difícils però, sobretot, m'has acompanyat en tot moment i en totes les decisions que prenia. Gràcies per tot l'esforç que has fet aquests últims mesos per tal de deixar-me el major temps possible, per esperar-me i per estar sempre al meu costat. Espero poder-te tornar tot el treball que has fet per mi. T'estimo molt a tu i a tota la nova i increïble família olotina!

Moltes gràcies a tothom. Many thanks. Muito obrigado.
Comencem!

List of Publications

The present Ph.D. thesis has been prepared as a compendium of peer-reviewed journal papers, according to the regulations of the Universitat de Girona.

Publications in refereed journals

The main body of this thesis is comprised of the following papers:

A) **O. Vallmajó**, I. R. Cózar, C. Furtado, R. Tavares, A. Arteiro, A. Turon, P. P. Camanho. Virtual calculation of the B-value allowables of notched composite laminates. *Composite Structures*, 212 (2019) 11-21. doi: https://doi.org/10.1016/j.compstruct.2018.12.049.
ISSN: 0263-8223, Impact Factor: 6.3, ranked 7/28 in the category of *Materials Science, Composites* and ranked 11/137 in the category of *Mechanics* (1st quartile)[1].

B) I. R. Cózar, A. Turon, E. V. González, **O. Vallmajó**, A. Sasikumar. A methodology to obtain material design allowables from high-fidelity compression after impact simulations on composite laminates. *Composites Part A: Applied Science and Manufacturing*, 139 (2020) 106069. doi: https://doi.org/10.1016/j.compositesa.2020.106069.
ISSN: 1359-835X, Impact Factor: 8.7, ranked 9/50 in the category of *Engineering, Manufacturing* and ranked 5/28 in the category of *Materials Science, Composites* (1st quartile)[1].

C) **O. Vallmajó**, M. Descamps, A. Arteiro, A. Turon. Effect of ply misalignment on the notched strength of composite laminates. *In preparation for submission*.

D) **O. Vallmajó**, A. Arteiro, J. M. Guerrero, A. R. Melro, A. Pupurs, A. Turon. Micromechanical analysis of composite materials considering material variability and microvoids. *International Journal of Mechanical Sciences*, 263 (2024) 108781. doi: https://doi.org/10.1016/j.ijmecsci.2023.108781.
ISSN: 0020-7403, Impact Factor: 7.3, ranked 7/136 in the category of

[1] According to the 2022 Journal Citation Reports

Engineering, Mechanical and ranked 5/137 in the category of *Mechanics* (1st quartile)[1].

Other publications that have been derived from this thesis but do not belong to this thesis, and are not included in this document, are listed below:

– A. Sasikumar, A. Turon, I.R. Cózar, **O. Vallmajó**, J.C. Casero, M. De Lozzo, S. Abdel-Monsef. Sensitivity analysis methodology to identify the critical material properties that affect the open hole strength of composites. *Journal of Composite Materials* 57(10) (2023) 1791-1805. doi: https://doi.org/10.1177/00219983231163272.
ISSN: 0021-9983, Impact Factor: 2.9, ranked 15/28 in the category of *Materials science, composites* (3rd quartile)[1].

Conference participation

Finally all these publications have also been presented in different conferences:

– **O. Vallmajó**, I.R. Cózar, A. Turon, C. Furtado, R. Tavares, A. Arteiro, P. P. Camanho. On the virtual definition of B-value design chart for the open hole strength of laminated composites. *21st ICCS: International Conference on Composite Structures (ICCS 21)*. Bologna, 04th-07th September 2018.
International Conference. Oral presentation.

– **O. Vallmajó**, R. Tavares, I.R. Cózar, A. Arteiro, C. Furtado, L. Pereira, F. Otero, S. Abdel, P. P. Camanho, A. Turon. Towards the definition of an hybrid experimental/virtual test matrix to obtain design allowables of composite structures. *SAMPE Europe Student Symposium 2020 (SAMPE 20)*. Amsterdam online event, 30th-01st October 2020.
International Conference. Oral presentation.

– **O. Vallmajó**, A. Turon, A. Arteiro. Microscale analysis of the influence of void content, distribution and size of fiber-reinforced polymers. *8th ECCOMAS Thematic Conference on the Mechanical Response of Composites (COMPOSITES 2021)*. Online event, 22nd-24th September 2021.
International Conference. Oral presentation.

– A. Turon, **O. Vallmajó**, S. Abdel-Monsef, S. Medina, J. Ejarque, G. Guillamet, A. Sasikumar. A methodology to compute the knock down factors due to the presence of manufacturing defects using high fidelity models. *9th ECCOMAS Thematic Conference on the Mechanical Response of Composites (COMPOSITES 2023)*. Trapani, 12th-14th September 2023 International Conference. Oral presentation.

Declaration

Universitat de Girona

Dr. Albert Turon Travesa, Professor of the Dept. d'Enginyeria Mecànica i de la Construcció Industrial at Universitat de Girona, and senior member of AMADE Research Group,

hereby CERTIFIES that

The work entitled *On the generation of design allowables of composite coupons accounting for defects using a multi-fidelity approach*, submitted for the doctoral degree by Oriol Vallmajó Martín, has been conducted under my supervision and that it fulfills the requirements to aim for the *International Mention*.

Girona, February 2024.

Albert Turon Travesa
Universitat de Girona

U.PORTO

Dr. Albertino José Castanho Arteiro, Professor of the Department of Mechanical Engineering, Faculdade de Engenharia at Universidade do Porto,

hereby CERTIFIES that

The work entitled *On the generation of design allowables of composite coupons accounting for defects using a multi-fidelity approach*, submitted for the doctoral degree by Oriol Vallmajó Martín, has been conducted under my supervision and that it fulfills the requirements to aim for the *International Mention*.

Porto, February 2024.

Albertino José Castanho Arteiro
Universidade do Porto

List of Symbols

Acronyms

BBA	Building block approach
C3D8R	8-node linear brick reduced integration element
CAI	Compression After Impact
CCA	Concentric Cylinder Assembly
CFRP	Carbon Fiber Reinforced Polymer
CDF	Cumulative Density Function
CMCS	Crude Monte Carlo Simulation
CMH-17	Composite Materials Handbook [1]
CoV	Covariance
DOE	Design Of Experiments
ECDF	Empirical Cumulative Density Function
ERR	Energy Release Rate
FE	Finite Element
FEM	Finite Element Method
FFM	Finite Fracture Mechanics
FORM	First Order Reliability Method
FOSM	First Order Second Moment
LHS	Latin Hypercube Sampling
LSA	Local Sensitivity Analysis
MCS	Monte Carlo Simulation
OH	Open Hole
OSL	Observance Significance Level
PBC	Periodic Boundary Conditions
RBM	Rigid Body Motion
RMSE	Root Mean Square Error
RoM	Rule of Mixtures
RS	Response Surface
RVE	Representative Volume Element
SFEM	Stochastic Finite Element Method
SSFEM	Spectral Stochastic FEM
SIF	Stress Intensity Factor

SORM	Second Order Reliability Method
SRVE	Statistically Representative Volume Element
STDV	Standard Deviation
UQ&M	Uncertainty Quantification and Management
VVUQ	Verification and Validation with Uncertainty Quantification

Mechanical and statistical symbols

$2D$	Two-Dimensional
$3D$	Three-Dimensional
α	Probability of rejecting the null hypothesis
β	Parameter determined to obtain the best fit of the $\mathscr{R}$-curve
BK_η	B-K exponent parameter for mixed mode propagation
χ^2	Pearson goodness-of-fit statistic
C_{iijj}	Stiffness tensor component (with different sub-indices)
C_H	Coefficient of the honeycomb[1]
d_1	Damage variable for the fibers
d_2	Damage variable for the matrix
d_6	In-plane shear degradation
ρ	Density
E	Longitudinal Young's modulus (with different sub-indices)
E_1	Young's modulus in fiber direction (with different sub-indices)
E_2	Young's modulus in matrix direction
E_3	Young's modulus in height direction
F_0	Test statistic for standard deviations comparison
F_{n_1-1,n_2-1}	F-ratio value
f_{XT}	Ratio of the first branch of tensile cohesive law
f_{XC}	Ratio of the first branch of compressive cohesive law
$f_{\mathscr{G}_{XT}}$	Ratio of $\mathscr{G}_{XT}$ dissipated by the first branch
$f_{\mathscr{G}_{XC}}$	Ratio of $\mathscr{G}_{XC}$ dissipated by the first branch
G	Shear modulus (with different sub-indices)
G_{12}	Shear modulus in the 1-2 plane (with different sub-indices)
G_{13}	Shear modulus in the 1-3 plane
G_{23}	Shear modulus in the 2-3 plane
$\mathscr{G}$	Energy dissipated during the damage development
$\mathscr{G}_{Ic}$	Mode I interlaminar fracture toughness

$\mathscr{G}_{IIc}$	Mode II interlaminar fracture toughness
$\mathscr{G}_{SL}$	Transverse shear fracture toughness
$\mathscr{G}_{XT}$	Longitudinal tensile fracture toughness
$\mathscr{G}_{XC}$	Longitudinal compressive fracture toughness
$\mathscr{G}_{YT}$	Transverse tensile fracture toughness
$\mathscr{G}_{YC}$	Transverse compressive fracture toughness
H_0	Null hypothesis
H_1	Alternative hypothesis
h	Height
K	Penalty stiffness
K_P	Shear plasticity parameter
k	Constant value (with different sub-indices)
k^*	Hill's elastic plane-strain bulk modulus for lateral dilatation without longitudinal extension
l^*	Hill's elastic cross modulus
l_{fpz}	Length of the fracture process zone
m_{imp}	Impactor mass
m^*	Hill's elastic shear modulus in any transverse direction
μ	Friction coefficient
n	Number of samples
N	Number of repetitions
n^*	Hill's elastic longitudinal uniaxial modulus
P_{10}	10th percentile
p^*	Hill's elastic shear modulus for longitudinal shearing
ν	Poisson's ratio (with different sub-indices)
ν_{12}	Poisson's ratio in 1-2 plane (with different sub-indices)
ν_{13}	Poisson's ratio in 1-3 plane
ν_{23}	Poisson's ratio in 2-3 plane
R or r	Radius (with different sub-indices)
R^2	Coefficient of determination
$\mathscr{R}$	R-curve
$\mathscr{R}_{ssT}$	Ply longitudinal steady-state fracture toughness
$\bar{\sigma}$	Volume average stress component (with different sub-indices)
$\overline{\sigma}^{\infty}(w)$	Specimen strength
$\bar{\varepsilon}$	Volume average strain component (with different sub-indices)

s	Standard deviation
S_p	Pooled standard deviation
$\hat{s}$	Sample standard deviation
S_{LP}	Yield stress
S_j	First-order sensitivity index
S_L	Longitudinal shear strength
$Coh-t3$	Strength in pure mode I
$Coh-t1$	Strength in pure mode II
τ_{II}	Mode II interlaminar strength
t_0	Test statistic for means comparison
$t_{a,n}$	t-student value
T	Thickness of the specimen
V	Volume fraction (with different sub-indices)
W	Width (with different sub-indices)
$\bar{x}$	Mean value
X	Input parameter (with different sub-indices)
X_T	Longitudinal tensile strength
X_C	Longitudinal compressive strength
Y	Output result (with different sub-indices)
Y_T	Transverse tensile strength
Y_C	Transverse compressive strength

Subscripts

f	Fiber
m	Matrix
v	Voids
H	Honeycomb

Contents

List of Figures

List of Tables

Abstract

Composite structures play a crucial role in lightweight applications due to their exceptional mechanical performance and low density. However, their anisotropic behavior and susceptibility to uncertainties, such as manufacturing defects, bring challenges during the design process. Traditional approaches involving extensive testing are being replaced by computational simulations for efficiency and cost-effectiveness. These simulations not only replace traditional methods but also yield a multitude of results, accommodating various uncertainties.

Design allowables are widely used as design values which account for all the uncertainties associated with composite structures. Obtaining these values requires accurate computational models and a thorough analysis of the composite structure behavior. Moreover, microstructural mechanics aids in understanding both their mechanical behavior and the sources of variability.

This thesis addresses the need for accurate virtual calculation of design allowables that account for inherent uncertainties and manufacturing defects in composite structures. The overarching goal is to develop computational tools that systematically propagate uncertainties and provide statistical parameters representing material behavior. The research contributes to both the accuracy and efficiency of composite structures design, aligning with the industry's shift toward more cost-effective and practical methodologies.

To achieve these objectives, the thesis focuses on three main components: statistical modelling for design allowables, computational analysis for mechanical response simulations, and an advanced micromechanical model for understanding material behavior at the micro-scale. Each component contributes to a comprehensive framework for managing and mitigating uncertainties effectively in composite materials.

In the first contribution of this thesis, an efficient tool is introduced to predict notched design allowables, specifically the B-value. This novel approach employs an analytical model that meticulously accounts for intrinsic material variability and geometrical tolerances. The work significantly advances the understanding of predicting design allowables at the coupon level, providing a

clear and applicable methodology across various structural levels.

The second article develops a systematic methodology for obtaining design allowables using a numerical model. Given the complexity of the mechanical response of composite materials, especially in scenarios like compression after impact, sophisticated modelling techniques are imperative. Analytically modelling this phenomenon is highly complex, necessitating the use of numerical models based on the finite element method to predict their mechanical behavior accurately. However, these numerical models demand robust computational resources and extended simulation times compared to the analytical ones, presenting difficulties in obtaining large sample sizes. The proposed methodology addresses this handicap by constructing a precise response surface from available numerical data, enabling the interpolation of numerous values. This facilitates statistical analysis, streamlining the process of obtaining design allowables efficiently.

The third article focuses on predicting notched design allowables at the coupon level, considering the presence of defects through both analytical and numerical models. Defects in composite structures, an inevitable reality during the manufacturing process, require meticulous consideration. At the coupon level, where achieving the intended layup through the precise alignment of each ply is a complex task, ply deviations must be taken into account. Analytical models contribute to the generation of large sample sizes, enhancing the accuracy of statistical analysis, while numerical simulations provide heightened precision. The study compares these computational tools and suggests a hybrid approach to establish design allowables when accounting for the presence of ply misalignment as well as the intrinsic composites variability, achieving a balance between computational efficiency and results reliability.

In the final contribution of this thesis, the emphasis is placed on understanding the origin of variability while accounting for design allowables in composite structures. Micromechanical models emerge as powerful tools to describe the mechanical behavior of materials at the microscopic level, focusing on understanding how the individual constituents, such as fibers and matrix, interact to influence the composite mechanical properties. Additionally, at the microscale, the influence of defects, particularly voids, significantly contributes to the variability in the properties of composite structures. This research paper proposes

an innovative methodology employing an enhanced micromechanical model to determine elastic mesoscale properties and their associated uncertainties.

The thesis is structured into several parts, including a literature review, peer-reviewed publications, and a discussion of results and conclusions. Through the development and validation of these models, the research contributes not only to the understanding of uncertainties in composite structures but also provides valuable tools for engineers to optimize designs iteratively and rigorously.

Resum

Les estructures de material compost són sobretot utilitzades per estructures que requereixen ser lleugeres gràcies al seu rendiment mecànic excepcional i baixa densitat. No obstant això, el seu comportament anisotròpic i la susceptibilitat a incerteses, com ara defectes de fabricació, plantegen reptes durant el procés de disseny. Els enfocaments tradicionals involucraven proves experimentals extenses. Actualment, aquestes estan sent substituïdes per simulacions computacionals que són molt més eficients i rendibles. A més, no només reemplacen els mètodes tradicionals, sinó que també proporcionen una gran quantitat de resultats, els quals permeten tenir en compte les diverses incerteses.

Els admissibles de disseny són àmpliament utilitzats com a paràmetres de disseny que tenen en compte totes les incerteses associades amb les estructures de materials compost. Obtenir aquests valors requereix poder executar models computacionals precisos i una anàlisi exhaustiva del comportament de l'estructura composta. A més, la mecànica microestructural ajuda a comprendre tant el seu comportament mecànic com les fonts de variabilitat.

Aquesta tesi aborda la necessitat de predir virtualment admissibles de disseny precisos que tinguin en compte les incerteses inherents i els defectes de fabricació en estructures compostes. L'objectiu principal és desenvolupar eines computacionals que propaguin sistemàticament les incerteses i proporcionin paràmetres estadístics que representin el comportament del material. La recerca contribueix tant a la precisió com a l'eficiència del disseny d'estructures compostes, alineant-se amb el canvi de la indústria cap a metodologies més econòmiques i pràctiques.

Per assolir aquests objectius, la tesi es centra en tres parts principals: la modelització estadística per obtenir admissibles de disseny, l'anàlisi computacional mitjançant simulacions per obtenir una resposta mecànica i el desenvolupament d'un model micromecànic per comprendre el comportament del material a l'escala microscòpica. Cadascuna de les parts contribueix a un marc complet per gestionar i mitigar eficaçment les incerteses en els materials compostos.

En la primera contribució d'aquesta tesis es presenta una eina eficient per predir

admissibles de disseny en un laminat amb un forat passant, específicament el *B-value*. Aquest nou enfocament utilitza un model analític que meticulosament té en compte la variabilitat intrínseca del material i les toleràncies geomètriques. Aquest treball millora significativament la comprensió de la predicció d'admissibles de disseny al nivell més baix de la piràmide de certificació, a nivell d'espècimen, proporcionant una metodologia clara i aplicable a diferents nivells estructurals.

El segon article desenvolupa una metodologia sistemàtica per obtenir admissibles de disseny mitjançant un model numèric. Donada la complexitat de la resposta mecànica dels materials compostos, especialment en escenaris com la compressió després d'impacte, són imprescindibles tècniques de modelització sofisticades. Modelar-ho analíticament és molt complex, per la qual cosa és necessari l'ús de models numèrics basats en el mètode d'elements finits per predir amb precisió el seu comportament mecànic. No obstant això, aquests models numèrics requereixen recursos computacionals robustos i temps de simulació extensos en comparació amb els models analítics, la qual cosa presenta dificultats per obtenir grans mostres. La metodologia proposada aborda aquesta limitació construint una superfície de resposta precisa a partir de les dades numèriques disponibles, permetent la interpolació de nombrosos valors. Això facilita l'anàlisi estadística, simplificant el procés d'obtenció d'admissibles de disseny de manera eficient.

El tercer article es torna a centrar en la predicció d'admissibles de disseny de laminats amb un forat passant, tenint en compte la presència de defectes mitjançant models analítics i numèrics. La presència de defectes en estructures compostes és una realitat inevitable durant el procés de fabricació que requereix d'una consideració meticulosa. A aquest nivell d'anàlisi, on aconseguir la disposició desitjada mitjançant l'alineació precisa de cada capa es converteix en una tasca complexa, cal tenir en compte les desviacions de les capes. Els models analítics faciliten la generació de àmplies mostres per a una anàlisi estadística més precisa, mentre que les simulacions numèriques ofereixen una precisió més gran. L'estudi compara aquestes eines computacionals i suggereix un enfocament híbrid per establir admissibles de disseny, aconseguint un equilibri entre eficiència computacional i fiabilitat dels resultats.

En la darrera contribució d'aquesta tesi, s'accentua la importància de compren-

dre l'origen d'aquesta variabilitat a l'hora de tenir en compte els admissibles de disseny en estructures compostes. Els models micromecànics emergeixen com a eines poderoses per descriure el comportament mecànic dels materials a l'escala microscòpica, centrant-se en comprendre com interactuen individualment cadascun dels constituents, com ara les fibres i la matriu, per influir en les propietats mecàniques dels materials compostos. A més, a l'escala microscòpica, la influència de defectes, particularment els porus, contribueix significativament a la variabilitat de les propietats de les estructures compostes. Aquest article de recerca proposa una metodologia innovadora que utilitza un model micromecànic millorat per predir les propietats elàstiques a escala mesoscòpica i les seves incerteses associades.

La tesi s'estructura en diverses parts, incloent una revisió bibliogràfica, publicacions avaluades per experts i una discussió dels resultats i les conclusions. Mitjançant el desenvolupament i la validació d'aquests models, la recerca contribueix no només a la comprensió de les incerteses en les estructures compostes, sinó que també proporciona eines valuoses per als enginyers per poder optimitzar els dissenys de manera iterativa i rigorosa.

Resumen

Las estructuras de material compuesto son ampliamente utilizadas en aplicaciones ligeras debido a su rendimiento mecánico excepcional y baja densidad. Sin embargo, su comportamiento anisotrópico y su susceptibilidad a incertidumbres, como defectos de fabricación, presentan desafíos durante el proceso de diseño. Los enfoques tradicionales, que involucraban extensas pruebas experimentales, están siendo reemplazados por simulaciones informáticas para mayor eficiencia y rentabilidad. Estas simulaciones no solo reemplazan los métodos tradicionales, sino que también generan una multitud de resultados, teniendo en cuenta diversas incertidumbres.

Los admisibles de diseño son muy utilizados como valores de diseño que consideran todas las incertidumbres asociadas con las estructuras de materiales compuestos. Obtener estos valores requiere modelos computacionales precisos y un análisis exhaustivo del comportamiento de la estructura compuesta. Además, la mecánica microestructural ayuda a comprender tanto su comportamiento mecánico como las fuentes de variabilidad.

Esta tesis aborda la necesidad de predecir virtualmente admisibles de diseño precisos que tengan en cuenta las incertidumbres inherentes y los defectos de fabricación en estructuras compuestas. El objetivo principal es desarrollar herramientas computacionales que propaguen sistemáticamente las incertidumbres y proporcionen parámetros estadísticos que representen el comportamiento del material. La investigación contribuye tanto a la precisión como a la eficiencia del diseño de estructuras compuestas, alineándose con el cambio de la industria hacia metodologías más rentables y prácticas.

Para lograr estos objetivos, la tesis se centra en tres componentes principales: el modelado estadístico para admisibles de diseño, un análisis computacional para simulaciones de respuesta mecánica y el desarrollo de un modelo micromecánico avanzado para comprender el comportamiento del material a escala microscópica. Cada componente contribuye a un marco integral para gestionar y mitigar eficazmente las incertidumbres en materiales compuestos.

En la primera contribución de esta tesis, se presenta una herramienta eficiente

para predecir admisibles de diseño en un laminado con un agujero pasante, específicamente el *B-value*. Este enfoque novedoso utiliza un modelo analítico que tiene en cuenta meticulosamente la variabilidad intrínseca del material y las tolerancias geométricas. Este trabajo mejora significativamente la comprensión de la predicción de admisibles de diseño en el nivel más bajo de la pirámide de certificación, a nivel de espécimen, proporcionando una metodología clara y aplicable a diferentes niveles estructurales.

El segundo artículo derivado de esta tesis desarrolla una metodología sistemática para obtener admisibles de diseño utilizando un modelo numérico. Dada la complejidad de la respuesta mecánica de los materiales compuestos, especialmente en escenarios como la compresión después del impacto, son necesarias técnicas de modelado sofisticadas. Modelarlo analíticamente es muy complejo, por lo que es necesario utilizar modelos numéricos basados en el método de elementos finitos para predecir con precisión su comportamiento mecánico. Sin embargo, estos modelos numéricos requieren recursos computacionales robustos y tiempos de simulación extendidos en comparación con los modelos analíticos, lo que presenta dificultades para obtener tamaños de muestra grandes. La metodología propuesta aborda esta limitación al crear una superficie de respuesta precisa a partir de los datos numéricos disponibles, permitiendo la interpolación de numerosos valores. Esto facilita el análisis estadístico, simplificando el proceso de obtención de admisibles de diseño de manera eficiente.

El tercer artículo se vuelve a centrar en la predicción de admisibles de diseño en un laminado con un agujero pasante, considerando la presencia de defectos mediante modelos analíticos y numéricos. La presencia de defectos en estructuras compuestas es una realidad inevitable durante el proceso de fabricación que requiere una consideración meticulosa. A nivel de espécimen, donde lograr la disposición deseada mediante la alineación precisa de cada capa se convierte en una tarea compleja, se debe tener en cuenta las desviaciones de las capas. Los modelos analíticos facilitan la generación de grandes tamaños de muestra para un análisis estadístico más preciso, mientras que las simulaciones numéricas ofrecen una precisión más alta. El estudio compara estas herramientas computacionales y sugiere un enfoque híbrido para establecer admisibles de diseño, logrando un equilibrio entre eficiencia computacional y fiabilidad de los resultados.

En la última contribución de esta tesis, se destaca la importancia de comprender el origen de esta variabilidad al tener en cuenta los admisibles de diseño en estructuras compuestas. Los modelos micromecánicos surgen como herramientas poderosas para describir el comportamiento mecánico de los materiales a escala microscópica, centrándose en comprender cómo interactúan individualmente cada uno de los constituyentes, como las fibras y la matriz, para influir en las propiedades mecánicas de los materiales compuestos. Además, a escala microscópica, la influencia de defectos, particularmente los poros, contribuye significativamente a la variabilidad de las propiedades de las estructuras compuestas. Este artículo de investigación propone una metodología innovadora que utiliza un modelo micromecánico mejorado para predecir las propiedades elásticas a escala mesoscópica y sus incertidumbres asociadas.

La tesis se estructura en varias partes, incluyendo una revisión bibliográfica, publicaciones revisadas por expertos y una discusión de resultados y conclusiones. A través del desarrollo y validación de estos modelos, la investigación contribuye no solo a la comprensión de las incertidumbres en las estructuras compuestas, sino que también proporciona herramientas valiosas para que los ingenieros puedan optimizar los diseños de manera iterativa y rigurosa.

Part I

Introduction and literature review

Introduction

1

1.1 Contextual background

Composite materials consist of mixing two or more constituents, with the aim of generating a material with better characteristics compared to each constituent in isolation. One constituent serves as a matrix, while the other works as a reinforcement. Polymer composite materials, in particular, are widely used thanks to their specific properties. In other words, they ensure great mechanical performance with a low density. Notwithstanding these advantages, it is worth mentioning that their anisotropic behavior make their design a complex process. Furthermore, the inherent brittleness in polymer composites means that failure emanates from a stress raiser, which may be a geometric feature, localized damage, or the presence of defects.

Therefore, composite materials are highly susceptible to uncertainties such as the applied load, the intrinsic material variability, the geometry, and the presence of defects. Due to the statistical nature of composite materials, the design and certification of composite structures requires extensive test campaigns structured according to the building-block approach. This process consists on a step-by-step analysis, with each incrementally expanding the preceding one as illustrated in Fig. 1.1. The initial phase involves the characterization of the material at the coupon level, which relies on the definition of statistically representative parameters, referred as design allowables. These allowables follow statistical definitions outlined in the Composite Material Handbook (CMH-17) [1]. The second phase, conducted at the element level, entails the acquisition of data that enriches the understanding of how the material behaves in a specific configuration under defined loads. Moving forward, the component level is tested to understand the structural integrity and performance of larger components under realistic conditions. Afterwards, assessments focus on the examination of joint effects, load distribution, and the overall response of the assembly. Finally, the entire system including composite structures in conjunction with other materials is evaluated to ascertain its overall performance and reliability.

Composite structures exhibit high variability due to the presence of different

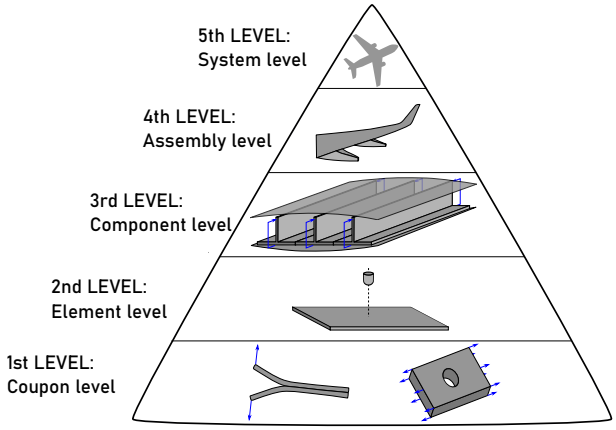

Figure 1.1: Pyramid followed for the certification of composite structures.

materials assembled together. This combination introduces a complex interaction of all the properties, contributing to a complex structural behavior. Within this context, the presence of defects emerges as a critical factor influencing the overall structural performance of these composites. These defects, ranging from manufacturing irregularities to material imperfections, might exhibit a pronounced impact on the overall performance. Therefore, recognizing and comprehending the role of defects is crucial for quality control, structural optimization, and ensuring the reliability of composite structures throughout the design and manufacturing process.

Furthermore, the industry is pushing for current technological advancements to enable the replacement of intensive test campaigns with computational simulations, encompassing both analytical and numerical methodologies, towards certification by analysis. This new approach offers a transformation in the traditional building-block method, presenting opportunities for enhanced efficiency, cost-effectiveness, and accelerated design iterations. The integration of computational simulations allows for the virtual exploration of material behaviors under diverse scenarios, contributing valuable insights across all phases of the building-block approach. Analytical methods, characterized as low fidelity models, provide theoretical frameworks for understanding fundamental material characteristics and generating estimators of the design values. These models involve assumptions and simplifications to make the design more manageable. Numerical simulations, known as high fidelity approaches, enable the explo-

ration of complex structural responses in diverse configurations and loading conditions. These simulations try to replicate the real behavior with higher accuracy using the appropriate mechanical response of each material. These advanced computational tools, with the traditional testing framework, introduce an analysis synergy, empowering engineers to optimize composite structures iteratively and rigorously.

1.2 Motivation

The generation of accurate design allowables, while considering intrinsic material variability, coupon geometry tolerancing, and the presence of defects in composite structures, is a current critical point. This challenge is further heightened by the objective within industry to minimize costs associated with the design process. Consequently, traditional experimental test campaigns are being replaced by accurate simulations.

In light of these new dynamics, there is an opportunity to systematically address and account for all these uncertainties when developing composite structures. The overarching goal is to obtain computational statistical parameters that faithfully represent the material behavior. This research not only look for accuracy and reliability in composite structures design, but also responds to the practical need for more cost-effective and efficient methodologies, like computational tools, within the landscape of composite materials engineering.

1.3 Objectives

This thesis is centred around two primary objectives. The initial one involves **the generation of design allowables that appropriately account for uncertainties and manufacturing defects inherent to composite structures, employing suitable computational analysis methods.** Furthermore, it is important to understand the source of all these uncertainties. Following on from this, the second main objective entails **an in-depth analysis of the micromechanical behavior of composite materials.** This analysis aims to propagate uncertainties from the constituents, accounting for the presence of defects, to the whole composite structure, specifically within the meso-scale model.

To achieve these goals, different specific objectives have been derived.

i) **Develop a statistical model to calculate design allowbles for composite structures in accordance with the CMH-17.** This point requires a comprehensive analysis to identify and quantify statistical values used during the design process. First of all, it is important to detect the intrinsic uncertainties present in composite structures. Subsequently, it is necessary to formulate a methodology to systematically propagate these uncertainties throughout the design process.

ii) **Formulate the corresponding modelling and simulation strategy to capture the mechanical response of composite structures under various stress raisers.** This entails the development of a robust numerical framework capable of capturing the mechanical behaviors exhibited by composite materials under different loading conditions. The computational model should encompass key parameters such as material properties, geometric configurations, and the presence of defects. Additionally, it is important to enhance the accuracy and efficiency of the simulations. The goal is to establish an accurate modelling and simulation strategy for each analysis that not only replicates real-world responses but also provides valuable insights into the structural performance and integrity of composite structures in the first steps of the design process.

iii) **Calculate the design allowables numerically employing the appropriate analysis method and accounting for uncertainties and defects.** This involves selecting the computational tool that best fits the requirements of the design process. Analytical models will be chosen for fast predictions, prioritizing the efficiency. Meanwhile, high fidelity models will be necessary to better understand the mechanical behavior exhibited by composite structures, ensuring a comprehensive and accurate analysis.

iv) **Develop an advanced micromechanical model that considers the constituent material within composite structures.** This model may capture the mechanical response of composite structures accounting for uncertainties and the presence of defects at the micro-scale. Therefore, it can be used as a valuable tool not only for predicting the mechanical performance, but also for identifying the sources of uncertainty inherent to composite materials. The insights gained from this micromechanical analysis should contribute to a better comprehension of the material behavior, facilitat-

ing the development of strategies to manage and mitigate uncertainties effectively.

1.4 Thesis structure

The present thesis has been developed as a compendium of four peer-reviewed publications, trying to addresses the specific objectives i)-iv) of the thesis. With this in mind, the document has been divided into several chapters, grouped into different parts according to their context.

In Chapter 2, a literature review of design allowables is thoroughly outlined. This review first gives an introductory overview of the importance of employing statistical values during the design process of composite structures. Afterwards, the effect of defects on the mechanical response of these materials is highlighted. It is worth mentioning that this review, and the greater part of this thesis, will deal with continuous fiber reinforced polymer (FRP) composites, made of carbon fibers, since these materials are more attractive thanks to their high performance. Together with Chapter 1, this constitutes Part I of this thesis.

The core of this work is presented in Part II, which is composed of Chapters 3, 4, 5, and 6. In these chapters, each publication derived from this thesis is presented. To give the present thesis coherence, an introductory overview is given to contextualize each paper and emphasize its relevance to the overall objectives of this thesis.

The culmination of this thesis is presented in Part III, with Chapter 7 providing a general discussion of the results obtained from all the papers, and Chapter 8 drawing the general conclusions and outlining future work.

Finally, a reproduction of the papers published at the time of the submission of the thesis, in their journal form, is included in Appendix A.

Literature review

2

2.1 Design allowables in composite structures

The Building Block approach (BBA) outlined in the Composites Material Handbook (CMH-17) [1] forms the foundation for the certification of composite structures. This approach involves a systematic progression from small specimens to full-scale products, emphasizing cost efficiency and risk assessment at each stage. Small specimen and element tests, at the lowest Building Block level, play a crucial role in characterizing material properties, notch sensitivity, and operational limits [1]. These tests provide data for preliminary designs, facilitating the development of material scatter factors and design allowables.

Design allowables are paramount in material selection, structural design, and certification of composite structures. They guide engineers in crafting structures that meet performance requirements while adhering to safety standards. In the complex realm of composite materials, with challenges like anisotropy, material variability, and the presence of defects, accurate design allowables are essential. Inaccuracies in these values can have far-reaching consequences, impacting the structural robustness of composite components. Thus, meticulous determination of design allowables is imperative for advancing and applying composite materials across diverse scales.

Variability in composite material properties arises from fabrication, raw material batch variations, testing, and intrinsic material factors. Acknowledging and incorporating this variability into design allowables is crucial for ensuring structural integrity and regulatory compliance.

The CMH-17 introduces the A and B-basis values as statistically-based design allowables for composite structures:

i) A-basis value: a statistically-based material property; a 95% lower confidence bound on the first percentile of a specified population of measurements. Also a 95% lower tolerance bound for the upper 99% of a specified population.

ii) B-basis Value: a statistically-based material property; a 95% lower con-

fidence bound on the tenth percentile of a specified population of measurements. Also a 95% lower tolerance bound for the upper 90% of a specified population.

The definitions of these statistically-based material properties involve modelling a deterministic property with a probability distribution to account for observed scatter. Tentative definitions in terms of percentiles are then adjusted conservatively to accommodate the additional uncertainty arising from limited data.

Calculating the basis value involves determining the distribution of percentiles (10th for B-value and 1st for A-value) and calculating the confidence interval of the percentile, particularly the 95% lower confidence bound corresponding to the 5th percentile of their distribution [2].

2.2 Computational tools for composites behavior prediction

Testing all possible scenarios for composite structures is expensive and impractical. Analysis alone may not cover all conditions adequately. Therefore, a combination of testing and analysis, as exemplified by the BBA [1], offers a cost-effective strategy. The BBA involves iterative testing and analysis at different levels to mitigate risks and ensure that surprises are minimized.

To address the challenge of high costs, literature explores the use of high-fidelity simulations or low-fidelity models with a reduced set of experimental data. Techniques involving Finite Fracture Mechanics (FFM), Finite Element Method (FEM), and failure theories are employed to provide direct estimations of design allowables.

2.2.1 Low-fidelity model based on Finite Fracture Mechanics

A robust analytical model capable of accurately predicting composite material behavior is highly efficient. Fracture mechanics takes center stage in understanding and addressing fundamental questions related to component and process design with a focus on fracture resistance. The driving forces within fracture

mechanics pivot around the loads acting at the crack tip, quantified by the stress intensity factor (SIF), and the energy available to propagate the crack. Material resistance to fracture is defined as the fracture toughness, denoted as $\mathscr{G}_c$. The criteria for fracture onset can be viewed as a delicate equilibrium between the loads at the crack tip and the material fracture toughness [3].

While traditional FFM deals with homogeneous and isotropic materials, the usage of composite structures necessitates tailored solutions for anisotropic materials [4].

Assumptions underlying fracture mechanics for composites encompass:

i) All bodies inherently contain cracks or stress raisers, and FFM analyzes crack propagation.

ii) Crack growth is characterized by the energy required per unit area, defined as the crack resistance $\mathscr{R}$ [4].

This foundational framework provides an understanding for assessing the fracture behavior of composite materials, taking into account anisotropy and emphasizing the critical interplay between crack growth, stress intensity, and material toughness.

Based on FFM, Furtado et al. [5] enhanced the model proposed by Camanho et. al. [6] to determine the open hole (OH) strength of notched composites from a low-fidelity model.

The FFM model developed by Camanho et. al. [6] worked as a fast and accurate method to predict the OH tensile strength of composite laminates based on a stress and energy balance. It only required the ply elastic constants and two additional independent material properties: the laminate unnotched strength and the laminate fracture toughness. Therefore, predictions can be obtained rapidly without employing FEM analysis or complex computational methods. Furtado et al. [5] extended this model, reducing the required material properties to three ply properties: the longitudinal Young's modulus (E_1), the fracture toughness ($\mathscr{G}_{IC}$), and the tensile strength (X_T). This enhancement is based on the Trace theory, Master Ply concept [7], and Omni Strain Last-Ply Failure envelopes [8]. However, this tool has some limitations: i) the equations are only applicable to balanced laminates, ii) it does not account for delamination, and iii) failure must

be lumped on a single plane [5].

2.2.2 High-fidelity models in composite behavior prediction: a comprehensive overview

In the intricate landscape of engineering analysis, understanding the complex behavior of systems poses a substantial challenge for the human mind. To overcome this, engineers employ a systematic approach called discretization, breaking down complex systems into individual elements. The FEM is grounded in this principle, offering a robust framework for analyzing and simulating the behavior of structures [9]. This approach facilitates a more manageable analysis, enhancing the understanding of the response of the system under various conditions. It serves as a fundamental principle in numerical simulations, enabling the study of diverse engineering phenomena.

In the contemporary landscape, an array of commercial software programs has emerged, bringing robust FEM capabilities for different engineering disciplines. These software tools have become indispensable for solving a wide spectrum of engineering problems, ranging from simple linear static analyses to intricate nonlinear transient analyses. Among the most renowned software packages in this domain are ANSYS [10] and ABAQUS [11]. These platforms empower engineers with the tools needed to simulate and analyze complex systems, providing insights that are crucial for design optimization, structural integrity assessments, and performance predictions.

As technology advances, these FEM software solutions continue to evolve, incorporating sophisticated algorithms and user-friendly interfaces. They have become essential companions in the engineer's toolkit, enabling efficient and accurate analyses that would otherwise be impractical or impossible.

The inherent variability in composite materials necessitates accounting for uncertainties in material properties and processes. Failure theories applied to FEM are widely adopted, giving rise to the need for running FEM multiple times to consider parameter variability with associated probability distributions. Therefore, a sampling method should be carefully chosen for the generation of FEM results obtained from samples combining different sets of parameters. In this realm, the Stochastic Finite Element Method (SFEM) emerges as a crucial

tool [12, 13].

Three prominent SFEM solutions are frequently employed:

i) Monte Carlo Simulation (MCS): MCS stands out as a robust model employed to predict the probability of various outcomes when random variables are considered. It operates through repetitions, allowing for a comprehensive understanding of the potential outcomes [14]. This method has been a useful tool in materials science and structural applications for decades, offering accurate solutions for stochastic problems involving nonlinearities, dynamic loading, stability effects, and parametric excitations [14], at the cost of running several deterministic simulations.

ii) Perturbation Method: In the Perturbation Method, all random variables of an uncertain system are expanded around their mean values using Taylor series. This approach derives analytical expressions for variations in desired response quantities, such as natural frequencies and mode shapes, due to small variations in these random variables [15]. Although providing high accuracy and computational efficiency, its precision relies on the Taylor series, and it is limited to linear problems for first order approximations. Additionally, its accuracy diminishes with an increase in the number of uncertainties [16].

iii) Spectral Stochastic FEM (SSFEM): SSFEM introduces a spectral expansion of nodal random variables, incorporating a basis in the space of random variables. This basis comprises polynomial chaos, orthogonal polynomials concerning the Gaussian probability measure. The unique formulation allows the computation of probability distribution functions of response variables efficiently [17]. While SSFEM is computationally efficient and precise, it is restricted to linear problems, and its accuracy tends to decrease with a rising number of uncertainties [16].

Perturbation-based SFEM requires knowledge of only the first two moments of random variables, presenting a favorable aspect compared to statistical techniques like MCS, which often require intricate probability density functions that are not readily available. Both Perturbation Method and SSFEM provide high accuracy and computational efficiency. However, the first relies on Taylor series accuracy, and the latter is limited to linear problems, with reduced accuracy as

uncertainties increase [15, 16].

Therefore, MCS remains the first choice solution in material science and structural applications such as the effect on hybrid composites [18], on the tensile strength and fracture process for unidirectional FRP [19, 20] or on a perforated plate [21]. Moreover, Latin Hypercube Sampling (LHS) emerges as a technique for selecting a reduced yet well-distributed set of random samples. LHS is particularly valuable because it avoids clustering, ensuring a more representative sample set [12, 22].

Therefore, using MCS in a FEM model emerges as a powerful tool for obtaining design allowables in the composite industry, addressing critical design drivers. Two primary focuses include:

i) OH strength: a crucial aspect in composite structures, especially those assembled with mechanical fasteners. Stress concentration around holes significantly impacts tensile and compressive strength, making OH strength a vital design driver [1].

ii) Damage characterization: involves assessing material resistance to impact (damage resistance) and its ability to perform safely after damage (damage tolerance). Damage resistance of a material is commonly considered to be the resistance of the material to impact damage in aerospace applications. Impacts may arise from dropped tools, foreign objects such as rocks on runways, from hail or ice. Therefore, low velocity impact (LVI) is a common test to check the effect of damage resistance. The compression after impact (CAI) test is an empirical evaluation of the degradation of laminate compressive strength (damage tolerance) due to out-of-plane impact [23].

2.2.2.1 Advancements in modelling open hole strength of fiber-reinforced polymers

One of the common design drivers during the qualification of a composite structure is the characterization of the notched strength of FRP typically determined from an OH specimen. Furtado et al. [24] provides a foundational framework for simulating OH tensile specimens, incorporating advanced damage models to enhance predictive accuracy.

The continuum damage model utilized in the OH tensile specimen simulation draws inspiration from [25, 26]. However, Furtado et al. [24] introduced modifications to improve the efficacy of the model in predicting damage initiation and evolution under diverse loading conditions. Notably, the model enhancements maintain a balance, ensuring improved accuracy without an undue increase in computational cost.

A pivotal aspect in the OH specimen simulation is the incorporation of a cohesive zone model to predict delamination onset and propagation. Challenges in existing formulations, often tailored for pure mode I and II loading, prompted a critical evaluation. Most formulations struggle with validation under mixed-mode loading conditions, and friction is commonly overlooked.

Furtado et al. [24] innovatively proposed the adoption of the cohesive zone model introduced by Turon et al. [27]. This model stands out for its accurate prediction of damage propagation under mixed-mode loading. The inclusion of a mode-dependent penalty stiffness, coupled with the integration of the Coulomb friction law [28], addresses the limitations observed in prior cohesive zone models. The nuanced approach considers the complex interplay of factors influencing damage evolution, ensuring a more realistic representation.

The advancements in modelling OH strength of fiber-reinforced polymers, as guided by the strategy of Furtado et al. [24], signify a higher accuracy. This refined modelling approach holds promise for more precise simulations, contributing significantly to the qualification and optimization of composite structures in diverse engineering applications.

2.2.2.2 Advances in simulating low-velocity impact and compression after impact in composite structures

In the aeronautical industry, assessing the compression after impact (CAI) strength stands as a critical metric for damage tolerance design allowables. This strength is determined through standardized tests, where a laminate, post-impact, undergoes compression loading to evaluate its residual strength. The correlation between impact energy levels and CAI strength is established by conducting tests at various impact energy levels. In one test configuration, the monolithic specimen is positioned over a metal frame, impacted using a drop-tower. After

the impact, the impacted specimen and a pristine specimen (of the same laminate of the impacted one) are glued to both sides of a honeycomb specimen to prevent failure due to buckling. The specimen is loaded under in-plane compression to obtain its residual strength. The CAI test is vital for airworthiness certification, and numerical simulations play a crucial role in predicting and understanding complex interactions.

Numerous numerical studies have emerged to simulate LVI and CAI tests on composite structures [29–38], reflecting the growing interest in predicting CAI strength. This interest is fueled by CAI strength being a pivotal design driver for certain aeronautical components. Simulating CAI tests is intricate, involving complex contact interactions, progressive material degradation, and the interplay of multiple failure mechanisms.

Recent findings [23, 39, 40] indicate that conventional shell elements are a suitable choice for successful CAI simulations, offering a balance between analysis time and accuracy. Key numerical parameters, such as criteria to prevent excessive finite element distortion, mass distribution between shell and cohesive elements, and mesh size, must be well-defined for accurate predictions. For instance, a criterion to avoid excessive distortion of degraded shell elements involves considering residual stress in each material loading direction. Regarding the cohesive elements, the isotropic damage variable of the cohesive (interlaminar) elements is limited to a value of 0.9999, so that a residual stiffness remains constant at any propagation mode once the element is degraded. To define the composite material behavior, models featuring intra- [25, 26] and interlaminar [41] damage can be used.

English et al. [22] employed the Stochastic Finite Element Method (SFEM) to simulate an LVI test on a laminate. Latin Hypercube Sampling (LHS) was utilized to define an input test matrix, and results were compared with experimental data for model adjustment and validation. Patel et al. [42, 43] conducted a probabilistic analysis using SFEM in an LVI test, estimating the probability of failure criteria for matrix cracking and delamination at different impacted energies.

Despite a wealth of published works, there is a notable gap in directly determining design allowables from damage tolerance simulations using advanced

constitutive models. This presents a challenge and an avenue for future research to establish design allowables based on sophisticated constitutive models in the context of CAI strength.

2.3 Defects in composite structures: unraveling influences on mechanical performance

The meticulous consideration of defects is paramount in comprehending and optimizing the mechanical performance of composite structures. Defects play a pivotal role in influencing the initiation and progression of damage within these structures, thereby exerting a profound impact on their overall mechanical behavior. In the context of FRPs, defects are intricately linked to the constituents, encompassing a spectrum of challenges. Fiber-related defects, including but not limited to degradation or in-plane misalignment, introduce variability and vulnerability into the structural integrity of composites. Matrix defects, ranging from porosity to contaminants, further contribute to the intricacies associated with defect-induced mechanical anomalies. Additionally, defects at the interface of fibers and matrix, such as debonding or inadequate wetting of fibers, introduce vulnerabilities that can significantly compromise the structural robustness of composite materials [44, 45].

The holistic understanding and characterization of these defects become imperative for engineers and researchers, guiding strategies for defect mitigation, structural optimization, and the establishment of robust design principles in composite material applications.

This thesis is dedicated to unraveling the profound impact of two prevalent defects on distinct scales: voids at the micro-scale and ply misalignment at the ply level (meso-scale). Voids, characterized by trapped air or gaps within the matrix, and ply misalignment, stemming from the improper orientation of fiber layers, emerge as critical actors affecting the mechanical behavior of composite materials. The micro-scale manifestation of voids introduces structural irregularities, potentially leading to stress concentration points and compromising material uncertainty. In contrast, ply misalignment, occurring at the meso-scale, disrupts the intended load-bearing pathways within the composite structure. By meticulously exploring these defects, this thesis aims to provide

a comprehensive understanding of their effects, offering valuable insights for optimizing composite material design and advancing the field of composite structural analysis.

2.3.1 Voids in composite materials: microscale manifestations and mechanical implications

Voids are among the most important defects since they affect a wide range of composite properties and they tend to be common in many different manufacturing techniques [46, 47].

Characteristically, voids are cylindrical branch-type defects [48], often aligned with the fiber direction, and their presence stems from multiple sources such as air entrapment during initial manufacturing and the introduction of volatile components or contaminants during curing [49].

The size, shape, and content of voids can vary considerably within a composite. Macrovoids, studied extensively in carbon/carbon composites, have been found to exhibit irregular shapes, challenging the conventional assumption of voids aligning with fibers [50]. Irregularly shaped macrovoids demonstrated nuanced effects on longitudinal and transverse stiffness, emphasizing the need for a comprehensive understanding of void geometry in composite materials. In this thesis, however, the focus shifts to the microscale, particularly on voids at the constituent level, associated with porosity occurrence.

Microvoids, investigated through 3D micro-CT scanning, exhibit a rod-like geometry oriented along the fiber direction [51–62]. Their cross-sections, often irregular or nearly circular, present challenges in modelling but are crucial for capturing their impact on composite behavior. Microvoids, typically featuring equivalent diameters ranging from 3 to 20 μm [57–60], pose complex challenges during manufacturing, especially when comparable in size to the fiber diameter.

Insights from studies by Vajari et al. [59], Hyde et al. [63], and Daggumati et al. [64] suggest that microvoids, comparable in size to fiber diameter, are present among irregularly shaped fiber clusters, indicating challenges in matrix flow during manufacturing. Additionally, microvoids may manifest as small air bubbles trapped in the matrix. The nature of microvoids, their irregular shapes,

and diverse sizes underscore the importance of accounting for these intricacies in modelling composite materials.

Examining the mechanical implications of voids in FRPs reveals a range of detrimental effects. The experimental findings of Almeida and Neto [65] underscore the negative influence of voids on fatigue life. Chambers et al. [60] have observed that an increased void content diminishes flexural strength and fatigue performance, influencing the initiation and propagation of failure mechanisms. Zhu et al. [55] reported that cracks emanating from voids lead to reduced tensile strength and modulus. Additionally, Chu et al. [66] noted the detrimental effect of porosity on transverse and shear moduli, while its impact on longitudinal properties remained comparatively lower.

This comprehensive understanding of the intricate interplay between voids and composite mechanical properties is indispensable for advancing the design and manufacturing of high-performance composite materials.

2.3.2 Ply misalignment in composite structures: unraveling meso-scale dynamics

Within the scope of composite structures, misalignments manifest at different scales, including the ply and individual fiber levels, with the latter referred to as in-plane waviness [67]. This section delves into ply misalignment at the meso-scale, focusing on its often-termed synonym, fiber straightness, where the primary variability stems from fiber waviness [68].

The impact of ply misalignment has been subjected to extensive exploration in the literature. This broad investigation, spanning various methodologies and material types, has significantly contributed to our understanding of the multifaceted effects of misaligned plies on composite structures.

Hinckley et al. [69] employed classical laminated plate theory to rigorously assess the repercussions of ply misalignment. This foundational work laid the groundwork for subsequent studies, establishing a statistical framework for evaluating the impact of misalignment on composite material behavior. Arao et al. [70] delved into the intricate realm of out-of-plane deformation in CFRP, shedding light on the potential for unpredictable deformations arising from deviations

in ply angles. This investigation provided valuable insights into the complex behavior of misaligned plies, particularly in the context of CFRP. Steeves et al. [71] extended the analysis of ply misalignment to ultra-thin composite materials. Their exploration, focused on materials with reduced thickness, contributed to a more comprehensive understanding of how misalignment manifests in structures with unique geometric and mechanical characteristics. Thompson et al. [72] focused on the specific context of angular errors during ply placement in unidirectional FRP composites. By meticulously examining the influence of misalignment on the peak-to-valley surface deformation values of circular plates, this study provided targeted insights into the consequences of misaligned plies on the structural integrity of composite components.

Collectively, these studies, based on diverse methodologies and applications, form a cohesive body of knowledge that enriches our appreciation of the intricate interplay between ply misalignment and the mechanical behavior of composite materials. Despite these extensive investigations, an unexplored dimension persists, as existing literature studies have yet to collectively address all uncertainties associated with this complex phenomenon.

2.4 Micromechanical models for composite materials

The meso-scale simulations are based on uncertainties stemming from the inherent variability of constituents, their stochastic spatial arrangement, and the presence of defects at this lower scale. Consequently, micromechanical models prove to be valuable tools for quantifying and addressing these uncertainties. By leveraging micromechanical models, one can gain deeper insights into the intricate interactions among constituents, consider their random spatial distribution, and assess the impact of defects on the prediction of the properties to be used at the meso-scale. This approach becomes pivotal in enhancing the accuracy and reliability of meso-scale simulations, contributing to a more comprehensive understanding of the material behavior and performance under various conditions.

Therefore, this section provides an overview of the most important micromechanical models presented in the literature that are able to reproduce the behavior

of UD composite materials. It is also worth noting that each model possesses unique features and limitations.

Composite materials are studied on three distinct levels: micromechanical, mesomechanical, and macromechanical (see Fig. 2.1). The micromechanical level involves the representation of fibers and the matrix, enabling the study of their interactions. Moreover, it considers the presence of defects at this scale, such as the presence of voids, fiber-matrix decohesions or fiber degradation. The mesomechanical level considers fibers and the matrix as a unified material with homogeneous mechanical properties at the layer level, capturing interaction between layers but not between fibers and the matrix. Lastly, the macromechanical level takes into account the global structure or mechanical component using, for example, laminate theory [73].

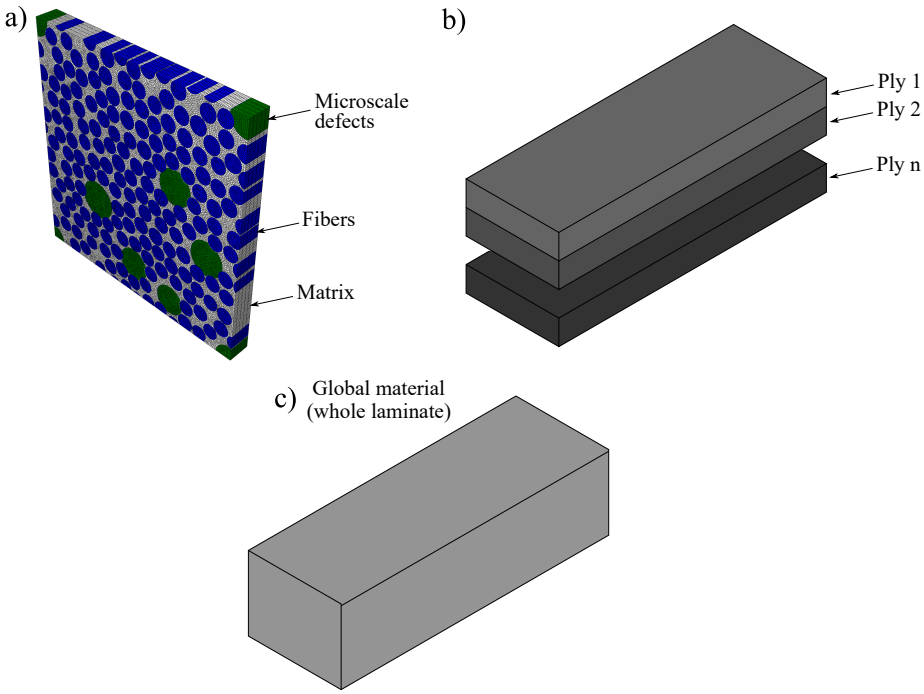

Figure 2.1: The three mechanical levels for studying composite materials: a) micromechanical, where fibers and matrix are represented, b) mesomechanical, where fibers and matrix are homogenized at the level of each layer and c) macromechanical, where a homogeneous material is considered for the entire laminate.

When studying composite materials at the micromechanical scale, fibers and matrix are typically represented by generating a Representative Volume Element

(RVE). This RVE serves as a volume encapsulating the genuine characteristics of the material, encompassing both fibers and matrix within the context of composite materials. It is defined based on a balance between being representative and sufficiently large to capture all relevant physics, but computational constraints often impose limitations on its size. Studies suggest that the RVE should be approximately fifty times the fiber radius for accurate predictions of elastic properties [74, 75]. However, for damage analysis, a larger size may be imperative to consider stress redistribution around breaks.

Consequently, the RVE must be large enough to be representative of the continuum at a higher level. An infinitesimal RVE may be employed in theory, but practical numerical analysis necessitates a finite size [74]. Hence, statistically Representative Volume Elements (SRVEs) are utilized as they replicate the same statistics related to stress and strain fields observed at the macroscopic material level. To validate the statistical representativeness of the RVE (SRVE), a contrast of hypotheses for the mean and standard deviation of the predicted results must be conducted.

In determining the appropriate size for SRVEs, Li et al. [76] found that fibers should be discretized using finite elements with dimensions as small as 0.0008 mm. Trias et al. [74] established that the minimum RVE size should fall within the range of 5×5 to 25×25 fiber diameters. Additionally, González and Llorca [77] predicted that an RVE containing 30 fibers is representative of the macroscopic material. These considerations underscore the importance of selecting an appropriately sized SRVE for micromechanical analyses in composite materials.

Spatial positioning of fibers within the SRVE is a key aspect. In 1D SRVEs, only one row of fibers is considered, but 2D SRVEs offer a more realistic representation. In the latter case, fibers can be allocated within a square, hexagonal, or randomly packed arrangement, with the latter being the most realistic for composite materials, since the spatial allocation of the fibers is always random, and allows the stress distribution to be captured more accurately [78, 79].

Generating a Statistically Representative Volume Element (SRVE) with hexagonal or square packing is a relatively straightforward process, but achieving the same with random packing presents challenges. Various methods are available

in the literature for generating SRVEs with a random distribution of fibers. One approach involves digital image analysis, employing sophisticated software tools [80–84]. Alternatively, an algorithmic method can be used, with two primary approaches: the 'hard-core' model and the 'shaking' model.

In 'hard-core' models, random fiber coordinates are continuously generated within the SRVE, and acceptance criteria ensure that new fibers do not overlap with any existing fibers in the domain [78, 81, 82, 85–87]. Some models use different criteria to move fibers around, filling empty spaces and adding more fibers until the desired fiber volume fraction is achieved. On the other hand, 'shaking' models start with a predefined square or hexagonal distribution of fibers, which is then shaken to achieve a random arrangement [88–93].

One widely acknowledged model that adopts a 'hard-core' approach was developed by Melro et al. [78] and extended by Tavares et al. [94] for generating hybrid intrayarn composites. This algorithm is robust, having undergone statistical validation against experimental RVEs [80], and demonstrates the capability to achieve a fiber volume fraction exceeding 65% [78].

2.4.1 Micromechancial models addressing the effect of defects: the presence of voids

Studies, employing 3D micro-CT scanning, reveal that microvoids typically exhibit a rod-like geometry aligned along the fiber direction. Their cross-sections can vary from irregular shapes to approximations of a circular form, with an equivalent diameter falling within the range of 3 to 20 µm, even for thermoplastic matrices (see Chapter 2.3.1).

The algorithm developed by Melro et al. [78], initially designed for random fiber distribution in an RVE, and later extended by Tavares et al. [94] to simulate the microstructure of composite materials with different fiber types (i.e., fiber-hybrid composites), can be effectively employed to model both fibers and voids assumed to have a rod-like geometry.

Numerous investigations have delved into the effects of voids on the mechanical properties of FRPs. These investigations, each contributing unique insights, collectively enhance our understanding of the complex interplay between voids

and composite material behavior.

Vajari et al. [59] conducted a noteworthy study employing 2D numerical simulations. Their focus encompassed elongated voids aligned parallel to the fiber direction, featuring a circular cross-section. Additionally, the investigation extended to consider inter-fiber voids characterized by irregular shapes, providing a comprehensive examination of void impact. Dong [95] explored the effects of randomly distributed voids on the stiffness and strength of FRPs. This investigation not only delved into the empirical observations but also engaged in a comparative analysis with analytical models, contributing valuable insights into the multifaceted aspects of void-induced effects. Mehdikhani et al. [46, 62] undertook simulations to dissect the impact of microvoids on the elastic moduli of carbon fiber-reinforced polymers. Their meticulous examination included the consideration of a single ellipsoidal void embedded in the matrix, referred to as 'matrix voids', shedding light on the intricacies of void morphology and its repercussions. Hyde et al. [58, 63] adopted a micromechanics-based finite element modelling strategy to check the influence of a single matrix or inter-fiber void on the strength of composite structures. This approach allowed for a detailed investigation into the nuanced effects of void type on the overall structural integrity of FRPs. Sharifpour et al. [96] developed a 2D micromechanical model specifically tailored to assess the effect of microvoids on the local stress state in a cross-ply laminate. The focus on a circular void shape provided specific insights into the localized stress distribution within the composite material. Chu et al. [66] contributed to the body of knowledge by examining the influence of voids on the stiffness properties of unidirectional FRPs. Their study, which considered very small spherical voids, added granularity to our understanding of the size-dependent effects of voids on material properties. In a more recent investigation, Daggumati et al. [64] conducted a comprehensive assessment of the effect of matrix and inter-fiber voids. Additionally, they considered other factors such as thermal residual stresses and the random spatial distribution of reinforcements, providing a holistic understanding of the synergistic influences at play in a 2D cell under transverse loading. Vinot et al. [97] brought attention to the quantification of uncertainties, specifically porosity, in continuous unidirectional composites. Their model not only addressed the uncertainties associated with voids but also evaluated their broader influence on the mechanical properties of the material, contributing to a more nuanced comprehension of

composite behavior under stochastic conditions.

Despite the extensive research on voids, a notable gap exists in the current literature studies. Simultaneous consideration of the random spatial distribution of constituents, variability in their properties, and the diverse characteristics of voids in defining SRVEs for FRPs is often overlooked. This comprehensive approach is essential for a more accurate and holistic understanding of the behavior of fiber-reinforced polymers.

2.4.2 Micromechanical analytical models

Several analytical models are available in the literature for micromechanical analysis. Some of them are useful for determining the strength but in this thesis the focus is performed in determining the mesoscale elastic properties with the presence of defects, i.e., voids. Therefore, three noteworthy models include the Rule of Mixtures (RoM), the Mori-Tanaka mean field theory, and the Concentric Cylinder Assembly (CCA) model.

2.4.2.1 The Rule of Mixtures

The Rule of Mixtures (RoM) provides reasonable estimates for the longitudinal stiffness (E_1) by assuming that fibers and the matrix work in parallel. Similarly, the major Poisson's ratio (ν_{12}) can be estimated under the same assumption. However, the transverse and shear properties, such as the transverse Young's modulus (E_2) or the longitudinal shear modulus G_{12}, is calculated assuming that the fibers and matrix are working as springs in series.

However, predictions for transverse and shear stiffness using RoM are less accurate. To address this limitation, alternative models, such as the Halpin-Tsai model [98] provide more accurate values from empirical evidences. However, these models only account for the presence of voids by reducing the matrix volume fraction. Therefore, to really account for the presence of multiple types of inclusions (here fibers and voids), the elastic properties are better estimated using other models such as the Mori-Tanaka mean field theory [99].

2.4.2.2 The Mori-Tanaka mean field theory

The Mori-Tanaka mean field theory is designed to account for the presence of multiple types of inclusions, such as fibers and voids. It calculates the effective elastic moduli and Poisson's ratios of a system with unidirectional fibers having a transversely isotropic behavior and multiple inclusions. The Hill's elastic moduli are determined for both isotropic matrix and transversely isotropic reinforcement, considering their specific material properties. The Hill's elastic moduli of each reinforcement are used to determine the overall mesoscale elastic properties.

The Mori-Tanaka mean field theory provides better predictions than with the RoM since it considers a more realstic case. However, when introducing the presence of voids it only considers the case in which voids are embedded in the matrix. Therefore, finally, the CCA model [100] is also checked since it also allows the presence of multiple phases and it can account for voids within the matrix or between fiber bundles.

2.4.2.3 The concentric cylinder assembly model

The Concentric Cylinder Assembly (CCA) model [100] extends Hashin's [101] and Christensen and Lo's models [102] to multilayered (N-phased) inclusions with transversely isotropic material properties. It consists of N-cylinders perfectly bonded together, each representing a homogeneous, linear elastic phase with transversely isotropic behavior. The model addresses loading scenarios for bulk modulus, axial loading, in-plane shear loading, and shear loading transverse to the fibers, providing an effective approach for analyzing composite materials with multiple phases.

To incorporate voids, the CCA model embeds a first phase representing voids with near zero elastic properties inside a cylinder representing the matrix. This void and matrix unit is surrounded by a cylinder representing fibers, and the final outer phase in the 4-cylinder model represents the matrix. Moreover, changing the position of the phase representing the voids, allows considering other cases such as the presence of voids between fiber bundles.

In conclusion, micromechanical models play a pivotal role in unraveling the complexities of composite materials. Understanding the behavior of constituents

at the micro-scale, considering the presence of defects like voids, and employing analytical models contribute significantly to the overall understanding of composite material performance. Further research is essential for refining and expanding these models to address evolving challenges and advance the field of composite materials science.

2.5 Literature review conclusions

The in-depth exploration of existing literature offers valuable insights that span the intricate domain of composite materials, encompassing facets ranging from their manufacturing intricacies to the complexities of their mechanical behavior at various scales. This discourse is organized into distinct yet interconnected sections, each delving into pivotal themes within the realm of composite materials science. The synthesis of these sections yields several overarching conclusions.

Starting with a critical perspective on the study of composite structures, the initial section underscores the paramount importance of addressing uncertainties inherent in these structures. From small coupons to full-scale applications, the discussion advocates for a comprehensive understanding of the uncertainties associated with composite materials. The essence lies in the necessity of defining accurate design allowables to ensure the structural integrity and reliability of composite components.

The succeeding section illuminates the dynamic landscape of composite manufacturing, accentuating a paradigm shift towards advanced techniques facilitated by computational tools. This transformation introduces the potential to substitute laborious experimental test campaigns with low or high-fidelity models. The choice between these models is contingent upon the specific requirements, being the need for large sample sizes or precise results, thereby offering a flexible and efficient approach to composite design and certification.

The subsequent part delves into the complex domain of defects and their pivotal role in influencing the mechanical performance of composite structures. A meticulous examination of fiber-related defects, matrix defects, and interface defects underscores their significance in the structural integrity of composites. The dedicated focus on unraveling the impact of micro-scale voids and meso-scale ply misalignment exemplifies a commitment to understanding and mitigating the

challenges posed by defects in composite applications. The section underscores the need for a holistic comprehension of these defects, guiding the formulation of strategies for defect mitigation, structural optimization, and the establishment of robust design principles.

The last section delved into micromechanical models, emphasizing their significance in addressing uncertainties arising from constituent variability, spatial arrangement, and the presence of defects. The overview of micromechanical models as well as some analytical ones, such as the Mori-Tanaka mean field theory and Concentric Cylinder Assembly model, highlighted their role in providing deeper insights into the interactions among constituents and assessing the impact of defects on meso-scale predictions. The section also identified the importance of considering the presence of defects, in that case voids, for a more accurate understanding of composite behavior.

In conclusion, this holistic literature review underscores the multidimensional nature of composite materials science. From design advancements to defect analysis and micromechanical modelling, the literature reflects the continuous evolution and interdisciplinary nature of the field. The identified gaps and avenues highlight the challenges and objectives of this thesis. As the field continues to progress, these insights will contribute to the development of more robust, reliable, and innovative composite structures across various industries.

Part II

Publications

3

Paper A – Virtual calculation of the B-value allowables of notched composite laminates

The paper has been published in *Composite Structures* 212 (2019) 11-21.

Overview

One of the main objectives of this thesis is to develop a suitable statistical model that can be used to obtain design allowables for composite structures. One coupon configuration emerging from the Building Block approach of main interest in the design process of composite materials is a specimen with a centrally located hole that acts as a stress raiser. In this case, the generation of the notched strength allowable must consider the intrinsic material variability and the geometrical tolerances.

While several models exist for predicting notched strength, the primary goal of this research is to establish a methodology for calculating the B-value in notched specimens. The lack of a comprehensive approach for predicting design allowables in notched coupons prompted the choice of a low fidelity model based on finite fracture mechanics. In particular, the model chosen relies just on three key material properties: the longitudinal Young's modulus (E_1), the longitudinal tensile strength (X_T) and the fracture toughness $\mathcal{G}_{Ic}$ of the 0 ° ply. Consequently, only these three material properties needed to be well characterized to feed the model.

In this chapter, a novel and efficient tool is proposed to predict notched design allowables, specifically the B-value, while accounting for the intrinsic material variability and geometrical tolerances. This model is based on the analytical model developed by Furtado et al. [5], which has been previously validated as a fast tool to predict the notched strength of composite structures. Furthermore, the model has been enhanced to propagate uncertainties in composite structures and to quantify their effect on the design allowables.

This work offers a comprehensive understanding of predicting design allowables at the coupon level, providing a clear methodology for obtaining statistical values that can be extended to larger scales, ensuring their applicability and reliability across various structural levels.

Virtual calculation of the B-value allowables of notched composite laminates

O. Vallmajó[a], I.R. Cózar[a], C. Furtado[b, c], R. Tavares[b, c], A. Arteiro[b, c], A. Turon[a,*], P.P. Camanho[b, c]

[a] *AMADE, Polytechnic School, Universitat de Girona, Campus Montilivi s/n, E-17003 Girona, Spain*

[b] *DEMec, Faculade de Engenharia, Universidade do Porto, Rua Dr. Roberto Frias, 4200-465 Porto, Portugal*

[c] *INEGI, Rua Dr. Roberto Frias, 400, 4200-465 Porto, Portugal*

Abstract

The design of composite structures relies on the accurate determination of design allowables, which are statistically based material parameters that take into account manufacturing, geometrical and microstructure variability. The accurate determination of these design parameters requires extensive experimental testing, which makes the certification process of a composite material extremely costly and time consuming. To increase the efficiency of the design process, there is the need to develop alternatives to the mostly experimental material characterization process, ideally based on accurate and quick modelling analysis combined with powerful statistical tools.

In this work an analytical model to compute the notched strength of composite structures based on three ply based material properties (elastic modulus, un-notched strength and $\mathscr{R}$-curve) is combined with an uncertanty quantification and management (UQ&M) framework to compute the B-basis allowables of notched configurations of CFRPs laminates. The framework is validated with open-hole tension experimental results for the IM7/8552 material. Given the analytical nature of the developed framework and consequent computational efficiency, the UQ&M methodology is applied to the generation of design charts for notched geometries, whose generation would otherwise be impractical, using experimental test based methods.

* Corresponding author

Paper published in: *Composite Structures 212 (2019) 11-21*
Doi: https://doi.org/10.1016/j.compstruct.2018.12.049

3.1 Introduction

The design and certification of composite structures is based on the building block approach [1]. This approach relies on the accurate determination of design allowables that drive the design of structures at larger scales. These design allowables are statistically based material parameters that define an acceptable stress value for a material and, therefore, ensure their safe and efficient use. Design allowables have to account for the variability of the material properties and of the manufacturing process, and are a function of the structural details and loading conditions [103] and, consequently, their experimental determination is an extremely costly and time-consuming process. The standard design allowable used in the aeronautical industry for fail safe structures is the B-basis [1, 104], which is defined as the 95% lower confidence bound on the tenth percentile of a specified population of measurements. This is a conservative allowable that ensures with 95% confidence that 90% of the population will have a given property, e.g. strength, higher than the B-value allowable.

It is of key importance to accurately determine these design allowables, however, time consuming processes are not ideal during preliminary design. For this reason, alternatives to fully experimental material characterization have been proposed, namely, the use of statistically based numerical and analytical models [104–107]. These models include the influence of the uncertainty related to the determination of the input parameters and their intrinsic variability on the global response of the model. A convenient way to describe these uncertain quantities is to describe them using a probability distribution which can be defined through experimental measurements or assumed based on empirical evidence.

The stochastic finite element method [12, 106] is a powerful tool to address the influence of the uncertainty related to the determination of the material and geometrical properties and loading conditions on the global response of composite structures. Nam et al. [12] proposed a methodology to determine the design allowables of composite laminates using lamina level test data and finite element analysis and validate the proposed methodology for both un-notched and open hole strength. However, stochastic finite element method solutions rely on computationally expensive procedures, which makes the consideration of the variability of the input parameters an extremely time consuming and, therefore,

impracticable process quick design.

Quick analytical prediction tools are therefore desirable, specially for preliminary design and material selection. Furtado et al. [5] proposed an analytical framework to estimate the notched strength of multidirectional carbon-epoxy laminates based on three ply properties (the longitudinal Young's modulus, the longitudinal strength, and the longitudinal crack resistance curve) and concluded that the framework was able to provide good predictions for the open-hole tensile and compressive strengths of general balanced carbon/epoxy laminates. Since the model uses ply-level properties as building blocks, it is ideal for preliminary design, since the notched strength of different layups and geometries can be quickly estimated.

The authors validated the analytical framework for the nominal values of the material properties and the geometrical parameters. However, the uncertainty associated to the material properties and dimensions may be taken into account in an attempt to define design allowables for the notched strength.

In this work, a methodology to predict the B-value of notched composite laminates using the analytical framework proposed by Furtado et al. [5] is proposed by taking the variability of the material properties that dominate failure and the effect of geometrical imperfections into account. The proposed Uncertainty Quantification and Management (UQ&M) methodology is validated against available experimental data and is applied to generate practical engineering design tools.

3.2 Methodology

3.2.1 Description of the analytical framework

Furtado et al. [5] proposed an analytical framework to estimate the notched strength of multidirectional carbon-epoxy laminates based on three ply properties: the longitudinal Young's modulus, E_1, the longitudinal strength, X, and the longitudinal crack resistance curve, $\mathscr{R}$-curve. The framework combines the finite fracture mechanics model proposed by Camanho et al. [6] with the invariant-based approaches to estimate stiffness and strength proposed by Tsai and Melo [7, 8] and with an analytical model based on linear elastic fracture

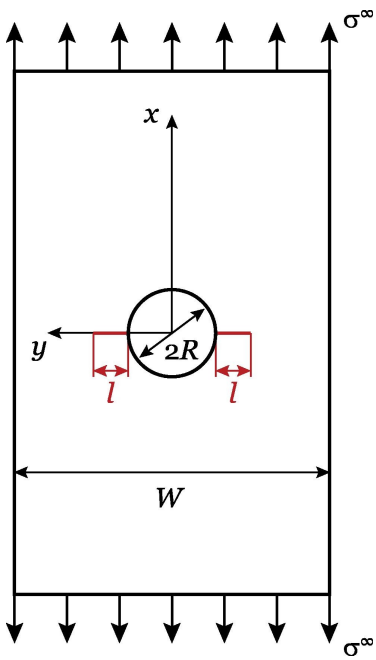

Figure 3.1: Notched laminate with central circular open hole [5].

mechanics to estimate the laminate fracture toughness proposed by Camanho et al. [108].

The coupled Finite Fracture Mechanics (FFMs) model proposed by Camanho et al. [6] is used to predict the notched strength of open-hole laminate specimens (Fig 3.1) with fibre dominated failure. Both a stress-based and energy-based criteria must be satisfied during crack propagation:

$$\begin{cases} \frac{1}{l}\int_R^{R+l} \sigma_{xx}(0,y)dy = X^L \\ \int_R^{R+l} \mathscr{G}_I(a)da = \int_0^l \mathscr{R}(\Delta a)d\Delta a \end{cases} \tag{3.1}$$

where R is the hole radius, $\sigma_{xx}(0,y)$ is the stress distribution along the ligament section perpendicular to the loading direction (along the transverse axis), X^L is the laminate unnotched strength, $\mathscr{G}_I(a)$ is the mode I energy release rate (ERR) of a laminated plate with a central circular hole of radius R and two symmetric cracks propagating from the hole edge, $\mathscr{R}(\Delta a)$ is the $\mathscr{R}$-curve of the laminate and l is the crack extension at failure.

The first equation corresponds to the average-stress criterion while the second

represents an energy balance. Therefore, a stress equilibrium between the average stress in the narrowest critical section with the hole and the maximum admissible strength of the laminate, and an equilibrium between the energy released and the maximum admissible fracture energy of the laminate in a finite length must be satisfied during crack propagation. The model only requires two independent laminate properties: the laminate unnotched strength X^L and the laminate $\mathscr{R}$-curve.

The FFMs model is therefore based on properties at laminate level, which need to be determined each time the layup changes. To determine the laminate unnotched strength X^L, Furtado et al. [5] proposed the use of the invariant-based approach to estimate stiffness and strength proposed by Tsai and Melo [7, 8]. This approach is based on the Unit Circle failure envelope, which was proposed by Tsai and Melo [8] as a conservative simplification of the last ply failure Omni Strain Failure Envelope. The Unit Circle envelope is defined by the uniaxial tensile and compressive strains-to-failure. Following Tsai and Melo [8], the laminate unnotched strength under uniaxial loading is estimated by a simple maximum strain criterion:

$$X^L \approx \frac{X}{E_1} \times E^L \tag{3.2}$$

where X is the laminate unnotched strength, E_1 is the longitudinal Young's modulus and E^L is the laminate longitudinal Young's modulus, which can be estimated using the Trace theory and Master Ply concept [7]. Tsai and Melo [7] defined a Master Ply for CFRPs based on the finding that the normalised UD stiffness components of several CFRP systems (normalized by the trace) is almost constant. The authors concluded that the stiffness of CFRPs along the fibre direction is responsible for about 88% of the value of trace, which means that the value of trace can be estimated from the longitudinal stiffness E_1 as

$$Tr \approx \frac{E_1}{0.88} \tag{3.3}$$

The Young's modulus of a given laminate can be determined as a product of the value of trace and a laminate factor, which can be determined using laminate

plate theory and the Master Ply presented in table 3.1:

$$E^L \approx E_x/Tr \times \frac{E_1}{0.88} \tag{3.4}$$

Table 3.1: Universal Laminate Factors of the Master Ply.

Lay-up	E_x/Tr	E_y/Tr	G_{xy}/Tr	ν_{xy}
Master Ply	0.880	0.052	0.031	0.320

To estimate the laminate $\mathscr{R}$-curve, the analytical model proposed by Camanho et al. [108] can be used. The model is based on a combination of linear elastic fracture mechanics and laminate plate theory and can be used to estimate the fracture toughness of balanced multidirectional laminates, $\mathscr{G}_{Ic}$, using the fracture toughness of the 0° ply, $\mathscr{G}^0_{Ic}$.

Furtado et al. [5] concluded that the framework is able to provide good predictions for the open-hole tensile and compressive strengths of general balanced carbon/epoxy laminates with fibre dominated failure using only the lay-up, the geometry of the specimen (the radius, R, and the width, W) and three ply properties as inputs: the longitudinal Young's modulus, E_1, the longitudinal strength, X, and the longitudinal crack resistance curve, $\mathscr{R}$-curve. Since the model uses only three ply level parameters as building blocks, the framework can be particularly useful for preliminary design and optimization, as the number of elementary tests needed to characterize the composite system is drastically reduced. In addition, due to the computational efficiency of the model it can be used to perform uncertainty quantification and management (UQ&M) analysis, allowing not only the analysis of the effects of the mean parameters on the response, but also the analysis of the influence of their variability.

3.2.2 Uncertainty quantification of the model parameters

The analytical framework [5] summarized in the previous section requires three ply material parameters to estimate the strength of a multidirectional notched laminate: the longitudinal Young's modulus, the longitudinal strength and the $\mathscr{R}$-curve of the 0° plies. The model was validated using the mean ply properties determined experimentally, resulting in the prediction of a nominal notched strength for a given nominal dimension (hole radius and specimen width). In this work, the variability associated with the determination of the ply properties and

the geometry of the specimens is accounted for. The variability associated with the geometrical parameters (notch radius and specimen width) is directly related to the manufacturing process, namely the cutting methodology and respective tolerances. Since direct measurements were not available, the dimensions of the specimen were assumed to follow a uniform distribution.

Accounting for the variability of the longitudinal Young's modulus and the longitudinal strength is straightforward since these properties are obtained directly from the experimental tests and have an associated standard deviation. It is assumed here that these two properties follow a normal distribution with known mean and standard deviation, corresponding to the values obtained experimentally.

Accounting for the variability of the $\mathscr{R}$-curve is less clear since the $\mathscr{R}$-curves are generally not measured directly but determined from notched strengths measured experimentally. Thus, it is of key importance to define a methodology to randomly generate statistically representative $\mathscr{R}$-curves. Such methodology is proposed in section 3.2.2.1.

3.2.2.1 Mode I crack resistance curve in the fibre direction

Catalanotti et al. [109, 110] proposed a methodology to determine the $\mathscr{R}$-curve of polymer composites reinforced by unidirectional fibres based on the size effect law, i.e the relation between the size of the specimens and their notched strength $\overline{\sigma}^{\infty}(w)$. The size effect law can be determined by experimentally testing geometrically similar double edge notch specimens, i.e. with the same width-to-crack length ratio $2w/a$ and different widths $2w$. The size effect law can be determined by finding a fitting regression that best approximates the experimental data [111] and the $\mathscr{R}$-curve parameters (length of the fracture process zone, l_{fpz}, and the fracture toughness at propagation $\mathscr{R}_{ss}$) can then be obtained as a function of these fitting parameters [109–111]. Catalanotti et al. [109] also suggested to express the $\mathscr{R}$-curve analytically. In this work, the following analytical expression is proposed to represent the $\mathscr{R}$-curve:

$$\begin{cases} R(\Delta a) = R_{ss}\left[1-(1-\Delta a/l_{fpz})^{\beta}\right] & \text{if} \quad \Delta a < l_{fpz} \\ R(\Delta a) = R_{ss} & \text{if} \quad \Delta a \geq l_{fpz} \end{cases} \tag{3.5}$$

where β is a parameter determined to obtain the best fit of the $\mathscr{R}$-curve. The proposed equation guarantees that the steady state value of the fracture toughness is reached when $\Delta a = l_{fpz}$.Since the mean $\mathscr{R}$-curve is determined from the mean experimental notched strengths of the double edge notch specimens, accounting for the variability of the $\mathscr{R}$-curves implies accounting for the variability of the size effect law. Two methodologies to determine the variability of the $\mathscr{R}$-curves are proposed in this section.

Method 1. The variability is obtained by generating a large number of $\mathscr{R}$-curves accounting for the variability of the notched strength ($\bar{\sigma}^{\infty}$) of the specimens with different geometries by:

1. Randomly generating N_i strengths per each specimen geometry following a statistical distribution determined experimentally for each specimen geometry.

2. Fitting the data to one of the fitting regressions proposed in Ref. [111].

3. Determining the $\mathscr{R}$-curve parameters (l_{fpz} and $\mathscr{R}_{ss}$) as proposed in Ref. [109–111].

4. Fitting the $\mathscr{R}$-curve to the analytical expression proposed in Equation (3.5) .

5. Repeat 1-4, N times obtaining a large number of R-curves and the distribution of the fitting parameters.

Using this methodology, a set of statistically representative crack resistance curves is obtained. With the generated $\mathscr{R}$-curves it is possible to determine the mean values and standard deviation of the three $\mathscr{R}$-curve fitting parameters (l_{fpz}, $\mathscr{R}_{ss}$ and β). However, due to the nature of the crack resistance curves, the fitting parameters cannot be treated independently as that would lead to unrealistic and potentially non-continuous $\mathscr{R}$-curves. For this reason, a relation between the parameters should be established as a function of $\mathscr{R}_{ss}$, i.e $l_{fpz} = f(\mathscr{R}_{ss})$ and $\beta = g(\mathscr{R}_{ss})$. These functions can vary and should be analysed for each material system considered. A more detailed analysis is given in section 3.3.3.

Method 2. The variability is obtained from the determination of the 95% prediction bounds of the linear regression used to fit the size effect law measured experimentally. Either the whole set of experimental points or the mean strengths per specimen geometry can be used, however, the confidence intervals will be generally narrower if only the mean size effect law is used. This process allows the determination of the mean $\mathscr{R}$-curve and the two 95% confidence $\mathscr{R}$-curves. The three $\mathscr{R}$-curve parameters and the respective standard deviations can also be determined.

This method provides only three sets of $\mathscr{R}$-curve parameters and therefore, $\mathscr{R}_{ss}$, l_{fpz} and β are considered independent. This second method is simpler to apply and less computationally expensive, however, the relation between $\mathscr{R}_{ss}$ and the remaining parameters has to be assumed, so caution is required when applying this method.

3.2.3 Estimation of the B-basis value

In the design of a composite structure it is important to take into account the variability of the design parameters, namely the material properties. According to the Composite Materials Handbook (CMH17) [1], variability should be taken into account in the design of composite structures by using the B-basis for the design allowables. The B-basis (B-value) is a statistically-based design allowable defined as the 95% lower confidence bound on the tenth percentile of a specified population of measurements [1].

By taking the variability of the input parameters (material and geometrical) and using the proposed analytical model, it is possible to propagate the uncertainty of the input parameters to the notched strength, i.e. a statistical distribution of the notched strength can be obtained, based on the variability of the input parameters, which can then be used to compute the statistical design allowables. To obtain the B-value for the open hole strength, two methodologies have been used: (i) the CMH-17 approach and (ii) a Monte Carlo based approach.

Both approaches rely on the set of material and geometrical properties and respective statistical distribution and differ in how the strength data is dealt with to determine the B-value. Nevertheless, for a given run of the analytical model the geometrical and material properties are considered deterministic.

CMH-17 approach The CMH-17 [1] defines different methods to determine the B-value depending on the distribution that best fits the data. As summarised in Figure 3.2, for unstructured data, the CMH-17 suggests to successively test if the Weibull, normal and lognormal distributions are adequate fits to the data. If any of these distributions fits the data then the respective methods to calculate the B-basis should be used. If none of these three distributions can be assumed, nonparametric procedures should be used to determine the B-value.

To find the best fitting distribution, the CMH-17 suggests the use of the Anderson-Darling test. This test compares the Cumulative Distribution Function (CDF) of the distribution of interest with the CDF of the data, which allows the determination of a Observance Significance Level (OSL). If the calculated OSL is greater than 0.05, it is concluded that the distribution analysed fits the data. Otherwise, the analysed distribution does not fit the data and the subsequent distribution is analysed. Once a fitting distribution has been found, the B-value can be computed according to the procedures in the CMH-17 for that statistical distribution [1]. If none of these distributions fit the data, nonparametric procedures are used. These procedures depend on the sample size, being the Hanson-Koopmans method used for small sample sizes ($n < 28$). For large sample sizes the B-value can be computed from tabulated data in the CMH-17. For more information on these procedures, the reader is referred to the CMH-17 [1].

Monte Carlo simulations The Monte Carlo Methods (MCS) rely on the repeated random sampling to obtain numerical results. To determine the B-value using this approach it is necessary to run the analytical model a large number of times to determine an Empirical Cumulative Distribution Function (ECDF) for the parameter in study, namely the notched strength. For each set of n results, where n is the sample size that should be large enough to be representative of the population, it is possible to determine the ECDF and extract the 10th percentile value, $P_{10,j}$. This process is repeated N times, determining a distribution for the 10th percentile. From this distribution the B-value can be computed by considering the 95% lower confidence bound [2], which corresponds to the 5^{th} percentile of the ECDF. The MCS based methodology to calculate the B-value can be summarised as follows (see Figure 3.3):

1. Design of the experiments (DOE). The material properties and geomet-

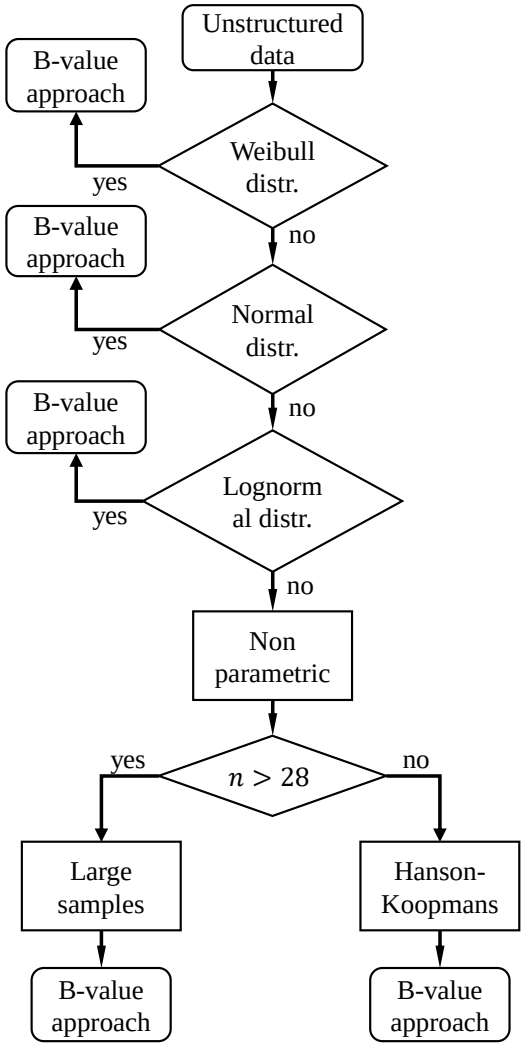

Figure 3.2: Schematic representation of the steps to calculate the B-value using the CMH-17 methodology.

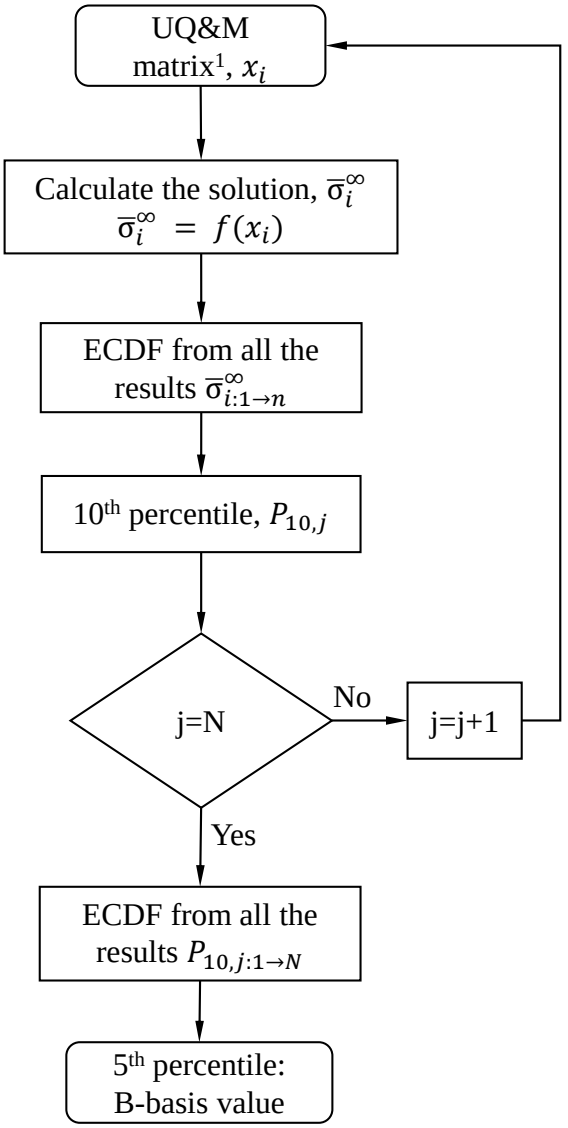

[1] UQ&M matrix dimensions are: n different cases per 5 input variables (x_i); in the first iteration $j = 1$.

Figure 3.3: Schematic representation of the steps to calculate the B-value using the Monte Carlo based methodology.

rical parameters are distributed according to their associated statistical distributions to define the uncertainty quantification and management matrix. Using the current analytical framework, the dimensions of the matrix are n x 5 where n are the different cases to be analysed and 5 are the model input parameters (E_1, X_T, $\mathscr{R}_{ssT}$, R and W).

2. Notched strength computation. For each case i the notched strength ($\bar{\sigma}_i^{\infty}$) is calculated using the analytical model described in Section 3.2.1.

3. Determination of the 10th percentile. Once all the cases have been computed ($\bar{\sigma}_{i:1\rightarrow n}^{\infty}$) the ECDF of the notched strengths is used to determine the $P_{10,j}$.

4. Computation of the B-basis allowable. Steps 1, 2 and 3 are repeated N times to obtain the ECDF of the $P_{10,j:1\rightarrow N}$ and to determine the 5^{th} percentile which corresponds to the B-basis value.

If the sample size (n) is large enough, then the 10^{th} percentile of the population can be directly approximated by the 10^{th} percentile of the sample, as the variability between the samples will be minimal. This will be explored in more detail in Section 3.5.1.

3.3 Case study

3.3.1 Description of the case

To exemplify and validate the methodology proposed to calculate the B-value of the notched strength, IM7/8552 $[90/0/\text{-}45/45]_{3s}$ quasi isotropic laminate with a central circular hole loaded in tension was used. Hole diameter-to-width ratios of $0.05 < 2R/W < 0.6$ and hole diameters of 2, 4, 6, 8 and 10mm were used.

As explained in section 3.2.2, the variability associated with the material parameters and with the geometry of the specimens is considered to calculate the B-value. The input parameters used are presented hereafter.

3.3.2 Uncertainty quantification associated with the geometry of the specimens

The variability associated with the geometry of the specimens is directly related to the manufacturing process, namely the cutting methodology and respective allowed tolerances. The specimen dimensions were assumed to follow a uniform distribution with a maximum deviation of $\pm 2\%$ of the nominal value of the width and hole diamater.

Table 3.2: Variability of the geometry of the specimen [112].

Geometry	W [mm]	R [mm]
tol	$\pm 2\% \times W$	$\pm 2\% \times R$

3.3.3 Uncertainty quantification associated with the determination of the material properties

In this work, it is assumed that the material properties follow a normal distribution with known mean and standard deviation. These properties are summarised in Table 3.3. The uncertainty related to the longitudinal Young's modulus and strength is directly related to the the mean values ($\bar{x}$) and respective standard deviation (s) determined experimentally [113] while the variability of the $\mathscr{R}$-curve is determined as explained in section 3.2.2.

Table 3.3: Value of the material properties used for the analysis [113].

IM7/8552	E_1 [GPa]	X_T [GPa]	$\mathscr{R}_{ssT}$ [N/mm]
$\bar{x}$	171.42	2323.47	206.75
s	2.38	127.45	23.64

The determination of the $\mathscr{R}$-curve is based on the size effect law which can be determined from the strengths of geometrically similar double edge notched specimens with different widths. Table 3.4 shows the notched strengths and respective standard deviations of the double edge notch tension specimens that were used to determine the longitudinal crack resistance curve of IM7/8552 material system [109].

Using Method 1 described in Section 3.2.2.1, a set of statistically representative

Table 3.4: Double Edge Notched Tension Strength for IM7/8552 $[90/0]_{8s}$ [109].

Ref.	w [mm]	$\bar{x}$ [MPa]	s [MPa]
B	7.5	309	9
C	10	289	16
D	12.5	269	11
E	15	256	10

crack resistance curves, with a known mean and standard deviation of the three fitting parameters (l_{fpz}, $\mathscr{R}_{ss}$ and β) is obtained, as shown in Figure 3.4.

As explained in section Section 3.2.2.1, the fitting parameters of the crack resistance curves cannot be treated independently as that would potentially lead to non admissible $\mathscr{R}$-curves. For this reason, a dependence between the parameters was established as a function of $\mathscr{R}_{ss}$. As shown in figure 3.5, it was found that l_{fpz} varies linearly with $\mathscr{R}_{ss}$ and β is almost constant for the case analysed. Therefore, the crack resistance curves can be defined as a function of $\mathscr{R}_{ss}$. $\mathscr{R}_{ss}$ is generated randomly following a normal distribution with a known mean (206.75 N/mm) and standard deviation (23.64 N/mm) and the other two parameters are estimated as:

$$l_{fpz} = 2.7776 \times 10^{-2} \times \mathscr{R}_{ss} - 3.0598 \qquad [\text{mm}]$$
$$\beta = 2.9027 \qquad [\text{-}]$$

Using Method 2 the variability is obtained from the determination of the 95% prediction bounds of the fitting of the size effect law. Either the whole set of experimental points or the mean strengths per specimen geometry can be used. In this study only the mean strengths were used since the full set of results was not available.

Since this method provides only three sets of $\mathscr{R}$-curve parameters, the relation between l_{fpz}, $\mathscr{R}_{ss}$ and β is undefined. However, using method 1, it was shown that a linear functions can be used to relate $\mathscr{R}_{ss}$ to l_{fpz} and β, and so the fitting parameters of the curves can be easily determined as a function of $\mathscr{R}_{ss}$ as shown in figure 3.5. Using this method, $\mathscr{R}_{ss}$ is generated randomly following a normal

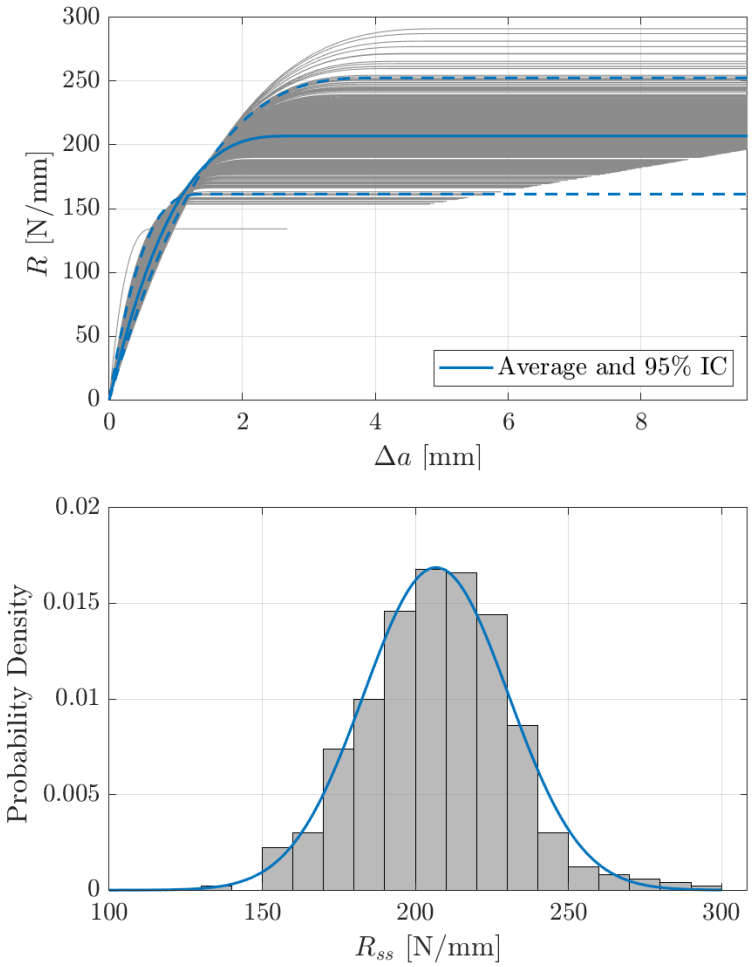

Figure 3.4: Schematic representation of randomly generated $\mathscr{R}$-curves using method 1 (top) and distribution of the steady state fracture toughness R_{ss} (bottom).

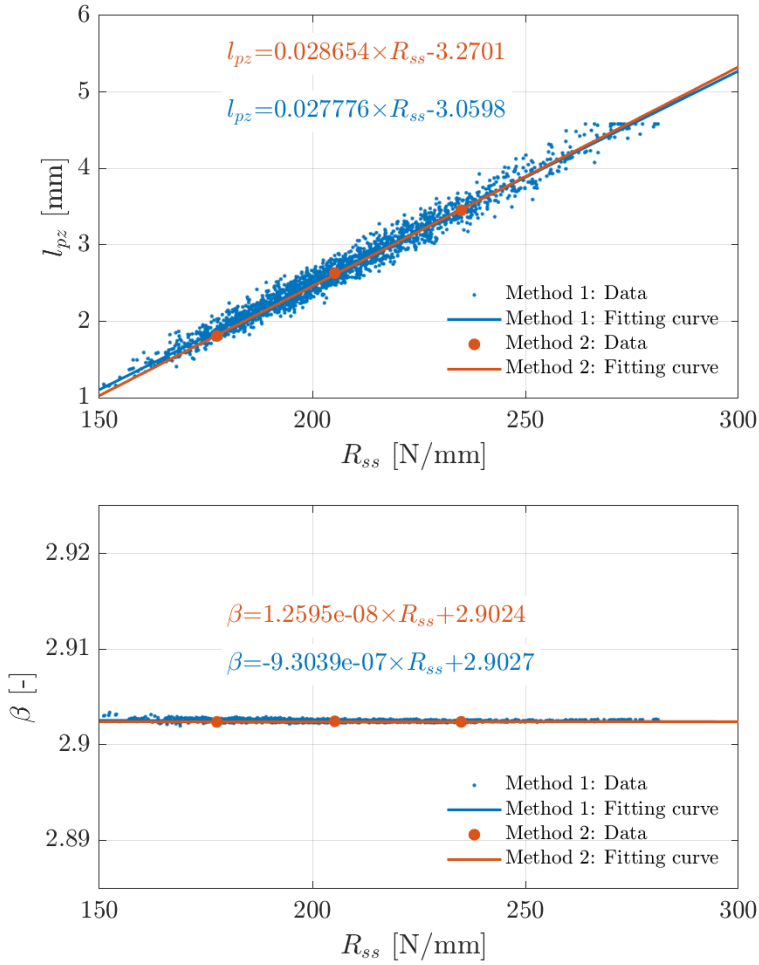

Figure 3.5: l_{fpz}= f($\mathscr{R}_{ss}$) (top) and β= g($\mathscr{R}_{ss}$) (bottom) obtained with method 1 and method 2.

distribution with a known mean (205.26 N/mm) and standard deviation (14.83 N/mm) and the other two parameters are estimated as:

$$l_{fpz} = 2.8654 \times 10^{-2} \times \mathscr{R}_{ss} - 3.2701 \qquad [\text{mm}]$$
$$\beta = 2.9024 \qquad [\text{-}]$$

As shown in figure 3.5 the fitting curves obtained with both methods show similar trends. Figure 3.6 shows the normal distribution and the corresponding average and 95% IC $\mathscr{R}$-curves obtained with both methods. Only a 1.5 N/mm difference in the mean $\mathscr{R}_{ss}$ using methods 1 and 2 was found. However, since the standard deviation obtained using method 2 is around 40% lower than the one measured using method 1 because the confidence bounds were determined using the mean double edge notch strengths, the normal distribution of $\mathscr{R}_{ss}$ is significantly narrower if method 2 is used. Using the whole set of data would be preferred in method 2. Therefore, method 1 was used to characterize the distribution of the crack resistance curve parameters.

3.4 Sensitivity analysis

Due to the analytical nature of the model, it is possible to run a large number of simulations within a reasonable time frame, enabling the performance of numerical analysis that would not be possible via experimental characterization or finite element simulations.

The proposed framework depends on three material properties and two geometrical properties. It is interesting to understand their influence on the expected notched strength of the laminate selected for this study. To do so, a sensitivity analysis was performed on these five parameters. The sensitivity analysis is performed by considering that the parameter in study varies while the remaining are kept constant and with a value equal to the nominal one. Here the material and layup considered are the ones presented in Section 3.3 and an open-hole tension specimen with width equal to 36 mm and hole radius of 3 mm is considered. For each material property a range from $\bar{x}_i - 3s_i$ to $\bar{x}_i + 3s_i$ was considered. For the geometrical parameters a variation of $\pm 2\%$ was considered. The results

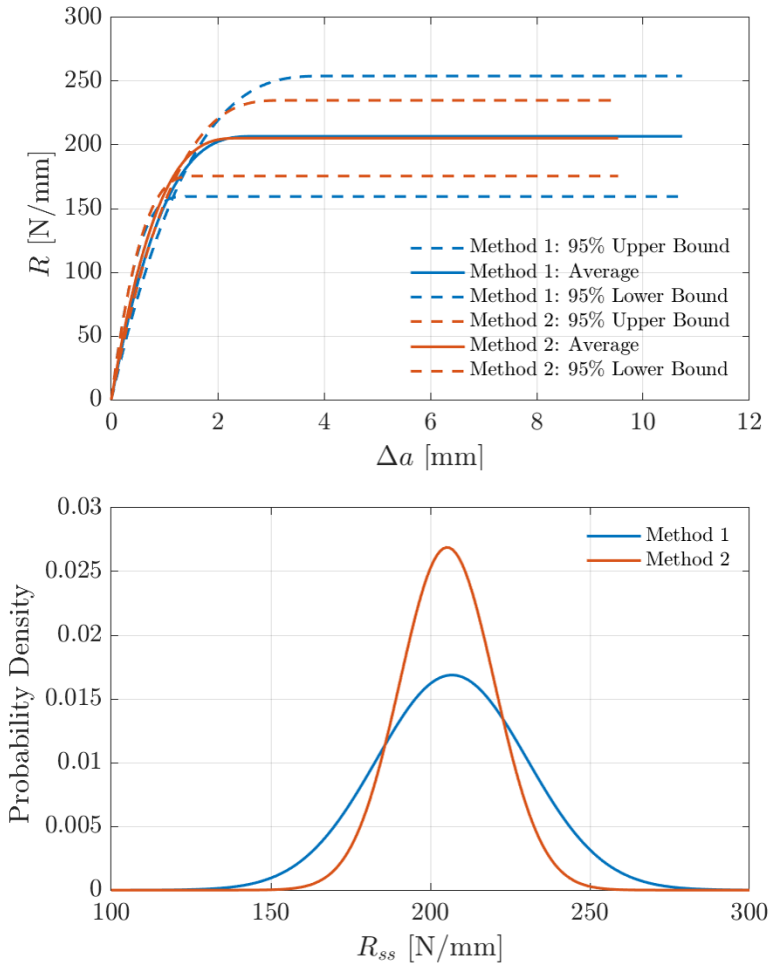

Figure 3.6: Average and 95% confidence bounds $\mathscr{R}$-curves (top) and predicted normal distribution of $\mathscr{R}_{ss}$ using method 1 and method 2 (bottom).

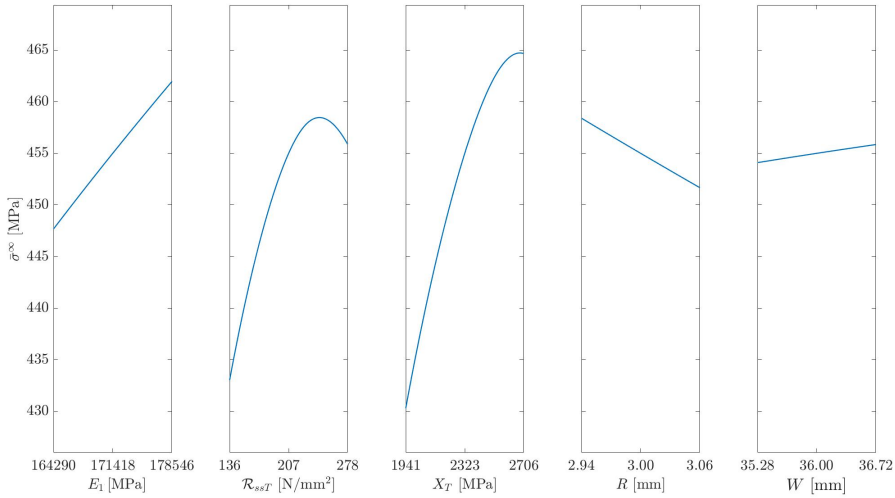

Figure 3.7: Sensitivity analysis on the notched strength for $W = 36$ mm and $R = 3$ mm.

of the sensitivity analysis are shown in Figure 3.7.

From the sensitivity analysis, it is possible to conclude that, as expected, the material properties have a larger influence on the notched strength than the geometrical properties. For the Young's modulus the variation of the OH strength is linear, being lower for lower elastic moduli. Both the tensile strength and toughness of the material have a more complex influence on the open hole strength of the material. In addition, both have a higher influence on the open hole strength of the material, therefore, it is essential to accurately characterize these properties to ensure accurate predictions of the notched strength of composite laminates.

3.5 UQ&M framework validation

In this section the sample sizes required to accurately take into account geometrical and material variability within the UQ&M framework is analysed and the results are validated against available experimental data.

3.5.1 Effect of the sample size on the mean notched strength and on B-basis value using the MCS method

To validate the proposed UQ&M methodology, it is important to analyse the number of simulations required to ensure an accurate determination of the output parameters. The fact that the framework used is fully analytical, allows a very large number of simulations to be performed, however, it is of key importance to ensure that the open-hole strength (mean and B-basis) are determined efficiently, i.e. performing the minimum number of simulations required to obtain accurate and statistically consistent results.

The methodology to determine the B-basis using MCS is described in Section 3.2.3. This methodology requires the computation of $n \times N$ number of simulations to determine the B-value. This may lead to a very high number of simulations, rendering the methodology computationally expensive. However, it is possible to determine the B-basis based on a smaller number of simulations if we consider $N = 1$ and have a sample size (n) sufficiently large to be representative of the population of results. With this methodology, the B-basis can be approximated by the 10^{th} percentile of the sample, therefore, reducing the number of simulations to be performed.

To determine the minimum sample size that ensures this representativeness, the sample size was varied between 10 and 100,000. For each sample size 10 random samples were obtained to compute both the average and standard deviation of the mean open hole strength ($\bar{\sigma}^{\infty}$) and the respective B-basis (P_{10}). Figure 3.8 shows the convergence analysis of both the average OH strength and B-basis.

Analysing the data, it is possible to conclude that the variability of both the mean OH strength and B-basis is reduced with increasing sample size, however, the computational cost increases. It is possible to conclude that for a sample size of 10,000 the Coefficient of Variation (CoV) of both the mean OH strength and B-basis is very low, 0.02% and 0.05%, respectively. Therefore, a sample size of 10,000 can be considered as representative of the population of results and be used to obtain the average OH strength and respective B-basis. If we consider a sample size of 30,000, which has a three times increase in computational time, there is an insignificant reduction in the CoV for the mean strength and B-basis

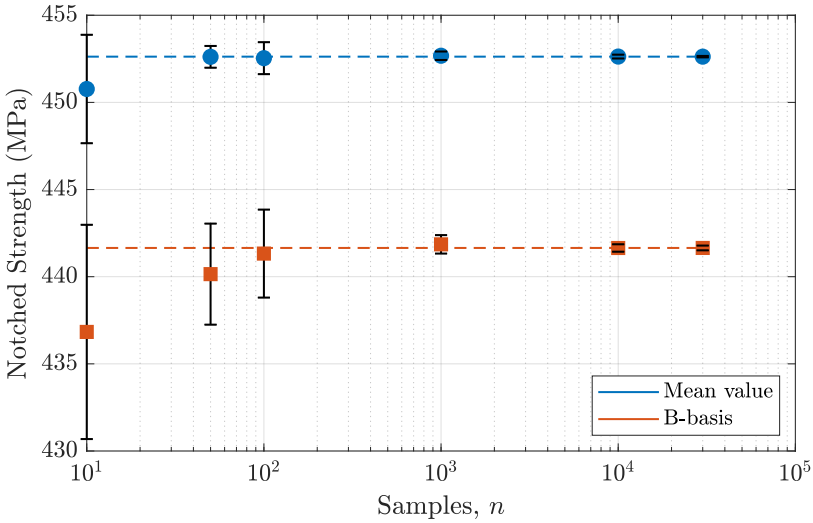

Figure 3.8: Average OH strength and 10th percentile from $N = 10$ simulations determined from different number of samples n.

(to 0.01% and 0.03% respectively). Therefore, it is concluded that a sample size of 10,000 is large enough and ensures a good compromise between the accuracy and computational cost.

To summarize, the calculation of the B-basis allowable using MCS can be done in a computationally efficient way by running 10,000 simulations ($N = 1$) and determining the 10^{th} percentile of the sample as this number of samples is considered representative of the whole population. This methodology will be considered for the determination of the B-basis allowables using Monte Carlo

Table 3.5: Mean value and variance of the average OH strength ($\bar{\sigma}^{\infty}$) and B-value (P_{10}) according to the number of samples when $N = 10$.

Samples, n	$\bar{\sigma}^{\infty}$		P_{10}	
	$\overline{\sigma^{\infty}}$ [MPa]	$s_{\sigma^{\infty}}$ [MPa]	$\overline{P_{10}}$ [MPa]	$s_{P_{10}}$ [MPa]
10	450.77	3.11	436.83	6.15
50	452.61	0.62	440.15	2.90
100	452.54	0.91	441.33	2.52
1000	452.68	0.24	441.86	0.53
10000	452.63	0.11	441.65	0.21
30000	452.62	0.04	441.64	0.13
100000	452.62	0.03	441.64	0.05

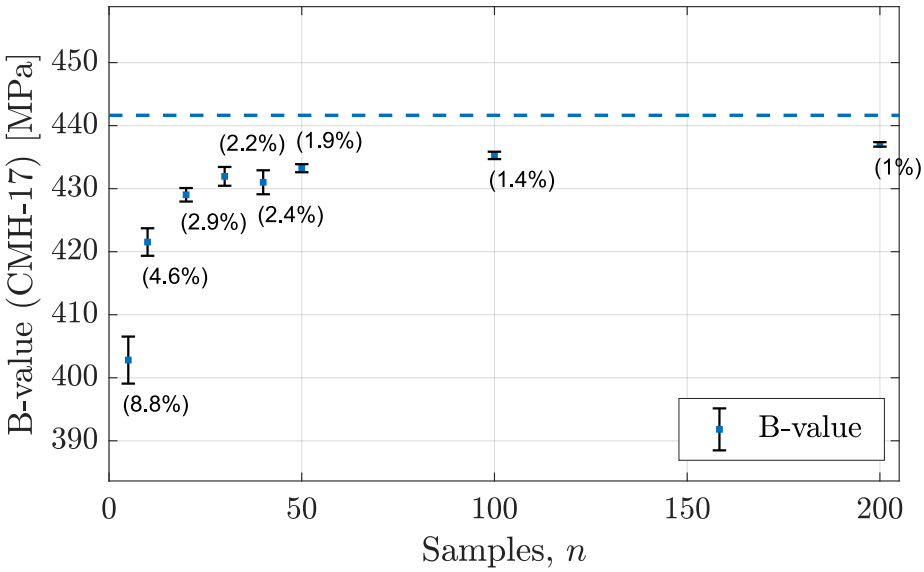

Figure 3.9: Comparison of the B-value obtained from the CMH-17 approach with its 95% interval of confidence, for different sample sizes (n) and the B-value obtained from MCS (dashed line).

simulations in the following sections.

3.5.2 Effect of the sample size on the B-basis using the CMH-17 approach

In Section 3.2.3 the methodology to determine the B-basis allowable based on the CMH-17 was presented. In this section a comparison between the B-basis determined using this methodology is compared with the results obtained using Monte Carlo simulations. The CMH-17 approach is useful since it takes into account the size of the population and the distribution that most accurately represents the data to determine the B-basis and therefore, a good estimate of this parameter can be obtained using a small number of data points.

In Figure 3.9 the B-basis allowable for OH strength determined using the CMH-17 methodology for different sample sizes is shown and is compared with the value obtained using MCS. For each sample size, 100 simulations were performed based on different randomly generated samples, to get not only an average value for the B-basis but also to determine its dispersion for each sample size.

As the sample size increases, the B-value determined with the CMH-17 approach becomes less conservative and the confidence interval is reduced, as bigger samples are considered more representative of the population. In Table 3.6 the results of the B-value are also shown for different sample sizes. In addition, the methodologies from the CMH-17 that were applied for each sample are shown, as different distributions were seen to best fit the data depending on the sample considered.

For a sample size of 30 it is seen that the variability of the calculated B-basis increases. This increase in variability with increased sample size can be justified with the fact that for the mentioned sample size, there was an increase in the number of samples that could not be represented by a Weibull distribution (see Table 3.6) and, therefore, a different distribution had to be used, or even the non-parametric methodology, which increased the dispersion in the determination of the B-basis.

Table 3.6: Results for the B-basis determination using the CMH-17 methodology.

Samples, n	Weibull	Normal	Lognormal	Non parametric	$\tilde{B}$ [MPa]	s_B [MPa]	IC_B [$\pm$ MPa]	error %
5	92	8	0	0	411.35	17.992	3.5696	6.858
10	93	3	0	0	428.77	9.5808	1.9008	2.9152
15	88	3	0	0	431.84	8.0774	1.6026	2.2193
20	94	2	0	0	434.78	4.2685	0.84686	1.553
25	94	2	0	0	435.92	4.3825	0.86948	1.2953
30	91	4	0	5	438.17	7.051	1.3989	0.78675
40	94	3	0	3	437.74	3.4001	0.67458	0.88285
50	92	5	0	3	437.24	3.2488	0.64456	0.99621
100	78	5	0	17	438.76	2.7482	0.54525	0.65224
150	91	1	0	8	439.43	1.5205	0.30167	0.50112

In the remainder of this study, a sample size of 25 is considered when determining the B-basis with the CMH-17 methodology, as it is seen to be a reasonable sample size, which might be used in experimental campaigns, that ensures a good B-basis estimation.

3.5.3 Validation of the UQ&M framework

A comparison between the experimental results presented in Ref. [113] and the predictions using the proposed framework is shown in Figure 3.10. Both the OH strengths computed using the nominal values of the material and geometrical properties and the results obtained when these properties are considered stochastic are included. The latter methodology allows not only to obtain the average value for OH strength for each geometry but also the expected variability.

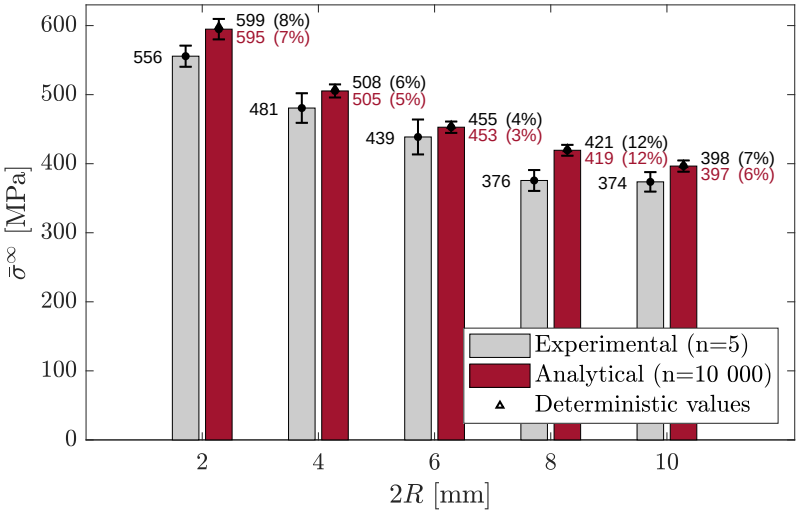

Figure 3.10: Comparison between the mean open hole strength of experimental results [113] and the analytical results of five different $2R$ and a fixed ratio $2R/W = 1/6$, where $\bar{\sigma}^{\infty}$ is the notched strength, R the radius of the hole and W the width.

As expected, using the nominal values of the geometrical and material parameters results in approximately the same open hole strength as the average of the stochastic results, ensuring the consistency of the uncertainty quantification framework developed. The results shown in Figure 3.10 indicate that the proposed framework is capable of accurate predictions of the open-hole tension strength. The maximum error obtained for this case study was 12% which, taking into account that this is an analytical formulation with very reduced computational cost, is very reasonable.

As the developed framework is aimed at the determination of the B-basis allowable for open hole strength, the comparison between the B-basis obtained analytically, with the two presented methods, and experimentally is shown in Figure 3.11. For consistency, as the experimental sample size used was 5 specimens [113], the same sample size was considered when computing the B-value with the CMH-17 approach. This allows a direct comparison between the experimental B-basis and the one obtained numerically. Nevertheless, the results with a sample size of 25 are also shown. To ensure that the results obtained did not result in outliers, 10 B-basis calculations were performed for each geometry. For the Monte Carlo simulations approach a larger number of simulations is

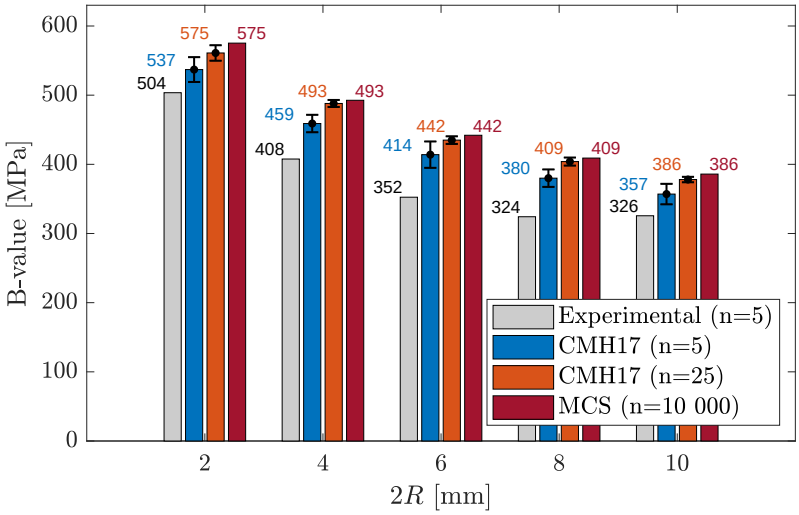

Figure 3.11: Comparison between the B-value obtained experimentally ($n = 5$), with the CMH-17 ($n = 5$ and $n = 25$) and with the MCS method ($n = 10,000$).

always required to ensure the representativeness of the population, therefore, the sample size was kept at 10,000.

Observing the previous results it is concluded that the B-value determined with the CMH-17 approach is similar to that obtained experimentally, for the same sample size ($n = 5$), which reflects not only the ability of the framework to accurately compute the open hole strength of a given configuration, but also its ability to propagate the uncertainty of the input parameters to the open hole strength. The B-basis obtained with the MCS approach is always less conservative than the one obtained with the CMH-17 approach due to the larger sample size, which is reflected in the results of Figure 3.11 and was also obtained in the numerical comparison provided in Figure 3.9. The same sample size effect can be observed comparing the CMH-17 approach with $n = 5$ and $n = 25$. Nevertheless, the results obtained are consistent with the experimental ones.

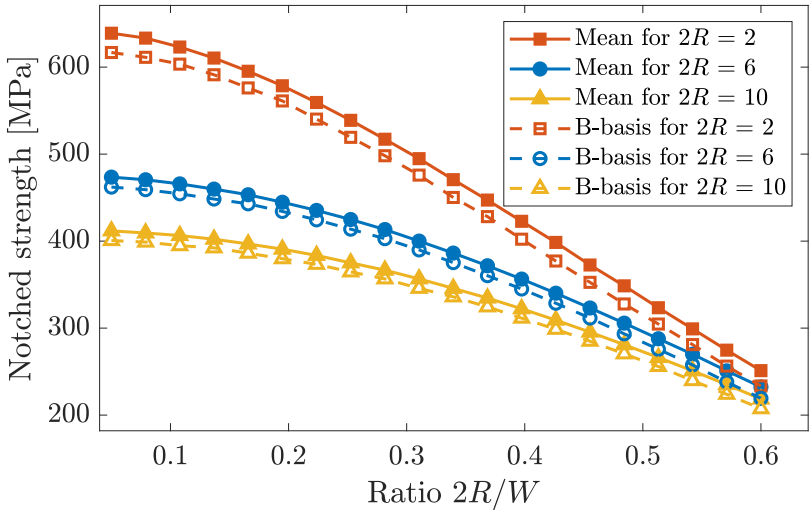

Figure 3.12: Design chart of the mean and B-basis value of the open hole strength calculated by means of MCS for different $2R$ and $2R/W$ ratios.

3.6 Applications

3.6.1 Design charts for open hole tension

Taking into account that the analytical UQ&M framework developed enables the quick estimation of the notched strength of laminated composites and the respective B-basis allowables, it can be used to generate design charts and compare the performance of different layups and materials in a preliminary stage of the design process.

Following Camanho et al. [6], design charts that relate the diameter-to-width ratio to the notched tensile strength of specimens with diameters 2, 6 and 10mm were generated. Monte Carlo simulations with $n = 10,000$ were used to generate the average notched strength distribution of each point and compute the mean value and respective B-basis allowable, as defined in Section 3.5.1 (Fig. 3.12). To calculate the B-value, the CMH-17 approach could also have been used without significant loss of accuracy as shown in Fig. 3.13 for a specimen with a hole diameter of 6mm, however, given the computational efficiency of the model, performing Monte Carlo simulations is not a particularly limiting approach.

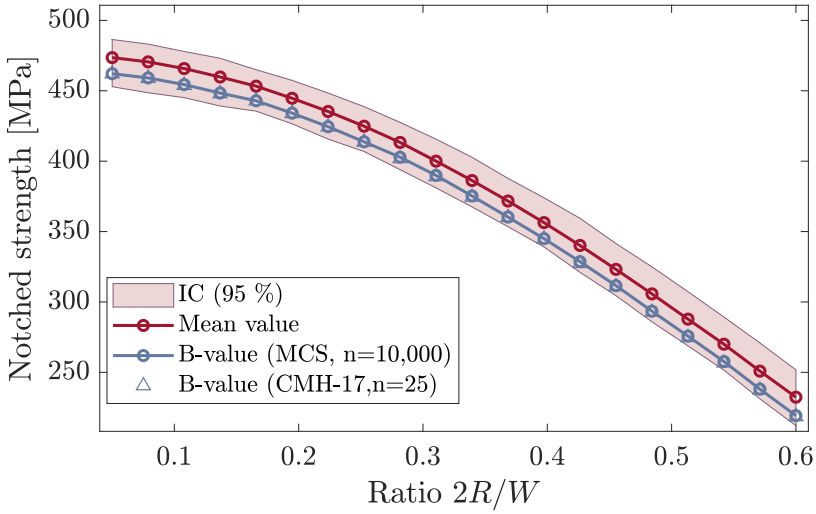

Figure 3.13: Design chart of the notched strength for $2R = 6$ mm.

Experimentally generating statistically representative design charts is unreasonable given the number of specimens, specimen configurations, layups and materials required to populate them. The analytical UQ&M framework here proposed can help overcome this limitation and assist engineers during the design process given its simplicity and efficiency.

3.6.2 Influence of the load direction on the open hole strength

The framework was developed to work as a fast design tool that is capable to predict the notched strength of a laminate in the most varied cases. In this section, the variation of the loading direction and its effect on the open hole tensile strength is explored. The design of a laminate for a given structure is usually optimized for a given load direction, however, it is not acceptable to have a laminate whose strength is very high in one direction but any misalignment in the load, which most certainty occurs in real usage, leads to a high reduction of its strength. Therefore, being able to rapidly predict the notched strength in a multitude of loading directions is an useful design tool. The variation of the mean open hole strength as a function of the load direction and the respective 95% confidence interval and predicted B-basis value based on MCS ($n = 10,000$)

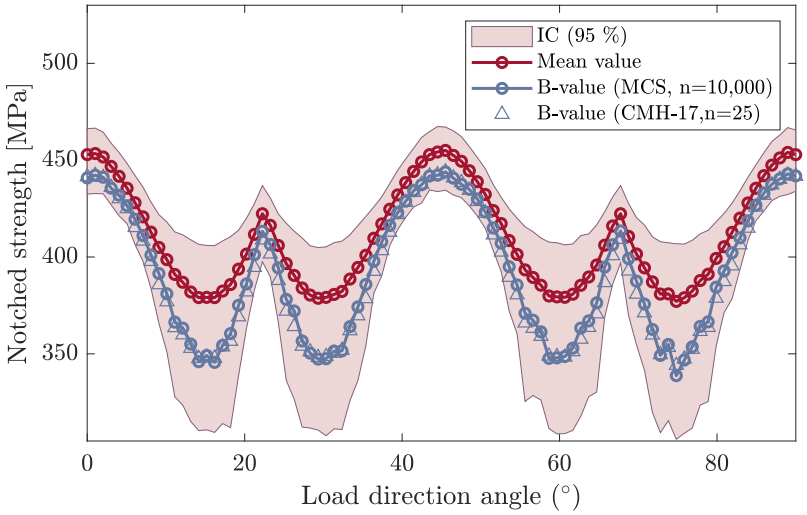

Figure 3.14: Notched strength variation with the load direction.

and on the CMH-17 ($n = 25$) are shown in Figure 3.14. This analysis was done for the baseline configuration of a width of 36 mm and a diameter of 6 mm.

Due to the fact that the laminate in study is quasi isotropic (Section 3.3), the notched strengths at 0, 45 and 90° are equal. However the strength is reduced for any other load direction. From the shown results it is possible to conclude that with the given laminate the reduction of strength due to changing the load direction is small, being the lowest value equal to 377.1 MPa, while the maximum (for 0, 45 and 90°) is equal to 455.0 MPa. Additionally, it is observed that small variations around the principal load direction (0°) have only a small effect on the notched strength. Regarding the B-basis allowable it is seen that for the analysed cases the results from the CMH-17 and MCS approach are similar. It is interesting to note that the difference between the B-basis and the mean value for the open hole strength is not constant throughout the angle space. This difference is highest when the average strength is lowest, which creates a wider span of the B-basis allowable between its maximum and minimum. This can be explained by the fact that at these load angles the variability of the material and geometrical parameters leads to a higher variability of the notched strength and, therefore, a reduced B-basis allowable.

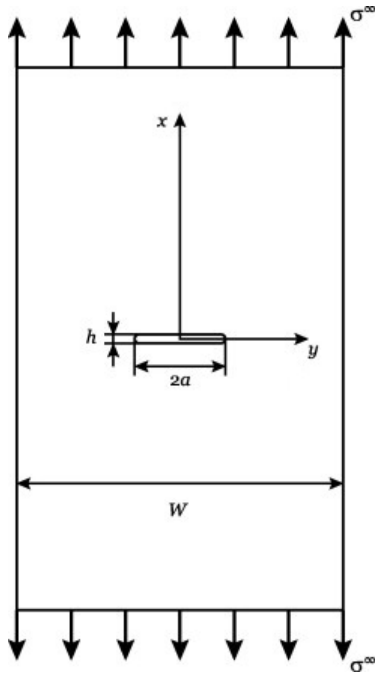

Figure 3.15: Centre notched plate configuration [114].

3.6.3 Large damage capability

The proposed framework was developed with the aim of predicting the open-hole strength of laminate structures, however, it is general enough to be able to predict the strength of different notched geometries, provided the stress distribution and energy release rate are known for those geometries and loading conditions. As it is well known, the tensile strength of composite laminates in the presence of through-the-thickness notches is significantly affected by size, being the smallest geometries strength-dominated and large ones toughness-dominated [114]. Therefore, the analysis tools must be able to account this distinct material behaviors when computing the notched strength. Following Arteiro et al. [114] the developed framework is used to predict the large damage capability of the laminate in study, considering a centre notched plate under tension loading (Figure 3.15).

In Figure 3.16, the mean notched strength and respective B-basis allowable of centre notched plates with a constant plate width-to-notch lentgth ratio ($W/2a$) equal to 7.5 with different notch sizes are shown. The notches were considered

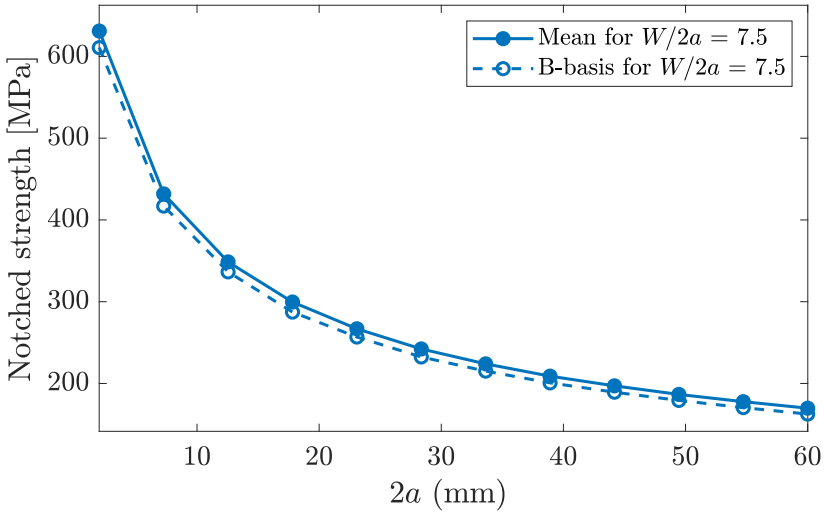

Figure 3.16: Design chart of the mean and B-basis value of the notched strength calculated by means of MCS ($n = 10,000$) for centre notched plates.

to have a constant tip radius of 0.5 mm ($h = 1$ mm). For the smaller geometries the traditional methods that only consider the steady state value of the fracture toughness in their formulation are able to predict the notched strength, however, for larger specimens and large damage capability analysis the introduction of the R-curve in the modelling strategy is of utmost importance [114]. This is taken into account in the present framework, which increases the reliability of the modelling strategy. It is possible to see in Figure 3.16 that both the mean notched strength and its respective B-basis allowable follow the same trends, being the difference between both parameters similar throughout the analysed space.

In this study, two notched geometries are analysed, open-hole tension and centre-notched tension, however the framework is generic enough to take into account other geometries such as open-hole compression and bolted joints failing by net-tension [115], given that the stress concentration factors and energy release rates of the configuration in study are known.

3.7 Conclusions

The current approach to determine the design allowables in the aeronautical industry relies in extensive testing based on the building block approach, which makes the selection and certification of composite materials expensive and time consuming. To increase the efficiency of material and laminate selection during preliminary design, there is a need to reduce the number of experimental tests required during this process, and replace or complement them with accurate modelling strategies coupled with the statistical tools to account for material, manufacturing and geometrical variability.

In this work an UQ&M framework was developed to estimate the B-basis design allowable for notched components. This framework is based on the analytical model developed by Furtado et al. [5] that only requires three lamina level material properties to estimate the notched strength of a laminate, given that the stress distribution and energy release rate are known for the geometries and loading conditions in study. This model is coupled with the statistical tools required to take into account the variability of both the material and geometrical parameters and propagate this uncertainty to the notched strength, therefore allowing the quick estimation of B-basis allowable.

The developed framework allows the computation of the B-basis allowable based on Monte Carlo simulations and on the the approach proposed in the CMH-17, which requires a lower number of samples. Both approaches are compared and it is concluded that the CMH-17 gives a more conservative estimation of the B-basis allowable due to the lower number of samples usually used. Given that the current modelling strategy is computationally efficient, the usage of Monte Carlo simulations allows the estimation of a less conservative B-basis as a large number of samples can be computed in a reasonable time frame. This makes the proposed framework specially interesting in the preliminary design and selection of materials and layups.

The proposed framework is validated successfully with the open-hole tension experimental campaign for the IM7/8552 material [113], ensuring a maximum error around 10%, which is very reasonable given the analytical formulation of the model.

Additionally, the framework is used to develop design charts for notched specimens, tools that are useful for design engineers and would otherwise be infeasible to attain as they require a large number of testing or time consuming simulations to be performed.

Note that in this paper, the methodology is applied to open hole tension and center notched specimens, but the framework can be enriched with other notched configurations, provided the stress distribution and energy release rate are known for those geometries and loading conditions.

4

Paper B – A methodology to obtain material design allowables from high-fidelity compression after impact simulations on composite laminates

The paper has been published in *Composites Part A: Applied Science and Manufacturing* 139 (2020) 106069.

Overview

The growing demand for lightweight and high-strength materials, particularly in aerospace and structural applications, has led to an increased reliance on composite materials. Certifying the structural integrity of these composites relies on the Building Block approach. At the element level, i.e., meso-scale, ensuring their reliability and damage tolerance involves analysing their behavior under complex conditions like compression after impact (CAI).

The mechanical response of composite materials, especially in scenarios like CAI, demands sophisticated modelling techniques due to the intricate interactions of various damage mechanisms. Analytically modelling this phenomenon is very complex, necessitating the use of numerical models based on the finite element method to predict their mechanical behavior accurately.

While numerical tools are powerful for simulating these scenarios, they come with the trade-off of requiring robust computational resources and extended simulation times compared to analytical models. Consequently, obtaining large sample sizes, as feasible with analytical models, becomes challenging. The proposed methodology addresses this challenge by performing a sensitivity analysis to identify the potential input parameters and creating an accurate response surface from available numerical data. This surface allows for the interpolation of numerous values, facilitating statistical analysis to obtain design allowables.

This article introduces a novel approach to determine design allowables for compression after low-velocity impact using a well-defined response surface. By doing so, it contributes significantly to the ongoing advancements in the field of structural certification for composite materials, offering a systematic and potentially cost-effective approach.

A methodology to obtain material design allowables from high-fidelity compression after impact simulations on composite laminates

I.R. Cózar[a,*], A. Turon[a], E.V. González[a], O. Vallmajó[a], A. Sasikumar[a]

[a]*AMADE, Polytechnic School, Universitat de Girona, Campus Montilivi s/n, E-17003 Girona, Spain*

Abstract

Aeronautical industries address the structural reliability of designs by defining design allowables that account for any uncertainties. The Composite Materials Handbook-17 proposes A/B-basis values as design allowables. In this study, a new methodology to estimate the design allowables of the Compression After Impact (CAI) strength is presented. The CAI strength is predicted with high-fidelity simulations using finite element models featuring in-house constitutive damage models. The uncertainty associated to parameters of the model is defined and propagated to obtain the CAI strength distribution. To efficiently estimate this distribution, a Monte Carlo simulation is carried out employing a response surface previously calibrated with a reduced number of high-fidelity simulations. The A/B-basis values for the CAI strength are estimated from the strength distribution obtained and then compared with experimental results. The methodology proposed allows to reduce the number of experimental tests associated with generating design allowables, thus leading to an optimised cost-effective design.

keywords: Strength, Statistical properties, Statistical method, Numerical analysis

* Corresponding author

Paper published in: *Composites Part A: Applied Science and Manufacturing 139 (2020) 106069*

Doi: https://doi.org/10.1016/j.compositesa.2020.106069

4.1 Introduction

The design allowables most widely used in the aeronautic sector are the A/B-basis values, which are defined as 95% of the lower one-sided confidence bound of the 1^{st} and 10^{th} percentiles of the population measured [1], respectively. Consequently, if the load or stress in the part is greater than the allowable design value, then the design criteria is not fulfilled. Current industry practice uses experimental tests that generally adhere to the Composites Materials Handbook-17 (CMH-17 approach) [1] to determine design allowables (as in Laurin et al. [116]). According to the CMH-17 approach, design allowables are approximated by using the localization and scale parameters of the results (i.e. mean value and standard deviation, respectively, in a normal distribution) and a coefficient factor according to the distribution of the results and the number of samples. To obtain accurate design allowables, the population distribution of the parameter must be measured, which implies a large number of laboratory tests and, therefore, the associated increase in time and economic costs.

Alternatively, the basis values can be obtained using advanced models and an appropriate methodology to quantify and manage uncertainty. The uncertainty associated to the analysis method can be grouped into two types: (i) uncertainty associated to the repeatability of the model or (ii) uncertainty due to the intrinsic variability of the parameters of the model. The uncertainty associated to the repeatability of the model does not apply to this study because the prediction from the high-fidelity model will only change if the parameters of the model are changed. Hence, the variability in the output results is caused by the uncertainty associated to the input parameters. This uncertainty can derive from different sources such as the manufacturing process, batch-to-batch variability of raw materials, the test method used to characterize the material, or the intrinsic variability of the material [1]. In addition, it can also be uncertainty associated to the boundary conditions (e.g., a misalignment in the applied load) and to the geometry of the specimen.

Therefore, to determine the design allowable values from high-fidelity simulations, the uncertainty associated to the different input parameters must be quantified. This uncertainty is propagated into the model to obtain the population of the output results. Further, the design allowables are estimated using a

proper statistical analysis.

One way to propagate the uncertainty is to use the Stochastic Finite Element Method (SFEM) [13], which is based on the random variation of the input parameters of the model according to their distribution. Meanwhile, the easy-to-implement Crude Monte Carlo Simulations (CMCS) makes it a widely-used method for uncertainty propagation analysis. Vallmajó et al. [117] proposed a new methodology for estimating the B-basis value of notched composite laminates by means of CMCS using an analytical framework. The authors demonstrated that, for large sample sizes ($> 10^4$), the B-value can be estimated to the 10^{th} percentile. However, as the CMCS requires a large number of results, this is not feasible for simulations that require high computational times (e.g., FE analysis), thus, more economic methods, in terms of computational time, need to be employed.

The First Order Reliability Method (FORM) and the Second Order Reliability Method (SORM) are used in some applications to approximate the probability of a function with random input parameters. They are based on a Taylor series assuming that the output results follow a normal distribution and, therefore, require a small number of simulations. Gosling et al. [118] presented a methodology to estimate the reliability of a complex shear-deformable composite laminate using FORM, while Delbariani-Nejad et al. [119] studied the reliability of the delamination growth under mode I, mode II and mixed mode in composite laminates applying the FORM and SORM methods. According to their results, FORM provides a good balance between accuracy and economic cost in terms of computational time. Hussein at el. [120] used the First Order Second Moment (FOSM) method to maximize plate stiffness using the minimum carbon reinforcement polymer volume fraction in a plate under uniform pressure loading. The authors concluded, however, that these methods are not suitable when the model has non-linearities.

Nowadays, a large number of numerical works addresses the simulation of Low-Velocity Impact (LVI) and Compression After Impact (CAI) tests on composite structures [29–38]. The interest in simulating the CAI test has grown considerably, as CAI strength is a design-driver for some aeronautical components. The prediction of CAI strength is quite complex and challenging as it is based on the previous impact simulation and involves complex contact interactions and pro-

gressive material degradation and the interaction of several failure mechanisms. For airworthiness certification, the analysis must be supported by test. For this study, the analysis of the CAI strength is performed in sub-element-level and, hence, the input parameters that feed the model have been experimentally tested.

English et al. [22] used the SFEM approach to simulate an LVI test on a laminate. The authors used the Latin Hypercube Sampling (LHS) technique to define an input test matrix. Afterwards, the results from the FE simulations were compared with experimental data to adjust and validate the FE model. Patel et al. [42, 43] performed a probabilistic analysis using a Gaussian response surface method in an LVI test by SFEM. The authors estimated the probability of the failure criteria for the matrix cracking and the delamination with different impacted energies by taking into account the uncertainty of the material properties. A sensitivity analysis was performed to determine which input parameters had a greater influence on the probability of failure.

Despite the large amount of published works, there is hardly any work that addresses determining design allowables directly from damage tolerance simulations using advanced constitutive models. This work proposes a cost-effective methodology to estimate the A/B-basis values for the CAI strength of laminated composites using high-fidelity FE simulations and statistical analysis. The main objective of this study is to present the methodology in detail, followed by the accurate design allowables. Nevertheless, the authors would like to remark that the methodology presented in this study to obtain the design allowables of the LVI & CAI test can reduce the number of tests to be performed but, it will not ever completely replace the experimental tests. Details of the modeling approach used to simulate the LVI and CAI experimental tests performed by Airbus and the post-processing of the results are presented in Section 4.2. Section 4.3 details the methodology used to obtain the A/B-basis values, while the results and discussion are presented in Section 4.4. All the data shown in this study is normalized, due to confidentiality and data rights from Airbus. The paper ends with concluding remarks in Section 4.5.

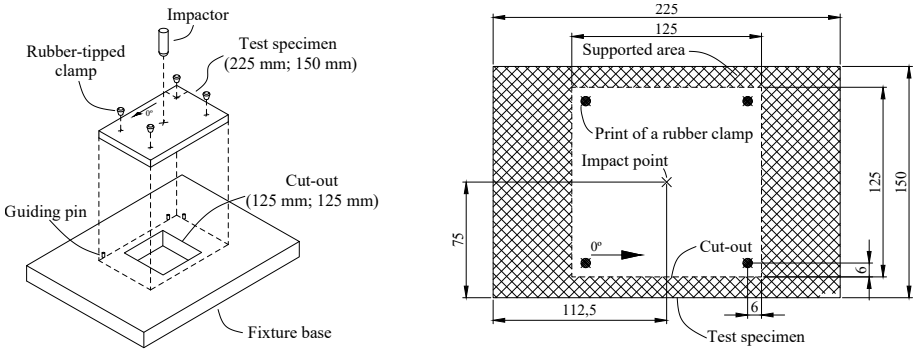

Figure 4.1: Schematic representation of the LVI test: assembly (left) and general dimensions of the specimen in mm (right).

4.2 Damage tolerance simulation

The aeronautical industry judges CAI strength to be a damage tolerance design allowable. CAI strength is measured using a standard test where a laminate, after having been impacted, is subjected to compression loading to evaluate its residual strength. By repeating the test for different levels of impact energy, a correlation between the impact energy level and CAI strength is thus obtained.

In the present work, the LVI and CAI tests are simulated using economical FE models and advanced in-house constitutive damage models. The LVI and CAI experimental tests were performed by Airbus following an internal procedure based on the AITM-1.0010 standard [121]. The specimen is positioned over a metal frame and constrained by four fixture rubber pads (see Fig. 4.1). Using a drop-tower, the specimen is then impacted. After the impact, the specimen is loaded under in-plane compression to obtain its residual strength.

The laminate thickness used in this study is very low, around 1.8 mm. Thin laminates are subjected to global buckling when tested under CAI [122] and hence a strategy is used in this study to avoid this phenomenon. The impacted specimen and a pristine specimen (with of the same laminate as that of the impacted one) are glued to both sides of a honeycomb specimen to prevent failure due to buckling. Fig. 4.2 illustrates the assembly of the above-mentioned specimens. Finally, the assembled sandwich specimen is loaded under compression to measure the CAI strength.

The LVI and CAI tests considered here meet the AITM 1.0010 standard [121],

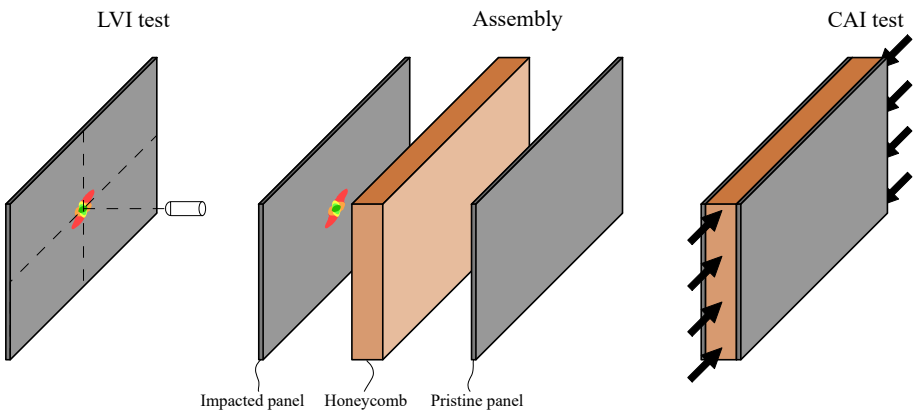

Figure 4.2: Schematic representation of the LVI test, the assembly of the panels to be tested and the CAI test.

despite the dimensions of the specimen, the size of the LVI window, and the position of the fixture rubber pads being slightly different. Specimen geometry and details of the LVI test configuration are summarized in Table 4.1.

Table 4.1: Technical characteristics of the LVI and CAI laboratory test.

Material type	UD tape - CFRP	
Stacking sequence	$[45/-45/90/0/0]_s$	
Specimen dimensions	225 x 150	mm
Thickness of the laminate	1.84	mm
LVI test window	125 x 125	mm
Impact energy	25	J
Impactor mass	3.2	kg
Honeycomb type	HRH-10-6.0-0.96	
Thickness of the honeycomb	30	mm

4.2.1 High-fidelity model

The simulation of the LVI and CAI events on composite materials relies on selecting a suitable modeling strategy. This means selecting an appropriate element type and interaction technology for ply and delamination modeling, respectively. Also, it is important to decide on the number of potential interfaces susceptible to delamination.

It was recently demonstrated that the use of conventional shell elements is a suitable choice, resulting in reasonable time analysis and accurate predictions [23, 39, 40]. In this work, the modeling strategy presented by Soto et al.

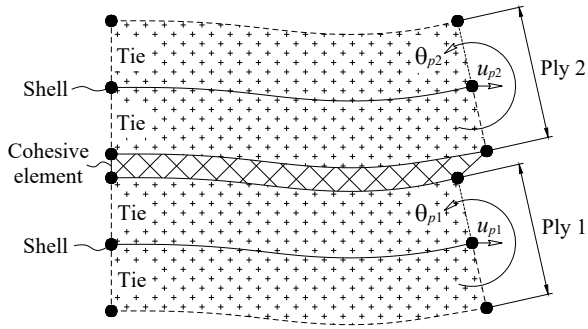

Figure 4.3: FE modeling strategy based on using conventional shell elements, cohesive elements and tie connections. Note: although the cohesive element is sketched with thickness, they are modeled with zero-thickness elements.

[23] is applied, in which conventional shell elements are used together with zero-thickness cohesive elements. All the interfaces with mismatch oriented surrounding plies are considered for delamination and the kinematics of the shell elements are transferred to the cohesive elements using tie constraints, thus allowing two different surfaces, without relative motion between them, to be joined. Fig. 4.3 illustrates the modeling approach used [23].

For successful simulations, there are some key numerical parameters that must be well defined, for example, a criterion to avoid excessive finite element distortion, the mass distribution between shell and cohesive elements, and the mesh size.

The criterion selected to avoid excessive distortion of degraded shell (intralaminar) elements is based on considering a residual stress in each material loading direction. The residual stress is calculated as the stress associated to the corresponding damage variable equal to 0.99 (i.e. for the fiber (d_1), for the matrix (d_2) and for the in-plane shear degradation (d_6)). Therefore, the damage increases while the residual stress is kept constant.

For cohesive elements, the same strategy as in [23] is used, the isotropic damage variable of the cohesive (interlaminar) elements is limited to a value of 0.9999, so that a residual stiffness remains constant at any propagation mode once the element is degraded. No element deletion criteria is considered. In-house constitutive models featuring intra- [25, 26] and interlaminar [41] damage are

also used. Both models were implemented in a VUMAT user-written subroutine.

The simulations are run in an explicit solver. Therefore, the density of each element type, including cohesive elements, must be defined. The whole mass of the structure is distributed between the shell and cohesive elements. As performed in [23], the density of the shell elements and the surface density of zero-thickness cohesive elements are defined so that the corresponding stable time increment associated to shell elements, cohesive elements and contact interactions are similar.

As outlined earlier, a pristine panel and a honeycomb are bonded to the impacted panel after impact. For this step, the *import* option of ABAQUS is used, since it allows an FE model with previously simulated and non-simulated parts to be built. The strategy followed is: (i) an LVI is performed on a single panel, (ii) the impacted panel is imported to a new model and bonded to a honeycomb and a pristine laminate and (iii) the sandwich structure is loaded under compression to determine the CAI strength. The honeycomb is bonded to the panels by tie constraints on the corresponding interaction surfaces. An area 25 mm in diameter at the centre of the impacted panel is not glued to the honeycomb, following the same procedure used for the physical specimens. To simplify the model, the honeycomb is defined using linear elastic solid elements and no damage is modelled for this part. It is assumed that it will fail after the first load drop of the load-displacement curve (CAI strength), see Section 4.2.2. The total number of elements for the LVI FE model is 114692 and for the CAI model is 340830.

4.2.2 Post-processing output results of the FE models

The main output result from the LVI model is the projected delaminated area. In the experimental LVI test, the projected delaminated area is measured by performing an ultrasonic C-Scan analysis. In the LVI FE model, the projected delaminated area can be estimated from the damaged cohesive elements. However, there is no general rule to compare the projected delaminated area from the test with the one numerically obtained from the cohesive damage variable. In this work, the numerical projected delaminated area is estimated spanning over all the cohesive elements with a damage variable larger than the damage corresponding to the dissipation of the visual onset mode II interlaminar fracture

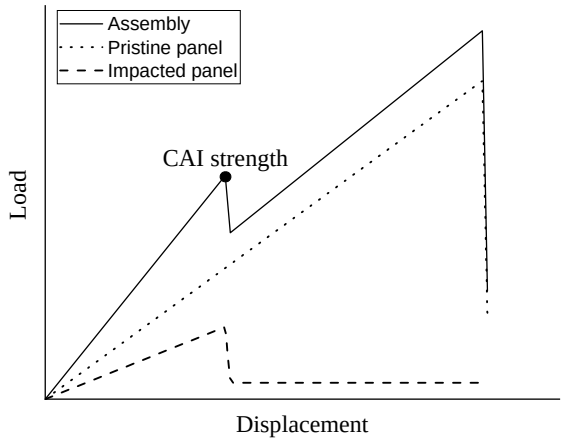

Figure 4.4: Schematic representation of the load vs displacement curve obtained from the CAI FE model.

toughness ($\mathcal{G}_{IIc,vis}$). Two mode II interlaminar fracture toughness are obtained from the laboratory test: visual onset value ($\mathcal{G}_{IIc,vis}$) and crack propagation value ($\mathcal{G}_{IIc}$). According to the constitutive model, the relation between the energy dissipated during the damage development ($\mathcal{G}$) and the damage variable (d) is [123]:

$$\mathcal{G} = \frac{\mathcal{G}_{II_c}\tau_{II}^2 d}{2K\mathcal{G}_{II_c}(1-d)+\tau_{II}^2 d} \tag{4.1}$$

where K is the penalty stiffness and τ_{II} is the mode II interlaminar strength. Therefore, when the energy dissipated is equal to the visual onset value of the fracture toughness the damage variable reads:

$$d_{vis} = \frac{2\mathcal{G}_{IIc}\mathcal{G}_{IIc,vis}K}{\mathcal{G}_{IIc}\tau_{II}^2 - \mathcal{G}_{IIc,vis}\tau_{II}^2 + 2\mathcal{G}_{IIc}\mathcal{G}_{IIc,vis}K} \tag{4.2}$$

and the delaminated area is computed with all the elements with a damage variable higher than d_{vis}. The numerical simulation under predicted the projected delaminated by 10.63% compared to the mean experimental value.

The output result of the CAI simulation is the CAI strength. This is obtained when the load-displacement curve (adding the contributions of the impacted and the pristine panel and the honeycomb) presents the first load drop (as is schematically shown in Fig. 4.4). In the numerical simulations, this first load drop takes place when the impacted laminate fails. It is assumed the same

behavior in the experimental test.

4.3 Methodology to obtain A/B-basis values

The A-basis value of the CAI strength is defined as the 5^{th} percentile of the distribution of the 1^{st} percentile of the CAI strength distribution. The B-basis value is the 5^{th} percentile of the distribution of the 10^{th} percentile of the CAI strength distribution, according to the definition from [1]. The methodology followed in this study to estimate the design allowables is as follows (see Fig. 4.5): i) a Local Sensitivity Analysis (LSA) is performed to identify the input parameters (independent variables X) that have a greater impact on the output results (dependent variables Y), defined as key parameters; ii) an input test matrix for the FE models is created varying only the key parameters, submitted and post-processed to obtain the output results; iii) using the inputs and outputs of the previous analyzes, a Response Surface (RS) of the CAI FE model is created; iv) Monte Carlo Simulations (MCS) with a size of n cases using the previous RS is applied and the Empirical Cumulative Distribution Function (ECDF) of the CAI strength is calculated; v) the 1^{st} and 10^{th} percentile from the ECDF are obtained; vii) steps iv and v are repeated N times; viii) the ECDF of the 1^{st} and 10^{th} percentiles are calculated and the A/B-basis values, respectively, are estimated.

The whole procedure is automated by a Python script which generates the input test matrix for the FE simulation, submits them to ABAQUS and performs the post processing. The script also automatically computes the LSA, the UQ&M and the calculus of the design allowables.

The input parameters of the FE models can be grouped into: material properties, specimen dimensions, impact energy, position of impactor/load and supports, and stacking sequence. In this work, only the material properties required for the FE models are varied to estimate the design allowables. Hence, the LSA and the UQ&M are performed considering only the variability of the material properties. The variation of the mode II interlaminar fracture toughness requires redefining the mesh element size to properly capture the interlaminar behavior. However, in the current study, the element size was decided to be kept constant to simplify the modeling strategy. The list of the material properties used as

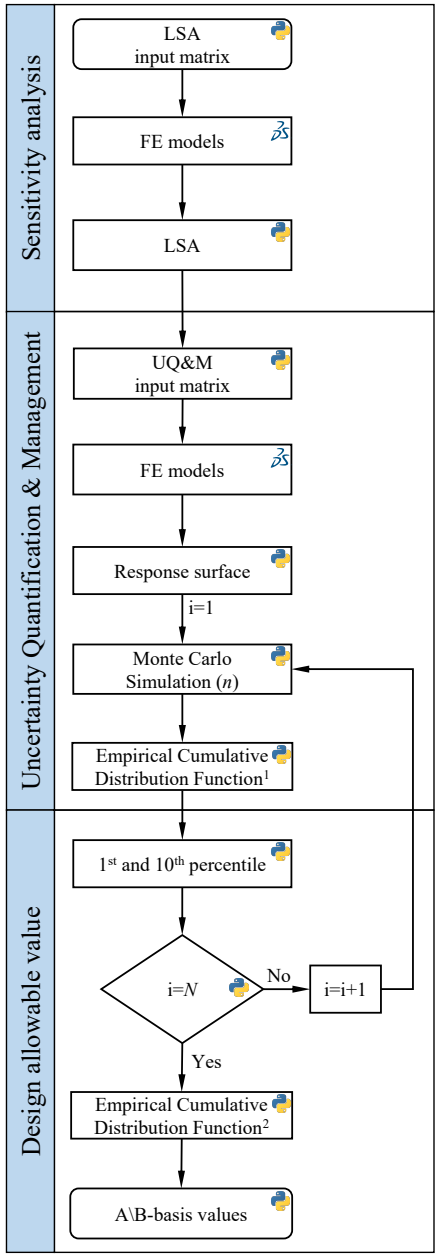

Figure 4.5: Flowchart of the methodology to estimate the A/B-basis values.

input parameters in the LSA are summarized in Table 4.2.

Table 4.2: Input parameters used for the LSA.

Symbol	Input parameter
m_{imp}	Impactor mass
μ	Friction coefficient
$\mathcal{G}_{Ic}$	Mode I interlaminar fracture toughness
$\mathcal{G}_{IIc}$	Mode II interlaminar fracture toughness
BK_η	B-K exponent parameter for mixed mode propagation
τ_{II}	Mode II interlaminar strength
ρ	Density
E_1	Young's Modulus in fiber direction
E_2	Young's Modulus in matrix direction
ν_{12}	Poisson's ratio in 1-2 plane
ν_{23}	Poisson's ratio in 2-3 plane
G_{12}	Shear modulus in the 1-2 plane
X_T	Longitudinal tensile strength
X_C	Longitudinal compressive strength
f_{XT}	Ratio of the first branch of tensile cohesive law
f_{XC}	Ratio of the first branch of compressive cohesive law
Y_T	Transverse tensile strength
Y_C	Transverse compressive strength
S_L	Longitudinal shear strength
S_{LP}	Yield shear strength
K_P	Shear plasticity parameter
$\mathcal{G}_{XT}$	Longitudinal tensile fracture toughness
$\mathcal{G}_{XC}$	Longitudinal comprresive fracture toughness
$f_{\mathcal{G}_{XT}}$	Ratio of $\mathcal{G}_{XT}$ dissipated by the first branch
$f_{\mathcal{G}_{XC}}$	Ratio of $\mathcal{G}_{XC}$ dissipated by the first branch
E_{3_H}	Longitudinal Young's Modulus of the honeycomb
ν_{12_H}	Transverse Poisson's ratio of the honeycomb
C_H	Coefficient of the honeycomb[1]
G_{12_H}	Shear modulus in the 1-2 plane of the honeycomb
G_{13_H}	Shear modulus in the 1-3 plane of the honeycomb
G_{23_H}	Shear modulus in the 2-3 plane of the honeycomb

[1] C_H is a parameter to estimate the Young Modulus in the transverse direction and the longitudinal Poisson ratio of the honeycomb by means of empirical equations provided by Airbus.

The following subsections describe the LSA, the UQ&M analysis and the procedure with which to estimate the design allowables.

4.3.1 Local sensitivity analysis

The LSA is performed to select the input parameters that have the greatest influence on the output results (key parameters). In this study, the independent variables are varied within their 95.4% confidence interval (i.e., ± 2 standard deviations for a normal distribution) to establish their influence on the output

results within their probable values because in the MCS the input parameters will be also varied within their probability range. This range has been considered to have enough distance between the bounds of each input variable to capture its influence on the model, but also, to have physically meaningful, but avoiding potential numerical errors caused by extreme values.

The LSA is applied before the UQ&M analysis, thus allowing the number of the independent variables of the UQ&M analysis to be reduced and, as such, reduce the total computational time. Thus, in the UQ&M analysis only the key parameters selected in the LSA are used to propagate their uncertainty into the model.

The LSA is performed using a one-at-a-time analysis, because the main objective of the study is to describe a new methodology to obtain the design allowables. This approach is based on the variation of only one parameter for each simulation and helps to analyze the relative contribution the different input parameters have on the output of the model. However, this approach will not capture any possible interaction between the parameters and it can be non-conservative. Therefore, a global sensitivity analysis should be carried out to account for the interaction between parameters.

In this work, two cases per independent variable are studied in the LSA. The variation of the independent variables is defined by the limits of the 95.4% confidence interval of each parameter, while the rest of the parameters are fixed to their mean values. The LSA test matrix is schematically displayed in Table 4.3.

Table 4.3: Schematic representation of the LSA test matrix, where m refers to the number of independent variables. The values are normalized as $\frac{X_j - \bar{X}_j}{\hat{s}_j}$, where j refers to the input parameters, X_j is the lower/upper value, $\bar{X}_j$ is the mean value and $\hat{s}_j$ is the sample standard deviation.

No.	X_1	X_2	$\cdots$	X_m
1	0	0	$\cdots$	0
2	-2	0	$\cdots$	0
3	2	0	$\cdots$	0
4	0	-2	$\cdots$	0
$\vdots$	$\vdots$	$\vdots$	$\ddots$	$\vdots$
$2m$+1	0	0	$\cdots$	2

The first case (first row in Table 4.3) has all the parameters equal to the corresponding mean value (all the input variables are distributed by means of a normal distribution, in the same way as in [119] [42]).

The cases of the test matrix in Table 4.3 are calculated using the methodology presented in Section 4.2. Then, the first-order sensitivity index is calculated as:

$$S_j = E\left(\left|\frac{\frac{\partial Y}{\partial X_j}}{\hat{s}_j}\right|\right) \tag{4.3}$$

where j refers to the input parameters and $\hat{s}_j$ is the sample standard deviation. The derivative in Eq. (4.3) is normalized by $\hat{s}_j$, as the objective is to determine the input parameters that generate more dispersion on the output results of the model within their probable values. On the contrary, if the derivative is not normalized by the sample standard deviation, the correct dispersion of the results in the MCS will not be obtained.

The comparison between an index calculated using only the derivative $E\left(\left|\frac{\partial Y}{\partial X_j}\right|\right)$ or using Eq. (4.3) is shown in Fig. 4.6 together with the variability of the output results.

The scatter data and the error bars are the mean value and the uncertainty associated, respectively. They are obtained when an MCS is performed by only varying one of the input parameters X_j while keeping the rest of the parameters constant. Each bar represents the sensitivity index of each input parameter calculated by the corresponding equation. The first input parameter $|\bar{X}_1|$ has an absolute mean value much lower than the second input parameter $|\bar{X}_2| \gg |\bar{X}_1|$, indicating that they correspond to parameters with different orders of magnitude (e.g., Poisson's ratio and fiber Young's modulus). In this case, both input parameters ($|\bar{X}_1|$ and $|\bar{X}_2|$) produce the same dispersion in the output results. However, the sensitivity index of the $|\bar{X}_2|$ calculated by the derivative is greater than that obtained by Eq. (4.3). Therefore, if the sensitivity index is calculated using $E\left(\left|\frac{\partial Y}{\partial X_j}\right|\right)$, the effect of each variable on the output results will not be properly captured. On the other hand, if the sensitivity index is calculated employing Eq. (4.3), the selected input parameter will be the one that

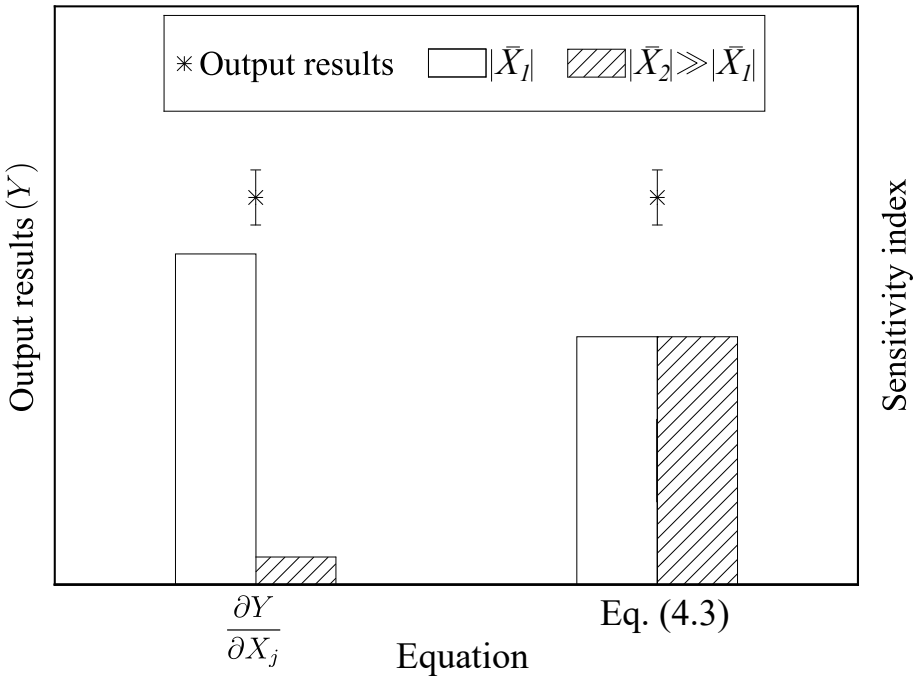

Figure 4.6: Schematic representation of the sensitivity index calculated by the derivative of the output results with respect to the input parameters, and by Eq. (4.3). A first input parameter $|\bar{X}_1|$ has an absolute mean value much lower than a second input parameter $|\bar{X}_2| \gg |\bar{X}_1|$. The scatter data and the error bar are the mean value and the variability, respectively, of the output results when an MCS is performed modifying $|\bar{X}_1|$ and $|\bar{X}_2|$ within their range of uncertainty, relatively.

generates the correct dispersion on the results when the MCS is applied. In the case represented in Fig. 4.6, both input parameters would be selected since they provide the same scatter in the predictions.

Finally, the sensitivity index for each input parameter is calculated using its expected value. The absolute values are used as in Campolongo et. al [124] who estimated the mean value of each sensitivity index to prevent opposing components being canceled. The input parameters with the greater S_j in both models (LVI and CAI FE models) are selected as the key parameters.

4.3.2 Uncertainty quantification and management analysis

An RS is adjusted for the CAI FE model to obtain the correlation between the key parameters and the CAI strength. This allows the total computational time of the UQ&M analysis to be reduced because the RS makes it possible to estimate the results of several cases in a few seconds. The design of experiment used to create the UQ&M test matrix is the LHS technique; it is not fully random sampling because it avoids the clustering of samples. After the test matrix is defined, it is submitted to the FE models, and then the CAI strength is obtained for each case. Next, the Kriging algorithm is used to create the RS. Finally, the accuracy of the RS is estimated with the coefficient of determination (R^2) and the Root Mean Square Error (RMSE) of the goodness-of-fit plot. In addition, a chi-squared test is applied to determine if there is any statistical evidence that the predicted values from the RS are reproducible from the observed values from the FE models. The Pearson goodness-of-fit statistic is defined as:

$$\chi^2 = \sum \frac{(Observed - Predicted)^2}{Predicted} \tag{4.4}$$

where the *Observed* and the *Predicted* values are the data used to create a goodness-of-fit plot. If an improvement in the accuracy of the RS is required, new cases should be added to the UQ&M test matrix in the region needing to be improved.

Next, a large number of MCS (N) are performed using the RS, where the size of each MCS is n. Finally, the ECDF of each previous MCS is calculated, thus obtaining N ECDF from the distribution of the CAI strength (see Fig. 4.7).

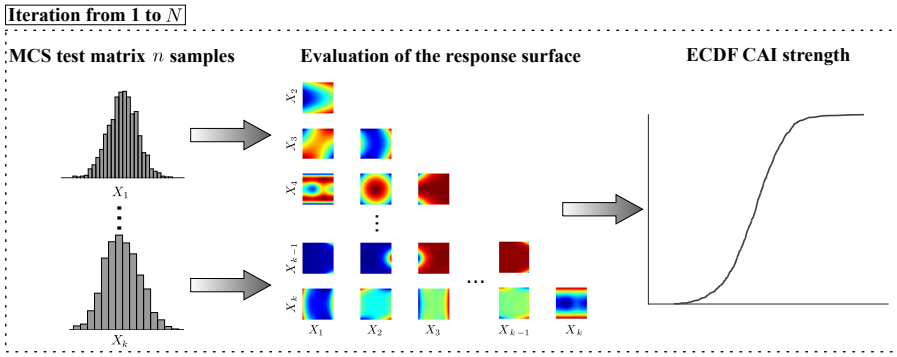

Figure 4.7: Schematic representation of the loop of the UQ&M. In accordance with the Fig. 4.5 flowchart, the left and center parts correspond to the "Monte Carlo Simulation (n)" box and the right to the first "Empirical Cumulative Distribution Function" box.

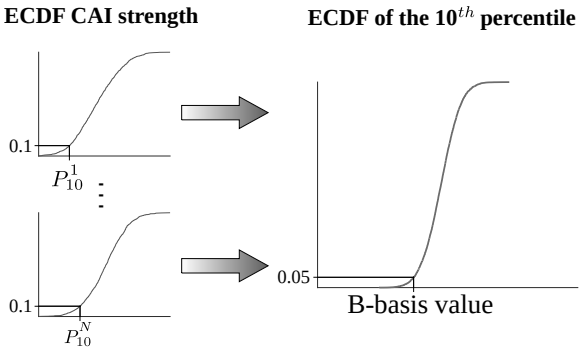

Figure 4.8: Schematic representation of the steps to estimate the B-basis value. In accordance with the Fig. 4.5 flowchart, the left part corresponds to the last "Empirical Cumulative Distribution Function" box and the right part corresponds to the "A/B-basis value" box. P_{10} is the 10^{th} percentile from the ECDF of the CAI strength of iteration i^{th}.

4.3.3 Determining the A/B-basis value

The 1^{st} and 10^{th} percentiles of the CAI strength are obtained from each previously calculated ECDF. Thus, N values of the 1^{st} and also the 10^{th} percentile are provided. Next, the ECDF for both percentiles are calculated. Finally, the 5^{th} percentile of the ECDF from the distribution of the 1^{st} percentile is the A-basis value. Likewise, the B-basis value is the 5^{th} percentile of the ECDF from the distribution of the 10^{th} percentile (see Fig. 4.8).

4.4 Results and discussion

First, the CAI strength from the deterministic FE result using the mean input values is obtained following the FE methodology described in Section 4.2 and the prediction is compared with those obtained from the laboratory test (see Table 4.4).

Table 4.4: Comparison of the experimental CAI strength values with the one obtained using the deterministic FE model. The values are normalized with respect to the mean value of the experimental CAI strength.

	Experimental	Deterministic
mean	1.000	1.096
median	0.957	
Percentile 5	0.847	
Percentile 95	1.193	

The FE model over predicts the median CAI strength by 14.6% and the mean value by 9.6% and it falls within the 90% confidence bound of the experimental data. These over predictions are in concordance with the results obtained in previous works [31, 36] and are considered acceptable, given the complexity of the simulations. The difference can be attributed to some of the simplifications done in the modeling approach such as assuming linear elastic behavior of the honeycomb or possible loading misalignments.

Once the damage tolerance simulation methodology is validated, an LSA is launched and then, using the procedure of Section 4.3.2, the UQ&M results are analyzed. Finally, the A/B-basis value results estimated with the methodology proposed in this work are discussed. A comparison with the results obtained using a replication of the CMH-17 approach [1] is also given. It is worth mentioning that the results from the LSA and the desig allowables obtained in this section are only valid for this particular case. If the input parameters change, a new analysis must be carried out.

The computational time for the deterministic LVI and CAI FE models is around 29 h and 10 h, respectively, with 8 cpus (3.1 GHz CPU and 32 GB RAM for each CPU). However, the computational time for the LVI and CAI FE models used in the UQ&M analysis is in average around 39 h (from 21 h to 96 h) and 14 h (from 5 h to 44 h), respectively. The difference in computational time is due

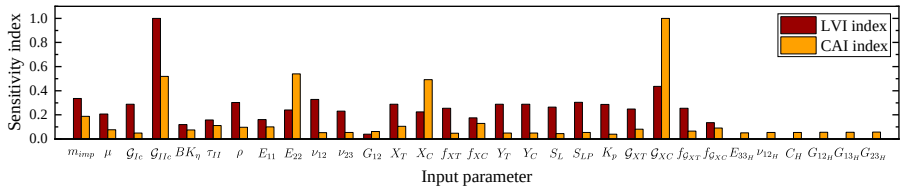

Figure 4.9: Sensitivity index of each input parameter for the LVI FE model and for the CAI FE model. The indices are normalized with respect to the highest sensitivity index for each FE model.

to the variation in the different values of the input parameters. For example, for a higher value of $\mathcal{G}_{Xc}$, the CAI strength and ultimate strain also increase which leads to a large computational time.

4.4.1 Local sensitivity analysis

The sensitivity indices using Eq. (4.3) for the LVI and CAI FE models are presented in Fig. 4.9. The indices are normalized with respect to the highest sensitivity index for each FE model. The LVI sensitivity index is calculated since the UQ&M analysis takes into account the projected delaminated area as an input variable for the creation of the RS of the CAI model. Therefore, the parameters of the model that generate the highest dispersion in the LVI results and the CAI strength are selected as key parameters. In this case, the key parameters are: $\mathcal{G}_{IIc}$ for the LVI and $\mathcal{G}_{XC}$ for the CAI strength. The large influence of $\mathcal{G}_{IIc}$ on the projected delamination area is explained because it is the interlaminar fracture toughness in mode II that corresponds to the delamination damage mechanism. In addition, the high impact of $\mathcal{G}_{XC}$ on the CAI strength is plausible because it is the longitudinal compression fracture toughness linked with the fiber kinking damage mechanism. Moreover, $\mathcal{G}_{XC}$ is also the second independent variable that generates the most dispersion in the LVI index (projected delaminated area). For the CAI strength, $\mathcal{G}_{IIc}$ also has a high sensitivity index.

Out of the 31 input parameters analyzed, the LVI FE model has 19 input parameters with a sensitivity index greater than 0.2. This indicates that the LVI results are sensitive to several input parameters and, therefore, this model demands a more accurate calibration of a larger number of input parameters than the CAI strength, since the latter has only four input parameters greater than 0.2. To fully capture the influence of all the input parameters, a global sensitivity analysis

with interactions should be carried out.

4.4.2 Response surface analysis

Firstly, the UQ&M test matrix is created with 80 FE models defined by means of the LHS method. The cases are distributed following a uniform distribution narrowed to $\pm 3\hat{s}_j$ for each key parameter to obtain an RS within the range described. Therefore, the probability of evaluating the RS by means of MCS outside the previous range is 0.26%. In addition, 20 more FE models are defined with the normal LHS method. These cases follow a normal distribution to obtain a more accurate RS in the center range of each key parameter; because the RS will be more thoroughly evaluated in the center range of each key parameter in the MCS. Therefore, the total number of cases for the UQ&M test matrix is 100.

Then, the test matrix is submitted to the FE models and the projected delaminated area and the CAI strength are obtained for each case. Further, the RS is generated by randomly selecting 90 cases (out of the total 100 cases) from the UQ&M test matrix as explained below. The input variables of the CAI RS are the key parameters and the projected delaminated area obtained from the LVI simulations. Finally, the accuracy factors presented in Section 4.3.2 are calculated using the remaining ten cases for validation. The most accurate RS is obtained using an optimization algorithm to maximize the accuracy factors.

Two different RSs for the CAI model are used to determine the influence accuracy of the RS has on the design allowables. CAI90A and CAI90I are the RSs for the CAI strength generated with 90 randomly selected cases from the UQ&M test matrix. The accuracy of CAI90A (RS of CAI model with 90 cases and Accurate) is greater than CAI90I (RS of CAI model with 90 cases and Inaccurate).

In addition, the effect of using or not the projected delaminated area as an input of the CAI RS on the design allowables is analyzed by comparing the results between CAI90A and CAI90AnD. The input parameters of CAI90AnD are only the key parameters but not the projected delaminated area.

The configuration of each RS analyzed and the accuracy analysis results are summarized in Table 4.5.

Table 4.5: Statistics of the RS for the CAI FE model created to estimate the design allowables. AD refers to the projected delaminated area.

Nomenclature	Samples	Input parameter	R^2	RMSE	p-value
CAI90A	90	AD, $\mathcal{G}_{IIc}$ and $\mathcal{G}_{XC}$	0.97	7.13	0.98
CAI90I	90	AD, $\mathcal{G}_{IIc}$ and $\mathcal{G}_{XC}$	0.84	12.91	0.32
CAI90AnD	90	$\mathcal{G}_{IIc}$ and $\mathcal{G}_{XC}$	0.98	5.87	0.98

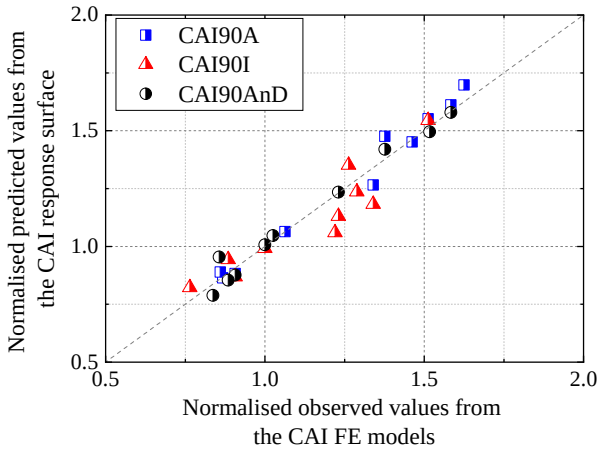

Figure 4.10: Goodness-of-fit plot for each RS in Table 4.5. The values are normalized with respect to the mean value of the CAI strength obtained from the 100 FE models used to create the RS.

The CAI90A and CAI90AnD R^2 coefficients are very close - 0.97 and 0.98 respectively. In addition, they have the same p-value for the Pearson goodness-of-fit statistic analysis (p-value equal to 0.98). Therefore, there is not enough evidence to reject the hypothesis that the RSs fit the CAI strength. However, the RMSE coefficient has significant differences for these two surfaces, with CAI90AnD having the best accuracy factors. Meanwhile, CAI90I has the poorest accuracy factors, and from a statistical point of view does not fit the CAI strength.

Fig. 4.10 compares the goodness-of-fit plot for each RS in Table 4.5. The values are normalized with respect to the mean value of the 100 FE models used to create the RSs. Data comparison confirms the accuracy coefficients in Table 4.5, where the more accurate RSs are CAI90A and CAI90AnD, because the R^2 and the p-value from the chi-squared test are close to 1 and the RMSE is small.

4.4.3 Design allowables

The A/B-basis values of the CAI strength obtained from each RS in Table 4.5 are displayed in Fig. 4.11. The results are represented as a function of n and N. They are normalized with respect to the mean value of the CAI strength obtained from the CAI90A RS with the maximum sample size ($n = 10^5$ and $N = 10^5$). The percentage difference between the mean value from $n = 10^2$ and $N = 10^2$ with respect to the one obtained from $n = 10^5$ and $N = 10^5$ is equal to 0.11%. The normalization allows the design allowables to be compared with the mean value.

The results obtained from the CAI90A and CAI90I RSs are lower than the mean value of the CAI strength from the CAI90A RS, whereas the values obtained from CAI90AnD are higher. This indicates that CAI90AnD overestimated the A/B-basis values since the 5^{th} percentile of the distribution of the 1^{st} percentile and the 10^{th} percentile, respectively, must be lower than the mean value of the measured population. Hence, the results obtained from CAI90AnD are rejected. It can be concluded that the projected delaminated area must be an input of the CAI RS to estimate the design allowables. In addition, the results obtained from CAI90I are close to those obtained from CAI90A and the sample size n of the MCS has a greater influence on the results than the number of repetitions of the MCS N.

The comparison of the design allowables obtained from CAI90A and CAI90I as a function of n shows the biggest discrepancies for small values of n (see Fig. 4.12). The maximum percentage differences for the design allowables between both RSs are lower than 7.7% and 3.5% for the A-basis value and the B-basis value, respectively. As expected, the calculus in the tail of a distribution requires a large sample size and, since the CAI90I RS is less accurate, the discrepancies between both RS for small sample size are higher. The A-basis values are almost constant when $n > 5 \cdot 10^6$. Using CAI90A RS, the A-value is 0.732 and using CAI90I it is 0.725. The B-basis value is almost constant when $n > 5 \cdot 10^5$ and it is 0.938 using CAI90A and 0.937 using CAI90I.

The influence of sample size n and the number of repetitions N on the design allowables is also described in Fig. 4.13. The ECDF for different values of n and N of the 1^{st} and 10^{th} percentile distributions are represented by CAI90A

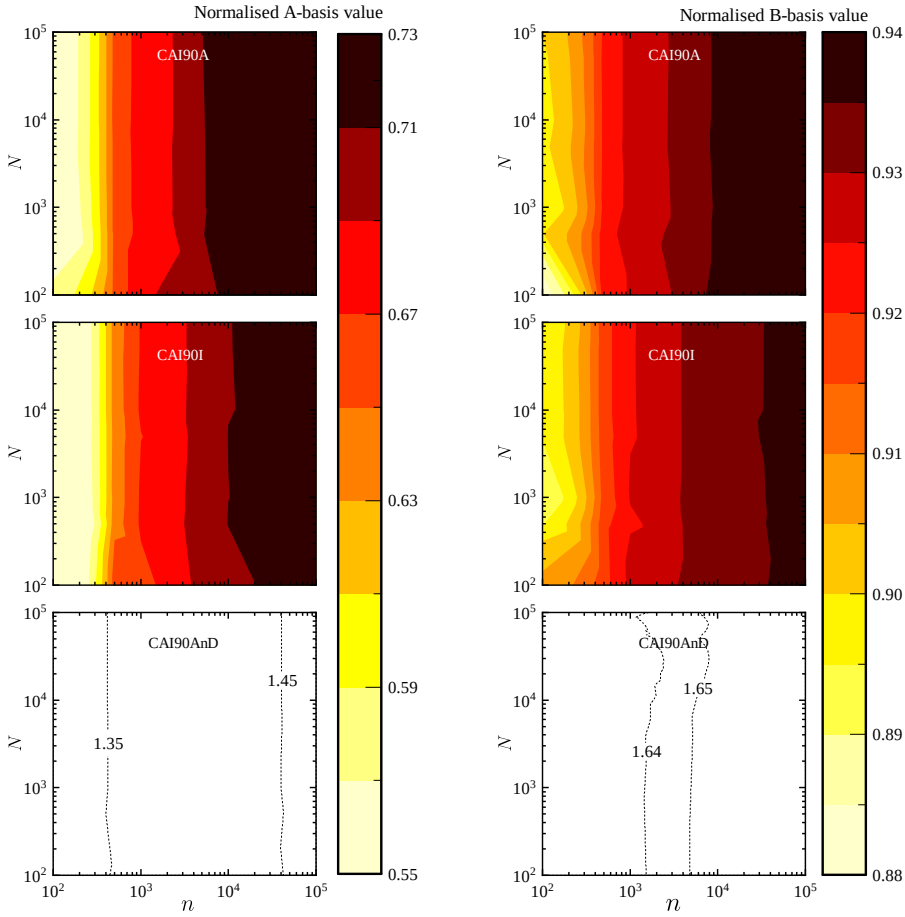

Figure 4.11: Comparison of the A-basis value (left) and the B-basis value (right) of the CAI FE model estimated with different sizes of the MCS (n) and with different repetition numbers of the MCS (N). Results obtained using the CAI90A RS (top), the CAI90I (centre) and the CAI90AnD RS (bottom). The values are normalized with respect to the mean value of the CAI strength obtained from the CAI90A RS with $n = 10^5$ and $N = 10^5$.

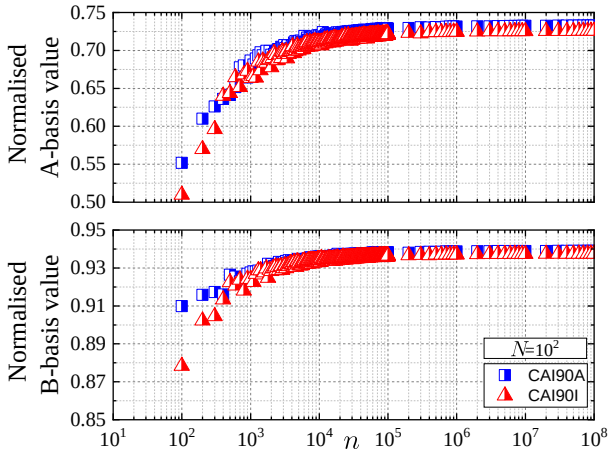

Figure 4.12: Comparison of the A-basis value (top) and the B-basis value (bottom) vs. the size of the MCS (n) repeated 10^2 times ($N = 10^2$), from the CAI90A and CAI90I RS. The values are normalized with respect to the mean value of the CAI strength obtained from the CAI90A RS with $n = 10^5$ and $N = 10^5$.

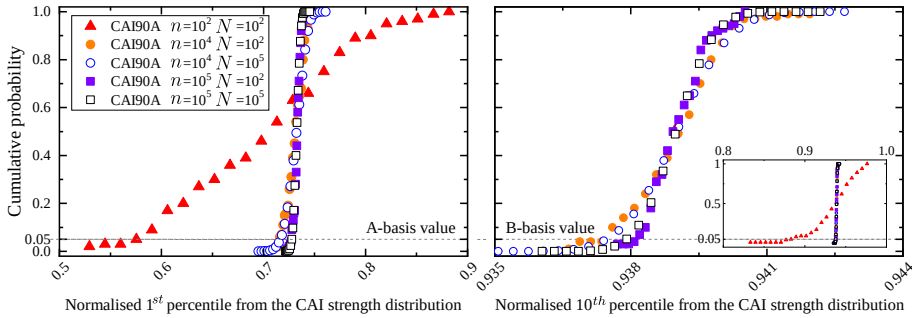

Figure 4.13: Comparison of the ECDF of the 1^{st} percentile (left) and the 10^{th} percentile (right) of the CAI strength for different sizes of the MCS (n) and for different repetition numbers of the MCS (N) from the CAI90A RS. The percentile values are normalized with respect to the mean value of the CAI strength obtained from CAI90A RS with $n = 10^5$ and $N = 10^5$.

RS. For $n = 10^2$ and $N = 10^2$, the dispersion of each percentile distribution is greater than the rest of the ECDFs. The difference for the A-basis value between the cases with $n = 10^2$ and $N = 10^2$ and $n = 10^4$ and $N = 10^2$ is equal to 21.5%. For the B-basis value it is equal to 5.9%. However, the results from $n = 10^4$ and $N = 10^2$ and those from $n = 10^4$ and $N = 10^5$ (with the same n and different N) are almost identical. Similarly, the results from $n = 10^5$ and $N = 10^2$ and those from $n = 10^5$ and $N = 10^5$ are also close.

The difference between the A-basis value and the mean of the 1^{st} percentile when $n = 10^5$ and $N = 10^5$ is 0.67%, and for the B-basis value the difference of the mean value of the 10^{th} percentile is 0.11%. This results suggest that the A-basis and B-basis values can be approximated using the 1^{st} and 10^{th} percentile, respectively, when n is sufficiently higher. This is in line with the conclusion of Vallmajó et. al. [117].

The design allowables selected from the MCS approach are those obtained from CAI90A with $n = 10^4$ and $N = 10^2$; since, from CAI90A a good compromise between the stabilization of the results and the computational time is obtained. This refers to a reduction in the computational effort by 7.5×10^3 times, whereas the percentage difference of the design allowables is lower than 1.2%, compared with respect to those obtained with $n = 10^5$ and $N = 10^5$. In addition, the best accuracy coefficients are obtained with the CAI90A RS.

The experimental data are compared with the numerical results in Fig. 4.14. The grey area is the 90% confidence bound of the experimental data. The values are normalized with respect to the mean value of the experimental CAI strength. The deterministic value is obtained using the FE models with the mean value of the input parameters. Ten samples randomly selected from the 20 normal LHS samples used to create the RSs are selected. The difference between the mean from the previous ten samples and the one obtained from the experimental data is equal to 6.1% and the difference of the median is equal to 10.9%. Both values (mean and median) from the ten random samples are within the 50% confidence bound of the experimental data. This demonstrates that the validation of a numerical model by comparing the deterministic numerical result with the mean from the experimental data is not a good procedure. The input variability of a numerical model is required for its validation. The mean and median values obtained from the MCS with $n = 10^4$ and $N = 10^2$ are within the 90% confidence

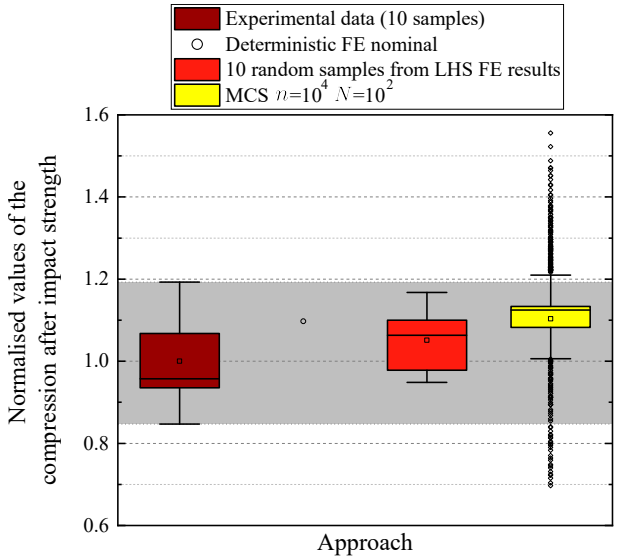

Figure 4.14: Comparison of the CAI strength values obtained for the different approaches. The grey area is the 90% confidence bound of the experimental data. The values are normalized with respect to the mean value of the experimental CAI strength.

bound of the experimental data and their difference is equal to 10.5% and 17.7%, respectively.

The accuracy of the CAI90A RS can be also observed in Fig. 4.14. The mean and median values from the MCS are within the outlier bounds of the ten randomly selected FE results. In addition, the difference of the mean and median values between these two approaches are equal to 6.0% and 5.1%, respectively. Thus is, in concordance with the results obtained in the accuracy analysis of the RSs. The differences between the experimental data and the numerical results can be associated to the same sources of the deterministic model, but also, due to the mesh size kept constant despite varying the $\mathcal{G}_{II_c}$ and the assumption on the statistical distributions of the input parameters.

The dispersion of the results of the experimental data is greater than that obtained numerically (from the FE models and the RS). This could imply that there are other input parameters that generate dispersion on the results apart from the key parameters ($\mathcal{G}_{IIc}$ and $\mathcal{G}_{XC}$). Another possibility is that the uncertainty of the key parameters are not properly defined (i.e., the coefficient of variation of the key parameters can be greater than those used in the analysis).

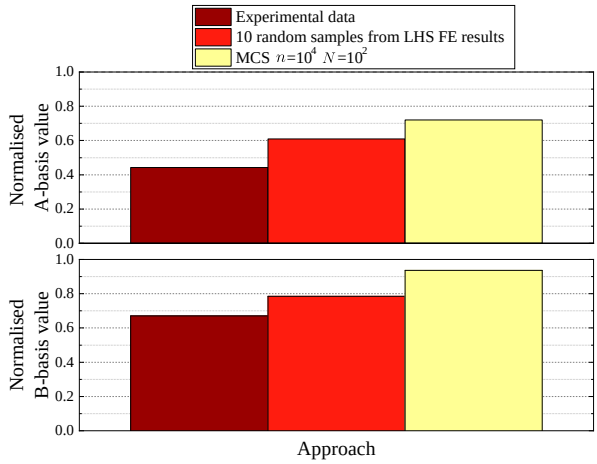

Figure 4.15: Comparison of the A-basis value (top) and B-basis value (bottom) obtained from ten experimental samples using the CMH-17 approach [1], from ten randomly selected samples from the 20 normalized LHS FE models used to create the response surfaces using the CMH-17 approach [1] and from the MCS (MCS) and ECDF function approach with a size of the MCS of 10^4 samples ($n = 10^4$) and 10^2 repetitions ($N = 10^2$) using the CAI90A RS. The values are normalized with respect to their mean value of the corresponding group.

4.4.4 CMH-17 approach vs. present methodology

The A/B-basis values obtained using the methodology presented in the previous section is also compared with the basis values obtained by a direct replication of the procedure used for the experimental results, i.e., following the CMH-17 guidelines (see Fig. 4.15). The values of the figure are normalized with respect to the mean value of the corresponding group. The values summarized in this figure are obtained from the ten experimental samples using the CMH-17 approach ($n = 10$ and $N = 1$), the ten samples randomly selected from the 20 normalized LHS FE models used to create the RSs and using the CMH-17 approach, and the CAI90A RS using the ECDF with $n = 10^4$ and $N = 10^2$. It is worth mentioning that, although the number of laboratory tested specimens is small, the sample size meets the requirements of the CMH-17 approach, because specimens from four different batches were tested to obtain the experimental data (more than the three batches required by CMH-17 approach).

The design allowables obtained from the experimental data are lower than those obtained from the ten samples randomly selected from the normal LHS FE

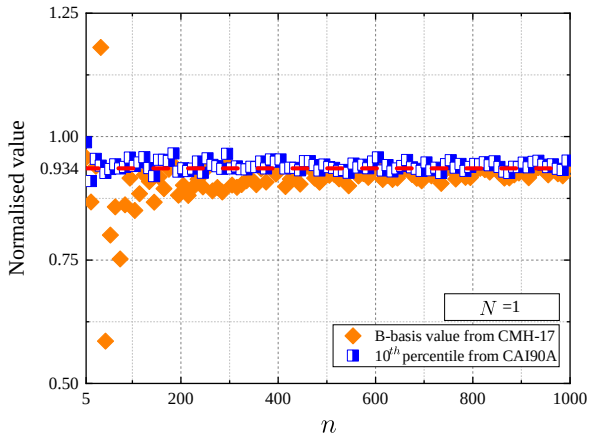

Figure 4.16: B-basis value estimated by means of the CMH-17 approach [1] and the 10^{th} percentile estimated by means of ECDF from the CAI90A RS with n samples repeated once (N=1). The red dashed line is the B-basis value obtained with $n = 10^4$ and $N = 10^2$. The values are normalized with respect to the mean value of the CAI strength obtained from the CAI90A RS with $n = 10^5$ and $N = 10^5$.

models. This trend is explained by the results in Fig. 4.14. Although the mean values of these two cases are closer, the dispersion of the experimental data is greater. Therefore, the 1^{st} and the 10^{th} percentiles obtained from the experimental data are lower than those estimated from the numerical results. Consequently, the design allowables of the experimental data are lower than those calculated from the numeric results. This is in agreement with the results obtained by Laurin et al. in [116].

The difference between the values calculated by the CMH-17 approach and those estimated using the CAI90A RS is explained in Fig. 4.16. It is created by computing the B-basis value for a different number of specimens using the CAI90A RS and (i) the guidelines given in the CMH-17 and (ii) using ECDF with $N = 1$ (i.e., the 10^{th} percentile). The red dashed line is the B-basis value obtained with $n = 10^4$ and $N = 10^2$. The values are normalized with respect to the mean value of the CAI strength obtained from CAI90A RS with $n = 10^5$ and $N = 10^5$. The B-basis values calculated with the CMH-17 approach are more conservative than the theoretical B-basis value (red dashed line). In addition, these values do not show a clear trend for small sample size ($n < 90$). However, the 10^{th} percentiles estimated with the ECDF are closer to the theoretical B-basis

value and there is no significant dispersion in function of n. In addition, when n increases, the difference in the values from the two approaches decreases, but the CMH-17 values remain more conservative.

4.5 Conclusions

A methodology to obtain the design allowables using high-fidelity models is proposed. The methodology is based on generating a Response Surface (RS) from a reduced number of high-fidelity simulations. Using the RS, an empirical cumulative density function is determined and used to obtain the basis value. The methodology was applied to the A/B-basis value calculation of the compression after impact strength of thin laminates. The experimental procedure used relies on first impacting a laminate, then gluing this impacted laminate to a honeycomb core and another pristine laminate, and finally loading the sandwich structure under compression. The same procedure was used for the high-fidelity simulations. The model strategy used was validated by comparing the distribution of the numerical results with the one obtained from the experimental data.

Next, several simulations were performed to generate the RS and apply the proposed methodology to obtain the A/B-basis values. When creating the RS, if the selection of the input parameters for the RS is not appropriate, good statistical coefficients in the accuracy analysis may not guarantee a proper reproduction of the model behavior. Moreover, the A/B-basis values obtained with a less accurate RS are very close to those obtained from a more accurate RS if the sample size is large. As the A-basis value is more towards the left tail of the distribution, it is more sensitive to the accuracy of the RS than the B-basis value. It has also been demonstrated that, when performing the Monte Carlo simulations, the sample size has more influence on the design allowables than the number of repetitions does. Hence, the A/B-basis value can be numerically estimated using a single Monte-Carlo simulation provided a large sample size.

The methodology presented has the potential to reduce non-recurring certification cost provided the reduction on the test cost and/or design span time is higher than the cost associated to perform the numerical simulations and to obtain the design allowables. The approach followed in this work, where the UQ&M methodology presented has been implemented using python scripts that

automate all the process (including the generation and post-process the finite element models) and reduces the engineering labour associated to obtain the design allowables.

5

Paper C – Effect of ply misalignment on the notched strength of composite laminates.

The paper is *in preparation for submission*.

Overview

The calculation of desing allowables has been demonstrated to be crucial on the certification of composite structures. Analytical models serve as swift and robust tools for preliminary design, offering a mathematical description of material behaviors. However, these models face limitations in replicating all damage mechanisms and their interactions, making them more suitable for predicting design values in the early stages of development.

In contrast, Finite Element numerical simulations provide a more comprehensive understanding of material behavior by employing sophisticated algorithms to simulate complex interactions. These simulations consider a multitude of factors, such as the nonlinear response of materials under varying conditions and intricate damage mechanisms. However, the information gained through numerical simulations comes at a cost of increased computational effort and time.

Furthermore, the presence of defects in composite structures is an unavoidable reality during the manufacturing process. During the fabrication of laminates, various manufacturing defects may emerge, introducing intricacies that need careful consideration. One important challenge arises while layup creation, where the meticulous alignment of each ply to achieve the intended layup becomes a complex task. The misalignment of individual plies during the layup process introduces variations in the structural integrity of the final composite material. Therefore, ply deviations may be taken into account.

This paper focuses on predicting notched design allowables at the coupon level, considering the presence of defects through both analytical and numerical models. Analytical models facilitate the generation of large sample sizes for a more accurate statistical analysis, while numerical simulations offer enhanced precision. The study compares these computational tools and suggests a hybrid approach to establish design allowables, achieving a balance between computational efficiency and results reliability.

Effect of ply misalignment on the notched strength of composite laminates

O. Vallmajó[a,*], M. Descamps[a], A. Arteiro[b,c], A. Turon[a]

[a] *AMADE, Polytechnic School, Universitat de Girona, Campus Montilivi s/n, E-17003 Girona, Spain*

[b] *DEMec, Faculade de Engenharia, Universidade do Porto, Rua Dr. Roberto Frias, 4200-465 Porto, Portugal*

[c] *INEGI, Rua Dr. Roberto Frias, 400, 4200-465 Porto, Portugal*

Abstract Predicting the notched strength of carbon fiber-reinforced polymers is a crucial aspect of composite structure design, particularly when considering the uncertainties stemming from geometric features, material variability and defects. This study focuses on the influence of ply misalignment at the meso-scale level. The research employs a comprehensive methodology to establish notched strength allowables, integrating analytical (low fidelity), which have limitations in the representation of stacking sequence effects and in the generation of ply misalignments, and computational (high fidelity), employing a finite element model (FEM), tools. The investigation emphasizes the need for a holistic understanding of these factors to enhance the accuracy of predictions. The results predicted by both models are in good agreement with experimental results, particularly the numerical ones. Both models underscore the decrease of the notched strength due to ply misalignment. Finally, a hybrid approach is proposed given that FEM predictions offer great accuracy and better comprehension of the damage mechanisms, while fast analytical models can be used to determine the allowables.

keywords: Composites, Ply deviation, OH strength, multi fidelity

* Corresponding author

5.1 Introduction

Numerous factors can influence the mechanical performance of composite materials. These include the presence of geometric features, e.g., a hole, the presence of defects, and the intrinsic material variability. Therefore, the design process of composite structures requires a profound understanding of mechanical performance under different loading conditions, while considering the uncertainties arising from the geometrical details, the presence of defects and the material variability. That is why the design process comprises different stages starting from the analysis of the constituents, i.e., micro-scale analysis, progressing to the analysis of small specimens with single or a reduced set of features, i.e., meso-scale analysis, and, finally, culminating with an exhaustive evaluation of more complex designs [1]. In the past, these analyses were primarily conducted through extensive test campaigns. Fortunately, nowadays, there is access to more computational resources and enhanced knowledge for designing composite materials. This includes the use of computational (or high fidelity) models or analytical (or low fidelity) models that account for the correct behavior of these materials.

One of the common design drivers during the qualification of a composite structure is the characterization of the notched strength of fiber-reinforced polymers typically determined from an open-hole (OH) specimen. To mitigate the time and cost constraints associated to extensive testing campaigns, predicting this property can be carried out through analytical or numerical models. Nevertheless, there are many uncertainties that need to be accounted for. Thus, providing a single value is not sufficient to ensure safety. Instead, the generation of design allowables is recommended [117, 125]. The main sources of variability that have been considered are the intrinsic material uncertainties and the geometric tolerances. However, the presence of manufacturing defects plays a major role on the damage onset and evolution, thus on the mechanical performance. One of the most defects ones at this scale (meso-scale) is the ply misalignment.

Based on the scale of observation, misalignments can be considered at either ply level or at the individual fiber level, the latter also known as in-plane waviness [67]. This work focuses on defects at the ply level, and consequently, it only considers ply misalignment. It is worth mentioning that, usually, ply misalign-

ment is known as fibre straightness, whose main source of variability is the presence of fiber waviness as reported by Potter et al. [68]. The impact of ply misalignment has been thoroughly investigated in previous research. Hinckley et al. [69] evaluated the effect of ply misalignment using the classical laminated plate theory. Arao et al. [70] assessed the effect of ply misalignment on the out-of-plane deformation of CFRP concluding that ply angle deviation can induce unpredictable out-of-plane deformations. Steeves et al. [71] predicted a similar effect in ultra-thin composite materials. Thompson et al. [72] investigated the effect of angular errors during ply placement in uni-directional fiber-polymer composites on the surface deformation peak-to-valley values of circular plates. However, to the authors' best knowledge, all the current literature studies have not taken into account simultaneously all uncertainties: the material variability, the geometric tolerances and the presence of ply misalignments.

Therefore, in this work, the effect of ply misalignment and the uncertainties within composite structures are taken into consideration while establishing the notched strength allowable of carbon fiber-reinforced polymers (CFRP) using computational and analytical tools.

The paper is organized as follows: Section 5.2 describes the methodology followed to propagate the uncertainties and determine the notched strength; Section 5.3 describes the materials considered, the geometry of the specimens as well as the description of the defects; Section 5.4 presents the results and their discussion. Finally, Section 5.5 summarizes the conclusions of this work.

5.2 Methodology

The notched strength allowables of a CFRP is calculated using two different approaches: (a) a Finite Fracture Mechanics (FFM) model and (b) a computational model based on the Finite Element Method (FEM). Material variability, the geometric tolerances and the effect of random ply misalignments is considered for both approaches. The flow chart in Fig. 5.1 shows the strategy followed in this study for the propagation of uncertainties, which is described in the following sections.

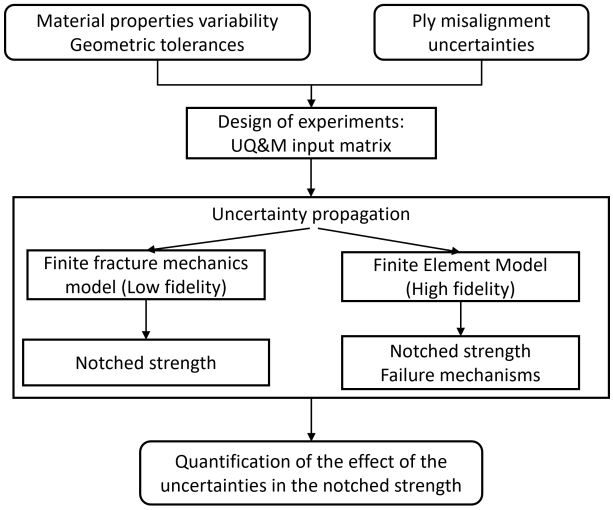

Figure 5.1: Flow chart of the propagation of the uncertainties on the notched strength of carbon fiber reinforced polymers.

5.2.1 Composite laminate uncertainties

Composite structures have many sources of variability. Due to their inherent orthotropic behavior, the material properties, the geometry and the presence of ply deviations are important factors to consider, as described in the following.

5.2.1.1 Material properties variability and geometric tolerances

The constituent materials in a composite structure exhibit an intrinsic variability on their properties. Moreover, the processing residual stresses, e.g., due to the chemical shrinkage of the polymer matrix and the mismatch of thermal expansion coefficients between constituents and unidirectional plies of different orientation, and the effect of micro-defects amplify the uncertainties of the meso-scale properties [126]. Therefore, material suppliers and testing labs for material characterization do not provide a single value for the material properties; instead, they provide a mean value and the associated uncertainty, i.e., the statistical distribution or at least the standard deviation (STDV), of the meso-scale properties. This material variability is considered in this study when predicting the notched strength.

Similarly to other homogeneous materials, composite materials are manufactured

according to a particular geometry, which, in this study, includes specimens with a hole. However, manufacturing techniques include certain tolerances in the geometry that can potentially influence the material behavior. This study considers the dimensional tolerances of the hole drilled in the specimen and the width of the OH specimen.

5.2.1.2 Ply misalignment uncertainties

Composite materials exhibit an orthotropic behavior. However, by properly selecting ply angles and stacking sequence, a laminate composed of orthotropic plies can exhibit an isotropic in-plane behavior (quasi-isotropic laminate) or any other tailored (orthotropic or anisotropic) behavior. However, each ply in a laminate may exhibit deviations from the nominal material properties, from the nominal geometry or from the nominal orientation (see Fig. 5.2) [69]. In particular, the main factors contributing to ply misalignment can be summarized as:

- Imperfections in the alignment of fibers with the edges of the backing material, leading to potential errors in the alignment of templates used for ply cutting.
- Inherent difficulties in aligning and stacking the cut plies during the assembly process, resulting in alignment errors.
- During the curing process, plies may not be fully restrained, allowing for some degree of movement.
- Other defects, such as gaps and overlaps, can also contribute to increased misalignment, as noted by Nguyen et al. [127].

These deviations are likely to be random, normally distributed. However, some deviations, such as errors in the cutting or tape laying machine, would result in a systematic bias in the ply angle deviation [69]. Therefore, this study will take into account both the random deviations in individual plies and the inclusion of a bias factor in the most important load carrying plies, the 0° plies aligned with the loading direction.

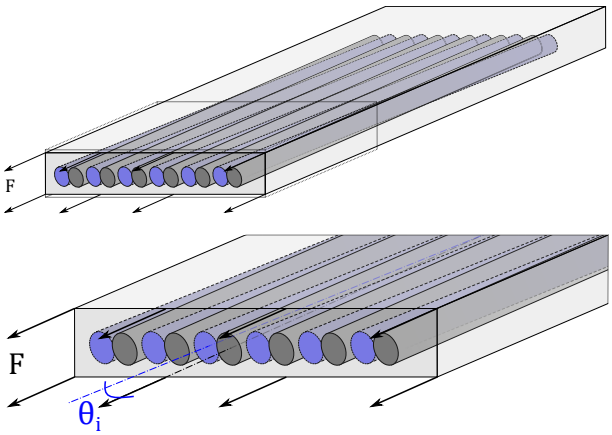

Figure 5.2: Representation of the ply deviation. In gray the fibers correctly aligned with the loading direction, whereas in blue are the deviated fibers accounting for ply misalignment.

5.2.2 Design of experiments: UQ&M input matrix

The uncertainty of the input parameters (the material and geometric variability and the presence of defects such as ply misalignment) is propagated to the notched strength to quantify their effect using the analysis models. To that end, a Monte-Carlo simulation (MCS) is carried out. The MCS relies on the repetition of random samples to obtain statistically representative numerical results. In other words, a sample is generated, where each specimen has different material properties, dimensions and ply misalignments.

5.2.3 Uncertainty propagation

In this study, an analytical model based on FFM will be used to obtain fast predictions of the notched strength and to propagate the uncertainties. However, it is worth mentioning that, due to the simplifying assumptions that enable an analytical or semi-analytical treatment of the equilibrium equations, this model possesses some limitations, e.g., in the representation of stacking sequence effects and in the representation of ply misalignments (low fidelity model). Therefore, a FEM model will be also developed to capture the onset and propagation of the different damage mechanisms and to obtain more accurate results, but also computationally more expensive (high fidelity model).

5.2.3.1 Finite fracture mechanics model (low fidelity)

Low fidelity models are efficient tools that offer reasonably good predictions, subjected to particular limitations and constraints. The analytical model employed in this study is founded on the principles of finite fracture mechanics. Hence, it assumes that the propagation of a finite crack results from the simultaneous fulfillment of a stress-based and an energy-based criterion. Furtado et al. [5] described a FFM model to calculate the notched strength of a CFRP laminate with only three material properties (the longitudinal Young's modulus (E_1), the fracture toughness ($\mathcal{G}_{IC}$) and the tensile strength (X_T)) based on the Trace theory and Master Ply concept [7] and on Omni Strain Last-Ply Failure envelopes [8]. Vallmajó et al. [117] utilized this analytical model to evaluate the derivation of design allowables. Furthermore, it demonstrated the suitability of the model for accommodating different loading directions. Therefore, in this study, it will be employed to account for ply misalignment.

The analytical model was thoroughly validated for quasi-isotropic laminates. More recently, Catalanotti et al. [128] developed a semi-analytical expression for the correction of the stress intensity factor for cracks emanating from circular holes taking into account the effect of geometry and orthotropy. Moreover, the orthotropy correction factor χ_i of each sub-laminate used in [5] was corrected [129, 130].

Nevertheless, this tool possesses some limitations that should be considered throughout the design process. First of all, the equations employed are only applicable to balanced laminates. Secondly, it does not account for delamination, i.e., it cannot predict the matrix failure between layers. Lastly, failure must be concentrated on a unique plane. In other words, it is assumed that damage initiates and propagates within the same plane.

The low fidelity model is implemented in a Python script which can be executed with minimal computational resources, enabling the rapid generation of a large amount of data within a short period of time.

5.2.3.2 Finite element model (high fidelity)

To overcome the constraints of the low fidelity model, a numerical model has been developed to determine the notched strength and investigate the failure mechanisms that lead to laminate failure. These FEM models rely on constitutive models developed through the principles of continuum damage mechanics. These models aid in characterizing the behavior of CFRP under different loading conditions and are capable of predicting damage initiation and evolution. Therefore, they enable the prediction not only of notched strength but also the understanding of the failure mechanisms that lead to the specimen failure.

The high fidelity model is developed in the finite element software ABAQUS/Explicit 6.14-2 [131]. The modeling strategy used to model the OH tensile specimen follows Furtado et al. [24]. Each ply is simulated using one 8-node linear brick reduced integration element (C3D8R) along the ply thickness and the plies are connected by 0.01 mm thick COH3D8 Abaqus cohesive elements. The laminate is clamped on one end while on the other a smooth displacement is applied to all nodes at the boundary (see Fig. 5.3). The mechanical behavior of the material is defined using a VUMAT subroutine based on Furtado et al. [24].

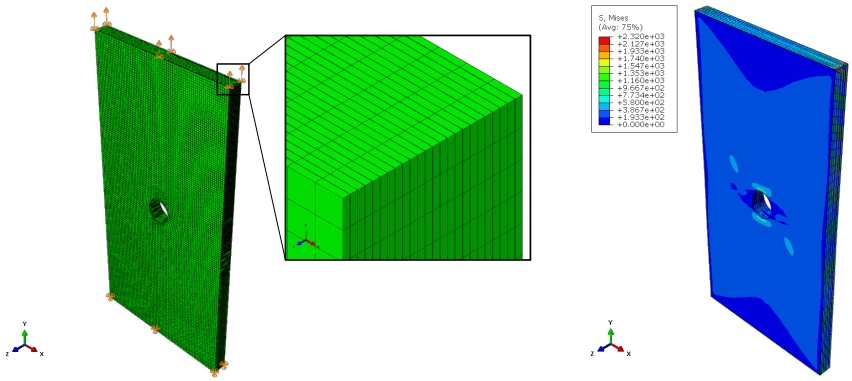

Figure 5.3: Modeling strategy of the OH specimen pointing out the mesh and boundary conditions and the results obtained in a representative simulation.

5.2.4 Virtual calculation of notched strength uncertainties

To address the influence of uncertainties and defects, a single, deterministic calculation is not enough. Consequently, statistically-based material parameters, known as design allowables, are used in the industry. The most commonly employed in the aeronautical industry is the B-basis value as proposed in the CMH-17 [1], which corresponds to the 95% lower confidence bound on the 10th percentile. The following procedure outlines the determination of the B-value implemented in this work:

1. Calculate notched strength values from multiple specimens, accounting for material and geometric uncertainties, as well as ply misalignment defects.

2. Identify and delete any potential outliers within the sample following the CMH-17 approach. An outlier is a result that exhibits a quantity of interest that is much lower or much higher than most other observations. Therefore, they are assumed to be erroneous values. In that case, the maximum normed residual method is used to screen and identify these extreme values. This method consists in comparing the deviation between each value and the sample mean considering the sample standard deviation.

3. Compute the 10th percentile with 95% confidence. This value is derived from the empirical cumulative density function (ECDF). However, it is important to note that obtaining an ECDF typically requires large sample sizes. This may not be practical for FEM analysis due to the associated computational costs. Therefore, for high fidelity analysis, the B-value is determined following the CMH-17 specifically and also compared with the 10th percentile obtained from the ECDF of the data generated.

5.3 Case study

This section describes the ply properties used in the low and high fidelity uncertainty propagation analyses and the uncertainties in the material properties, in the geometry and in the ply deviations (or misalignments).

5.3.1 Material selection and material properties

The proposed methodology can be applied to any CFRP. In this study, the IM7/8552 carbon/epoxy system is considered due to the availability of material properties and due to the fact that the models considered in the OH strength calculations had been previously validated with this material system. As mentioned in Section 5.2.3.1, the analytical model only requires three material properties which are summarized in Table 5.1. However, for the FEM analysis, more parameters are needed to account for the elastic, strength and fracture properties of both the fiber and the matrix of the material system (see Table 5.2). In both cases, it is assumed that the material properties follow a normal distribution.

Table 5.1: Material properties for the low fidelity model [117].

Input parameter for FEM analysis	Unit	Mean	CoV (%)
Ply longitudinal Young's modulus, E_1	GPa	171.42	1.39
Ply longitudinal tensile strength, X_T	GPa	2323.47	5.48
Ply longitudinal steady state fracture toughness, $\mathscr{R}_{ssT}$	N/mm	206.75	11.43

Table 5.2: Material properties for the high fidelity model [132].

Input parameter for FEM analysis	Unit	Mean	CoV (%)
Young's modulus in fiber direction, E_1	GPa	171.42	1.39
Young's modulus in matrix direction, E_2	GPa	9.08	1.03
Poisson's ratio in 1-2 plane, ν_{12}	-	0.32	6.18
Poisson's ratio in 2-3 plane, ν_{23}	-	0.487	2.20
Shear modulus in the 1-2 plane, G_{12}	MPa	5290	2.53
Longitudinal tensile strength, X_T	MPa	2323.50	5.5
Ratio of the first branch of tensile cohesive law, f_{XT}	-	0.40	8
Longitudinal compressive strength, X_C	MPa	1200.10	12.1
Ratio of the first branch of compressive cohesive law, f_{XC}	-	0.20	8
Transverse tensile strength, Y_T	MPa	62.30	8.5
Transverse compressive strength, Y_C	MPa	253.70	10.2
Longitudinal shear strength, S_L	MPa	92.30	3.1
Longitudinal tensile fracture toughness, $\mathscr{G}_{XT}$	kJ/m^2	133.30	5
Ratio of $\mathscr{G}_{XT}$ dissipated in the first branch, $f_{\mathscr{G}_{XT}}$	-	0.30	8
Longitudinal comprresive fracture toughness, $\mathscr{G}_{XC}$	kJ/m^2	61	2
Mode I interlaminar fracture toughness, $\mathscr{G}_{Ic}$	kJ/m^2	0.28	5
Transverse tensile fracture toughness, $\mathscr{G}_{YT}$	kJ/m^2	0.28	5
Transverse compressive fracture toughness, $\mathscr{G}_{YC}$	kJ/m^2	1.31	2
Mode II interlaminar fracture toughness, $\mathscr{G}_{IIc}$	kJ/m^2	0.79	18
Transverse shear fracture toughness, $\mathscr{G}_{SL}$	kJ/m^2	0.79	18
Strength in pure mode I, $Coh-t3$	MPa	62.30	5
Strength in pure mode II, $Coh-t1$	MPa	92.30	5
B-K exponent parameter for mixed mode propagation, BK_η	-	1.45	10

Concerning the geometry, a rectangular specimen with a central circular hole, subjected to tensile loading, is considered. The hole diameter-to-width ratio ($2R/W$) is $1/6$ and the hole diameter is 6mm. Furthermore, for a better understanding of the impact of ply misalignment, different configurations of balanced laminates, each consisting of 24 plies, were studied:

- Quasi-isotropic (QI) laminate: $[90, 0, -45, 45]_{3s}$
- Soft laminate: $[45, 90, -45, 90, 45, 90, -45, 0, 45, 90, -45, 90]_s$
- Hard laminate: $[45, 0, -45, 0, 45, 90, -45, 0, 45, 0, -45, 0]_s$

5.3.2 Discretization of defects

Ply misalignment refers to a deviation in the orientation of each individual ply within a composite structure. Instead of assuming a deterministic layup, variability in each ply orientation was introduced. While many companies agree that ply misalignment should be kept between 2° and 3° [69, 71, 133], it is noteworthy that deviations of up to 7° have been identified by the industry. To provide a comprehensive assessment of the effect of ply misalignment, this study considers deviations around 7°, although it is acknowledge as an extreme value. Ply misalignment is commonly assumed to follow a normal distribution. However, it can also be conceptualized as a tolerance which is randomly, uniformly distributed. Moreover, in cases where errors occur in the template alignment during the ply cutting or in the placement of each ply to build the laminate, this can introduce a bias deviation, leading to a specific ply deviation in all plies or just those using the incorrect template. Therefore, in this study, three different scenarios of misalignment are considered:

- Normal distributed ply misalignment with a STDV of 7° and a mean value of 0°.
- Uniformly distributed ply misalignment in the range $[-2 \times 7^\circ, +2 \times 7^\circ]$.
- A bias ply deviation of 7° for the 0° plies, in addition to a normal distributed ply misalignment with a STDV 7°.

Moreover it is worth mentioning that different considerations were applied for each modelling approach, linked to the constraints of the low fidelity model:

- The FFM model is valid for balanced laminates. Therefore, the ply deviations (θ_i) cannot be completely random for all plies in the laminate. Instead, only some ply misalignments are randomly generated, while some need to be adjusted accordingly to maintain the laminate balanced. For instance, for the QI laminate, only 5 different misalignment angles (θ_i) were introduced to ensure that the laminate remains balanced: $[90+\theta_1, 0+\theta_2, -45+\theta_3, 45-\theta_3, 90-\theta_1, 0-\theta_2, -45+\theta_4, 45-\theta_4, 90, 0, -45+\theta_5, 45-\theta_5]_s$.
- The FEM model does not have those constraints. Therefore, a random deviation has been considered for each ply in this case.

5.4 Results and discussion

5.4.1 Results comparison: FFM vs FEM

Before accounting for the effect of ply misalignment, the results obtained from the low and high fidelity models are compared with experimental results available for the QI laminate. The comparison between the analytical predictions, accounting for both material and geometric variability, and the experimental results was reported in [117]. Nevertheless, as mentioned in section 5.2.3.1, the analytical model has been further improved to consider the orthotropy of the laminate and it incorporates a corrected χ_i definition [129, 130]. The implementation is used to calculate 10 000 predictions (following the same strategy presented in [117]) to predict the mean and standard deviation (STDV) results. The FFM model is still subjected to certain constraints. Hence, in this study, FEM analysis is also conducted to provide more accurate predictions of damage onset and propagation. The modelling strategy based on FEM is used to generate 200 simulations to predict the mean value and STDV. The comparison of both results with experiments is presented in Fig. 5.4.

The results show that the analytical model predicts higher notched strength compared with the experimental results, with errors ranging between 13% and 23% according to the studied diameter. Yet, it is important to highlight that these analytical models are fast tools that aid in understanding the behavior of the composite structure and provide a first approximation of the notched strength, which can be valuable for preliminary assessments. The results obtained using

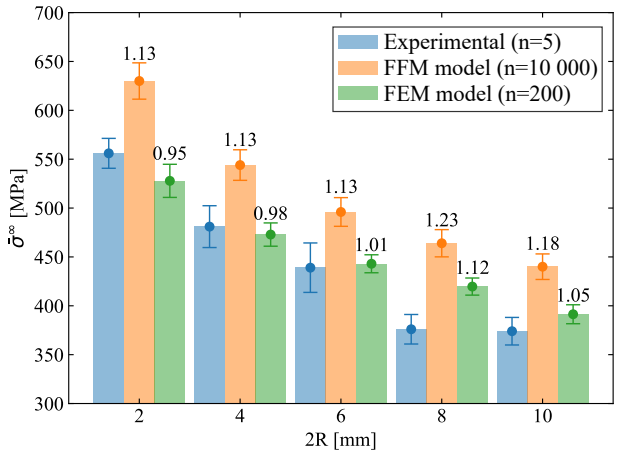

Figure 5.4: Comparison of the experimental results [134] with the analytical and FEM results. The values presented correspond to the ratio between the predicted mean value and the mean experimental value.

the high fidelity model exhibit a closer agreement with experimental data when compared with those obtained with the analytical model. As mentioned earlier, the low fidelity model has certain limitations and constraints. Notably, it does not account for delamination, leading to significantly higher values in the analytical model results. However, it is evident that delamination plays a significant role, as illustrated in Fig. 5.5.

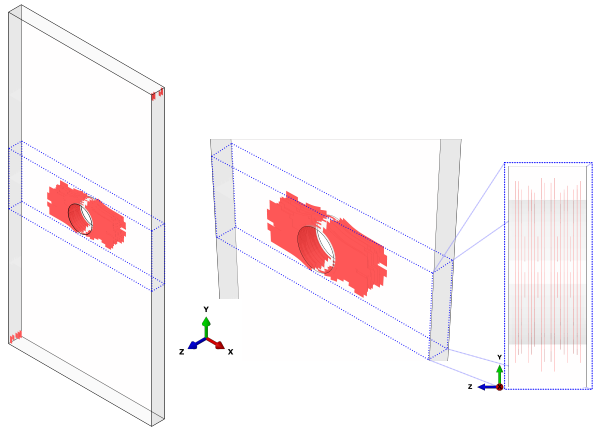

Figure 5.5: Delamination (in red), i.e., inter-ply damage, at the peak load predicted by FEM analysis for the QI laminate.

5.4.2 Determination of the sample size to account for ply misalignment

In accordance with the findings of Vallmajó et al. [117], it has been demonstrated that, for large samples, the B-basis value can be directly predicted as the 10th percentile. This is due to the minimal deviation in such cases, so the 95% lower confidence bound tends to the mean value. Considering this insight, this section incorporates a comprehensive analysis to determine the minimum number of samples for which the B-value can be approximated as the 10th percentile when also considering ply misalignment. Fig. 5.6 shows the error bars corresponding to one STDV of the mean values and of the B-values of the notched strength calculated from 10 groups of samples of n predictions.

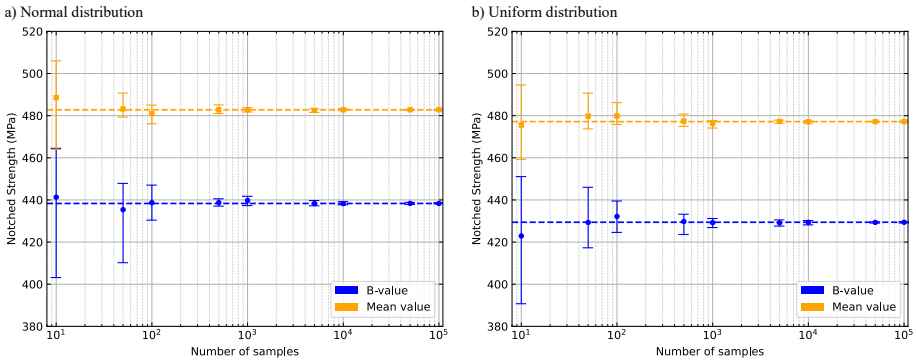

Figure 5.6: Average OH strength and 10th percentile from $N = 10$ samples of different size n using the analytical approach. Each sample considers material variability, geometric tolerances and random ply misalignments following a normal and uniform distribution, respectively.

The results demonstrate that when accounting for fiber misalignment, a sample size of 10 000 predictions is high enough for uncertainty propagation considering a normal distribution or a uniform distribution.

Regarding the FEM analysis, the sample size (n) was reduced due to the significantly higher computational costs. This reduction was determined following a balance between the accuracy of the results and the computational cost. Fig. 5.7 illustrates the predictions using different sample sizes, up to a maximum of 300 virtual specimens.

Consequently, a sample size of 200 values was considered suitable for the FEM analysis, since the mean value is close to the one obtained with 300 samples.

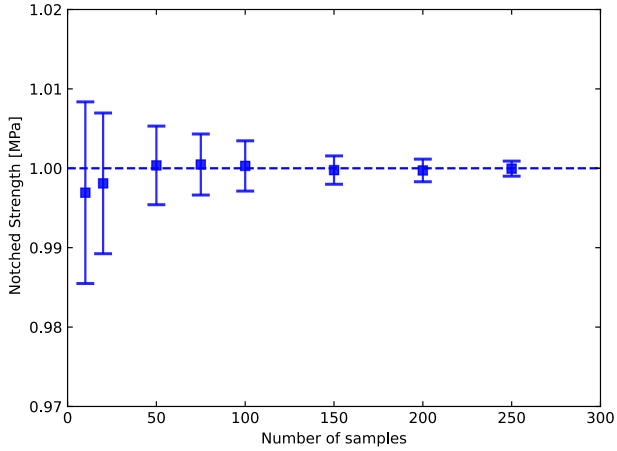

Figure 5.7: Average OH strength from $N = 10$ samples of different size n using the FEM approach. Each sample considers material variability, geometric tolerances and random ply misalignments following a normal and uniform distribution, respectively.

Moreover, the low STDV suggests that a plateau has likely been reached.

5.4.3 Effect of random ply misalignment

Both methods are now used to determine the effect of ply misalignment in all the scenarios considered in this study. The ECDF distribution of the results, the histogram, and the B-value prediction obtained from the FEM model and the analytical model are presented in Fig. 5.8 for the QI laminate and Fig. 5.9 for the hard and soft laminates.

As expected, when comparing the different laminates, the QI results fall between the hard laminate, which achieved the highest notched strength, and the soft laminate, with the lowest values. Fig. 5.10 presents the stress-displacement curves for the three studied laminates and the main failure mechanisms. As discussed in Section 5.4.1, the analytical predictions are higher than the numerical results because they solely consider fracture within the same plane, without accounting for delamination or other subcritial damage mechanisms. However, for the soft laminate, the prediction from the low fidelity model is lower than the value predicted by the high fidelity analysis. This can be explained by the presence of very few 0° plies, which are the main responsible for bearing the applied load, and a significant role of delamination and other subcritical damage mechanisms. In fact, the delaminated area of the soft laminate is 50% larger than that of the hard laminate, and 35% larger than that of the QI laminate. Consequently,

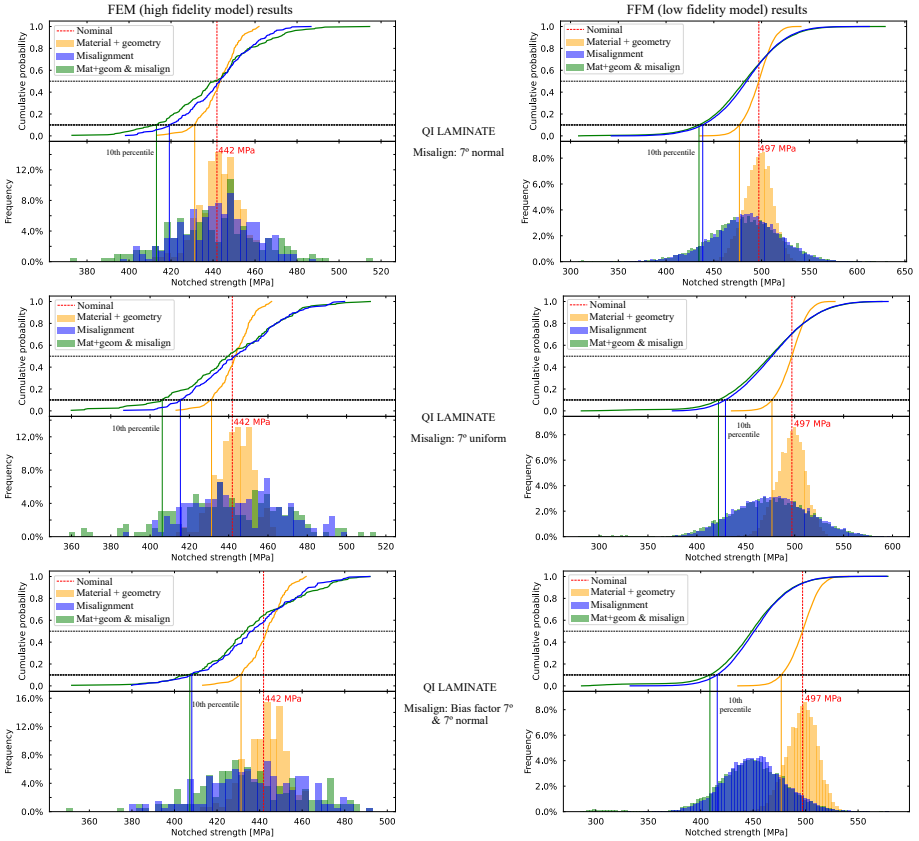

Figure 5.8: Distributions of the notched strengths and B-value for the quasi-isotropic (QI) laminate obtained by the FEM (left) and analytical models (right).

the distribution of the notched strength of the soft laminate obtained using the analytical model is not correct as can be identified in Fig. 5.8 and 5.9 where the ECDF when employing the analytical models exhibits a bimodal shape.

It can be concluded that, beyond the application domain, there are large differences between the analytical and the FEM results, whether in the nominal case or the stochastic analysis. This underscores the importance of recognizing the limitations of analytical models, even though they are valuable tools.

With both approaches, analytically and numerically, the B-value when incorporating ply misalignment is lower than when only considering material and geometric variability. That can be attributed to the increase in the STDV, i.e., the ECDF is wider. Moreover, in the analytical analysis, the distribution shifts to the left side when accounting for ply deviation, resulting in a lower mean

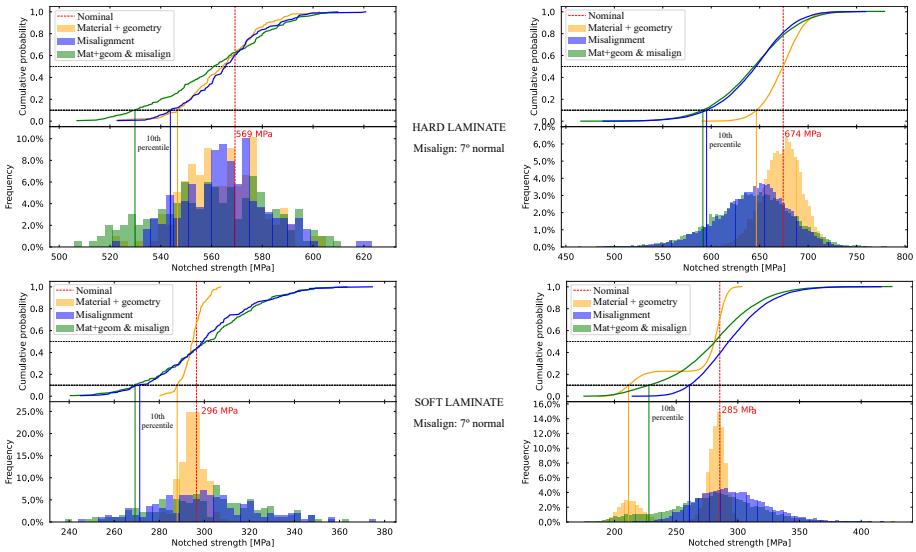

Figure 5.9: Distributions of the notched strengths and B-value for the hard and soft laminate obtained by the FEM (left) and analytical models (right).

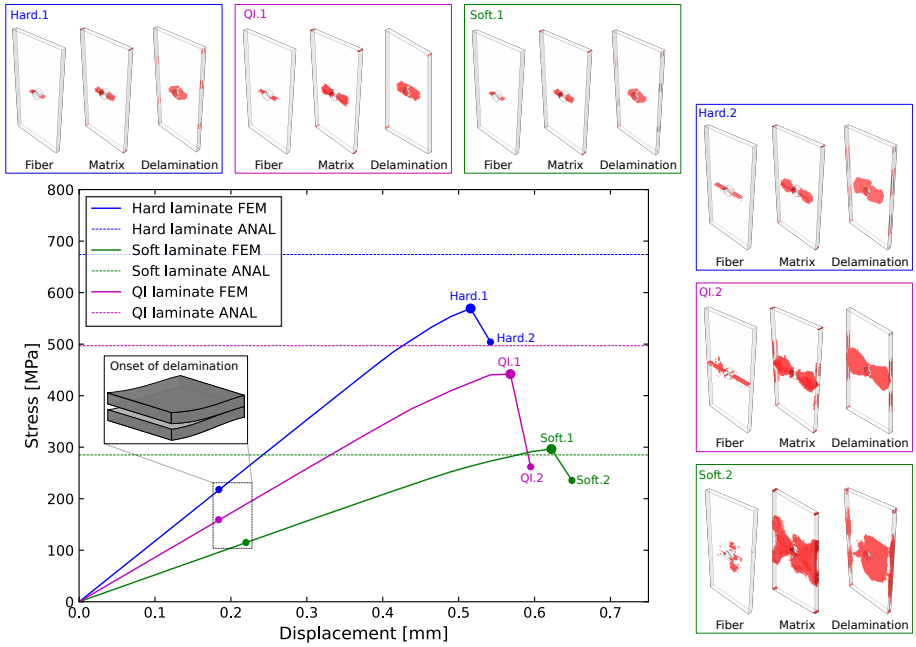

Figure 5.10: Stress-displacement curve and failure mechanisms (fiber and matrix intra-ply damage and delamination shown in red) predicted for the QI, soft and hard laminates.

value. Interestingly, despite the analytical nominal values being higher than those obtained by FEM, the B-values for the QI and hard laminates are more

conservative. In contrast, in the FEM analysis, the mean values remain almost constant for all scenarios, except when introducing a bias factor. In that last scenario, the mean value is lower when accounting for ply misalignment than when only considering material and geometric variability. The lowest B-value is always obtained when considering all the uncertainties simultaneously. This implies that each uncertainty contributes to the overall variability. However, the relationship of the density function when considering only one uncertainty versus the density function when considering that uncertainty along with another one does not follow a straightforward pattern.

To better discuss the results obtained numerically and analytically, Tables 5.3, 5.4 and 5.5 summarize the different deterministic and statistical measures of the predicted notched strength.

Table 5.3: Comparison of the analytical and FEM results considering material and geometric variability only.

Case Study	Analysis	Nominal value [MPa]	Mean value [MPa]	CoV [%]	10th percentile ECDF [MPa]	B-value CMH-17 [MPa]	B-value calc. difference [%]	B-value-to-mean ratio [%]	Ratio calc. difference [%]
QI laminate	FEM	442	443	2.1	431	427	-11.5	97	0.9
	Anal	497	496	2.9	477	476		96	
Hard laminate	FEM	569	564	2.6	547	543	-19.0	95	-0.4
	Anal	674	673	3.0	646	646		96	
Soft laminate	FEM	296	295	1.7	288	287	26.5	97	23.6
	Anal	285	266	11.3	211	211		74	

When only accounting for material and geometric variability, the difference between the B-values computed using the CMH-17 approach from both solutions exhibits a large discrepancy, with differences above 10%. This difference is even more pronounced for the soft laminate, because the analytical model does not provide good predictions. Nevertheless, when evaluating the ratio between the B-value and the mean value, the difference between the two cases is lower than 1%. Therefore, a valuable approach would be to predict the nominal value through the high fidelity analyses while determining the B-value by calculating the B-value-to-mean ratio with the analytical model.

Table 5.4: Comparison of the analytical and FEM results considering the effect of ply misalignment only.

Case Study	Analysis	Nominal value [MPa]	Mean value [MPa]	CoV [%]	10th percentile ECDF [MPa]	B-value CMH-17 [MPa]	B-value calc. difference [%]	B-value-to-mean ratio [%]	Ratio calc. difference [%]
QI laminate	FEM	442	441	3.9	419	418	-4.5	97	7.0
Normal, 7°	Anal	497	483	7.2	438	437		88	
QI laminate	FEM	442	445	5.1	415	412	-3.9	93	7.6
Uniform, 7°	Anal	497	477	7.7	429	428		86	
QI laminate	FEM	442	437	5.0	408	405	-2.5	92	8.9
Bias 7° + Normal, 7°	Anal	497	452	6.4	416	415		84	
Hard laminate,	FEM	569	566	2.9	544	542	-9.6	95	7.5
Normal, 7°	Anal	674	643	5.6	595	594		88	
Soft laminate	FEM	296	301	7.8	271	268	3.0	91	-0.8
Normal, 7°	Anal	285	265	13.9	261	260		91	

When only addressing ply misalignment, the error in the predicted B-value decreases. However, the analytical model predicts a notable decrease in the mean values, while the FEM outcomes exhibit similar mean values, except when introducing ply misalignment and a bias factor in the 0° plies. Furthermore, the STDV due to ply misalignments obtained from high fidelity analysis is higher than the STDV when considering material and geometric variability only. Consequently, the difference between the B-value-to-mean ratios obtained from the analytical or FEM models increases when considering ply misalignments.

Comparing the results when the misalignment is modeled with a normal or a uniform distribution, the latter exhibits larger variability due to the wider range of variance, resulting in a lower B-value. Moreover, when introducing a bias misalignment in all 0° plies, the mean value decreases leading to the lowest predictions.

Table 5.5: Comparison of the analytical and FEM results when considering material and geometric variability and ply misalignments.

Case Study	Analysis	Nominal value [MPa]	Mean value [MPa]	CoV [%]	10th percentile ECDF [MPa]	B-value CMH-17 [MPa]	B-value calc. difference [%]	B-value-to-mean ratio [%]	Ratio calc. difference [%]
QI laminate	FEM	442	441	5.1	413	408	-6.1	92	5.6
Normal, 7°	Anal	497	481	7.9	434	433		87	
QI laminate	FEM	442	440	6.3	406	400	-5.3	90	6.4
Uniform, 7°	Anal	497	474	8.9	422	421		85	
QI laminate	FEM	442	436	5.5	407	401	-1.7	91	9.5
Bias 7° + Normal, 7°	Anal	497	447	7.9	409	408		82	
Hard laminate,	FEM	569	561	3.9	530	529	-11.5	93	5.8
Normal, 7°	Anal	674	643	6.2	591	590		88	
Soft laminate	FEM	296	300	7.5	269	267	15.4	90	12.1
Normal, 7°	Anal	285	279	13.0	228	226		79	

Finally, when considering all differences, the distinctions between both analyses remain equivalent to considering ply misalignment only. In other words, the difference between the B-value-to-mean ratios obtained from the low and high fidelity models increases when considering ply deviation. This can be attributed to the impact of the fiber deviation on the damage mechanisms that trigger specimen failure. To further investigate this, a comparison between the stress-displacement curves and the main failure mechanisms for the QI laminate is presented in Fig. 5.11, considering material and geometry variability alone and also accounting for ply misalignment following a normal distribution.

For a more accurate analysis, the case with the highest strength (obtained when only considering material and geometry variability) is compared against the lowest one (when ply deviation is also taken into account). The results demonstrate a reduction in strength around 25% due to the absence of 0º plies

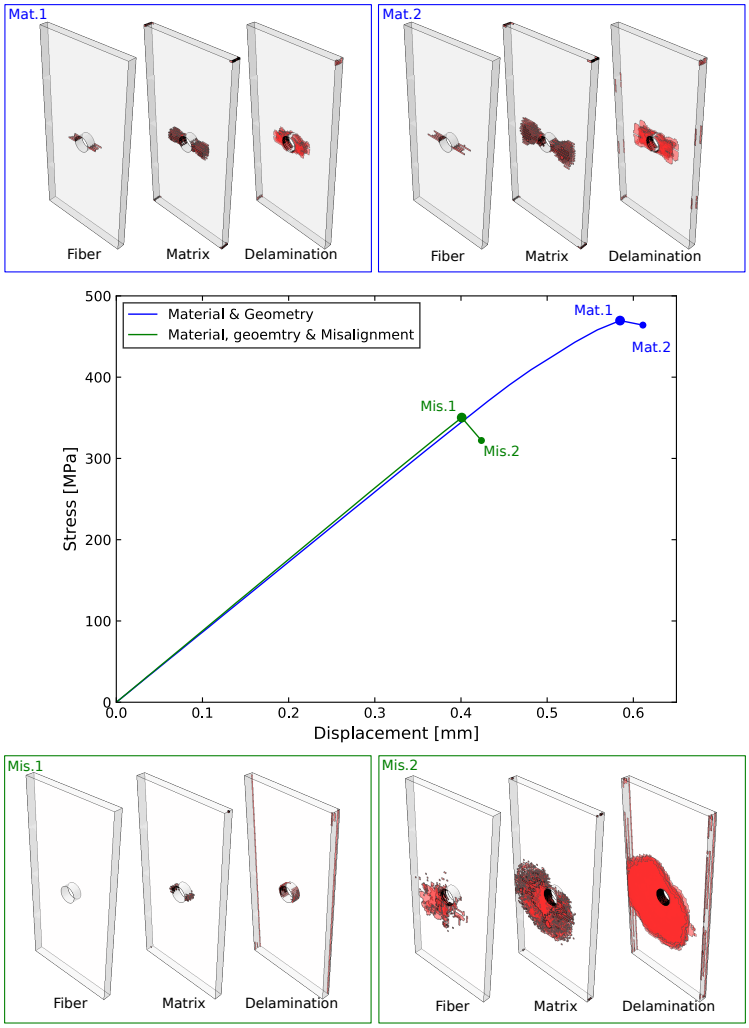

Figure 5.11: Stress-displacement curve and failure mechanisms (fiber and matrix intra-ply damage and delamination shown in red) predicted for the QI laminate when considering material and geometry variability (highest value in blue) and when also accounting for ply misalignment following a normal distribution (lowest value in green).

that can carry the applied load. Moreover, the comparison between fiber, matrix and inter-ply damage clearly shows that the specimen failure is more catastrophic when introducing ply misalignment, without following a clear pattern. However, when assuming the nominal laminate, there is fiber damage around the hole in the 0º plies, as expected [134]. Furthermore, this failure triggers delamination on the adjacent plies, leading to final failure of the specimen.

5.5 Conclusions

In this study, the use of analytical and numerical modelling and simulations approaches was exploited to assess the effect of meso-scale defects, specifically, ply misalignments in the calculation of design allowables of notched specimens. Different virtual specimens, considering both material and geometric variability as well as ply deviations were studied. This analysis involved the application of an analytical model and a FE numerical simulation employing the appropriate mechanical constitutive model. Therefore, a precise methodology has been described for the propagation of the aforementioned uncertainties to determine the notched strength of different laminates: quasi-isotropic, hard and soft.

Based on the nominal OH strength, the hard laminate, which is mainly composed of 0° plies, exhibits the highest resistance compared with the QI and soft laminates, which, in contrast, exhibit the lowest strengths. The analytical predictions for the hard and quasi-isotropic laminate are in good agreement with the numerical values, aligning well with the experimental data available for the QI laminate. In contrast, the soft laminate predictions with the analytical model are less accurate, due to the omission of delamination and other subcritical damage mechanisms, which, as revealed in the FEM analysis, play a major role on the failure development process. When introducing geometric and material variability, the uncertainty increases while the mean value remains constant. Moreover, when accounting for ply deviation, the uncertainties further increase. When comparing the predictions of the analytical and FEM models, the B-value-to-mean ratio are in good agreement, although the differences increase when introducing ply deviation due to changes in the damage mechanisms triggered by the absence of 0º plies.

To sum up, this study underscores the ability of analytical models, which are fast tools, to predict the notched strength while accounting for material and geometric variability, as well as ply misalignment. These analytical tools can be valuable as a guideline in the preliminary design of composite structures. On the other hand, FEM simulations provide more accurate results and offer insights into the failure mechanisms responsible for laminate failure. Therefore, it is crucial to establish the necessary level of accuracy required during the design stage. Additionally, considering a hybrid approach may be useful, given that

FEM predictions offer great accuracy in determining the mean values, while fast analytical models can be used to determine the allowables thanks to good predictions of the allowable-to-mean ratios.

6

Paper D – Micromechanical analysis of composite materials considering material variability and microvoids

The paper has been published in *International Journal of Mechanical Sciences.* 263 (2024) 108781

Overview

Previous studies underscore the need for accounting for the intrinsic material variability within composite structures. This entails a comprehensive characterization of the material properties essential for feeding computational models.

Therefore, it is important to understand the origin of this variability. In this thesis, the focus is on composite structures with carbon fibers embedded in a thermoset polymer matrix. Consequently, these two constituents stand out as the primary sources of variability. Analysing each material independently proves more feasible than characterizing the entire assembly, given the greater number of influential parameters.

Micromechanical models emerge as a powerful tool to describe the mechanical behavior of materials at the microscopic level. It focuses on understanding how the individual constituents, such as fibers and matrix, interact to influence on the overall mechanical properties.

Additionally, at the micro-scale, the influence of defects, particularly voids, significantly contributes to the variability in the properties of composite structures. Recognizing the possible inevitability of voids at this scale, it becomes imperative to incorporate their presence into predictions of material variability. This acknowledgment enhances the comprehensiveness of the analysis and ensures a more accurate understanding of the factors affecting the mechanical behavior of composite structures.

Hence, this research paper proposes an innovative methodology employing an enhanced micromechanical model to determine the elastic mesoscale properties and their associated uncertainties. The proposed approach involves a robust characterization of constituents and defects, typically provided by the material supplier themselves. Consequently, this work serves as a powerful tool for acquiring essential parameters needed to input data into more complex models. By focusing on simple homogeneous materials, which are comparatively easier to obtain, the methodology facilitates the extraction of critical parameters, enhancing the efficiency of larger-scale models, as well as the prediction of the effect of manufacturing defects at larger-scales.

Micromechanical analysis of composite materials considering material variability and microvoids

O. Vallmajó[a,*], A. Arteiro[b,c], J.M. Guerrero[a], A.R. Melro[d], A. Pupurs[e], A. Turon[a]

[a] *AMADE, Polytechnic School, Universitat de Girona, Campus Montilivi s/n, E-17003 Girona, Spain*

[b] *DEMec, Faculade de Engenharia, Universidade do Porto, Rua Dr. Roberto Frias, 4200-465 Porto, Portugal*

[c] *INEGI, Rua Dr. Roberto Frias, 400, 4200-465 Porto, Portugal*

[d] *ACCIS, Bristol Composites Institute, University of Bristol, Queen's Building, BS8 1TR, UK*

[e] *LEMM, Laboratory of Experimental Mechanics of Materials, Riga Tehcnical university, Riga, LV-1048, Latvia*

Abstract

One of the main challenges for fiber-reinforced polymers (FRP) is the difficulty to predict their mechanical behavior. At the microscale, the properties of the constituents, their spatial distribution and the defects arising from manufacturing affect the mechanical behavior. In this work, statistically representative volume elements (SRVEs) are proposed based on a micromechanical finite element model to determine the effect of content, distribution and size of microstructural defects and, material uncertainties on the elastic mesoscale properties of FRPs. To that end, different cylindrical void sizes are considered as well as irregular shaped voids between fiber tows (inter-fiber voids). Fibers and voids are randomly distributed in a SRVE. An uncertainty quantification and management analysis is employed to obtain statistical descriptors of the effective mesoscale mechanical properties of FRPs. The results obtained are compared with analytical models. It is demonstrated that, for carbon fiber/epoxy composites, SRVEs with lateral dimensions equivalent to 15 times the average fiber diameter and a length of 0.01 mm along the longitudinal direction remain statistically

* Corresponding author

Paper published in: *International Journal of Mechanical Sciences (2023)*
Doi: https://doi.org/10.1016/j.ijmecsci.2023.108781

representative with or without the presence of voids. The results show that the presence of voids reduces the transverse and shear elastic properties of FRPs. The smaller the voids are, the bigger is the reduction. Regarding the presence of inter-fiber voids, the reduction is lower. This trend is well predicted by the Mori-Tanaka mean field theory. However, the relative difference between the numerical and the analytical predictions increases for high void volume fractions. Regarding the effective longitudinal Young's modulus, the rule of mixtures, the Mori-Tanaka mean field theory and the concentric cylinder assembly model provide similar predictions for the mean value, but the uncertainty is overestimated by the analytical models because the properties of the fibers take a single value for each calculation with the analytical model, while they more realistically change from fiber to fiber in the numerical SRVEs.

keywords: Fiber reinforced polymers (FRP), Microvoids, Mechanical properties, Micro-mechanics

6.1 Introduction

Composite materials are of special interest in modern industry due to their excellent specific mechanical properties. However, the brittle nature of polymer composites means that failure initiates from a stress raiser. This can be a geometrical feature, e.g., a hole, damage, e.g., impact on a surface, or the presence of defects, e.g., the existence of voids. In fiber-reinforced polymers (FRPs) there are many defects related to the constituents: fiber defects, such as fiber degradation or in-plane misalignment, matrix defects, such as porosity or contaminants, and fiber-matrix defects, such as debonding or poor wetting of the fibers [44]. Voids are among the most important defects since they affect a wide range of composite properties and they tend to be common in many different manufacturing techniques [46, 47].

Voids can usually be defined as cylindrical branch-type defects generally aligned with the fiber direction [48]. The main sources of porosity in composite materials are air entrapment during the initial manufacturing stage and volatile components or contaminants generated during curing [49]. Voids may be present in a composite with different sizes, shapes and content. When studying macrovoids in carbon/carbon composites, Drach et al. [50] showed that, in unidirectional

composites, assuming voids aligned with the fibers and extending continuously with constant cross-section may significantly overestimate the longitudinal and slightly underestimate the transverse stiffness of the material when compared with irregularly shaped macrovoids. On the other hand, parallel 2:1 spheroidal voids randomly distributed in the same transversely isotropic matrix result in closer predictions of the effective moduli. In the present study, however, focus will be given to the presence of voids at the level of the constituents, linked to the occurrence of porosity at the microscale. Most of the authors found, by 3D micro-CT scanning, that microvoids have a rod-like geometry oriented along the fiber direction [51–62]. Regarding the cross-section, some microvoids present an irregular shape which, for the sake of simplicity, can be fitted into a circle [61, 62, 135], whereas others are almost circular [59, 63]. These microvoids typically have an equivalent diameter of 3 to 20 μm [57–60] even for thermoplastic matrices [136]. Vajari et al. [59], Hyde et al. [63] and Daggumati et al. [64] concluded that, microvoids whose size is comparable with the fiber diameter are present in a composite between fiber clusters with an irregular shape, since the matrix cannot easily flow-in during manufacturing. They also concluded that microvoids can be present as small air bubbles being trapped in the matrix.

Several studies have been focused on the effect voids have on the mechanical properties of FRPs. Experimentally, Almeida and Neto [65] determined that voids have a high detrimental effect on the fatigue life of composite structures. Chambers et al. [60] found that an increasing void content reduces the flexural strength and the fatigue performance acting on the initiation and propagation of failure mechanisms. Zhu et al. [55] concluded that cracks emanate from the voids and so both tensile strength and modulus decrease. Finally, Chu et al. [66] also observed that porosity have a detrimental effect on the transverse and shear moduli, whereas the effect on the longitudinal properties is much lower.

Accurate numerical simulations, with advanced constitutive models, can help understand the mechanical behavior at the microscale (constituents level) and their effect on the mesoscale properties (ply level). Melro et al. [78] defined a methodology to generate a micromechanical 3D representative volume element (RVE) containing randomly distributed fibers in accordance to the fiber volume fraction. Tavares et al. [94] extended this version of the random fiber generator to obtain the microstructure of a composite material with different types of fibers,

i.e., a fiber-hybrid composite. In the present work, this methodology is further extended to take into account the presence of voids. To that end, an RVE of the composite material with defects needs to be defined. That is, a sample that is structurally entirely typical of the whole mixture on average and contains a sufficient number of inclusions to be effectively independent, so that the results are macroscopically uniform [137].

The analysis of the effect of matrix voids using computational micro-mechanics is not new. Previous studies include the work of Vajari et al. [59], where 2D numerical simulations were performed considering elongated voids parallel to the fiber direction with a circular cross section. Inter-fiber voids with an irregular shape were also considered. Dong [95] studied the effect of randomly distributed voids on the stiffness and strength of FRP also comparing the results with analytical models. Mehdikhani et al. [46, 62] also simulated the effect of microvoids on the elastic moduli of carbon fiber reinforced polymers considering a single ellipsoidal void embedded in the matrix. These voids will be simply referred to as ”matrix voids”. Hyde et al. [58, 63] used a micromechanics-based finite element modeling strategy to study the effect of a single matrix or inter-fiber void on the strength of composite structures. Sharifpour et al. [96] developed a 2D micromechanical model to assess the effect of microvoids on the local stress state, with a circular shape, in a cross-ply laminate. Chu et al. [66] studied the influence of voids on the stiffness properties of unidirectional FRPs, considering very small spherical voids. More recently, Daggumati et al. [64] checked the effect of matrix and inter-fiber voids, as well as other geometrical and material features such as thermal residual stresses and the random spatial distribution of the reinforcements, in a 2D cell under a transverse loading state. Vinot et al. [97] developed a model to quantify uncertainties, e.g., porosity, in continuous unidirectional composites and evaluate their influence on the mechanical properties of the material. However, to the authors' best knowledge, all the current literature studies have not taken into account simultaneously the random spatial distribution of the constituents, the variability in their properties and the variability of the characteristics of microvoids in the definition of statistically representative volume elements (SRVEs) for fiber-reinforced polymers.

In the design of composite structures it is also important to take into account the uncertainties in the design parameters, arising, for example, from the scatter in

the material properties. Vallmajó et al. [117] defined a methodology to account for the uncertainty of an open-hole specimen by calculating analytically B-value design allowables through Monte Carlo simulation (MCS). The B-value is a statistically-based design allowable, recommended by the Composite Materials Handbook (CMH-17) [1], and defined as the 95% lower confidence bound on the tenth percentile of a specified population of measurement. Cózar et al. [125] also created a methodology to calculate the B-value from a high-fidelity numerical model creating a response surface of the results and, afterwards, performing a MCS. These strategies rely on input material properties at the ply level, and their uncertainties, characterized by experimental results to, finally, obtain the B-value allowables. However, contribution to uncertainty is not only based on the scatter in the material properties, but also from the presence of defects and their characteristics. Currently, there is a lack of studies considering the definition of SRVEs that, besides the random distribution of the reinforcements, also take into account the uncertainty of the material properties as well as the presence of defects. Therefore, SRVEs are generated herein that account for the effect of the uncertainties related to void content, distribution and size, and for the effect of the uncertainties of material properties on the elastic mesoscale properties of a carbon fiber reinforced polymer (CFRP). The methodology proposed in this work can be used to guide the quantification of uncertainties at the micro-scale, for example, to help defining knock-down factors for the effect of voids and void content, or to generate statistically representative material allowables to be used in analysis methods at the meso and macroscales. Rather than simply providing deterministic predictions of effective properties (and strengths), this methodology will enable the calculation of reliable statistical descriptors, herein focused on the effective elastic properties, but with the possibility to be extended to the stochastic prediction of damage initiation and propagation. This first step considering only the effective elastic properties will allow the assessment of the proposed approach with alternative methods, incl. well established analytical models.

The paper is organized as follows: Sect. 2 shows the methodology followed to generate, simulate and post-process the results from an RVE with the presence of defects; Sect. 3 describes the composite material and defects considered in this study; Sect. 4 presents the results and their discussion; finally, Sect 5. summarizes the conclusions of this work.

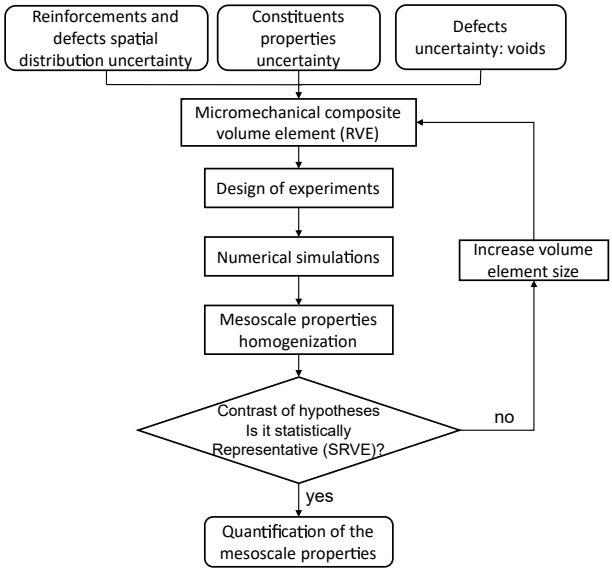

Figure 6.1: Flow chart of the propagation of the uncertainties related to a composite structure to quantify their effect on the elastic mesoscale properties of the composite.

6.2 Methodology

In this work, an exhaustive methodology is proposed to define SRVEs and determine the elastic properties of FRPs accounting for the uncertainty due to the material and geometric variability in the constituents, their spatial distribution and the presence of defects, in the form of matrix and inter-fiber voids. The flow chart in Figure 6.1 shows the uncertainties propagation procedure followed in this study, as described in the following sections.

6.2.1 Composite microscopic uncertainties

In previous studies addressing the effect of the presence of microvoids on fiber-reinforced composite systems [46, 52, 64, 66, 138], the determination of the elastic properties did not account for the uncertainties associated with the intrinsic variability of the constituent properties, their spatial distribution and the characteristics of this class of defects.

6.2.1.1 Reinforcement and defects spatial distribution uncertainty

The reinforcements of FRPs are randomly distributed inside a ply. In addition, the distribution of the defects also does not follow a deterministic dispersion. Therefore, their random spatial distribution is taken into account in this study when generating the micromechanical model.

6.2.1.2 Constituent properties uncertainty

The different materials present in a composite system exhibit an intrinsic variability in their properties. Moreover, the size of the fibers are not constant. Therefore, the variability in the properties of the constituents and in their geometrical parameters, such as the fiber diameter, is taken into account in this study to quantify the elastic material properties of the composite.

6.2.1.3 Defects uncertainty: Voids

In the present work, following the data available from the literature (see Section 6.1), all voids are assumed to be aligned with the fiber direction (see Figure 6.2).

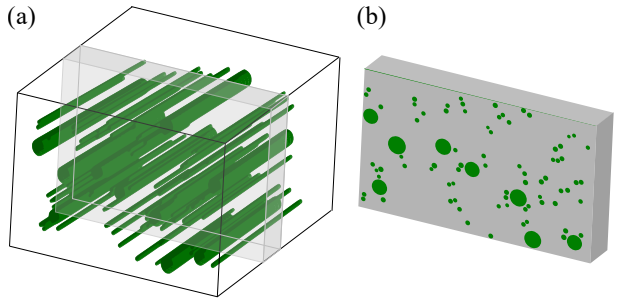

Figure 6.2: A schematic 3D representation of voids inside a unidirectional ply obtained from micro-computed tomography in the literature [51, 61, 62, 136] (a) and the corresponding representative volume element considered in this study (b).

Looking to the literature, most authors agree that voids can be represented with a circular cross-section. Moreover, in this study optical microscopy images were analysed to characterize typical voids in glass/epoxy cross-ply laminates manufactured using pre-preg lay-up. Optical microscopy images were taken observing polished specimen edges with magnification of 200x. It is assumed that the typically observed shape and distribution of voids in glass/epoxy composite

shown in Figure 6.3a also applies for carbon/epoxy composites analysed in this study. The images support that porosity appears as voids with a circular shape entrapped in matrix-rich regions or as voids with an irregular shape within the fiber tows. Therefore, this study is focused on these two types of voids: matrix voids and inter-fiber voids. Moreover, in addition to the position of the voids, the effect of their size is also considered. According to the size, voids could be classified as voids with a diameter smaller than the fibers (small matrix voids) or voids with a larger diameter (large matrix voids), as shown in Figure 6.3b. It is important to note that, in this study, ”small” and ”large” voids (Figure 6.3b) refer simply to the relative size of the voids when studying the influence of their size (considering the relative size of the fibers just as a reference), and not to an absolute measure.

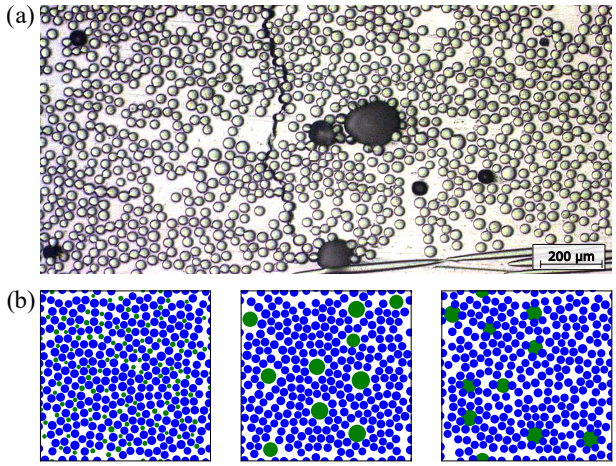

Figure 6.3: (a) Image from optical microscopy with the presence of voids in dark color and (b) the corresponding RVEs (in blue the fibers and the white region is the matrix) with the presence of three types of voids (in green). From left to right: matrix voids with a diameter smaller than the fibers (”small” matrix voids), matrix voids with a larger diameter (”large” matrix voids) and voids that intersect with the fibers (inter-fiber voids).

Void content is calculated as the void volume fraction in FRPs, e.g., following the ASTM D2734 standard that compares the theoretical and the measured composite density [139]. Although porosity should not exceed 1% for high-perfomance laminates and a void content greater than 5% for a composite is not acceptable in most industries, this work addresses void contents ranging up to 10% to characterize their effect in a wider range, including some of its highest and critical values reported in the literature [58, 61, 66, 140].

6.2.2 Micromechanical model with voids

In the following, the approach followed to generate the micromechanical finite element model including all uncertainties taken into account in this study, described in Section 6.2.1, is summarized.

Generation of an RVE The micromechanical model proposed by Melro et al. [78] to randomly distribute the fibers in an RVE and extended by Tavares et al. [94] to be able to define different types of fibers was modified to accurately represent an RVE with voids. The algorithm has been enhanced to generate voids with cylindrical shape parallel to the fiber direction, randomly distributed in the RVE. Two different populations are defined. The first one represents the fibers with its own geometrical properties, uncertainties and volume fraction. The second population includes the voids, which also have their own properties and uncertainties.

The algorithm consists of the following steps:

1. Hard-core model to randomly distribute the constituents in the RVE. Therefore, in this first step, the model simply generates randomly new fibers and voids in the RVE. These are accepted on the RVE depending on a distance criterion that checks if these overlap with other fibers or voids. This criterion is different for fibers and voids as will be clarified later.

2. First Heuristic to move closer the fibers and voids between them to gain more empty areas to fill afterwards.

3. Second Heuristic to move the constituents on the outskirts towards the center of the RVE and compact them for generating matrix-rich regions.

The use of the heuristics allows reaching fiber volume fractions over 65% [78]. After these steps, the model starts a new iteration and repeats all the steps to add more fibers and voids until the desired volume fraction is achieved. In-deep details about these steps can be found in Ref. [78]. Overall, the model has the following abilities:

- Adding either fibers or voids according to the RVE size and their volume fractions.

- Defining a mean value and standard deviation for the diameters of the fibers and voids to account for the uncertainties related to their size.

- Defining three different minimum distances while placing the fibers and voids. One between fibers, another between fibers and voids and, finally, between voids. Thus, the algorithm can generate different types of voids: voids embedded in matrix-rich regions or inter-fiber voids which overlap with the fibers. These distances are defined as the mean radius of two consecutive circles of radius r_i and r_{i+1}, respectively, multiplied by a different constant value (k) for each minimum distance previously described ($k_{fiber-fiber}$, $k_{fiber-void}$ and $k_{void-void}$, respectively). Hence, the minimum distance between two of these features is calculated as $k \times (r_i + r_{i+1})/2$. For the case of inter-fiber voids, the distance between fiber and void is negative to allow the overlap between them, thus $k_{fiber-void} < 0$. Instead, for the matrix voids, this distance must be larger than 0 since no overlap is permitted.

- Generating fiber-rich regions (fiber clusters) where fibers are more compacted.

Thus, different categories of RVEs with voids can be generated (see Figure 6.3) to assess the effect of shape and size of the voids, for example: i) matrix voids with a diameter smaller than the fibers (small matrix voids); ii) matrix voids with a diameter larger than the fibers (large matrix voids); iii) voids that intersect the fibers (inter-fiber voids).

To avoid the appearance of zero-volume elements when meshing the RVE, the algorithm was modified to force that fibers and voids close to the boundaries of the RVE remain, at least, at a distance from the boundaries equal to the average size of the matrix finite elements. Likewise, the fibers and voids cut by the RVE boundaries are cut, at least, at a section as large as their corresponding mesh size.

Modeling strategy. Once the RVE is generated according to the size, fiber volume fraction, void volume fraction and their respective diameters and variation, it needs to be discretized and analyzed using the Finite Element Method (FEM). Figure 6.4 shows the sequence of steps used to generate the FEM model of the RVE. It can be summarized as follows:

a Creation of each part, i.e., each fiber, each void and the matrix, independently as a plate, i.e., in two dimensions (2D).

b Assembly of all the plates and mesh of the whole model, with the possibility of defining a different mesh size for each constituent (fiber, matrix and defect). The element mesh shape is defined as quad-dominated. Thus, almost all the elements are quadrangular except in some regions where triangular elements are included. Linear elements with reduced integration are used.

c Extrusion of the mesh to convert each plate to a three-dimensional (3D) part. This strategy is followed to ensure that there is a mesh continuity in the longitudinal direction as done in previous works [138]. Hence, the periodic boundary conditions can be implemented afterwards without any problem. After the extrusion, the majority of the elements are C3D8R which correspond to linear brick elements with reduced integration, whereas in some regions the elements are C3D6 which correspond to linear triangular prism elements.

d Determination of each surface from each 3D part to define the constraints between the materials.

e Assembly of all 3D parts. The fibers and the matrix are connected with contact interactions, which adds the possibility of representing fiber-matrix debonding by employing cohesive surfaces, while the voids are assumed to be perfectly bonded to the matrix and fibers by defining contact interactions with a high penalty stiffness. It should be noted that tie constraints cannot be used since this would lead to over-constraining some nodes (the ones in the boundaries) with more than one equation: one for the periodic boundary conditions and another for the tie constraints.

f Implementation of the periodic boundary conditions (PBC) to link nodes

in opposite faces, edges or vertices, while the micromechanical model is generated to guarantee that the RVE is geometrically and materially periodic [141]. In other words, if a fiber crosses the boundary of an RVE, the external part must be cut and moved to the opposite side keeping the same material properties. Thus, the periodicity of stress/strain field is ensured. A set of constraint equations is defined between all the nodes at the boundaries of the RVE along all degrees of freedom, through a dummy node where the far-field strain is applied (see Figure 6.4f). For the complete set of equations defining the PBC, the reader is referred to Ref. [141]. To prevent rigid body motion (RBM) a random node in the middle of the RVE is fixed.

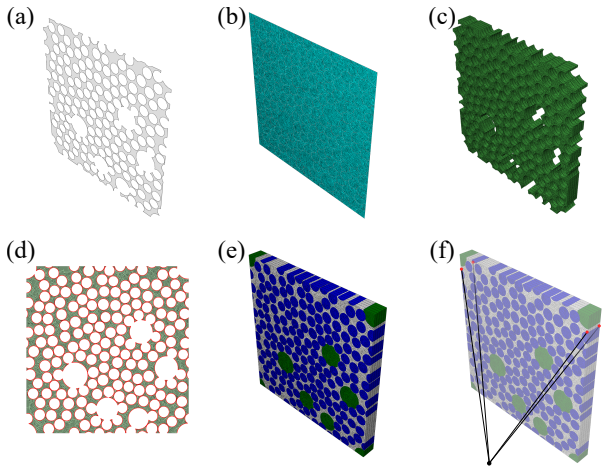

Figure 6.4: Steps to model the RVE: (a) creation of each part as a plate, (b) assembly of all the parts and meshing, (c) extrusion of the mesh and conversion to 3D parts, (d) creation of each surface to define the contacts between materials, (e) assembly of all 3D parts, and (f) example of application of the periodic boundary conditions in a specific node linked with the dummy node where the far-field strains are applied.

6.2.3 Design of experiments

Once the micromechanical RVE is created, the uncertainty of the input parameters, i.e., the variability in the constituents, the random spatial distribution and the presence of voids, is propagated to the mesoscale elastic properties (engineering constants) to quantify their effect. To that end, an MCS is carried out. The MCS relies on the repetition of random samples to obtain statistically relevant results. In other words, a sample with n RVEs is created, where each RVE has different material properties, random spatial distribution of the constituents and

random distribution of the different types of voids, and it is analyzed to obtain the distribution of the homogenized elastic material properties. The constituent properties are generated following a statistical distribution. In each RVE, the fibers are generated with different dimensions and properties according to their input distributions. The matrix properties also change, but from RVE to RVE, according to their corresponding input distributions.

6.2.4 Numerical simulation

The micromechanical model is simulated using the finite element software ABAQUS/Standard 6.14-2 [131]. To determine the effective elastic properties of the composite system, far-field strains of 0.001% were applied, and the stress and strain fields in the RVE post-processed (see Sect. 6.2.5).

6.2.5 Mesoscale properties homogenization

The uncertainties present in composite systems may be taken into account while predicting the elastic properties. According to the CMH-17 [1], the elastic properties should be defined with its mean and standard deviation. Therefore, from each simulation, the elastic properties of a composite material and their corresponding uncertainty are determined using a first-order homogenization technique.

6.2.5.1 First-order homogenization

The elastic properties of a composite material can be determined using a first-order homogenization technique. The Hooke's law for transversely isotropic materials can be defined as:

$$\begin{Bmatrix} \bar{\sigma}_{11} \\ \bar{\sigma}_{22} \\ \bar{\sigma}_{33} \\ \bar{\sigma}_{12} \\ \bar{\sigma}_{13} \\ \bar{\sigma}_{23} \end{Bmatrix} = \begin{bmatrix} C_{1111} & C_{1122} & C_{1122} & 0 & 0 & 0 \\ C_{1122} & C_{2222} & C_{2233} & 0 & 0 & 0 \\ C_{1122} & C_{2233} & C_{2222} & 0 & 0 & 0 \\ 0 & 0 & 0 & C_{4444} & 0 & 0 \\ 0 & 0 & 0 & 0 & C_{4444} & 0 \\ 0 & 0 & 0 & 0 & 0 & \frac{C_{2222}-C_{2233}}{2} \end{bmatrix} \begin{Bmatrix} \bar{\varepsilon}_{11} \\ \bar{\varepsilon}_{22} \\ \bar{\varepsilon}_{33} \\ \bar{\varepsilon}_{12} \\ \bar{\varepsilon}_{13} \\ \bar{\varepsilon}_{23} \end{Bmatrix} \tag{6.1}$$

where $\bar{\sigma}_{ij}$ represents the volume average of the ij stress component, C_{iijj} are the stiffness tensor components and $\bar{\varepsilon}_{ij}$ is the volume average of the ij strain com-

ponent. From the stiffness tensor components, the five independent engineering constants and the transverse Poisson's ratio, can be calculated as:

$$\begin{aligned} E_1 &= C_{1111} - \frac{2C_{1122}^2}{C_{2222}+C_{2233}} \\ \nu_{12} &= \frac{C_{1122}}{C_{2222}+C_{2233}} \\ E_2 &= C_{2222} + \frac{C_{1122}^2(C_{2233-C_{2222}}) + C_{2233}(C_{1122}^2 - C_{1111}C_{2233})}{C_{1111}C_{2222}+C_{1122}^2} \\ G_{12} &= C_{4444} \\ G_{23} &= \frac{C_{2222}-C_{2233}}{2} \\ \nu_{23} &= \frac{C_{1111}C_{2233}-C_{1122}^2}{C_{1111}C_{2222}-C_{1122}^2} \end{aligned} \tag{6.2}$$

where E_1 and E_2 are the longitudinal and transverse Young's moduli, G_{12} and G_{23} are the longitudinal and transverse shear moduli, ν_{12} is the major Poisson's ratio, and ν_{23} is the transverse Poisson's ratio. For a given applied far-field strain ε_{ij}^0, the volume average strain components can be calculated as:

$$\bar{\varepsilon}_{ij} = \frac{1}{V}\int_V \varepsilon_{ij} dV = \varepsilon_{ij}^0 \tag{6.3}$$

and the volume average stress field as:

$$\bar{\sigma}_{ij} = \frac{1}{V}\int_V \sigma_{ij} dV \tag{6.4}$$

Therefore, since the stiffness tensor is symmetric (Eq.(6.1)), and taking into account Eq.(6.2), applying ε_{11}^0, ε_{22}^0 and ε_{12}^0 far-field strains is sufficient to determine the components of the stiffness tensor and, consequently, all the homogenized elastic material properties.

The results of the computational micromechanics model obtained from first-order homogenization are compared with the results calculated analytically using the rule of mixtures (RoM), the Mori-Tanaka theory and the concentric cylinder assembly (CCA) model.

6.2.5.2 The Rule of Mixtures

The Rule of Mixtures (RoM) provides reasonable values for the longitudinal stiffness (E_1) assuming that the fibers and the matrix are working in parallel:

$$E_1 = V_f E_{1f} + V_m E_m \tag{6.5}$$

where V_f is the fiber volume fraction and V_m is the matrix volume fraction, and $V_f + V_m + V_v = 1$, where V_v is the void volume fraction. E_{1f} is the longitudinal Young's modulus of the fibers, assumed transversely isotropic, and E_m is the Young's modulus of the matrix, assumed isotropic. The major Poisson's ratio (ν_{12}) can be estimated following the same assumption, as:

$$\nu_{12} = V_f \nu_{12f} + V_m \nu_m \tag{6.6}$$

where ν_{12f} is the major Poisson's ratio of the fibers and ν_m the Poisson's ratio of the matrix.

The transverse Young's modulus (E_2) can be calculated assuming that the fibers and matrix are working as springs in series:

$$E_{2,RoM} = \frac{E_m E_{2f}}{E_m V_f + E_{2f} V_m} \tag{6.7}$$

where E_{2f} is the transverse Young's modulus of the fibers. Finally, the shear modulus can be calculated as:

$$G_{12,RoM} = \frac{G_m G_{12f}}{G_m V_f + G_{12f} V_m} \tag{6.8}$$

where G_{12f} is the longitudinal shear modulus of the fibers and G_m is the shear modulus of the matrix.

However, the predictions using the RoM for the transverse and shear stiffness are not accurate. Therefore, other micromechanical models have been proposed in the literature to determine these properties, such as the Halpin-Tsai [98] model. But to account for the presence of multiple types of inclusions (here fibers and voids), the elastic properties are better estimated using the Mori-Tanaka mean field theory [99].

6.2.5.3 The Mori-Tanaka mean field theory

The Mori-Tanaka mean field theory [99] account for the presence of multiple types of inclusions (here fibers and voids). In that case, for a system with unidirectional fibers with a transversely isotropic behavior and with more than one inclusion (fibers and voids), the overall elastic moduli and Poisson's ratio can be calculated as [142]:

$$
\begin{aligned}
p^* &= \frac{\sum_{i=1}^{n} \frac{V_i p_i}{p_m + p_i}}{\sum_{i=1}^{n} \frac{V_i}{p_m + p_i}} = G_{12} \\
\gamma_m &= \left(\frac{1}{m_m} + \frac{2}{k_m} \right)^{-1} \\
m^* &= \frac{\sum_{i=1}^{n} \frac{V_i m_i}{m_i + \gamma_m}}{\sum_{i=1}^{n} \frac{V_m}{m_i + \gamma_m}} = G_{23} \\
k^* &= \frac{\sum_{i=1}^{n} \frac{V_i k_i}{m_m + k_i}}{\sum_{i=1}^{n} \frac{V_i}{m_m + k_i}} = -\left(\frac{1}{G_{23}} - \frac{4}{E_2} + \frac{4\nu_{12}^2}{E_1} \right)^{-1} \\
l^* &= \frac{\sum_{i=1}^{n} \frac{V_i l_i}{m_m + k_i}}{\sum_{i=1}^{n} \frac{V_i}{m_m + k_i}} = 2k^* \nu_{12} \\
n^* &= \sum_{i=1}^{n} V_i n_i - \sum_{i=1}^{n} V_i \frac{(l_i - l_m)^2}{m_m + k_i} + \frac{\left[\sum_{i=1}^{n} V_i \frac{(l_i - l_m)}{m_m + k_i} \right]^2}{\sum_{i=1}^{n} \frac{V_i}{m_m + k_i}} = E_1 + 4k^* \nu_{12}^2
\end{aligned}
\tag{6.9}
$$

where k^*, l^*, m^*, n^* and p^* are Hill's elastic moduli [142], and the index i refers to each inclusion (i.e., fibers and voids) and m to the matrix. The Hill's elastic moduli for an isotropic material, such as the matrix, are:

$$
\begin{aligned}
m_m &= p_m = G_m \\
l_m &= 2k_m \nu_m \\
n_m &= E_m + 4k_m \nu_m^2 \\
k_m &= \frac{-1}{\frac{1}{G_m} - \frac{4}{E_m} + \frac{4\nu_m^2}{E_m}}
\end{aligned}
\tag{6.10}
$$

whereas for a transversely isotropic reinforcement, such as the fibers, they are described as:

$$\begin{aligned} m_i &= G_{i,23} \\ p_i &= G_{i,12} \\ l_i &= 2k_i\nu_{i,12} \\ n_i &= E_{i,1} + 4k_i\nu_{i,12}^2 \\ k_i &= \frac{-1}{\frac{1}{G_{i,23}} - \frac{4}{E_{i,2}} + \frac{4\nu_{i,12}^2}{E_{i,1}}} \end{aligned} \tag{6.11}$$

Finally, the CCA model [100] is also checked since it also allows the presence of multiple phases.

6.2.5.4 The concentric cylinder assembly model

The concentric cylinder assembly (CCA) model [100] also allows the presence of multiple phases. The micromechanical model is a straightforward extension of Hashin's [101] and Christensen and Lo's [102] models with the main novelty of its applicability to multilayered (N-phased) inclusions with transversely isotropic material properties. The composite consists of N-cylinders perfectly bonded together in which each phase (k) is homogeneous, linear elastic and with a transversely isotropic behavior. The outer (r_k) and inner radius (r_{k-1}) of each cylinder, i.e., the thickness, is determined according to each corresponding volume fraction (V_k) as:

$$V_k = \frac{r_k^2 - r_{k-1}^2}{r_N^2} \tag{6.12}$$

where $r_N = 1$ since the calculated effective elastic properties depend only on the relative dimensions of constituents. Thus, macroscopically, the composite is transversely isotropic. The problem of radial loading is solved to find the bulk modulus K_{23}, of axial loading to find E_1 and ν_{12}, of in-plane shear loading to find G_{12} and of shear loading in the plane transverse to the fibers to find G_{23}.

Finally, E_2 and ν_{23} are determined using:

$$E_2 = \frac{1}{\frac{1}{4K_{23}} + \frac{1}{4G_{23}} + \frac{\nu_{12}^2}{E_1}}$$
$$\nu_{23} = \frac{E_2}{2G_{23}} - 1 \tag{6.13}$$

In the present study, to account for the presence of voids, a first phase representing the voids with near zero elastic properties is embedded inside a cylinder representing the matrix. The void and matrix unit is surrounded by a cylinder which represents fibers. Finally, the final outer phase in the 4 cylinder model represents the matrix. It was found that such 4-phase CCA model (see Figure 6.1) is a more realistic representation of UD composite with voids in matrix compared to a similar 3-phase CCA model with outer phase being the fiber cylinder as the latter leads to underestimation of transverse modulus and a large overestimation of in-plane shear modulus.

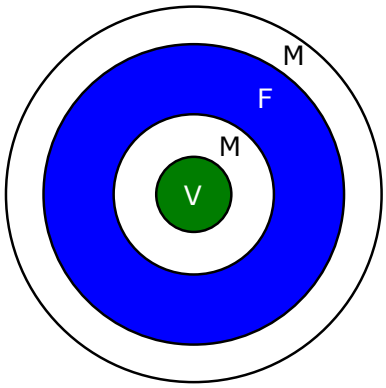

Figure 6.1: 4-phase CCA model representing UD composite with voids in the matrix phase: V – void, M – matrix, F - fiber.

The uncertainty quantification analyses performed numerically using computational micromechanics and analytically following the RoM, the Mori-Tanaka mean field theory, and the CCA model are compared, in terms of the obtained mean values and STDVs. The comparison considers the constituent properties variability in all cases, and includes the spatial distribution of the reinforcements and of the defects in the case of computational micromechanics (the only one herein that can account for these effects).

6.2.6 Definition of statistically representative volume elements (SRVEs)

The definition of an RVE implies that the results obtained are macroscopically uniform. That is, the RVE must be large enough to be representative of the continuum at a higher scale. Thus, an infinitesimal RVE may be used. However, in numerical analysis a finite size is required [74]. On the other hand, SRVEs must reproduce the same statistics related to the stress and strain fields of the macroscopic material. To account for the spatial distribution of constituents and defects and the possible material variation, a number of samples (n) is analyzed to determine these statistics.

To determine the minimum size of the SRVE, the mean values of the properties of interest obtained with volume elements of different size and discretization options (type and size of the finite elements) are determined and compared. A contrast of hypotheses is performed to check if two means can be assumed to be equal:

$$\begin{aligned} H_0 &: \bar{x_1} = \bar{x_2} \\ H_1 &: \bar{x_1} \neq \bar{x_2} \end{aligned} \tag{6.14}$$

where H_0 and H_1 are the null and alternative hypotheses assuming that $\bar{x_i}$ is the mean value of each sample. A pooled standard deviation, S_p, is used as an estimator of common population standard deviation:

$$S_p = \sqrt{\frac{(n_1-1)s_1^2 + (n_2-1)s_2^2}{n_1+n_2-2}} \tag{6.15}$$

where n_i is the sample size and s_i the standard deviation of each sample. Using the S_p and the $\bar{x_i}$ of the main data set and the ones to be compared, the test statistic

$$t_0 = \frac{\bar{x_1} - \bar{x_2}}{S_p - \sqrt{\frac{1}{n_1} + \frac{1}{n_2}}} \tag{6.16}$$

is used to determine if the null hypothesis can be accepted or if it must be rejected. Since this is a two-sided t-test, the required t value to accept the null

hypothesis, i.e., the mean values are equal, is:

$$t_{a,n} = t_{\frac{\alpha}{2},n_1-n_2-2} \tag{6.17}$$

where α is the probability of rejecting the null hypothesis when it is true. Finally, the p-value, which is the probability of obtaining test results outside the results observed under the assumption that the null hypothesis is true, is calculated. Therefore, the p-value to accept H_0 must satisfy that:

$$\text{p-value} = P(t_0 \leq t_{n_1-n_2-2}) \geq \alpha \tag{6.18}$$

Moreover, in this study, the variance in the results due to the uncertainty of the input parameters, such as the material variability, the spatial distribution and the presence of defects, is an important parameter that must be independent of the SRVE size and discretization. Thus, to determine the parameters for generation of SRVEs, a contrast of hypotheses is also performed to ensure that the standard deviations (STDVs) are independent of the modeling options:

$$\begin{aligned} H_0 &: s_1 = s_2 \\ H_1 &: s_1 \neq s_2 \end{aligned} \tag{6.19}$$

The test statistic used to determine if the null hypothesis can be accepted is F_0 defined as:

$$F_0 = \frac{s_1^2}{s_2^2} \tag{6.20}$$

Since this is an F-test, the F_{n_1-1,n_2-1} statistic is used to accept the null hypothesis, i.e., that the STDVs are equal. Thus, the p-value can be calculated as:

$$\text{p-value} = P(F_0 \leq F_{n_1-1,n_2-1}) \geq \alpha \tag{6.21}$$

So, the minimum size of the SRVE is determined by the one that provides the same mean values and STDVs of a larger one.

Table 6.1: Mean values of the elastic properties of the constituents and assumed standard deviations (STDVs).

Constituent	E_1 [MPa]		E_2, E_3 [MPa]		ν_{12}, ν_{13}		ν_{23}		G_{12}, G_{13} [MPa]		G_{23} [MPa]	
	Mean	STDV	Mean	STDV	Mean	STDV	Mean	STDV	Mean	STDV	Mean	STDV
Carbon fiber AS4	225 000	11 250	15 000	750	0.2	0.01	0.07	0.0035	15 000	750	7 000	350
Epoxy matrix 3501/6	4 200	210	-	-	0.34	0.017	-	-	1 567	78.35	-	-

6.3 Composite material selection and effect of defects

This section describes the properties of the constituents, i.e., fibers and matrix, and the characteristics of the defects, i.e., voids, which will be used to determine the effect of defects on FRPs.

6.3.1 Properties of the constituents

The proposed methodology can be applied to any FRP. In this study, the material system considered is composed of AS4 carbon fibers embedded in a 3501-6 epoxy matrix. The properties of the constituents are summarized in Table 6.1 [143]. However, the material properties variability has not been previously reported. Other studies, such as [144], which accounted for the uncertainty in the predicted mechanical properties and the failure strengths of composite laminates, also assumed a variation equivalent to 5% of the mean value for the properties of the constituent. Moreover, the CMH-17 [1] suggests defining the elastic properties with its mean and standard deviation. So, in this analysis, a normal distribution of the material properties is considered, with a coefficient of variation of 5%.

In this study, the fiber-matrix interface is assumed to be perfectly bonded. Thus, using the interaction properties in ABAQUS/Standard, a surface interaction between fibers and matrix is used with a high penalty stiffness and without taking damage into account (i.e., without interface degradation).

The fibers have a cylindrical shape with a mean diameter of 0.007 mm and a STDV of 0.0003 mm according to Ref. [145]. The minimum distance between them ($k_{fiber-fiber}$) is defined as 0.1 times the mean radius of the two adjacent fibers. Due to the presence of voids, the fiber volume fraction (V_f) tends to be lower than usual. Therefore, the fiber volume fraction considered in this study

Table 6.2: Mean value and assumed standard deviation (STDV) of the void diameter and the distance between fibers and voids, defined as $k_{void-fiber}$ multiplied by the mean radius, for each type of void analyzed in this study.

Void type	Mean diameter [mm]	STDV diameter [mm]	$k_{fiber-void}$ [-]
Small matrix voids	0.004	0.0004	0.1
Large matrix voids	0.014	0.001	0.1
Inter-fiber voids	0.014	0.001	-0.05

is 55%, i.e., it is kept constant with a value of 55% while the matrix volume fraction (V_m) is reduced according to the void volume fraction (V_v).

The dimensions of the RVE and the mesh size are determined according to the statistical analysis explained in Section 6.2.6 and developed in Section 6.4.1.

6.3.2 Distribution and discretization of defects

As discussed previously (see Section 6.1 and Section 6.2.1.3), at the microscale, voids can be represented with a cylindrical shape parallel to the fiber direction (longitudinal direction) with a circular cross-section (matrix voids), whereas inter-fiber voids present an irregular shape due to their intersection with the fibers.

The generation of voids in the finite element model is performed according to the assigned diameter and void content. Although most industries do not allow void contents above 5%, the void volume fraction considered in this study is 7% to promote a greater influence and characterize more clearly their effect, a similar approach to previous studies [58, 66, 95]. The characteristics of each type of voids analyzed in this study is summarized in Table 6.2. The minimum distance between voids ($k_{void-void}$) is two times the mean radius of two consecutive voids to allow to have fiber bundles around them.

For the sake of simplicity, and since all the SRVEs analyzed in this study are only a small portion of the whole ply (see Figure 6.2b), voids represented in this micromechanical model extend along the length the SRVE, although it is recognized that, unlike the fibers, voids are not continuous. Yet, given their rod-like geometry, this is considered a suitable approximation.

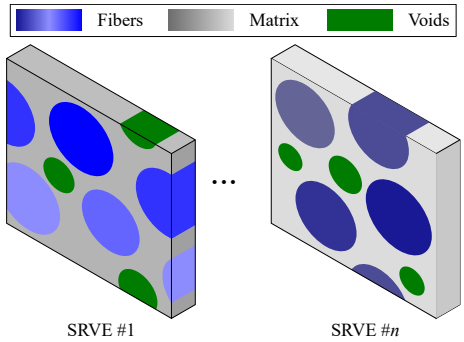

Figure 6.2: Illustration of two SRVEs containing small matrix voids. The different grades of the colors show the material variability of the matrix between samples and of the fibers in each sample. Material periodicity is ensured. Geometrical variability of the fibers and voids is also represented.

Voids dummy material. Voids represent air entrapped in the composite system. To avoid numerical problems and account for the volume variation of the RVE due to the elastic deformations, in this study voids are characterized using an isotropic dummy material [46]. A parametric analysis was conducted to assess the effect of the dummy material properties on the resulting homogenized composite properties. Finally, a value equal to 0.001 MPa for the Young's modulus and 0.001 for the Poisson's ratio resulted in no effect on the homogenized composite properties.

6.4 Results and discussion

This section presents, the statistical analysis to determine the SRVE, the effect of voids on FRPs and the discussion of the results obtained in this study.

6.4.1 Determination of the minimum size of the SRVE

A sample size n of 20 samples is analyzed. In each sample, all different fibers have random material and geometric properties according to their respective normal distribution, whereas voids have different dimensions according to their associated uncertainty. Each model also has different material properties for the matrix and a random spatial distribution of the fibers and of the defects. Therefore, each sample takes into account the material variability, the geometrical uncertainties, the effect of voids and the random spatial position of the fibers and defects (see Figure 6.2).

To determine the minimum size of the SRVE and its most efficient discretization, a contrast of hypotheses for the means and the STDVs with a significance level of 5% (α=5%) is performed. The parameters studied in this statistical analysis are:

1. The length on the longitudinal direction of the SRVE.
2. The mesh size. The fibers and the matrix can have different mesh sizes.
3. The size of the SRVE (width and height) considering a square cross-section. The SRVE size is determined relative to the fiber diameter, i.e., if the SRVE width is 20, that means that the width and height will be 20 times the mean fiber diameter (0.007 mm).
4. The presence of defects, i.e., whether the size of the SRVE is affected by the presence of voids.

Determination of the minimum length. To determine the minimum length of the SRVE, three different lengths are analyzed: 0.1 mm, 0.05 mm and 0.01 mm, in line with previous numerical studies [146]. Moreover, three model sizes were analyzed: 5×5, 10×10 and 15×15, corresponding to a width and height 5, 10 and 15 times the mean fiber diameter (0.007 mm), respectively. For this analysis, the size of the finite elements was 0.0007 mm. The RVE with a length equal to 0.1 mm is taken as the reference.

The contrast of hypotheses, for the mean and STDV, were true for all the cases analyzed. It can be concluded that the length has no effect when determining the elastic properties since, for any length and size, the mean value and the STDV can be assumed to be equal to the reference value (0.1 mm long RVE). SRVEs with a length of 0.01 mm are, therefore, chosen, discretized by 5 elements, leading to a mesh size in the longitudinal direction of 0.002 mm.

Determination of the mesh size. To perform the mesh convergence study, four different mesh sizes according to the fiber diameter were evaluated in an RVE with a model cross-section of 15×15 fibers. The reference one is the finest, which has an element size of 0.00035 mm for both the matrix and the fibers. This leads to approximately 20 elements across the fiber diameter. Moreover, different combinations of mesh sizes for the matrix and the fibers

Table 6.3: Contrast of hypotheses of the mean value ($H_{0,mean}$) and the STDV ($H_{0,STDV}$) of a 15×15 model to determine the minimum mesh size for discretization of fibers and matrix. The values in **bold** are the reference values used for the contrast of hypotheses.

Matrix finite element size	Fiber finite element size	
	0.00035 [mm]	0.00070 [mm]
0.00035 [mm]	**Ref value**	$H_{0,mean}$: False for E_1 $H_{0,STDV}$: False for G_{23}
0.00070 [mm]	$H_{0,mean}$: True $H_{0,STDV}$: True	$H_{0,mean}$: False for E_1, E_2, G_{12}, G_{23} $H_{0,STDV}$: True

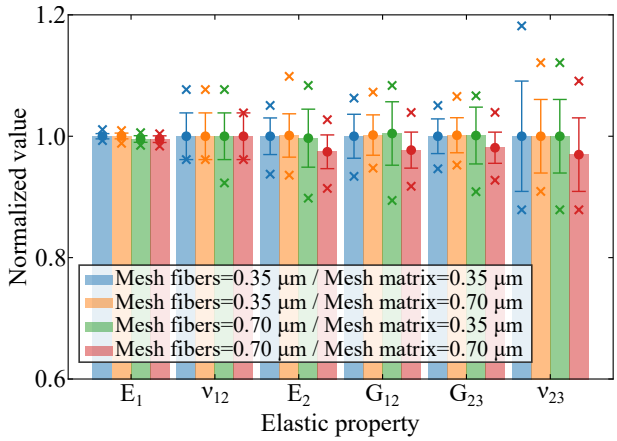

Figure 6.3: Normalized elastic properties from a cross-section size 15×15 with four different mesh sizes for the fibers and the matrix. The crosses are the minimum and maximum values, and the circle the mean value with an error bar equal to one STDV.

are considered. Figure 6.3 shows the results for the four different mesh size combinations normalized by the reference value. Table 6.3 summarizes the results of the contrast of hypotheses for the mean values and the STDVs for the mesh convergence study.

From the results of the contrast of hypotheses, the fibers will be discretized by finite elements with 0.00035 mm whereas the matrix will be discretized by finite elements with 0.00070 mm, very close to the values obtained by Li et al. [76], without compromising the accuracy of the results. The use of a heterogeneous mesh enables reducing the total number of elements and the computational cost with respect to the finest mesh attempted.

Table 6.4: Contrast of hypotheses of the mean value ($H_{0,mean}$) and the STDV ($H_{0,STDV}$) for different model dimensions to determine the smallest SRVE assuming a length of 0.01 mm and a mesh size of 0.00035 mm for the fibers and 0.00070 mm for the matrix. The values in **bold** are the reference values used for the contrast of hypotheses.

SRVE	$H_{0,mean}$	$H_{0,STDV}$
Cross-section size 20×20	**Ref value**	**Ref value**
Cross-section size 15×15	True	True
Cross-section size 10×10	True	False for E_1
Cross-section size 5×5	False for G_{12}, G_{23}	False for E_1

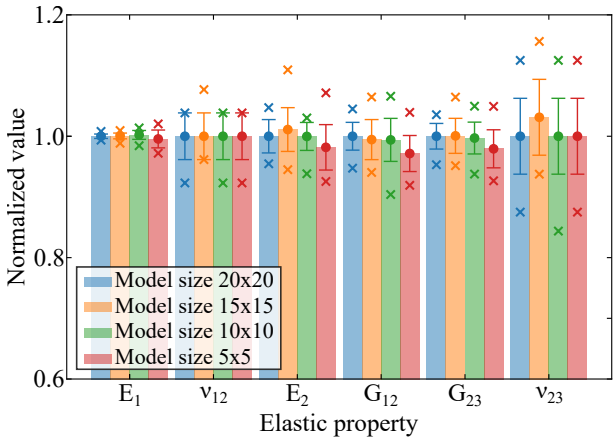

Figure 6.4: Normalized elastic properties from 5×5, 10×10, 15×15 and 20×20 cross-section size to determine the minimum size. The crosses are the minimum and maximum values, and the circle the mean value with an error bar equal to one STDV.

Determination of the SRVE size. Once the length of the SRVE has been determined to be 0.01 mm and the mesh size 0.00035 mm for the fibers and 0.00070 mm for the matrix, finally, the cross-section size of the SRVE is studied. Four possible SRVE sizes were studied. The reference has 20×20 fibers. The results are shown in Figure 6.4. The study of the contrast of hypotheses is summarized in Table 6.4.

From this statistical analysis, it can be concluded that the reference value previously selected (20×20) is representative since the contrast of hypotheses demonstrate that there is a smaller RVE (15×15) with the same mean and STDV for all the elastic properties. So, a convergence of the results is achieved. Therefore, to not compromise the computational time and resources needed, the SRVEs with a cross-section size of 15×15 fibers, i.e., 0.105 mm width and 0.105 mm height, are selected. These values are in good agreement with some other

Table 6.5: Contrast of hypotheses of the mean value ($H_{0,mean}$) and the STDV ($H_{0,STDV}$) to determine the effect of the presence of voids on the model size. Two RVEs with voids have been analyzed: small matrix voids and large matrix voids. The values in **bold** are the reference values used for the contrast of hypotheses.

SRVE	20x20 in plane size L=0.05 mm	15x15 in plane size L=0.01 mm
Small matrix voids	**Ref value**	$H_{0,mean}$: True $H_{0,STDV}$: False for ν_{23}
Large matrix voids	**Ref value**	$H_{0,mean}$: True $H_{0,STDV}$: True

studies available in the literature. For example, Trias et al. [74] determined that the minimum size should be between 5×5 and 25×25 fiber diameters. Moreover, it is also in good agreement with González and Llorca [77] who predicted that an RVE with 30 fibers is representative of the macroscopic material. In the present study, with a 15×15 cross-section, the number of fibers is much larger than 30.

To sum up, for a sample size of 20 SRVEs, the minimum lateral dimensions are 15×15 fibers, with a mesh size of 0.00035 mm for the fibers and 0.00070 mm for the matrix and a length in the longitudinal direction of 0.01 mm. With this combination, the number of finite elements for each SRVE is around 450 000.

Verification of the SRVE size with the presence of voids. The previous analyses, performed on "pristine" microstructures, is now repeated considering the presence of voids. The 20×20 RVEs with a length of 0.05 mm and matrix voids are taken as reference and compared with the previously determined: 15×15 fiber diameters cross-section and a length of 0.01 mm. In both cases, the mesh size for the fibers is 0.00035 mm, whereas for the matrix and the voids the mesh size is 0.00070 mm, which correspond to the best mesh combination found previously. The results of the elastic properties normalized by the reference values are shown in Figure 6.5, while Table 6.5 summarizes the results from the contrast of hypotheses for the mean values and the STDVs.

From the contrast of hypotheses, independently of the size of the matrix voids, the mean values can be considered statistically equivalent, while for small matrix voids the STDV of ν_{23} cannot. This is explained by the presence of two extremely high values (see the corresponding minimum and maximum value in Figure 6.5) in two of the 20 samples with small matrix voids. Neglecting these two extreme results, the STDVs turn out statistically equivalent.

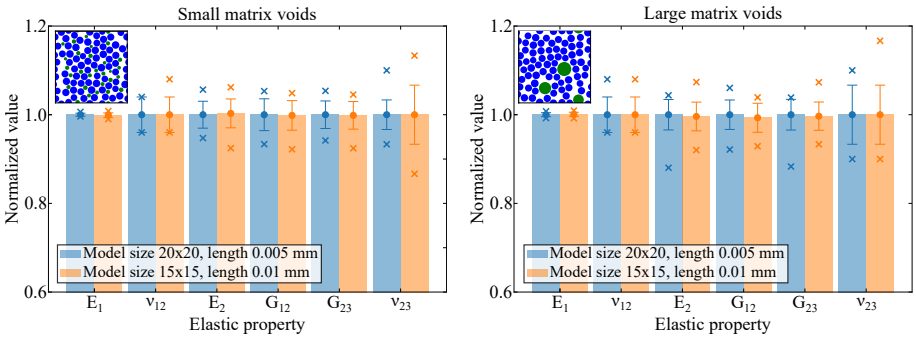

Figure 6.5: Normalized elastic properties with the presence of matrix voids. The crosses are the minimum and maximum values, and the circle the mean value with an error bar equal to one STDV.

Based on these results, it can be concluded that the size of the SRVE previously selected is practically independent of the presence of voids.

6.4.2 Effect of voids on the elastic properties

Finally, once the characteristics of the SRVE have been determined, the elastic engineering constants are calculated with the presence of voids. Different types of voids are analyzed, including matrix voids and inter-fiber voids to assess the effect of voids shape and size. For reference, SRVEs without defects or material variability and SRVEs without defects and material and geometric variability are also considered. The results are shown in Figure 6.6.

As expected, the presence of voids implies a reduction of the elastic properties, and the transverse and shear properties experience the highest reductions. Pristine SRVEs without material or geometrical variability exhibit very low variability of their elastic properties since they only account for the random spatial distribution of reinforcements. However, when introducing material and geometrical variability, the STDV increases without major changes in the mean values of the elastic properties. Interestingly, the presence of voids reduced the mean value of the elastic properties, but the variability (STDV) is barely affected. To check the effect of voids on the STDV, a set of analyses with large matrix voids but without material variability was performed. The results show that the mean value is almost the same, whereas the variability is smaller when only taking into account the uncertainty on the voids size and not the variability on the material properties. Therefore, for a fixed void content, the uncertainty is

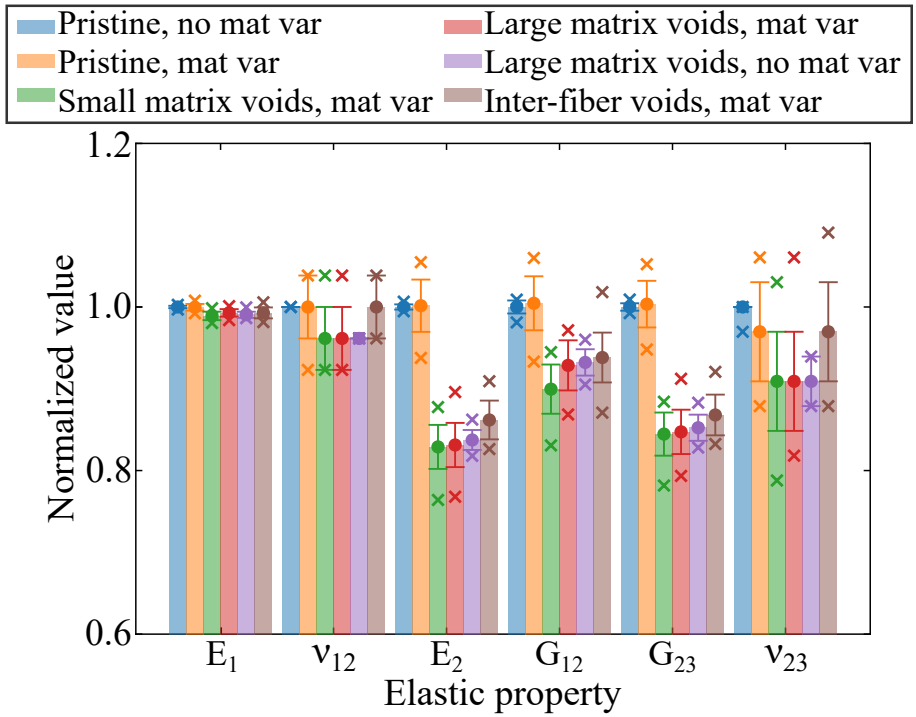

Figure 6.6: Normalized engineering constants obtained from six different SRVEs: (i) without defects (pristine) and without material variability, (ii) without defects (pristine) but with material variability, (iii) with small matrix voids and material variability, (iv) with large matrix voids and material variability, (v) with large matrix voids but without material variability and (vi) with inter-fiber voids and material variability. All models account for the spatial variability of the fibers (and voids). The crosses are the minimum and maximum values, and the circle the mean value with an error bar equal to one STDV.

Table 6.6: Effect of the presence of voids on the elastic properties of a composite system. The cases with voids include material variability.

Elastic Property		No material variability No defects	Material variability No defects	Small matrix voids	Large matrix voids	Large matrix voids No material variability	Inter-fiber voids
E_1 [MPa]	Mean	125 760	125 714	124 385	124 853	124 560	124 848
	STDV	182	511	651	577	471	842
	Rel. Dif.	-	-0.04 %	-1.09 %	-0.72 %	-0.95 %	-0.73 %
ν_{12} [-]	Mean	0.26	0.26	0.25	0.25	0.25	0.26
	STDV	0.0	0.01	0.01	0.01	0.01	0.01
	Rel. Dif.	-	0 %	-3.85 %	-3.85 %	-3.85 %	0 %
E_2 [MPa]	Mean	8 464	8 477	7 016	7 035	7 087	7 294
	STDV	27	271	228	229	103	201
	Rel. Dif.	-	0.15 %	-17.11 %	-16.88 %	-16.27 %	-13.82 %
G_{12} [MPa]	Mean	4 336	4 355	3 900	4 026	4 042	4 068
	STDV	35	143	131	133	70	132
	Rel. Dif.	-	0.44 %	-10.06 %	-7.15 %	-6.82 %	-6.18 %
G_{23} [MPa]	Mean	3 193	3 204	2 696	2 705	2 721	2 771
	STDV	15	91	84	87	51	80
	Rel. Dif.	-	0.34 %	-15.57 %	- 15.28 %	-14.78 %	-13.21 %
ν_{23} [-]	Mean	0.33	0.32	0.30	0.30	0.30	0.32
	STDV	0.0	0.02	0.02	0.02	0.01	0.02
	Rel. Dif.	-	-3.03 %	-9.09 %	-9.09 %	-9.09 %	-3.03 %

mainly related to the material variability whereas the knock-down factor of the mean properties comes from the presence of voids. Table 6.6 shows the results for the pristine SRVE and the relative difference, i.e., the knock down factor, with respect to the models considering material variability and the presence of voids.

The longitudinal Young's modulus, E_1, suffers a reduction of around 1% when the void content increases to 7% and the fiber volume fraction remains the same. This is expected, since E_1 is mostly governed by the longitudinal Young's modulus of the fibers and the fiber volume fraction which is not affected by the presence of voids, as in [76]. However, all the other elastic properties suffer a non-negligible reduction with the presence of voids, which leads to a reduction of the matrix volume fraction. For example, the reduction of the transverse Young's modulus, E_2, is around 17%.

Comparing the results between large matrix voids and inter-fiber voids, although both have similar diameter, it observed that the reduction with inter-fiber voids is lower than with matrix voids, except for E_1. To assess the effect of fiber-void intersection, a model allowing larger intersections was created. The results show lower knock-down factors for the properties dominated by the matrix, in particular E_2 and G_{23}, including a very small decrease for G_{12}, and a higher knock-down factor for E_1. Thus, it can be concluded that the position of the voids, in particular how much intersection is allowed with the fibers, affects

the global elastic response of the composite. If the voids are intersected by the fibers, instead of being completely embedded in the matrix, the transverse properties are less affected, whereas the longitudinal properties dominated by the fibers, suffer a higher reduction. Interestingly, in Ref. [58] it is shown that the effect of the position of the voids on the strength of FRPs is the opposite, i.e., the strength in the presence of inter-fiber voids tends to be lower because the intersection between fiber and voids implies higher stress concentration which induce the strength reduction.

Regarding the comparison between small and large matrix voids, there is also a clear trend that the smaller the voids are, the bigger is the reduction in the mechanical properties.

The effect of voids on the elastic properties is also compared with three analytical models. To determine the minimum number of samples, n_{anal}, to run the analytical models used in this study, a contrast of hypotheses was conducted comparing different number of samples from 20 to 50 000, with $n_{anal} = 50\,000$ used as the reference value. The contrast of hypotheses showed that with a 95% of confidence it can be assumed that the mean and the STDV for all the elastic properties with 20 samples are equal to the reference value. Thus, a number of samples $n_{anal} = 20$, which is the same sample size used for the numerical analyses, is used.

Figure 6.7 shows a comparison between the results obtained from computational micromechanics and the predictions of the RoM, the Mori-Tanaka mean field theory, and the CCA model for the same fiber volume fraction. Two SRVEs are considered: a pristine SRVE without defects and only considering material variability, and an SRVE with defects. The presence of voids with the RoM model can only be evaluated reducing the V_m whereas for the Mori-Tanaka and the CCA model they are assumed as a new inclusion with a dummy material. Because the analytical models do not account for the void size, the numerical results of the SRVEs with large matrix voids are selected for comparison.

For the pristine SRVE, while the predictions of the longitudinal properties are in good agreement with the numerical results (except for ν_{12} using the CCA model), the RoM, as expected, does not properly predict the transverse and shear properties, whereas the Mori-Tanaka mean field theory provides good

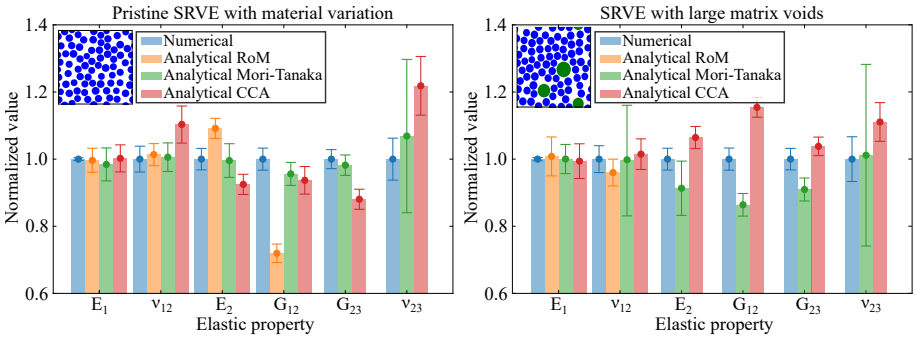

Figure 6.7: Normalized elastic properties from the numerical analysis, the rule of mixtures (RoM), the Mori-Tanaka mean field theory, and the concentric cylinder assembly (CCA) of a pristine SRVE and an SRVE with large matrix voids. The error bar corresponds to one STDV.

predictions of the transverse and shear properties. Finally, the results from the CCA model are worse than the ones from Mori-Tanaka but still in good agreement with the numerical predictions except for G_{12} and ν_{12}.

Considering the presence of defects, firstly, it is important to mention that Eqs.(6.7) and (6.8) (series model) for the prediction of the transverse Young's modulus and shear modulus of the composite using the RoM are not valid in the presence of voids, as the results would lead to higher stiffness since V_m is in the denominator. In other words, with a lower V_m, which means a higher V_v, a higher E_2 or G_{12} would be obtained. Nevertheless, the predictions of the longitudinal properties remain in good agreement with the numerical results, using either the RoM, the Mori-Tanaka mean field theory or the CCA model. For the transverse and shear properties, the Mori-Tanaka mean field theory still provides the best predictions compared to the numerical model, but with a higher difference compared to the pristine results.

The CCA model is also able to capture the effect of having the voids in the matrix or within the fibers by changing the position of each phase. In that case, 3-phase CCA model is considered with the voids in the middle, embedded by the fibers, and the matrix as the outer surface. Therefore, the effect of inter-fiber voids, in that case voids completely inside the fibers, can be also considered. Using this analytical model, the same trend observed in the numerical predictions was obtained: a lower reduction of the transverse properties and a significant effect on the longitudinal properties.

Regarding the uncertainty, which is mainly dominated by the variation of the material properties, both analytical models present similar predictions except for E_1 and ν_{23}. Regarding E_1, the STDV obtained analytically without or with defects is much higher (more than 10 times) than the one obtained with the micromechanical model. Taking into account that E_1 is mainly dominated by the fiber properties, a higher STDV can be explained because in the micromechanical model each SRVE has different material properties for each fiber according to their corresponding normal distribution (variability from fiber to fiber as shown in Figure 6.2). Thus, the different properties from fiber to fiber tends to cancel out in each SRVE. However, in the analytical models, the fiber properties only change from sample to sample inducing a higher variability between samples and, consequently, a higher STDV. A numerical analysis replicating the same conditions of the analytical models, i.e., with all fibers of each SRVE having the same randomly assigned material properties, was conducted and the STDV obtained was similar to the analytical one. Finally, it is important to note that, although there is no quantitative comparison with experimental results, the computational micromechanics modelling strategy employed here to predict the elastic properties of fiber reinforced polymers has been previously validated, e.g., Ref.[146]. Moreover, the results obtained with the presence of voids are in good agreement with the analytical models that have been already validated, incl. Mori-Tanaka mean field theory in Ref.[99] and the concentric cylinder assembly model in Ref.[100]. However, computational micromechanics provides higher flexibility in the parametrization of the SRVEs for uncertainty quantification analyses.

6.4.3 Parametric study of the influence of fiber and void content

The presented methodology can be used to study the influence of the input parameters (the geometry, the material variability and the presence of voids) on the mesoscale properties. This influence can be easily represented with a response surface which is a useful tool to compare the homogenized elastic properties obtained varying two of the input parameters. The previous discussed results (see Section 6.4.2) show that the highest effect of voids is in the transverse and shear properties. Since E_1 mainly depends on the longitudinal Young's

modulus of the fibers and the fiber volume fraction, E_1 is almost independent of the V_v. Thus, Figure 6.8 shows the prediction of the elastic transverse and shear moduli for different fiber (V_f) and void volume fractions (V_v) obtained numerically with the presence of large matrix voids and the relative difference between numerical predictions and analytical ones using the Mori-Tanaka mean field theory, which has been demonstrated to be the analytical model with closer predictions.

As expected, the elastic moduli are reduced with decreasing V_f. The elastic moduli governed mainly by the matrix, E_2 and G_{23}, show a pronounced reduction while increasing the V_v. However, as predicted by Tai et al. [147] in their micromechanical model with the presence of matrix microvoids, the reduction of G_{23} is more affected by the V_f rather than higher V_v. Regarding the longitudinal shear modulus G_{12}, which is more affected by the V_f rather than the V_v, the reduction due to a greater V_v is less noticeable.

The relative difference between the numerical results and the analytical Mori-Tanaka mean field theory increases with higher V_v. Regarding the V_f, the relative difference also increases with increasing V_f, although the increasing difference is less pronounced. For all the transverse and shear properties the analytical model underpredicts the elastic moduli. Nevertheless, the analytical model is able to capture the same trend obtained numerically for all the elastic properties.

The same analysis has been performed to check the effect of V_f and V_v on the uncertainty. However, no trend on the evolution of the STDV of the elastic properties with void and fiber volume fractions has been identified.

6.5 Conclusions

In this study, the definition of SRVEs to account for the effect of defects on the elastic properties of composite systems, including their uncertainty, is presented. An enhanced algorithm to generate the spatial distribution of the constituents in an RVE has been implemented with the ability of adding voids which have been represented as cylindrical branch-type defects aligned with the fiber direction. This RVE has been numerically simulated with a well parameterized modeling strategy, which accounts for different types of voids and materials. SRVEs are then determined for the uncertainty quantification and management of the

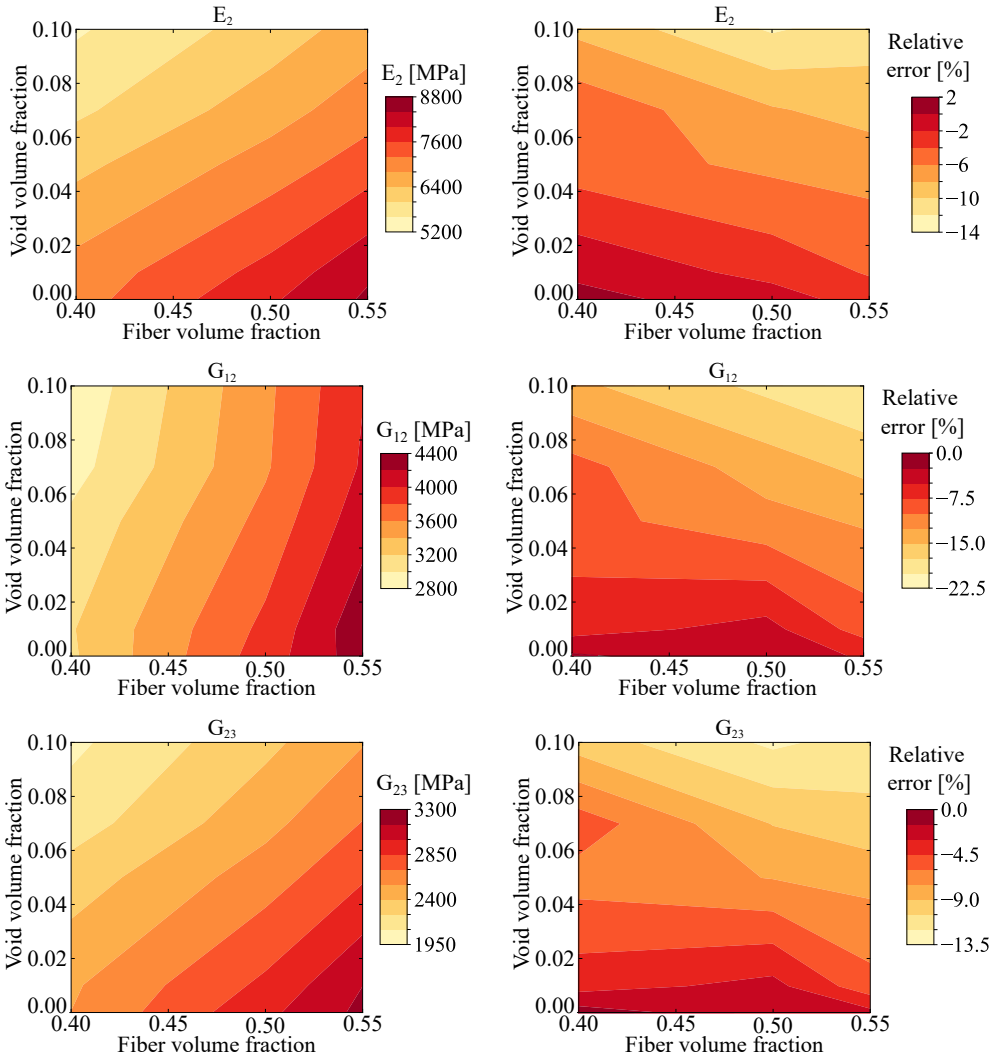

Figure 6.8: Prediction of the elastic transverse and shear moduli obtained numerically with the presence of large matrix voids and the relative difference between numerical results and the analytical ones from Mori-Tanaka mean field theory.

mechanical response of composite systems with defects at the micro-scale.

Based on the elastic response of the constituents, and through the analysis of contrast of hypotheses, it is demonstrated that, as expected, the presence of voids reduces the transverse and shear elastic properties. However, for the same fiber and void volume fractions, voids completely embedded in the matrix (matrix voids) lead to higher reductions in elastic properties than inter-fiber voids of similar size, except for E_1, showing that the position of the voids affects how detrimental is their effect on the elastic properties. On the other hand, the smaller the matrix voids, the larger is the reduction in the elastic properties of the composite. Regarding the effect on the uncertainties of the meso-scale properties, it is clear that, for a fixed void content, material variability has a larger effect than the presence of voids. The material variability, in this case, is responsible for the uncertainties at the meso-scale level, while the voids are mainly responsible for the reduction of the predicted elastic properties, in particular the transverse and shear ones. Finally, the comparison with analytical models shows that the Mori-Tanaka mean field theory provides the same trends of the numerical results for the transverse properties as a function of fiber and void volume contents. However, the relative difference between the numerical and the analytical predictions increases for high void volume fractions.

To sum up, this study shows how the added flexibility provided by computational micromechanics can aid in assessing the effect of material variability, geometric variability, as well as other microstructural effects, such as the presence of defects. Accounting for all these effects will be key in enabling multiscale reliability-based design of composite structures, linking the microstructural features with the macroscopic response and uncertainty management. Moreover, the methodology proposed herein can be extended to include the effects of other uncertainties, such as the presence of clusters of fibers or voids, and other types of defects.

Part III

Discussion and concluding remarks

Results and discussion

7

This section provides an in-depth discussion and synthesis of the outcomes derived from the four articles constituting this thesis. Each article tackled unique yet interconnected aspects of computational mechanics applied to composite materials. The investigations explored material variability, geometric features, and the influence of defects, ultimately contributing to an overall understanding of composite behavior.

7.1 Obtaining Design Allowables: insights from comprehensive studies on composite material behavior

Composite materials exhibit an intrinsic variability due to the uncertainties associated with constituents and specimen geometry. In fact, when performing any test, there is always variability on the results. Consequently, a singular value is insufficient, emphasizing the need for a statistical analysis across multiple results. This statistical value, derived from the collective results, serves as the design allowable.

Chapters 3 and 4 illustrate the use of statistical design values in the initial phases of the building block approach, enhancing safety and reliability in subsequent steps. Therefore, a thorough statistical analysis is imperative for establishing the design allowables of composite structures.

7.1.1 Definition of A and B-basis value

The CMH-17 [1] introduced the B-basis and A-basis values as design allowables for composite structures. These values correspond to the 10th percentile (B-basis) or 1st percentile (A-basis), each with a 95% lower confidence bound (for more details check Section 2.1). The CMH-17 proposes a methodology to calculate these design allowables based on the distribution that best fits the data. As shown in Figure 3.2, for unstructured data, the CMH-17 recommends sequentially testing the Weibull, normal, and lognormal distributions. If any of these distributions fits the data, the respective methods for calculating the B-

basis should be applied. If none of these distributions is suitable, nonparametric procedures are advised for determining the B-value.

This methodology is commonly employed for computing the B-value from experimental results, particularly when the sample size is limited. However, values predicted following the CMH-17 approach tend to be very conservative, especially with reduced data. As the sample size increases, the B-value determined using the CMH-17 approach becomes less conservative, as larger samples are considered more representative of the population.

Considering the definition of the B-value, it can also be calculated as the 5th percentile to ensure the 95% lower confidence bound, based on the distribution of 10th percentiles. Large sample sizes are required to compute the empirical cumulative density function (ECDF) of the desired strength and the ECDF of the 10th percentiles.

To incorporate variability and uncertainties into the calculated strength, Monte Carlo Simulation (MCS) is employed. In each simulation, input parameters are randomly defined, considering their distributions, to obtain a specific strength. The B-value can then be calculated from the ECDF using the results from various simulations.

Despite the significance of these design allowables, there is a lack of clear methodologies for their computational determination. Therefore, this work defined two methodologies for obtaining the B-basis value. One from a low fidelity model, employing a well-established analytical model, and the other from a high fidelity model, utilizing finite element (FE) analysis.

7.1.2 Optimizing computational model selection for robust analysis

Low fidelity approach. The low fidelity model used in this study predicts the notched strength of composite laminates based on the finite fracture mechanics model developed by Camanho et al. [6]. This model incorporates stress and energy-based criteria and has been further extended by Furtado et al. [5], requiring only three material properties of the 0º ply: longitudinal Young's modulus E_1, longitudinal tensile strength X_T, and the longitudinal crack resistance curve

or $\mathscr{R}$-curve. Hence, this model demands characterization of just three material properties.

Chapter 3 compares experimental results from Ref. [113] with predictions using the proposed framework. The study includes not only the open-hole (OH) strengths computed using nominal material and geometrical properties but also results when these properties are considered stochastic, allowing for the determination of both average OH strength and expected variability. Validation of this model involves comparing the predicted results with experimental data, as shown in Fig. 3.10. The proposed framework yields accurate predictions of OH tensile strength, with a maximum error of 12%. This demonstrates the capability of the analytical formulation to provide reliable predictions at a very reasonable computational cost.

High fidelity approach. The high fidelity model focuses on predicting the compression after low-velocity impact (LVI & CAI) strength of a panel. The analysis involves two steps: first, the laminate is impacted to induce structural damage (LVI FE model), and second, the effect of this damage is evaluated under compressive load (CAI FE model). This model requires a robust characterization of the non-linear behavior of material properties and a detailed description of all interactions between components, making numerical models, such as FE models, reliable tools.

Comparing the FE model with experimental results, it is observed that the FE model overpredicts the median CAI strength by 14.6% and the mean value by 9.6%, falling within the 90% confidence bound of the experimental data. Discrepancies can be attributed to simplifications in the modelling approach, such as assuming linear elastic behavior of the honeycomb or potential loading misalignments.

7.1.3 Sensitivity analysis: identifying key influential parameters

To account for uncertainties, a well-defined design of experiments matrix is created, encompassing various material properties and geometries within their tolerances. Thus, an accurate definition of the material properties is necessary. Therefore, first of all, it is important to perform a local sensitivity analysis

(LSA) to determine the properties with a major impact to perform adequate characterization and reduce the size of the problem addressed.

In the analytical model predicting notched strength, Fig. 3.7 illustrates that material properties exert a more significant influence than geometrical properties. The Young's modulus exhibits a linear variation, with lower elastic moduli leading to reduced open-hole (OH) strength. Tensile strength and material toughness demonstrate a more complex effect on OH strength, underscoring the need for accurate characterization of these properties to ensure precise predictions.

For the FE model predicting CAI strength, a more precise characterization is required. Among thirty one material properties, the independent variables are varied within their 95.4% confidence interval, i.e., ± 2 standard deviations for a normal distribution, to establish their influence on the output results within their probable values. The LSA is performed using a one-at-a-time analysis. This approach is based on the variation of only one parameter (X_j) for each simulation and to analyse the relative contribution of each input parameter on the output of the model (Y_j). The first-order sensitivity index (S_j) is calculated as:

$$S_j = E\left(\left|\frac{\frac{\partial Y}{\partial X_j}}{\hat{s}_j}\right|\right) \tag{7.1}$$

where j refers to the input parameters and $\hat{s}_j$ is the sample standard deviation. The derivative in Eq. (7.1) is normalized by $\hat{s}_j$, as the objective is to determine the input parameters that generate more dispersion on the output results of the model within their variation values according to their STDV. The input parameters with the greater S_j in both models (LVI and CAI FE models) are selected as the key parameters, with $\mathcal{G}_{IIc}$ crucial for LVI and $\mathcal{G}_{XC}$ playing a significant role in CAI strength. The pronounced impact of $\mathcal{G}_{IIc}$ on delamination area results from its role as interlaminar fracture toughness in mode II. Similarly, the notable influence of $\mathcal{G}_{XC}$ on CAI strength is rationalized by its connection to longitudinal compression fracture toughness, a crucial parameter for the fiber kinking damage. Additionally, $\mathcal{G}_{XC}$ emerges as the second independent variable contributing to the most dispersion in the LVI index. However, it is worth

mentioning that the LSA have not taken into account the potential interaction between parameters (one-at-a-time analysis) which could have an influence on the results.

7.1.4 Defining design allowables: a comprehensive approach accounting for uncertainty

To determine design allowables, the A-basis value represents the 5^{th} percentile of the distribution of the 1^{st} percentile of strength, while the B-basis value corresponds to the 5^{th} percentile of the distribution of the 10^{th} percentiles [1]. An MCS is employed to obtain these values by running the model numerous times, creating an ECDF for the parameter in study. For each set of n results, where n is the sample size that should be large enough to be representative of the population, it is possible to determine the ECDF and extract the 10th percentile value. This process is repeated N times, determining a distribution for the 10th percentile. From this distribution, the B-value can be computed by considering the 95% lower confidence bound [2], which corresponds to the 5^{th} percentile of the ECDF. Similarly, the A-value can be predicted from the distribution of the 1^{st} percentile. This requires large sample sizes, which can be easily achieve for the analytical model whereas for the FEM analysis, the computational cost is greater.

For the low fidelity model, firstly it is important to analyse the number of simulations required to ensure an accurate determination of the output parameters. A sample size of 10000 simulations is found to be sufficient for accurate predictions. The B-value is then compared with experimental results. The B-value determined with the CMH-17 approach is similar to that obtained experimentally, for the same sample size ($n = 5$), which reflects not only the ability of the framework to accurately compute the OH strength of a given configuration, but also its ability to propagate the uncertainty of the input parameters to the open hole strength. The B-basis obtained with the MCS approach is always less conservative than the one obtained with the CMH-17 approach due to the larger sample size.

For the high fidelity model, the determination of large samples requires high computational cost. Therefore, only few characteristic samples are simulated

following the Latin Hypercube Sampling (LHS) technique: 80 FE models distributed following a uniform distribution and 20 more FE models defined with the normal LHS method.

From the projected delaminated area after the LVI and the CAI strength obtained from these 100 simulations, a Response Surface (RS) of the CAI FE model is created using the Kriging algorithm. 90 samples out of the total 100 cases are used to create the RS whose input variables are the key parameters obtained from the LSA and the projected delaminated area obtained from LVI. The accuracy factors of each RS are calculated using the remaining 10 cases for validation. From the RS with the best accuracy factors, MCS with a size of n cases using the previous RS is applied and the ECDF of the CAI strength is calculated to obtain the 1^{st} and 10^{th} percentile. Finally, this process is repeated N times to obtain the ECDF of the 1^{st} and 10^{th} percentiles and to estimate the A/B-basis values, respectively. During this analysis, the sample size is shown to have a more significant impact on design allowables than the number of repetitions. Hence, the A/B-basis value can be numerically estimated using a single MCS providing a large sample size.

Experimental data are compared with numerical results, revealing that using only deterministic numerical results for validation is inadequate. Input variability is crucial for accurate model validation. The values obtained from the MCS of the RS align with the 90% confidence bound of the experimental data. However, the dispersion of the results of the experimental data is greater than that obtained numerically (from the FE models and the RS). This could imply that there are other input parameters that generate dispersion on the results apart from the key parameters ($\mathcal{G}_{IIc}$ and $\mathcal{G}_{XC}$).

The analytical model, due to its low resource consumption, is advantageous for obtaining large sample sizes. Thus, it is of great interest for the preliminary design of composite structures. At this step, design charts, such as the one presented in Fig. 3.12, are a useful tool which allows a fast estimation of the notched strength according to the configuration. The proposed UQ&M framework overcomes limitations in experimentally generating statistically representative design charts. Moreover, the analytical model is also evaluated to predict the strength of a center notched plate under tension loading, with the correct definition of the stress distribution and energy release rate following

Arteiro et al. [114].

Finally, this model can work as a fast design tool. Therefore, the variation of the loading direction and its effect is also assessed (see Fig. 3.14). Due to the fact that the laminate in study is quasi isotropic (Section 3.3), the notched strengths at 0°, 45° and 90° are equal. However the strength is reduced for any other load direction that does not align with any ply orientation.

7.2 Exploring the influence of ply misalignment on the notched allowables of composite laminates

Another significant source of variability in composite structures is the presence of defects. Manufacturing defects, such as ply deviation during layup, play a crucial role in the final configuration and resistance of the coupon. Therefore, it is desirable to account for defects while predicting design allowables. The previous analyses provided a comprehensive framework for obtaining B-value design allowables. Chapter 5 summarizes a new multi fidelity analysis of the notched allowable strength, considering the intrinsic variability of material properties, geometrical tolerances, and the presence of ply deviation in a quasi-isotropic (QI), hard, and soft laminate. Three different scenarios of misalignment are considered:

- Normal distributed ply misalignment with a STDV of 7° and a mean value of 0°.
- Uniformly distributed ply misalignment in the range $[-2 \times 7^\circ, +2 \times 7^\circ]$.
- A bias ply deviation of 7° for the 0° plies, in addition to normal distributed ply misalignment with a STDV of 7°.

The multi fidelity approach is based, on one hand, on an improved version of the analytical model proposed by Furtado et al. [5] and, on the other hand, on the simulation by a finite element (FE) model of the notched specimen.

Before accounting for the effect of ply misalignment, the results obtained from the low and high fidelity models are compared with experimental results avail-

able for the QI laminate. The analytical model predicts higher notched strength than the experimental results, with errors ranging between 13% and 23%. However, these analytical models are fast tools that aid in understanding the behavior of the composite structure and provide a first approximation of the notched strength, valuable for preliminary assessments. The results obtained using the high fidelity model exhibit a closer agreement with experimental data when compared with those obtained with the analytical model. As mentioned earlier, the low fidelity model has certain limitations and constraints. Notably, it does not account for delamination, which is demonstrated with the FE analysis to play a major role, as illustrated in Fig. 5.5.

While determining the minimum number of samples, the analytical results demonstrate that when accounting for fiber misalignment, a sample size of 10000 predictions is high enough for uncertainty propagation. Regarding the FE analysis, the sample size (n) is reduced to 200 samples due to significantly higher computational costs. This reduction is determined following a balance between the accuracy of the results and the computational cost.

Finally, both methods are used to determine the effect of ply misalignment in all the scenarios considered in this study. As expected, when comparing the different laminates, the QI results fall between the hard laminate, which achieved the highest notched strength, and the soft laminate, with the lowest values. For the soft laminate, the accuracy from the low fidelity model is lower than the value predicted by the high fidelity analysis. This can be explained by the presence of very few 0° plies, which are mainly responsible for bearing the applied load, and the significant role of delamination and other subcritical damage mechanisms.

Both solutions, analytically and numerically, agree that the B-value when incorporating ply misalignment is lower than when only considering material and geometric variability. When only accounting for material and geometric variability, the difference between the B-values from both solutions exhibits a large discrepancy, with differences above 10%. This difference is even more pronounced for the soft laminate because the analytical model does not provide good predictions. Nevertheless, when evaluating the ratio between the B-value and the mean value, the difference between the two cases is lower than 1%. Therefore, a valuable approach would be to predict the nominal value through

high fidelity analyses while determining the B-value by calculating the B-value-to-mean ratio with the analytical model. However, the difference between the B-value-to-mean ratios obtained from the analytical or FE models increases when considering ply misalignments.

Comparing the results when the misalignment is modelled with a normal or a uniform distribution, the latter exhibits larger variability due to the wider range of variance, resulting in a lower B-value. Moreover, when introducing a bias misalignment in all 0° plies, the mean value decreases leading to the lowest predictions.

The study presented in Chapter 5 underscores the significance of incorporating ply misalignment into the analysis, demonstrating its substantial impact. To validate this influence, Fig. 7.1 provides a comparison between the results obtained using the analytical model (low fidelity) proposed by Furtado et al. [5] only accounting for material and geometric tolerances (Chapter 3), and the results derived from the improved analytical model (low fidelity) and the FEM model (high fidelity). These latter models consider both material and geometric tolerances, along with the additional factor of ply misalignment (Chapter 5).

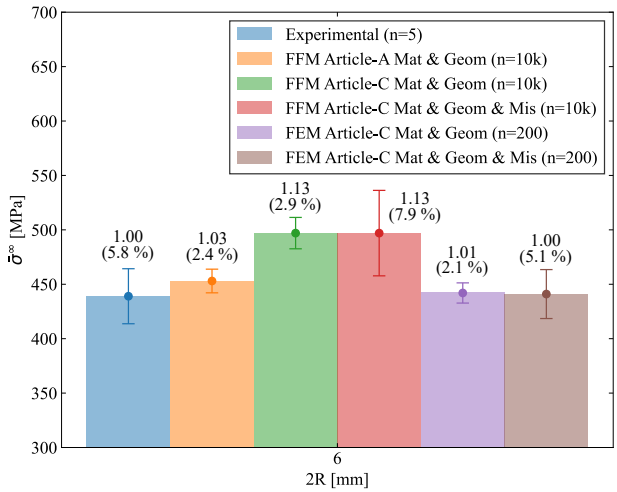

Figure 7.1: Comparison of the experimental results [134] with the analytical (Article A, Chapter 3, and Article C, Chapter 5) and FEM (Chapter 5) predictions when accounting for material and geometric variability (Mat & Geom). Additionally, the influence of ply misalignment (Mis) is considered. The values presented correspond to the ratio between the predicted mean value and the mean experimental value whereas the values in parentheses denote the experimental and predicted CoV, respectively.

The analytical model initially predicts a notched strength higher than the experimental results, and the refinements applied to the model result in even greater differences. Conversely, the results obtained using the high fidelity FEM model show a closer agreement with experimental data. Furthermore, a comparison of the STDV (or CoV) between experimental and numerical results reveals that when accounting for all uncertainties and defects, the predicted CoV aligns more closely with the experimental CoV, for both high and low fidelity models. This underscores the pivotal role of misalignment in composite structures, emphasizing its importance in uncertainty analyses.

7.3 Developing a micromechanical model for assessing the variability in meso-scale properties of composite materials

To address the inherent material variability within composite structures, a detailed understanding of material properties is essential for informing computational models. Micromechanical models serve as robust tools for elucidating the mechanical behavior of materials at the microscopic level, specifically on how constituents like fibers and matrix interact to influence the overall mechanical properties. At the micro-scale, the impact of defects, particularly voids, significantly contributes to the variability in composite structure properties (meso-scale).

In Chapter 6, a methodology is presented for defining statistically representative volume elements (SRVEs) and determining the elastic properties of fiber-reinforced polymers. This approach accounts for uncertainties stemming from material and geometric variability in constituents, spatial distribution, and the presence of defects, specifically three types of voids: i) matrix voids with a diameter smaller than the fibers (small matrix voids); ii) matrix voids with a diameter larger than the fibers (large matrix voids); iii) voids that intersect the fibers (inter-fiber voids).

The micromechanical model initially proposed by Melro et al. [78] for random fiber distributions in an RVE and extended by Tavares et al. [94] to accommodate different types of fibers was modified to accurately represent an RVE with voids.

The algorithm was enhanced to generate voids with a cylindrical shape parallel to the fiber direction, randomly distributed in the RVE.

Once the RVE is generated, incorporating parameters like size, fiber volume fraction (V_f), void volume fraction (V_v), and their respective diameters and variations, it undergoes discretization and analysis using FEM. The uncertainty associated with input parameters (constituent variability, random spatial distribution, and void presence) is then propagated to meso-scale elastic properties (engineering constants) through MCS.

To determine the effective elastic properties of the composite system, far-field strains of 0.001% were applied, and stress and strain fields in the RVE were post-processed using a first-order homogenization technique. The results obtained from computational micromechanics modelling using first-order homogenization were compared with analytical results using the rule of mixtures (RoM), the Mori-Tanaka theory, and the concentric cylinder assembly (CCA) model.

7.3.1 Ensuring statistically representative volume elements for meso-scale property assessment

In each analyzed RVE, fibers exhibit random material and geometric properties based on their respective normal distributions, while voids possess distinct dimensions reflecting associated uncertainties. The models also incorporate different material properties for the matrix and a random spatial distribution of fibers and defects. Thus, each sample comprehensively considers material variability, geometrical uncertainties, void effects, and the random spatial positions of fibers and defects.

To determine the minimum size of the SRVE and determine its most efficient discretization, a contrast of hypotheses for means and standard deviations (STDVs) is performed with a significance level of 5% ($\alpha = 5\%$). The parameters studied include:

1. The length along the longitudinal direction of the SRVE, revealing that SRVEs with a length of 0.01 mm, discretized by 5 elements, are suitable.

2. Mesh size differentiation, where fibers and matrix are discretized differently. The results suggest that fibers should be discretized by finite

elements with 0.00035 mm, while the matrix should be discretized by finite elements with 0.00070 mm.

3. The size of the SRVE (width and height), considering a square cross-section. SRVEs with a cross-section size of 15×15 fibers (0.105 mm width and 0.105 mm height) are selected to balance computational efficiency and resource requirements.

4. The impact of defects, indicating that the SRVE size is practically independent of the presence of voids.

7.3.2 Investigating the effect of voids on elastic properties

The study systematically investigates the influence of different void types on the elastic properties of composite materials, emphasizing the importance of considering material and geometrical variability. The introduction of voids results in a reduction of elastic properties, particularly affecting transverse and shear properties, while pristine SRVEs exhibit low variability in elastic properties. The presence of voids reduces mean elastic values, but variability (STDV) is minimally affected.

The study highlights specific trends in elastic property reductions due to voids. For instance, the longitudinal Young's modulus, E_1, shows a marginal reduction with increasing void content. In contrast, transverse properties, such as E_2, experience a notable reduction, around 17%, with void presence, due to a decrease in V_m.

Comparisons between different void types reveal that inter-fiber voids, despite having similar diameters to matrix voids, cause lower reductions in transverse properties, emphasizing the importance of void position. If the voids are intersected by the fibers, instead of being completely embedded in the matrix, the transverse properties are less affected, whereas the longitudinal properties dominated by the fibers suffer a higher reduction. The size of the matrix voids also affects the composite properties, with smaller voids causing more significant reductions.

Analytical models, including the RoM, Mori-Tanaka mean field theory, and the CCA, are employed for comparison. While the RoM and CCA models

show limitations in predicting transverse and shear properties in the presence of voids, the Mori-Tanaka model aligns well with numerical predictions. The study extends its analysis to defects, emphasizing that the RoM predictions for transverse and shear properties become invalid in the presence of voids. Nevertheless, the Mori-Tanaka model and CCA model provide reasonable predictions for longitudinal properties. The robustness of the methodology is demonstrated by capturing trends in the presence of defects, with the Mori-Tanaka model offering the best predictions. However, the CCA model is also able to capture the effect of having the voids in the matrix or within the fibers by changing the position of each phase. Therefore, the effect of inter-fiber voids, in that case voids completely inside the fibers, can be also considered. Using this analytical model, the same trend observed in the numerical predictions was obtained: a lower reduction of the transverse properties in the presence of inter-fiber voids.

Further analysis involves assessing uncertainties, primarily dominated by material property variations. The analytical models in general provide similar predictions, although significant differences are observed for E_1 and ν_{23}. Regarding E_1, the STDV obtained analytically without or with defects is much higher (more than 10 times) than the one obtained with the micromechanical model. Taking into account that E_1 is mainly dominated by the fiber properties, a higher STDV can be explained because in the micromechanical model each SRVE has different material properties for each fiber according to their corresponding normal distribution (variability from fiber to fiber as shown in Figure 6.2). Thus, the different properties from fiber to fiber tends to cancel out in each SRVE. However, in the analytical models, the fiber properties only change from sample to sample inducing a higher variability between samples and, consequently, a higher STDV.

The versatility of the methodology is showcased by using response surfaces to study the influence of V_f and V_m on meso-scale properties, offering a comprehensive tool for comparison. As expected, the elastic moduli are reduced with decreasing V_f. The elastic moduli governed mainly by the matrix, E_2 and G_{23}, show a pronounced reduction while increasing the V_v. However, the reduction of G_{23} is more affected by the V_f rather than higher V_v. Regarding the longitudinal shear modulus G_{12}, which is more affected by the V_f rather than the V_v, the reduction due to a greater V_v is less noticeable. The relative difference between

the numerical results and the analytical Mori-Tanaka mean field theory is also plotted. The difference increases with higher V_v. Regarding the V_f, the relative difference also increases with increasing V_f, although the increasing difference is less pronounced. For all the transverse and shear properties the analytical model underpredicts the elastic moduli. Nevertheless, the analytical model is able to capture the same trend obtained numerically for all the elastic properties.

Overall, the study provides valuable insights into the complex effect of voids and material variability on composite material properties. These findings contribute to a deeper understanding of how these factors influence elastic properties and offer a robust methodology for future investigations.

7.4 Synthesis and concluding insights

To conclude the discussion, this comprehensive exploration of computational mechanics applied to composite materials has yielded valuable insights into various aspects of material behavior. The work first focuses on obtaining design allowables, emphasizing the importance of statistical analyses to address the intrinsic variability of composite materials. Two methodologies for determining the B-basis value were established, one based on a low fidelity analytical model and the other utilizing a high fidelity finite element analysis. The sensitivity analysis underscored the critical role of material properties on the predicted strengths, guiding the selection of key parameters for subsequent investigations.

The optimization of computational model selection provided a detailed examination of low and high fidelity approaches. The low fidelity model demonstrated its efficiency in predicting notched strength with reasonable accuracy, particularly in the context of OH tensile strength. On the other hand, the high fidelity model showcased its reliability in capturing complex phenomena like CAI strength.

Moving forward, the discussion delved into the intricacies of defining design allowables, emphasizing the importance of MCS in obtaining A and B-basis values. While the low fidelity model facilitated the determination of B-values, the high fidelity model, due to its computational intensity, required careful consideration of sampling techniques like Latin Hypercube Sampling (LHS). The efficiency of the analytical model in providing large sample sizes was highlighted, reinforcing its utility in preliminary design stages.

The study then expanded to explore the influence of ply misalignment on notched allowables, introducing a new layer of complexity. The multi fidelity analysis considered different misalignment scenarios, providing a whole understanding of how deviations during layup affect notched strengths. The comparison between low and high fidelity models revealed the superiority of the latter in capturing intricate failure mechanisms, especially delamination, which significantly impacted results. This section highlighted the need for a balanced approach, leveraging the efficiency of analytical models alongside the accuracy of FE simulations.

The work finishes with an exploration of micromechanical models to assess meso-scale properties of composite materials. The detailed methodology for defining SRVEs and incorporating uncertainties, particularly the presence of voids, showcased a robust framework. The analysis of void effects on elastic properties revealed the significance of considering void position and size. The comparison with analytical models demonstrated the limitations of the latter in predicting certain properties, underlining the importance of leveraging both approaches for a comprehensive understanding.

All the work stemming from this thesis is encapsulated in the flow chart illustrated in Fig. 7.2. In summary, the micromechanical model aids in determining the uncertainties to feed the models at the meso-scale. Consequently, this variability, along with intricate meso-scale uncertainties, such as defects, must be incorporated into the definition of design allowables using the appropriate analysis method. To address the variability in predicting design allowables, it is essential to first choose an appropriate modeling and simulation approach. Low-fidelity models serve as rapid tools that enable the analysis of a large number of samples and are statistically representative. Conversely, high-fidelity models require substantial computational power but ensure greater accuracy. Therefore, if calculating large sample sizes is challenging, it becomes more efficient to define a response surface to properly calculate the design allowables. Finally, the impact of uncertainties is considered through Monte Carlo Simulation to obtain the corresponding B-value.

In essence, the methodologies established and insights gained contribute to a more holistic understanding of composite materials, laying the groundwork for informed design and analysis in the field of computational mechanics.

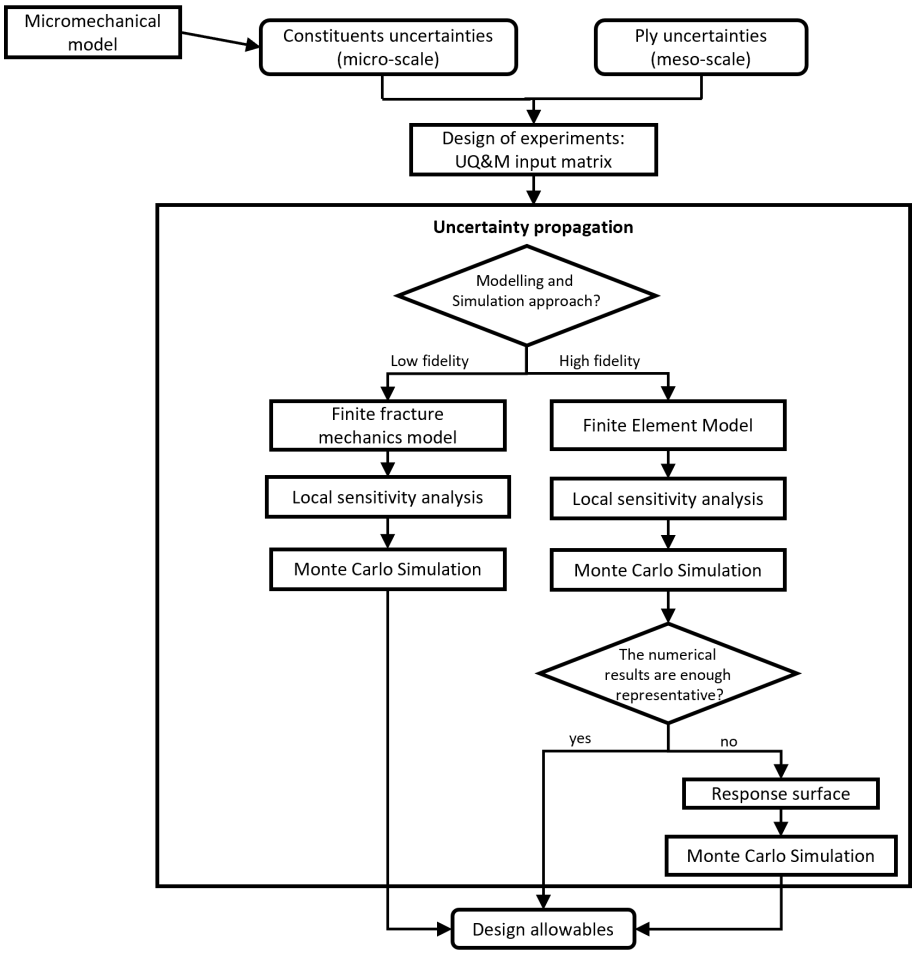

Figure 7.2: Flow chart derived from all the discoveries and methodologies presented in this thesis.

Conclusions and future work

8

8.1 Conclusions

The first objective, focused on generating design allowables for composite structures considering uncertainties and manufacturing defects, has been successfully addressed. The development of a comprehensive statistical model facilitates the identification and quantification of intrinsic uncertainties in composite structures. The formulated methodology for systematically propagating these uncertainties using a modelling and simulation (M&S) approach enhances the reliability of design allowables, laying the foundation for robust analysis in accordance with CMH-17 standards, and providing insights towards certification by analysis.

The definition of M&S to simulate the mechanical response of composite structures under various stress raisers represents a significant achievement. The robust M&S framework developed successfully captures the mechanical behaviors of composite materials under diverse loading conditions. This includes key parameters such as material properties, geometric configurations, and the presence of defects. The accuracy and efficiency of the simulations contribute to the establishment of a reliable computational tool, offering valuable insights into structural performance during the early stages of the design process.

The numerical calculation of design allowables, accounting for uncertainties and defects, marks a crucial step toward practical application. The selection of appropriate computational tools, balancing analytical models for efficiency and numerical simulations for a comprehensive analysis, showcases a detailed approach. This step not only ensures accurate predictions but also facilitates a deeper understanding of the mechanical behavior of composite structures, aiding in effective decision making during the design process.

Finally, the development of an advanced micromechanical model, considering constituent materials at the micro-scale as well as defects, is a noteworthy accomplishment. This model captures the mechanical response of composite structures while accounting for uncertainties and defects. Besides predicting mechanical performance, this micromechanical analysis provides insights into the sources of uncertainty inherent to composite materials. The understanding

gained serves as a foundation for developing strategies to manage and mitigate uncertainties effectively.

8.2 Future work

In this section different research lines to extend further the work carried out in this thesis are presented.

Future research could focus on refining and expanding the statistical models for calculating design allowables. This may involve incorporating additional sources of uncertainty, refining statistical values, assuming different distributions for the input parameters and exploring more advanced statistical techniques to enhance the accuracy of predictions. For instance, exploring the integration of machine learning techniques into the computational models could be a promising avenue. Machine learning algorithms could assist in refining predictions, optimizing simulations, and providing a data-driven approach to handle uncertainties in composite material behavior.

Building on the micromechanical model, future work could explore multi-scale computational modeling. Integrating insights from the micro-scale to the meso-scale would provide a more holistic understanding of material behavior, offering enhanced predictive capabilities and accounting for interactions between different scales. Moreover, the methodology proposed for the micromechanical model with the presence of defects could be extended including the definition of the correct damage mechanisms to predict the meso-scale strength and fracture toughness.

Conducting extensive experimental validation to calibrate and validate the developed computational models against real-world data taking into account the uncertainty (VVUQ from Verification and Validation with Uncertainty Quantification) would further strengthen the reliability of the findings. This VVUQ step is crucial for ensuring that the models accurately represent the complex stochastic behavior of composite materials in practical applications. However, this thesis has been focused on defining a methodology and providing the necessary tools for each modelling and simulation approach selected.

Considering the increasing importance of sustainability, future work could also investigate the impact of environmental factors on the mechanical behavior of

composite structures. Understanding how environmental conditions influence uncertainties and defects would contribute to more robust design processes.

The developed methodologies could be further extended to real-world industrial applications. Collaborating with industry partners to implement and validate the computational tools in practical settings would enhance the applicability and adoption of the developed approaches. Moreover, contributing to the standardization of methodologies within the industry could streamline the design process and ensure widespread acceptance.

In summary, the thesis has successfully achieved its objectives, providing a solid foundation for future research to refine, expand, and apply the developed methodologies in real-world scenarios. The suggested future work aims to address emerging challenges and further advance the field of computational analysis for composite materials.

Bibliography

[1] Composite Materials Handbook, Vol. 1. Polymer matrix composites guidelines for characterization of structural materials, SAE International on behalf of CMH-17, a division of Wichita State University, march 2012.

[2] S. Chakraborti, J. Li, Confidence interval estimation of a normal percentile, The American Statistician 61 (4) (2007) 331–336.

[3] A. T. Zehnder, Fracture mechanics, Vol. 62, Springer Science & Business Media, 2012.

[4] K. Friedrich, Application of fracture mechanics to composite materials, Elsevier, 2012.

[5] C. Furtado, A. Arteiro, M. Bessa, B. Wardle, P. P. Camanho, Prediction of size effects in open-hole laminates using only the Young's modulus, the strength, and the R-curve of the 0° ply, Composites Part A: Applied Science and Manufacturing 101 (AAA) (2017) 306–317.

[6] P. P. Camanho, G. Erçin, G. Catalanotti, S. Mahdi, P. Linde, A finite fracture mechanics model for the prediction of the open-hole strength of composite laminates, Composites Part A: Applied Science and Manufacturing 43 (8) (2012) 1219–1225.

[7] S. W. Tsai, J. D. D. Melo, An invariant-based theory of composites, Composites Science and Technology 100 (2014) 237–243.

[8] S. W. Tsai, J. D. D. Melo, A unit circle failure criterion for carbon fiber reinforced polymer composites, Composites Science and Technology 123 (2016) 71–78.

[9] O. C. Zienkiewicz, R. L. Taylor, The finite element method for solid and structural mechanics, Elsevier, 2005.

[10] J. Barbero Ever, Finite element analysis of composite materials using ansys® (2013).

[11] E. J. Barbero, Finite Element Analysis of Composite Materials using Abaqus®, CRC press, 2023.

[12] K. Nam, K. J. Park, S. Shin, S. J. Kim, I.-H. Choi, Estimation of composite laminate design allowables using the statistical characteristics of lamina level test data, International Journal of Aeronautical and Space Sciences 16 (3) (2015) 360–369.

[13] J. D. Arregui-Mena, L. Margetts, P. M. Mummery, Practical application of the stochastic finite element method, Archives of Computational Methods in Engineering 23 (1) (2016) 171–190.

[14] M. Papadrakakis, V. Papadopoulos, Robust and efficient methods for stochastic finite element analysis using monte carlo simulation, Computer methods in applied mechanics and engineering 134 (3-4) (1996) 325–340.

[15] Ö. Çavdar, A. Bayraktar, A. Çavdar, S. Adanur, Perturbation based stochastic finite element analysis of the structural systems with composite sections under earthquake forces.

[16] R. Cumbo, A. Baroni, A. Ricciardi, S. Corvaglia, Design allowables of composite laminates: A review, Journal of Composite Materials 56 (23) (2022) 3617–3634.

[17] R. G. Ghanem, P. D. Spanos, Spectral stochastic finite-element formulation for reliability analysis, Journal of Engineering Mechanics 117 (10) (1991) 2351–2372.

[18] H. Fukuda, T.-W. Chou, Monte carlo simulation of the strength of hybrid composites, Journal of Composite Materials 16 (5) (1982) 371–385.

[19] K. Goda, S. L. Phoenix, Reliability approach to the tensile strength of unidirectional cfrp composites by monte-carlo simulation in a shear-lag model, Composites science and technology 50 (4) (1994) 457–468.

[20] J. Yuan, Y. Xia, B. Yang, A note on the monte carlo simulation of the tensile deformation and failure process of unidirectional composites, Composites science and technology 52 (2) (1994) 197–204.

[21] G. Van Vinckenroy, W. De Wilde, The use of monte carlo techniques in statistical finite element methods for the determination of the structural behaviour of composite materials structural components, Composite Structures 32 (1-4) (1995) 247–253.

[22] S. A. English, T. M. Briggs, S. M. Nelson, Quantitative validation of carbon-fiber laminate low velocity impact simulations, Composite Structures 135 (2016) 250–261.

[23] A. Soto, E. González, P. Maimí, J. Mayugo, P. Pasquali, P. Camanho, A methodology to simulate low velocity impact and compression after impact in large composite stiffened panels, Composite Structures 204 (2018) 223–238.

[24] C. Furtado, G. Catalanotti, A. Arteiro, P. Gray, B. Wardle, P. Camanho, Simulation of failure in laminated polymer composites: Building-block validation, Composite Structures 226 (2019) 111168.

[25] P. Maimí, P. P. Camanho, J. Mayugo, C. Dávila, A continuum damage model for composite laminates: Part I–constitutive model, Mechanics of Materials 39 (10) (2007) 897–908.

[26] P. Maimí, P. P. Camanho, J. Mayugo, C. Dávila, A continuum damage model for composite laminates: Part II–computational implementation and validation, Mechanics of Materials 39 (10) (2007) 909–919.

[27] A. Turon, E. González, C. Sarrado, G. Guillamet, P. Maimí, Accurate simulation of delamination under mixed-mode loading using a cohesive model with a mode-dependent penalty stiffness, Composite Structures 184 (2018) 506–511.

[28] G. Catalanotti, C. Furtado, T. Scalici, G. Pitarresi, F. Van Der Meer, P. Camanho, The effect of through-thickness compressive stress on mode ii interlaminar fracture toughness, Composite Structures 182 (2017) 153–163.

[29] R. Bogenfeld, J. Kreikemeier, T. Wille, Review and benchmark study on the analysis of low-velocity impact on composite laminates, Engineering Failure Analysis 86 (2018) 72–99.

[30] E. González, P. Maimí, P. Camanho, A. Turon, J. Mayugo, Simulation of drop-weight impact and compression after impact tests on composite laminates, Composite Structures 94 (11) (2012) 3364–3378.

[31] S. Rivallant, C. Bouvet, N. Hongkarnjanakul, Failure analysis of cfrp laminates subjected to compression after impact: Fe simulation using discrete interface elements, Composites Part A: Applied Science and Manufacturing 55 (2013) 83–93.

[32] F. Caputo, A. De Luca, G. Lamanna, R. Borrelli, U. Mercurio, Numerical study for the structural analysis of composite laminates subjected to low velocity impact, Composites Part B: Engineering 67 (2014) 296–302.

[33] W. Tan, B. G. Falzon, L. N. Chiu, M. Price, Predicting low velocity impact damage and compression-after-impact (cai) behaviour of composite laminates, Composites Part A: Applied Science and Manufacturing 71 (2015) 212–226.

[34] H. Abdulhamid, C. Bouvet, L. Michel, J. Aboissière, C. Minot, Numerical simulation of impact and compression after impact of asymmetrically tapered laminated cfrp, International Journal of Impact Engineering 95 (2016) 154–164.

[35] G. Perillo, J. K. Jørgensen, R. Cristiano, A. Riccio, A numerical/experimental study on the impact and cai behaviour of glass reinforced compsite plates, Applied Composite Materials 25 (2) (2018) 425–447.

[36] X. Sun, S. Hallett, Failure mechanisms and damage evolution of laminated composites under compression after impact (cai): Experimental and numerical study, Composites Part A: Applied Science and Manufacturing 104 (2018) 41–59.

[37] H. Liu, B. G. Falzon, W. Tan, Predicting the compression-after-impact (cai) strength of damage-tolerant hybrid unidirectional/woven carbon-fibre reinforced composite laminates, Composites Part A: Applied Science and Manufacturing 105 (2018) 189–202.

[38] A. Sasikumar, J. Costa, D. Trias, E. González, S. García-Rodríguez, P. Maimí, Unsymmetrical stacking sequences as a novel approach to tailor damage resistance under out-of-plane impact loading, Composites Science and Technology 173 (2019) 125–135.

[39] E. González, P. Maimí, E. Martín-Santos, A. Soto, P. Cruz, F. M. de la Escalera, J. S. de Aja, Simulating drop-weight impact and compression after impact tests on composite laminates using conventional shell finite elements, International Journal of Solids and Structures 144 (2018) 230–247.

[40] A. Soto, E. González, P. Maimí, F. M. De La Escalera, J. S. De Aja, E. Alvarez, Low velocity impact and compression after impact simulation of thin ply laminates, Composites Part A: Applied Science and Manufacturing 109 (2018) 413–427.

[41] E. González, P. Maimí, A. Turon, P. Camanho, J. Renart, Simulation of delamination by means of cohesive elements using an explicit finite element code, Computers, Materials & Continua (CMC) 9 (1) (2009) 51.

[42] S. Patel, C. G. Soares, System probability of failure and sensitivity analyses of composite plates under low velocity impact, Composite Structures 180 (2017) 1022–1031.

[43] S. Patel, C. G. Soares, Reliability assessment of glass epoxy composite plates due to low velocity impact, Composite Structures.

[44] E. Greenhalgh, Failure analysis and fractography of polymer composites, Woodhead, Cambridge, 2009.

[45] R. Elhajjar, P. N. Grant, C. Ashforth, Composite structures: effects of defects.

[46] M. Mehdikhani, N. A. Petrov, I. Straumit, A. R. Melro, S. V. Lomov, L. Gorbatikh, The effect of voids on matrix cracking in composite laminates as revealed by combined computations at the micro-and meso-scales, Composites Part A: Applied Science and Manufacturing 117 (2019) 180–192.

[47] X.-Y. Zhou, S.-Y. Qian, N.-W. Wang, W. Xiong, W.-Q. Wu, A review on stochastic multiscale analysis for frp composite structures, Composite Structures 284 (2022) 115132.

[48] P. Yang, R. Elhajjar, Porosity content evaluation in carbon-fiber/epoxy composites using X-ray computed tomography, Polymer-Plastics Technology and Engineering 53 (3) (2014) 217–222.

[49] J. Thomason, The interface region in glass fibre-reinforced epoxy resin composites: 2. water absorption, voids and the interface, Composites 7 (26) (1995) 477–485.

[50] B. Drach, I. Tsukrov, T. Gross, S. Dietrich, K. Weidenmann, R. Piat, T. Böhlke, Numerical modeling of carbon/carbon composites with nanotextured matrix and 3D pores of irregular shapes, International Journal of Solids and Structures 48 (18) (2011) 2447–2457.

[51] K. Tserpes, A. Stamopoulos, S. G. Pantelakis, A numerical methodology for simulating the mechanical behavior of CFRP laminates containing pores using X-ray computed tomography data, Composites Part B: Engineering 102 (2016) 122–133.

[52] A. Matveeva, D. Garoz, R. Sevenois, M. Zhu, L. Pyl, W. Van Paepegem, L. Farkas, Effect of intra-ply voids on the homogenized behavior of a ply in multidirectional laminates, in: IOP Conference Series: Materials Science and Engineering, Vol. 406, IOP Publishing, 2018, p. 012009.

[53] A. Stamopoulos, K. Tserpes, P. Prucha, D. Vavrik, Evaluation of porosity effects on the mechanical properties of carbon fiber-reinforced plastic unidirectional laminates by X-ray computed tomography and mechanical testing, Journal of Composite Materials 50 (15) (2016) 2087–2098.

[54] H. Huang, R. Talreja, Effects of void geometry on elastic properties of unidirectional fiber reinforced composites, Composites Science and Technology 65 (13) (2005) 1964–1981.

[55] H. Zhu, B. Wu, D. Li, D. Zhang, Y. Chen, Influence of voids on the tensile performance of carbon/epoxy fabric laminates, Journal of Materials Science & Technology 27 (1) (2011) 69–73.

[56] P. Yang, R. El-Hajjar, Porosity defect morphology effects in carbon fiber–epoxy composites, Polymer-Plastics Technology and Engineering 51 (11) (2012) 1141–1148.

[57] A. Scott, I. Sinclair, S. M. Spearing, M. N. Mavrogordato, W. Hepples, Influence of voids on damage mechanisms in carbon/epoxy composites determined via high resolution computed tomography, Composites Science and Technology 90 (2014) 147–153.

[58] A. Hyde, J. He, X. Cui, J. Lua, L. Liu, Effects of microvoids on strength of unidirectional fiber-reinforced composite materials, Composites Part B: Engineering 187 (2020) 107844.

[59] D. A. Vajari, C. Gonzalez, J. Llorca, B. N. Legarth, A numerical study of the influence of microvoids in the transverse mechanical response of unidirectional composites, Composites Science and Technology 97 (2014) 46–54.

[60] A. Chambers, J. Earl, C. Squires, M. Suhot, The effect of voids on the flexural fatigue performance of unidirectional carbon fibre composites developed for wind turbine applications, International journal of fatigue 28 (10) (2006) 1389–1398.

[61] S. Hernández, F. Sket, J. Molina-Aldareguı, C. González, J. LLorca, et al., Effect of curing cycle on void distribution and interlaminar shear strength in polymer-matrix composites, Composites science and technology 71 (10) (2011) 1331–1341.

[62] M. Mehdikhani, N. Q. Nguyen, I. Straumit, L. Gorbatikh, S. V. Lomov, Analysis of void morphology in composite laminates using micro-computed tomography, in: IOP Conference Series: Materials Science and Engineering, Vol. 406, IOP Publishing, 2018.

[63] A. Hyde, L. Liu, X. Cui, J. Lua, Micromechanics-enriched finite element modeling of composite structures with fiber waviness and void defects, in: AIAA Scitech 2019 Forum, 2019, p. 0694.

[64] S. Daggumati, A. Sharma, W. Van Paepegem, Synergistic effects of microscale variabilities on the thermo-mechanical behavior of a UD CFRP ply, International Journal of Mechanical Sciences 242 (2023) 108004.

[65] S. F. M. de Almeida, Z. d. S. N. Neto, Effect of void content on the strength of composite laminates, Composite structures 28 (2) (1994) 139–148.

[66] Y. Chu, L. Sun, X. Yang, J. Wang, W. Huang, Multiscale simulation and theoretical prediction for the elastic properties of unidirectional fiber-reinforced polymer containing random void defects, Polymer Composites 42 (6) (2021) 2958–2972.

[67] T. Sebaey, G. Catalanotti, C. Lopes, N. O'Dowd, Computational micromechanics of the effect of fibre misalignment on the longitudinal compression and shear properties of ud fibre-reinforced plastics, Composite Structures 248 (2020) 112487.

[68] K. Potter, C. Langer, B. Hodgkiss, S. Lamb, Sources of variability in uncured aerospace grade unidirectional carbon fibre epoxy preimpregnate, Composites Part A: Applied Science and Manufacturing 38 (3) (2007) 905–916.

[69] M. Hinckley, Statistical evaluation of the variation in laminated composite properties resulting from ply misalignment, in: Advances in Optical Structure Systems, Vol. 1303, International Society for Optics and Photonics, 1990, pp. 497–511.

[70] Y. Arao, J. Koyanagi, S. Utsunomiya, H. Kawada, Effect of ply angle misalignment on out-of-plane deformation of symmetrical cross-ply cfrp laminates: Accuracy of the ply angle alignment, Composite Structures 93 (4) (2011) 1225–1230.

[71] J. Steeves, S. Pellegrino, Post-cure shape errors of ultra-thin symmetric cfrp laminates: Effect of ply-level imperfections, Composite structures 164 (2017) 237–247.

[72] S. J. Thompson, S. Bichon, R. J. Grant, Influence of ply misalignment on form error in the manufacturing of cfrp mirrors, Optical Materials Express 4 (1) (2014) 79–91.

[73] J.-M. Berthelot, Classical laminate theory, Springer New York, 1999.

[74] D. Trias, J. Costa, A. Turon, J. Hurtado, Determination of the critical size of a statistical representative volume element (SRVE) for carbon reinforced polymers, Acta materialia 54 (13) (2006) 3471–3484.

[75] J. Zangenberg, P. Brøndsted, Determination of the minimum size of a statistical representative volume element from a fibre-reinforced composite based on point pattern statistics, Scripta Materialia 68 (7) (2013) 503–505.

[76] Y. Li, L. Zhou, M. Zhang, C. Song, Study on the effect of void defect on mechanical properties of carbon fiber composites by finite element method, Journal of The Institution of Engineers (India): Series C 103 (6) (2022) 1433–1446.

[77] C. González, J. LLorca, Mechanical behavior of unidirectional fiber-reinforced polymers under transverse compression: Microscopic mechanisms and modeling, Composites Science and Technology 67 (13) (2007) 2795–2806.

[78] A. Melro, P. Camanho, S. Pinho, Generation of random distribution of fibres in long-fibre reinforced composites, Composites Science and Technology 68 (9) (2008) 2092–2102.

[79] D. Trias, J. Costa, J. Mayugo, J. E. Hurtado, Random models versus periodic models for fibre reinforced composites, Computational Materials Science 38 (2) 316–324.

[80] V. Romanov, S. V. Lomov, Y. Swolfs, S. Orlova, L. Gorbatikh, I. Verpoest, Statistical analysis of real and simulated fibre arrangements in unidirectional composites, Composites Science and Technology 87 (2013) 126–134.

[81] T. J. Vaughan, C. T. McCarthy, A combined experimental-numerical approach for generating statistically equivalent fibre distributions for high strength laminated composite materials, Composites Science and Technology 70 (2) (2010) 291–297.

[82] L. Yang, Y. Yan, Z. Ran, Y. Liu, A new method for generating random fibre distributions for fibre reinforced composites, Composites Science and Technology 76 (2013) 14–20.

[83] Z. Shan, A. M. Gokhale, Representative volume element for non-uniform microstructure, Computational Materials Science 24 (3) (2002) 361–379.

[84] R. M. Sencu, Z. Yang, Y. C. Wang, P. J. Withers, C. Rau, A. Parson, C. Soutis, Generation of micro-scale finite element models from synchrotron X-ray CT images for multidirectional carbon fibre reinforced composites, Composites Part A: Applied Science and Manufacturing 91 (2016) 85–95.

[85] R. Pyrz, Quantitative description of the microstructure of composites. Part I: Morphology of unidirectional composite systems, Composites Science and Technology 50 (2) (1994) 197–208.

[86] V. A. Buryachenko, R. Y. Kim, N. J. Pagano, J. E. Spowart, Quantitative description and numerical simulation of random microstructures of composites and their effective elastic moduli, International Journal of Solids and Structures 40 (1) (2003) 47–72.

[87] J. H. Oh, K. K. Jin, S. K. Ha, Interfacial strain distribution of a unidirectional composite with randomly distributed fibers under transverse loading, Journal of Composite Materials 40 (9) (2006) 759–778.

[88] T. Zhang, Y. Yan, A comparison between random model and periodic model for fiber-reinforced composites based on a new method for generating fiber distributions, Polymer Composites 38 (1) (2017) 77–86.

[89] Y. Ismail, D. Yang, J. Ye, Discrete element method for generating random fibre distributions in micromechanical models of fibre reinforced composite laminates, Composites Part B: Engineering 90 (2016) 485–492.

[90] Y. Ismail, Y. Sheng, D. Yang, J. Ye, Discrete element modelling of unidirectional fibre-reinforced polymers under transverse tension, Composites Part B: Engineering 73 (2015) 118–125.

[91] A. Wongsto, S. Li, Micromechanical FE analysis of UD fibre-reinforced composites with fibres distributed at random over the transverse cross-section, Composites Part A: Applied Science and Manufacturing 36 (9) (2005) 1246–1266.

[92] S. A. Elnekhaily, R. Talreja, Damage initiation in unidirectional fiber composites with different degrees of nonuniform fiber distribution, Composites Science and Technology 155 (2018) 22–32.

[93] H. Qing, L. Mishnaevsky, Unidirectional high fiber content composites: Automatic 3D FE model generation and damage simulation, Computational Materials Science 47 (2) (2009) 548–555.

[94] R. P. Tavares, A. R. Melro, M. A. Bessa, A. Turon, W. K. Liu, P. P. Camanho, Mechanics of hybrid polymer composites: analytical and computational study, Computational Mechanics 57 (3) (2016) 405–421.

[95] C. Dong, Effects of process-induced voids on the properties of fibre reinforced composites, Journal of Materials Science & Technology 32 (7) (2016) 597–604.

[96] F. Sharifpour, J. Montesano, R. Talreja, Assessing the effects of ply constraints on local stress states in cross-ply laminates containing manufacturing induced defects, Composites Part B: Engineering 199 (2020) 108227.

[97] M. Vinot, C. Liebold, T. Usta, M. Holzapfel, N. Toso, H. Voggenreiter, Stochastic modelling of continuous glass-fibre reinforced plastics–considering material uncertainty in microscale simulations, Journal of Composite Materials 57 (1) (2023) 133–145.

[98] A. Arteiro, L. Pereira, M. Bessa, C. Furtado, P. Camanho, A micro-mechanics perspective to the invariant-based approach to stiffness, Composites Science and Technology 176 (2019) 72–80.

[99] T. Mori, K. Tanaka, Average stress in matrix and average elastic energy of materials with misfitting inclusions, Acta metallurgica 21 (5) (1973) 571–574.

[100] E. Marklund, J. Varna, R. C. Neagu, E. K. Gamstedt, Stiffness of aligned wood fiber composites: effect of microstructure and phase properties, Journal of composite materials 42 (22) (2008) 2377–2405.

[101] Z. Hashin, Analysis of composite materials—a survey, Journal of Applied Mechanics 50 (3) (1983) 481–505.

[102] R. Christensen, K. Lo, Solutions for effective shear properties in three phase sphere and cylinder models, Journal of the Mechanics and Physics of Solids 27 (4) (1979) 315–330.

[103] C. Rousseau, How various uncertainties and assumptions affect b-basis allowables development., Lockheed Martin Corporation, 2013.

[104] P. R. Spendley, Design allowables for composite aerospace structures, Ph.D. thesis, University of Surrey (2012).

[105] F. Abdi, E. Clarkson, C. Godines, S. DorMohammadi, Ab basis allowable test reduction approach and composite generic basis strength values, in: 18th AIAA Non-Deterministic Approaches Conference, 2016, p. 0951.

[106] Y. Zhang, J. Schutte, J. Meeker, U. Palliyaguru, N. H. Kim, R. T. Haftka, Predicting b-basis allowable at untested points from experiments and simulations of plates with holes, in: 12th world congress on structural and multidisciplinary optimization, Braunschweig, Germany., 2017.

[107] G. Abumeri, F. Abdi, K. Raju, J. Housner, R. Bohner, A. McCloskey, Cost effective computational approach for generation of polymeric composite material allowables for reduced testing, in: Advances in Composite Materials-Ecodesign and Analysis, InTech, 2011.

[108] P. P. Camanho, G. Catalanotti, On the relation between the mode i fracture toughness of a composite laminate and that of a 0 ply: Analytical model and experimental validation, Engineering Fracture Mechanics 78 (13) (2011) 2535–2546.

[109] G. Catalanotti, A. Arteiro, M. Hayati, P. P. Camanho, Determination of the mode i crack resistance curve of polymer composites using the size-effect law, Engineering Fracture Mechanics 118 (2014) 49–65.

[110] G. Catalanotti, J. Xavier, P. P. Camanho, Measurement of the compressive crack resistance curve of composites using the size effect law, Composites Part A: Applied Science and Manufacturing 56 (2014) 300–307.

[111] Z. P. Bazant, J. Planas, Fracture and size effect in concrete and other quasibrittle materials, Vol. 16, CRC press, 1997.

[112] W. C. (PA), A. S. for Testing, M. (ASTM), Standard test method for open hole tensile strength of polymer matrix composite laminates, ASTM D 5766/D 5766M – 02a.

[113] P. P. Camanho, P. Maimí, C. Dávila, Prediction of size effects in notched laminates using continuum damage mechanics, Composites science and technology 67 (13) (2007) 2715–2727.

[114] A. Arteiro, G. Catalanotti, J. Xavier, P. Camanho, Large damage capability of non-crimp fabric thin-ply laminates, Composites Part A: Applied Science and Manufacturing 63 (2014) 110–122.

[115] G. Catalanotti, P. Camanho, A semi-analytical method to predict net-tension failure of mechanically fastened joints in composite laminates, Composites Science and Technology 76 (2013) 69–76.

[116] F. Laurin, P. Paulmier, F.-X. Irisarri, Determination of the longitudinal compressive strength of a cfrp ply through a tensile test on a laminate, Composites Part A: Applied Science and Manufacturing 113 (2018) 209–219.

[117] O. Vallmajó, I. Cózar, C. Furtado, R. Tavares, A. Arteiro, A. Turon, P. Camanho, Virtual calculation of the b-value allowables of notched composite laminates, Composite Structures 212 (2019) 11–21.

[118] P. D. Gosling, O. Polit, et al., A high-fidelity first-order reliability analysis for shear deformable laminated composite plates, Composite Structures 115 (2014) 12–28.

[119] A. Delbariani-Nejad, A. Farrokhabadi, S. R. Jafari, An energy based approach for reliability analysis of delamination growth under mode I, mode II and mixed mode I/II loading in composite laminates, International Journal of Mechanical Sciences 145 (2018) 287–298.

[120] O. S. Hussein, S. B. Mulani, Reliability analysis and optimization of in-plane functionally graded cnt-reinforced composite plates, Structural and Multidisciplinary Optimization 58 (3) (2018) 1221–1232.

[121] AITM, Airbus Test Method. Fibre Reinforced Plastics: Determination of Compression Strength after Impact, Tech. rep., Blagnac Cedex, France (2005).

[122] A. Sasikumar, D. Trias, J. Costa, N. Blanco, J. Orr, P. Linde, Effect of ply thickness and ply level hybridization on the compression after impact strength of thin laminates, Composites Part A: Applied Science and Manufacturing 121 (2019) 232–243.

[123] A. Turon, P. Camanho, J. Costa, J. Renart, Accurate simulation of delamination growth under mixed-mode loading using cohesive elements: definition of interlaminar strengths and elastic stiffness, Composite structures 92 (8) (2010) 1857–1864.

[124] F. Campolongo, J. Cariboni, A. Saltelli, An effective screening design for sensitivity analysis of large models, Environmental modelling & software 22 (10) (2007) 1509–1518.

[125] I. Cózar, A. Turon, E. González, O. Vallmajó, A. Sasikumar, A methodology to obtain material design allowables from high-fidelity compression after impact simulations on composite laminates, Composites Part A: Applied Science and Manufacturing 139 (2020) 106069.

[126] O. Vallmajó, A. Arteiro, J. Guerrero, A. Melro, A. Pupurs, A. Turon, Micromechanical analysis of composite materials considering material variability and microvoids, International Journal of Mechanical Sciences (2023) 108781.

[127] M. H. Nguyen, A. A. Vijayachandran, P. Davidson, D. Call, D. Lee, A. M. Waas, Effect of automated fiber placement (afp) manufacturing signature on mechanical performance of composite structures, Composite Structures 228 (2019) 111335.

[128] G. Catalanotti, R. M. Salgado, P. P. Camanho, On the stress intensity factor of cracks emanating from circular and elliptical holes in orthotropic plates, Engineering Fracture Mechanics 252 (2021) 107805.

[129] G. Bao, S. Ho, Z. Suo, B. Fan, The role of material orthotropy in fracture specimens for composites, International Journal of Solids and Structures 29 (9) (1992) 1105–1116.

[130] Corrigenda, International Journal of Solids and Structures 29 (16) (1992) 2115. doi:https://doi.org/10.1016/0020-7683(92)90198-3.
URL https://www.sciencedirect.com/science/article/pii/0020768392901983

[131] ABAQUS Inc., User's Manual, 6.14-2, Pawtucket, RI, USA (2014).

[132] A. Sasikumar, A. Turon, I. R. Cózar, O. Vallmajó, J. C. Casero, M. De Lozzo, S. Abdel-Monsef, Sensitivity analysis methodology to identify the critical material properties that affect the open hole strength of composites, Journal of Composite Materials 57 (10) (2023) 1791–1805.

[133] K. Potter, B. Khan, M. Wisnom, T. Bell, J. Stevens, Variability, fibre waviness and misalignment in the determination of the properties of composite materials and structures, Composites Part A: Applied Science and Manufacturing 39 (9) (2008) 1343–1354.

[134] P. P. Camanho, P. Maimí, C. Dávila, Prediction of size effects in notched laminates using continuum damage mechanics, Composites science and technology 67 (13) (2007) 2715–2727.

[135] M. Bodaghi, C. Cristóvão, R. Gomes, N. Correia, Experimental characterization of voids in high fibre volume fraction composites processed by high injection pressure RTM, Composites Part A: Applied Science and Manufacturing 82 (2016) 88–99.

[136] D. Zhang, D. Heider, S. G. Advani, J. Gillespie, Out of autoclave consolidation of voids in continuous fiber reinforced thermoplastic composites, SAMPE 2013-Long Beach, CA (2013) 16.

[137] R. Hill, Elastic properties of reinforced solids: some theoretical principles, Journal of the Mechanics and Physics of Solids 11 (5) (1963) 357–372.

[138] V. Tavaf, M. Saadatzi, S. Banerjee, Quantification of degraded constitutive coefficients of composites in the presence of distributed defects, Journal of Composite Materials 53 (18) (2019) 2517–2529.

[139] M. Mehdikhani, L. Gorbatikh, I. Verpoest, S. V. Lomov, Voids in fiber-reinforced polymer composites: A review on their formation, characteristics, and effects on mechanical performance, Journal of Composite Materials 53 (12) (2019) 1579–1669.

[140] K. J. Bowles, S. Frimpong, Relationship between voids and interlaminar shear strength of polymer matrix composites, in: International SAMPE Symposium and Exhibition, no. E-5825, 1991.

[141] A. Melro, P. Camanho, F. A. Pires, S. Pinho, Numerical simulation of the non-linear deformation of 5-harness satin weaves, Computational Materials Science 61 (2012) 116–126.

[142] T. Chen, G. J. Dvorak, Y. Benveniste, Mori-Tanaka estimates of the overall elastic moduli of certain composite materials, ASME Journal of Applied Mechanics 59 (3) (1992) 539–546.

[143] P. D. Soden, M. J. Hinton, A. Kaddour, Lamina properties, lay-up configurations and loading conditions for a range of fibre reinforced composite laminates, in:

Failure criteria in fibre-reinforced-polymer composites, Elsevier, 2004, pp. 30–51.

[144] D. G. Sotiropoulos, K. Tserpes, Interval-based computation of the uncertainty in the mechanical properties and the failure analysis of unidirectional composite materials, Mathematical and Computational Applications 27 (3) (2022) 38.

[145] C. Breite, A. Melnikov, A. Turon, A. de Morais, C. Le Bourlot, E. Maire, E. Schöberl, F. Otero, F. Mesquita, I. Sinclair, et al., A synchrotron computed tomography dataset for validation of longitudinal tensile failure models based on fibre break and cluster development, Data in Brief 39 (2021) 107590.

[146] A. Melro, P. Camanho, S. Pinho, Influence of geometrical parameters on the elastic response of unidirectional composite materials, Composite Structures 94 (11) (2012) 3223–3231.

[147] J.-H. Tai, A. Kaw, Transverse shear modulus of unidirectional composites with voids estimated by the multiple-cells model, Composites Part A: Applied Science and Manufacturing 105 (2018) 310–320.

Part IV

Appendices

Papers in their journal form

A

A.1 Paper A – Virtual calculation of the B-value allowables of notched composite laminates

The paper has been published in *Composite Structures* 212 (2019) 11-21.

Composite Structures 212 (2019) 11–21

Contents lists available at ScienceDirect

Composite Structures

journal homepage: www.elsevier.com/locate/compstruct

Virtual calculation of the B-value allowables of notched composite laminates

O. Vallmajó[a], I.R. Cózar[a], C. Furtado[b,c], R. Tavares[a,b,c], A. Arteiro[b,c], A. Turon[a,*], P.P. Camanho[b,c]

[a] AMADE, Polytechnic School, University of Girona, C/Universitat de Girona 4, 17003 Girona, Spain
[b] DEMec, Faculdade de Engenharia, Universidade do Porto, Rua Dr. Roberto Frias, 4200-465 Porto, Portugal
[c] INEGI, Rua Dr. Roberto Frias, 400, 4200-465 Porto, Portugal

A B S T R A C T

The design of composite structures relies on the accurate determination of design allowables, which are statistically based material parameters that take into account manufacturing, geometrical and microstructure variability. The accurate determination of these design parameters requires extensive experimental testing, which makes the certification process of a composite material extremely costly and time consuming. To increase the efficiency of the design process, there is the need to develop alternatives to the mostly experimental material characterization process, ideally based on accurate and quick modelling analysis combined with powerful statistical tools.

In this work an analytical model to compute the notched strength of composite structures based on three ply-based material properties (elastic modulus, un-notched strength and $\mathscr{R}$-curve) is combined with an uncertainty quantification and management (UQ&M) framework to compute the B-basis design allowables of notched configurations of CFRP laminates. The framework is validated with open-hole tension experimental results for the IM7/8552 material. Given the analytical nature of the developed framework and consequent computational efficiency, the UQ&M methodology is applied to the generation of design charts for notched geometries, whose generation would otherwise be impractical, using experimental test based methods.

1. Introduction

The design and certification of composite structures is based on the building block approach [1]. This approach relies on the accurate determination of design allowables that drive the design of structures at larger scales. These design allowables are statistically based material parameters that define an acceptable stress value for a material and, therefore, ensure their safe and efficient use. Design allowables have to account for the variability of the material properties and of the manufacturing process, and are a function of the structural details and loading conditions [2] and, consequently, their experimental determination is an extremely costly and time-consuming process. The standard design allowable used in the aeronautical industry for fail safe structures is the B-basis [1,3], which is defined as the 95% lower confidence bound on the tenth percentile of a specified population of measurements. This is a conservative allowable that ensures with 95% confidence that 90% of the population will have a given property, e.g. strength, higher than the B-value allowable.

It is of key importance to accurately determine these design allowables, however, time consuming processes are not ideal during preliminary design. For this reason, alternatives to fully experimental material characterization have been proposed, namely, the use of statistically based numerical and analytical models [4–6,3]. These models include the influence of the uncertainty related to the determination of the input parameters and their intrinsic variability on the global response of the model. A convenient way to describe these uncertain quantities is to describe them using a probability distribution which can be defined through experimental measurements or assumed based on empirical evidence.

The stochastic finite element method [7,5] is a powerful tool to address the influence of the uncertainty related to the determination of the material and geometrical properties and loading conditions on the global response of composite structures. Nam et al. [7] proposed a methodology to determine the design allowables of composite laminates using lamina level test data and finite element analysis and validate the proposed methodology for both un-notched and open hole strength. However, stochastic finite element method solutions rely on computationally expensive procedures, which makes the consideration of the variability of the input parameters an extremely time consuming and, therefore, impracticable process quick design.

Quick analytical prediction tools are therefore desirable, specially for preliminary design and material selection. Furtado et al. [8] proposed an analytical framework to estimate the notched strength of multidirectional carbon-epoxy laminates based on three ply properties (the longitudinal Young's modulus, the longitudinal strength, and the longitudinal crack resistance curve) and concluded that the framework was able to provide good predictions for the open-hole tensile and compressive strengths of general balanced carbon/epoxy laminates.

* Corresponding author.
E-mail address: albert.turon@udg.edu (A. Turon).

https://doi.org/10.1016/j.compstruct.2018.12.049
Received 14 December 2018; Accepted 19 December 2018
Available online 23 December 2018
0263-8223/ © 2018 Elsevier Ltd. All rights reserved.

Since the model uses ply-level properties as building blocks, it is ideal for preliminary design, since the notched strength of different layups and geometries can be quickly estimated.

The authors validated the analytical framework for the nominal values of the material properties and the geometrical parameters. However, the uncertainty associated to the material properties and dimensions may be taken into account in an attempt to define design allowables for the notched strength.

In this work, a methodology to predict the B-value of notched composite laminates using the analytical framework proposed by Furtado et al. [8] is proposed by taking the variability of the material properties that dominate failure and the effect of geometrical imperfections into account. The proposed Uncertainty Quantification and Management (UQ&M) methodology is validated against available experimental data and is applied to generate practical engineering design tools.

2. Methodology

2.1. Description of the analytical framework

Furtado et al. [8] proposed an analytical framework to estimate the notched strength of multidirectional carbon-epoxy laminates based on three ply properties: the longitudinal Young's modulus, E_1, the longitudinal strength, X, and the longitudinal crack resistance curve, $\mathscr{R}$-curve. The framework combines the finite fracture mechanics model proposed by Camanho et al. [9] with the invariant-based approaches to estimate stiffness and strength proposed by Tsai and Melo [10,11] and with an analytical model based on linear elastic fracture mechanics to estimate the laminate fracture toughness proposed by Camanho et al. [12].

The coupled Finite Fracture Mechanics (FFMs) model proposed by Camanho et al. [9] is used to predict the notched strength of open-hole laminate specimens (Fig. 1) with fibre dominated failure. Both a stress-based and energy-based criteria must be satisfied during crack propagation:

$$\begin{cases} \frac{1}{l}\int_R^{R+l} \sigma_{xx}(0,y)dy = X^L \\ \int_R^{R+l} \mathscr{G}_I(a)da = \int_0^l \mathscr{R}(\Delta a)d\Delta a \end{cases} \quad (1)$$

where R is the hole radius, $\sigma_{xx}(0,y)$ is the stress distribution along the ligament section perpendicular to the loading direction (along the transverse axis), X^L is the laminate unnotched strength, $\mathscr{G}_I(a)$ is the mode I energy release rate (ERR) of a laminated plate with a central circular hole of radius R and two symmetric cracks propagating from the hole edge, $\mathscr{R}(\Delta a)$ is the $\mathscr{R}$-curve of the laminate and l is the crack extension at failure.

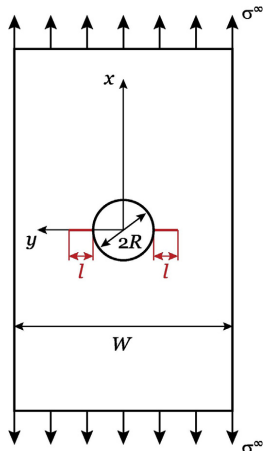

Fig. 1. Notched laminate with central circular open hole [8].

The first equation corresponds to the average-stress criterion while the second represents an energy balance. Therefore, a stress equilibrium between the average stress in the narrowest critical section with the hole and the maximum admissible strength of the laminate, and an equilibrium between the energy released and the maximum admissible fracture energy of the laminate in a finite length must be satisfied during crack propagation. The model only requires two independent laminate properties: the laminate unnotched strength X^L and the laminate $\mathscr{R}$-curve.

The FFMs model is therefore based on properties at laminate level, which need to be determined each time the layup changes. To determine the laminate unnotched strength X^L, Furtado et al. [8] proposed the use of the invariant-based approach to estimate stiffness and strength proposed by Tsai and Melo [10,11]. This approach is based on the Unit Circle failure envelope, which was proposed by Tsai and Melo [11] as a conservative simplification of the last ply failure Omni Strain Failure Envelope. The Unit Circle envelope is defined by the uniaxial tensile and compressive strains-to-failure. Following Tsai and Melo [11], the laminate unnotched strength under uniaxial loading is estimated by a simple maximum strain criterion:

$$X^L \approx \frac{X}{E_1} \times E^L \quad (2)$$

where X is the laminate unnotched strength, E_1 is the longitudinal Young's modulus and E^L is the laminate longitudinal Young's modulus, which can be estimated using the Trace theory and Master Ply concept [10]. Tsai and Melo [10] defined a Master Ply for CFRPs based on the finding that the normalised UD stiffness components of several CFRP systems (normalized by the trace) is almost constant. The authors concluded that the stiffness of CFRPs along the fibre direction is responsible for about 88% of the value of trace, which means that the value of trace can be estimated from the longitudinal stiffness E_1 as

$$Tr \approx \frac{E_1}{0.88} \quad (3)$$

The Young's modulus of a given laminate can be determined as a product of the value of trace and a laminate factor, which can be determined using laminate plate theory and the Master Ply presented in Table 1:

$$E^L \approx E_x/Tr \times \frac{E_1}{0.88} \quad (4)$$

To estimate the laminate $\mathscr{R}$-curve, the analytical model proposed by Camanho et al. [12] can be used. The model is based on a combination of linear elastic fracture mechanics and laminate plate theory and can be used to estimate the fracture toughness of balanced multidirectional laminates, G_{Ic}, using the fracture toughness of the 0° ply, G^0_{Ic}.

Furtado et al. [8] concluded that the framework is able to provide good predictions for the open-hole tensile and compressive strengths of general balanced carbon/epoxy laminates with fibre dominated failure using only the lay-up, the geometry of the specimen (the radius, R, and the width, W) and three ply properties as inputs: the longitudinal Young's modulus, E_1, the longitudinal strength, X, and the longitudinal

Table 1
Universal Laminate Factors of the Master Ply.

Lay-up	E_x/Tr	E_y/Tr	G_{xy}/Tr	ν_{xy}
Master Ply	0.880	0.052	0.031	0.320

crack resistance curve, $\mathscr{R}$-curve. Since the model uses only three ply level parameters as building blocks, the framework can be particularly useful for preliminary design and optimization, as the number of elementary tests needed to characterize the composite system is drastically reduced. In addition, due to the computational efficiency of the model it can be used to perform uncertainty quantification and management (UQ&M) analysis, allowing not only the analysis of the effects of the mean parameters on the response, but also the analysis of the influence of their variability.

2.2. Uncertainty quantification of the model parameters

The analytical framework [8] summarized in the previous section requires three ply material parameters to estimate the strength of a multidirectional notched laminate: the longitudinal Young's modulus, the longitudinal strength and the $\mathscr{R}$-curve of the 0° plies. The model was validated using the mean ply properties determined experimentally, resulting in the prediction of a nominal notched strength for a given nominal dimension (hole radius and specimen width). In this work, the variability associated with the determination of the ply properties and the geometry of the specimens is accounted for. The variability associated with the geometrical parameters (notch radius and specimen width) is directly related to the manufacturing process, namely the cutting methodology and respective tolerances. Since direct measurements were not available, the dimensions of the specimen were assumed to follow a uniform distribution.

Accounting for the variability of the longitudinal Young's modulus and the longitudinal strength is straightforward since these properties are obtained directly from the experimental tests and have an associated standard deviation. It is assumed here that these two properties follow a normal distribution with known mean and standard deviation, corresponding to the values obtained experimentally.

Accounting for the variability of the $\mathscr{R}$-curve is less clear since the $\mathscr{R}$-curves are generally not measured directly but determined from notched strengths measured experimentally. Thus, it is of key importance to define a methodology to randomly generate statistically representative $\mathscr{R}$-curves. Such methodology is proposed in Section 2.2.1.

2.2.1. Mode I crack resistance curve in the fibre direction

Catalanotti et al. [13,14] proposed a methodology to determine the $\mathscr{R}$-curve of polymer composites reinforced by unidirectional fibres based on the size effect law, i.e the relation between the size of the specimens and their notched strength $\bar{\sigma}^{\infty}(w)$. The size effect law can be determined by experimentally testing geometrically similar double edge notch specimens, i.e. with the same width-to-crack length ratio $2w/a$ and different widths $2w$. The size effect law can be determined by finding a fitting regression that best approximates the experimental data [15] and the $\mathscr{R}$-curve parameters (length of the fracture process zone, l_{fpz}, and the fracture toughness at propagation $\mathscr{R}_{ss}$) can then be obtained as a function of these fitting parameters [15,13,14]. Catalanotti et al. [13] also suggested to express the $\mathscr{R}$-curve analytically. In this work, the following analytical expression is proposed to represent the $\mathscr{R}$-curve:

$$\begin{cases} R(\Delta a) = R_{ss}[1-(1-\Delta a/l_{fpz})^{\beta}] & \text{if} \quad \Delta a < l_{fpz} \\ R(\Delta a) = R_{ss} & \text{if} \quad \Delta a \geqslant l_{fpz} \end{cases} \tag{5}$$

where β is a parameter determined to obtain the best fit of the $\mathscr{R}$-curve. The proposed equation guarantees that the steady state value of the fracture toughness is reached when $\Delta a = l_{fpz}$.Since the mean $\mathscr{R}$-curve is determined from the mean experimental notched strengths of the double edge notch specimens, accounting for the variability of the $\mathscr{R}$-curves implies accounting for the variability of the size effect law. Two methodologies to determine the variability of the $\mathscr{R}$-curves are proposed in this section.

2.2.1.1. Method 1.

The variability is obtained by generating a large number of $\mathscr{R}$-curves accounting for the variability of the notched strength ($\bar{\sigma}^{\infty}$) of the specimens with different geometries by:

1. Randomly generating N_i strengths per each specimen geometry following a statistical distribution determined experimentally for each specimen geometry.
2. Fitting the data to one of the fitting regressions proposed in Ref. [15].
3. Determining the $\mathscr{R}$-curve parameters (l_{fpz} and $\mathscr{R}_{ss}$) as proposed in Refs. [15,13,14].
4. Fitting the $\mathscr{R}$-curve to the analytical expression proposed in Eq. (5).
5. Repeat 1–4, N times obtaining a large number of R-curves and the distribution of the fitting parameters.

Using this methodology, a set of statistically representative crack resistance curves is obtained. With the generated $\mathscr{R}$-curves it is possible to determine the mean values and standard deviation of the three $\mathscr{R}$-curve fitting parameters (l_{fpz}, $\mathscr{R}_{ss}$ and β). However, due to the nature of the crack resistance curves, the fitting parameters cannot be treated independently as that would lead to unrealistic and potentially non-continuous $\mathscr{R}$-curves. For this reason, a relation between the parameters should be established as a function of $\mathscr{R}_{ss}$, i.e $l_{fpz} = f(\mathscr{R}_{ss})$ and $\beta = g(\mathscr{R}_{ss})$. These functions can vary and should be analysed for each material system considered. A more detailed analysis is given in Section 3.3.

2.2.1.2. Method 2.

The variability is obtained from the determination of the 95% prediction bounds of the linear regression used to fit the size effect law measured experimentally. Either the whole set of experimental points or the mean strengths per specimen geometry can be used, however, the confidence intervals will be generally narrower if only the mean size effect law is used. This process allows the determination of the mean $\mathscr{R}$-curve and the two 95% confidence $\mathscr{R}$-curves. The three $\mathscr{R}$-curve parameters and the respective standard deviations can also be determined.

This method provides only three sets of $\mathscr{R}$-curve parameters and therefore, $\mathscr{R}_{ss}$, l_{fpz} and β are considered independent. This second method is simpler to apply and less computationally expensive, however, the relation between $\mathscr{R}_{ss}$ and the remaining parameters has to be assumed, so caution is required when applying this method.

2.3. Estimation of the B-basis value

In the design of a composite structure it is important to take into account the variability of the design parameters, namely the material properties. According to the Composite Materials Handbook (CMH17) [1], variability should be taken into account in the design of composite structures by using the B-basis for the design allowables. The B-basis (B-value) is a statistically-based design allowable defined as the 95% lower confidence bound on the tenth percentile of a specified population of measurements [1].

By taking the variability of the input parameters (material and geometrical) and using the proposed analytical model, it is possible to propagate the uncertainty of the input parameters to the notched strength, i.e. a statistical distribution of the notched strength can be obtained, based on the variability of the input parameters, which can then be used to compute the statistical design allowables. To obtain the B-value for the open hole strength, two methodologies have been used: (i) the CMH-17 approach and (ii) a Monte Carlo based approach.

Both approaches rely on the set of material and geometrical properties and respective statistical distribution and differ in how the strength data is dealt with to determine the B-value. Nevertheless, for a given run of the analytical model the geometrical and material properties are considered deterministic.

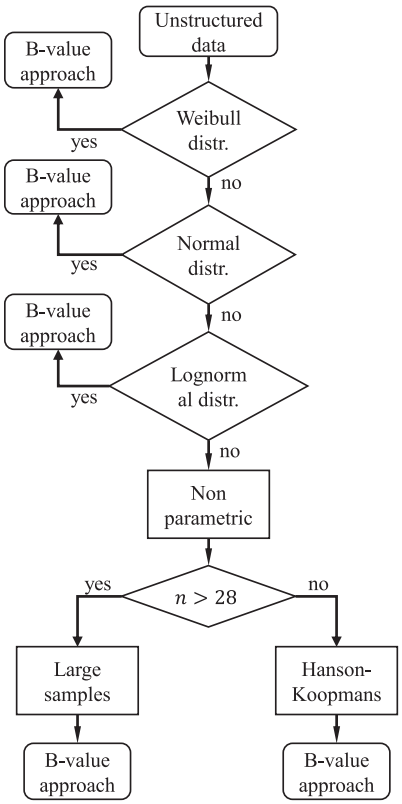

Fig. 2. Schematic representation of the steps to calculate the B-value using the CMH-17 methodology.

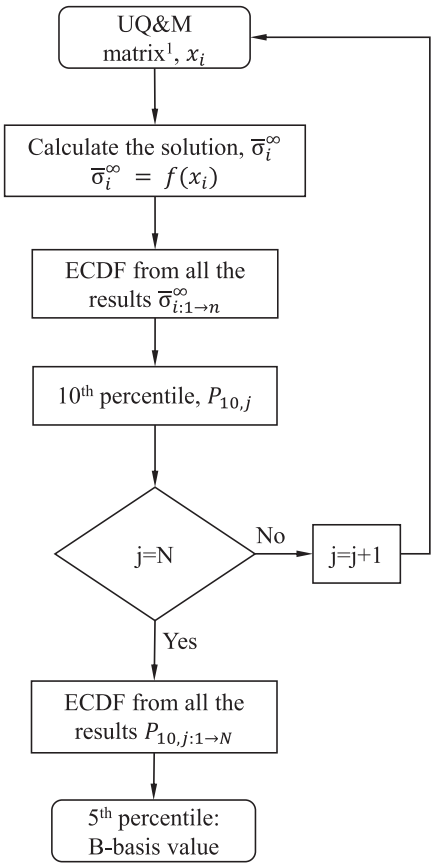

Fig. 3. Schematic representation of the steps to calculate the B-value using the Monte Carlo based methodology. [1]UQ&M matrix dimensions are: n different cases per 5 input variables (x_i); in the first iteration $j = 1$.

2.3.1. CMH-17 approach

The CMH-17 [1] defines different methods to determine the B-value depending on the distribution that best fits the data. As summarised in Fig. 2, for unstructured data, the CMH-17 suggests to successively test if the Weibull, normal and lognormal distributions are adequate fits to the data. If any of these distributions fits the data then the respective methods to calculate the B-basis should be used. If none of these three distributions can be assumed, nonparametric procedures should be used to determine the B-value.

To find the best fitting distribution, the CMH-17 suggests the use of the Anderson–Darling test. This test compares the Cumulative Distribution Function (CDF) of the distribution of interest with the CDF of the data, which allows the determination of a Observance Significance Level (OSL). If the calculated OSL is greater than 0.05, it is concluded that the distribution analysed fits the data. Otherwise, the analysed distribution does not fit the data and the subsequent distribution is analysed. Once a fitting distribution has been found, the B-value can be computed according to the procedures in the CMH-17 for that statistical distribution [1]. If none of these distributions fit the data, nonparametric procedures are used. These procedures depend on the sample size, being the Hanson-Koopmans method used for small sample sizes ($n < 28$). For large sample sizes the B-value can be computed from tabulated data in the CMH-17. For more information on these procedures, the reader is referred to the CMH-17 [1].

2.3.2. Monte Carlo simulations

The Monte Carlo Methods (MCS) rely on the repeated random sampling to obtain numerical results. To determine the B-value using this approach it is necessary to run the analytical model a large number of times to determine an Empirical Cumulative Distribution Function (ECDF) for the parameter in study, namely the notched strength. For each set of n results, where n is the sample size that should be large enough to be representative of the population, it is possible to determine the ECDF and extract the 10th percentile value, $P_{10,j}$. This process is repeated N times, determining a distribution for the 10th percentile. From this distribution the B-value can be computed by considering the 95% lower confidence bound [16], which corresponds to the 5th percentile of the ECDF. The MCS based methodology to calculate the B-value can be summarised as follows (see Fig. 3):

1. Design of the experiments (DOE). The material properties and geometrical parameters are distributed according to their associated

statistical distributions to define the uncertainty quantification and management matrix. Using the current analytical framework, the dimensions of the matrix are n x 5 where *n* are the different cases to be analysed and 5 are the model input parameters (E_{11}, X_T, $\mathscr{R}_{ssT}$, R and W).
2. Notched strength computation. For each case i the notched strength ($\bar{\sigma}_i^{\infty}$) is calculated using the analytical model described in Section 2.1.
3. Determination of the 10th percentile. Once all the cases have been computed ($\bar{\sigma}_{i:1\rightarrow n}^{\infty}$) the ECDF of the notched strengths is used to determine the $P_{10,j}$.
4. Computation of the B-basis allowable. Steps 1, 2 and 3 are repeated N times to obtain the ECDF of the $P_{10,j:1\rightarrow N}$ and to determine the 5th percentile which corresponds to the B-basis value.

If the sample size (n) is large enough, then the 10th percentile of the population can be directly approximated by the 10th percentile of the sample, as the variability between the samples will be minimal. This will be explored in more detail in Section 5.1.

3. Case study

3.1. Description of the case

To exemplify and validate the methodology proposed to calculate the B-value of the notched strength, IM7/8552 $[90/0/-45/45]_{3s}$ quasi isotropic laminate with a central circular hole loaded in tension was used. Hole diameter-to-width ratios of $0.05 < 2R/W < 0.6$ and hole diameters of 2, 4, 6, 8 and 10 mm were used.

As explained in Section 2.2, the variability associated with the material parameters and with the geometry of the specimens is considered to calculate the B-value. The input parameters used are presented hereafter.

3.2. Uncertainty quantification associated with the geometry of the specimens

The variability associated with the geometry of the specimens is directly related to the manufacturing process, namely the cutting methodology and respective allowed tolerances. The specimen dimensions were assumed to follow a uniform distribution with a maximum deviation of ± 2% of the nominal value of the width and hole diamater. (Table 2).

3.3. Uncertainty quantification associated with the determination of the material properties

In this work, it is assumed that the material properties follow a normal distribution with known mean and standard deviation. These properties are summarised in Table 3. The uncertainty related to the longitudinal Young's modulus and strength is directly related to the mean values ($\bar{x}$) and respective standard deviation (s) determined experimentally [18] while the variability of the $\mathscr{R}$-curve is determined as explained in Section 2.2.

The determination of the $\mathscr{R}$-curve is based on the size effect law which can be determined from the strengths of geometrically similar double edge notched specimens with different widths. Table 4 shows the notched strengths and respective standard deviations of the double edge notch tension specimens that were used to determine the longitudinal crack resistance curve of IM7/8552 material system [13].

Table 2
Variability of the geometry of the specimen [17].

Geometry	W [mm]	R [mm]
tol	± 2% × W	± 2% × R

Table 3
Value of the material properties used for the analysis [18].

IM7/8552	E_1 [GPa]	X_T [GPa]	$\mathscr{R}_{ssT}$ [N/mm]
$\bar{x}$	171.42	2323.47	206.75
s	2.38	127.45	23.64

Table 4
Double Edge Notched Tension Strength for IM7/8552 $[90/0]_{8s}$ [13].

Ref.	w [mm]	$\bar{x}$ [MPa]	s [MPa]
B	7.5	309	9
C	10	289	16
D	12.5	269	11
E	15	256	10

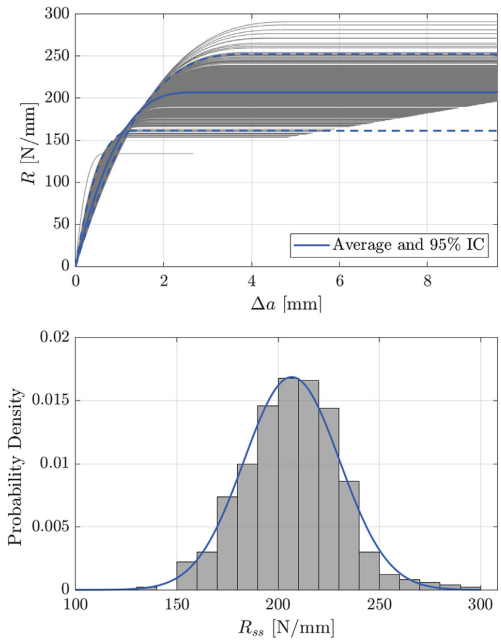

Fig. 4. Schematic representation of randomly generated $\mathscr{R}$-curves using method 1 (top) and distribution of the steady state fracture toughness R_{ss} (bottom).

Using Method 1 described in Section 2.2.1, a set of statistically representative crack resistance curves, with a known mean and standard deviation of the three fitting parameters (l_{fpz}, $\mathscr{R}_{ss}$ and β) is obtained, as shown in Fig. 4.

As explained in Section 2.2.1, the fitting parameters of the crack resistance curves cannot be treated independently as that would potentially lead to non admissible $\mathscr{R}$-curves. For this reason, a dependence between the parameters was established as a function of $\mathscr{R}_{ss}$. As shown in Fig. 5, it was found that l_{fpz} varies linearly with $\mathscr{R}_{ss}$ and β is almost constant for the case analysed. Therefore, the crack resistance curves can be defined as a function of $\mathscr{R}_{ss}$. $\mathscr{R}_{ss}$ is generated randomly following a normal distribution with a know mean (206.75 N/mm) and standard deviation (23.64 N/mm) and the other two parameters are estimated as:

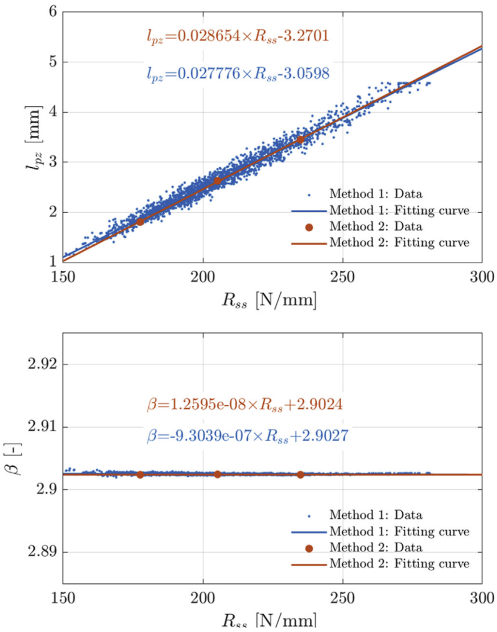

Fig. 5. $l_{fpz} = f(\mathscr{R}_{ss})$ (top) and $\beta = g(\mathscr{R}_{ss})$ (bottom) obtained with method 1 and method 2.

$$l_{fpz} = 2.7776 \times 10^{-2} \times \mathscr{R}_{ss} - 3.0598 \quad [\text{mm}]$$
$$\beta = 2.9027 \quad [-]$$

Using Method 2 the variability is obtained from the determination of the 95% prediction bounds of the fitting of the size effect law. Either the whole set of experimental points or the mean strengths per specimen geometry can be used. In this study only the mean strengths were used since the full set of results was not available.

Since this method provides only three sets of $\mathscr{R}$-curve parameters, the relation between l_{fpz}, $\mathscr{R}_{ss}$ and β is undefined. However, using method 1, it was shown that a linear functions can be used to relate $\mathscr{R}_{ss}$ to l_{fpz} and β, and so the fitting parameters of the curves can be easily determined as a function of $\mathscr{R}_{ss}$ as shown in Fig. 5. Using this method, $\mathscr{R}_{ss}$ is generated randomly following a normal distribution with a know mean (205.26 N/mm) and standard deviation (14.83 N/mm) and the other two parameters are estimated as:

$$l_{fpz} = 2.8654 \times 10^{-2} \times \mathscr{R}_{ss} - 3.2701 \quad [\text{mm}]$$
$$\beta = 2.9024 \quad [-]$$

As shown in Fig. 5 the fitting curves obtained with both methods show similar trends. Fig. 6 shows the normal distribution and the corresponding average and 95% IC $\mathscr{R}$-curves obtained with both methods. Only a 1.5 N/mm difference in the mean $\mathscr{R}_{ss}$ using methods 1 and 2 was found. However, since the standard deviation obtained using method 2 is around 40% lower than the one measured using method 1 because the confidence bounds were determined using the mean double edge notch strengths, the normal distribution of $\mathscr{R}_{ss}$ is significantly narrower if method 2 is used. Using the whole set of data would be preferred in method 2. Therefore, in, method 1 was used to characterize the distribution of the crack resistance curve parameters.

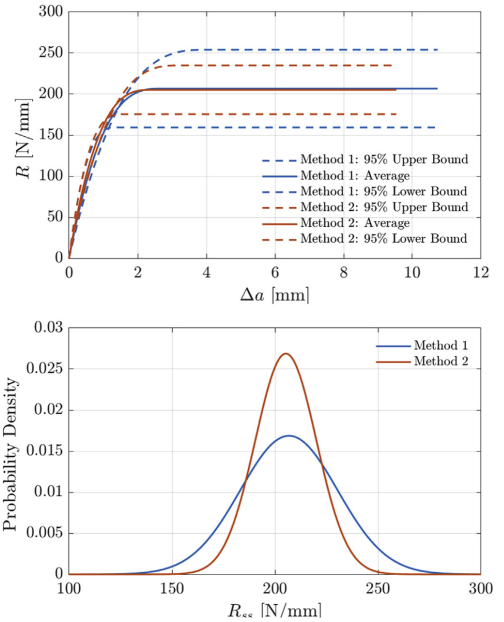

Fig. 6. Average and 95% confidence bounds $\mathscr{R}$-curves (top) and predicted normal distribution of $\mathscr{R}_{ss}$ using method 1 and method 2 (bottom).

4. Sensitivity analysis

Due to the analytical nature of the model, it is possible to run a large number of simulations within a reasonable time frame, enabling the performance of numerical analysis that would not be possible via experimental characterization or finite element simulations.

The proposed framework depends on three material properties and two geometrical properties. It is interesting to understand their influence on the expected notched strength of the laminate selected for this study. To do so, a sensitivity analysis was performed on these five parameters. The sensitivity analysis is performed by considering that the parameter in study varies while the remaining are kept constant and with a value equal to the nominal one. Here the material and layup considered are the ones presented in Section 3 and an open-hole tension specimen with width equal to 36 mm and hole radius of 3 mm is considered. For each material property a range from $\bar{x}_i - 3s_i$ to $\bar{x}_i + 3s_i$ was considered. For the geometrical parameters a variation of ± 2% was considered. The results of the sensitivity analysis are shown in Fig. 7.

From the sensitivity analysis, it is possible to conclude that, as expected, the material properties have a larger influence on the notched strength than the geometrical properties. For the Young's modulus the variation of the OH strength is linear, being lower for lower elastic moduli. Both the tensile strength and toughness of the material have a more complex influence on the open hole strength of the material. In addition, both have a higher influence on the open hole strength of the material, therefore, it is essential to accurately characterize these properties to ensure accurate predictions of the notched strength of composite laminates.

5. UQ&M framework validation

In this section the sample sizes required to accurately take into account geometrical and material variability within the UQ&M

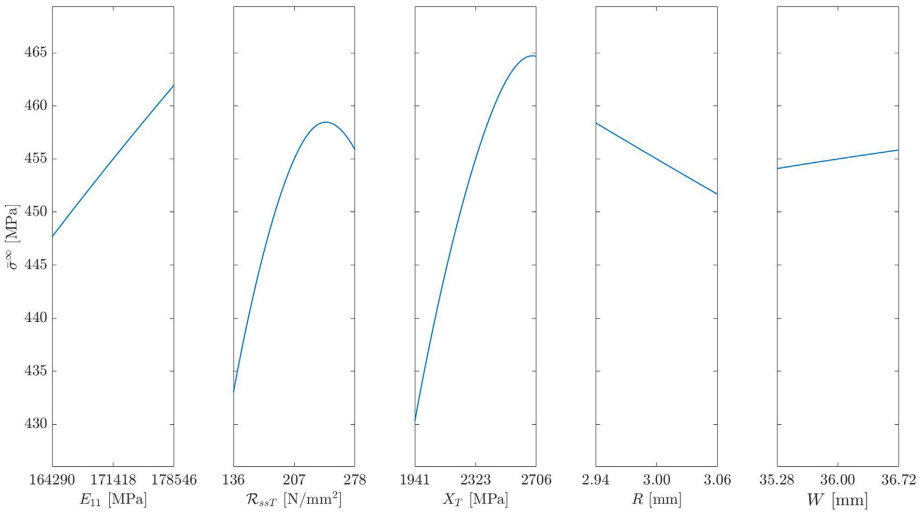

Fig. 7. Sensitivity analysis on the notched strength for $W = 36$ mm and $R = 3$ mm.

framework is analysed and the results are validated against available experimental data.

5.1. Effect of the sample size on the mean notched strength and on B-basis value using the MCS method

To validate the proposed UQ&M methodology, it is important to analyse the number of simulations required to ensure an accurate determination of the output parameters. The fact that the framework used is fully analytical, allows a very large number of simulations to be performed, however, it is of key importance to ensure that the open-hole strength (mean and B-basis) are determined efficiently, i.e. performing the minimum number of simulations required to obtain accurate and statistically consistent results.

The methodology to determine the B-basis using MCS is described in Section 2.3. This methodology requires the computation of $n \times N$ number of simulations to determine the B-value. This may lead to a very high number of simulations, rendering the methodology computationally expensive. However, it is possible to determine the B-basis based on a smaller number of simulations if we consider $N = 1$ and have a sample size (n) sufficiently large to be representative of the population of results. With this methodology, the B-basis can be approximated by the 10th percentile of the sample, therefore, reducing the number of simulations to be performed.

To determine the minimum sample size that ensures this representativeness, the sample size was varied between 10 and 100,000. For each sample size 10 random samples were obtained to compute both the average and standard deviation of the mean open hole strength ($\bar{\sigma}^{\infty}$) and the respective B-basis (P_{10}). Fig. 8 shows the convergence analysis of both the average OH strength and B-basis. (Table 5).

Analysing the data, it is possible to conclude that the variability of both the mean OH strength and B-basis is reduced with increasing sample size, however, the computational cost increases. It is possible to conclude that for a sample size of 10,000 the Coefficient of Variation (CoV) of both the mean OH strength and B-basis is very low, 0.02% and 0.05%, respectively. Therefore, a sample size of 10,000 can be considered as representative of the population of results and be used to obtain the average OH strength and respective B-basis. If we consider a sample size of 30,000, which has a three times increase in computational time, there is an insignificant reduction in the CoV for the mean strength and B-basis (to 0.01% and 0.03% respectively). Therefore, it is concluded that a sample size of 10,000 is large enough and ensures a good compromise between the accuracy and computational cost.

To summarize, the calculation of the B-basis allowable using MCS

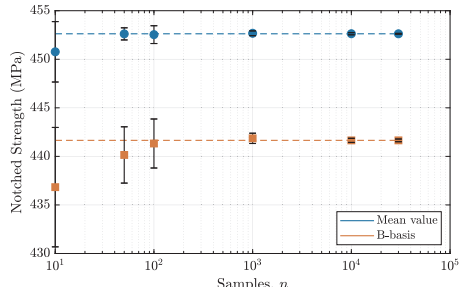

Fig. 8. Average OH strength and 10th percentile from $N = 10$ simulations determined from different number of samples n.

Table 5
Mean value and variance of the average OH strength ($\bar{\sigma}^{\infty}$) and B-value (P_{10}) according to the number of samples when $N = 10$.

Samples, n	$\bar{\sigma}^{\infty}$		P_{10}	
	$\overline{\bar{\sigma}^{\infty}}$ [MPa]	$s_{\bar{\sigma}^{\infty}}$ [MPa]	$\overline{P_{10}}$ [MPa]	s_{P10} [MPa]
10	450.77	3.11	436.83	6.15
50	452.61	0.62	440.15	2.90
100	452.54	0.91	441.33	2.52
1000	452.68	0.24	441.86	0.53
10,000	452.63	0.11	441.65	0.21
30,000	452.62	0.04	441.64	0.13
100,000	452.62	0.03	441.64	0.05

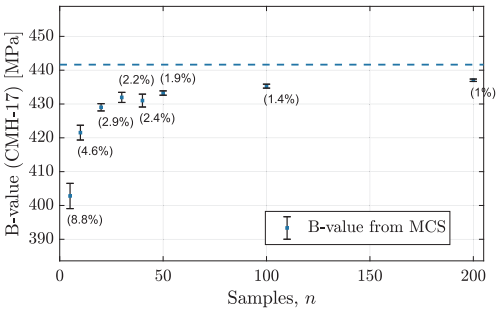

Fig. 9. Comparison of the b-value obtained from the CMH-17 approach with its 95% interval of confidence, for different sample sizes (n) and the B-value obtained from MCS (dashed line).

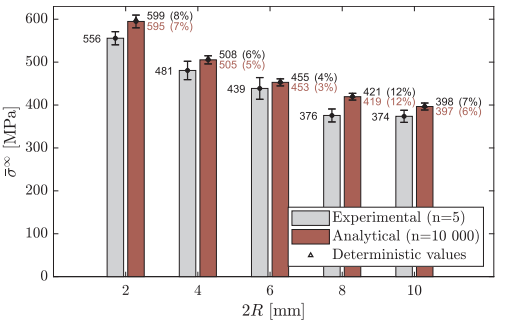

Fig. 10. Comparison between the mean open hole strength of experimental results [18] and the analytical results of five different $2R$ and a fixed ratio $2R/W = 1/6$, where $\bar{\sigma}^{\infty}$ is the notched strength, R the radius of the hole and W the width.

can be done in a computationally efficient way by running 10,000 simulations ($N = 1$) and determining the 10th percentile of the sample as this number of samples is considered representative of the whole population. This methodology will be considered for the determinantion of the B-basis allowables using Monte Carlo simulations in the following sections.

5.2. Effect of the sample size on the B-basis using the CMH-17 approach

In Section 2.3 the methodology to determine the B-basis allowable based on the CMH-17 was presented. In this section a comparison between the B-basis determined using this methodology is compared with the results obtained using Monte Carlo simulations. The CMH-17 approach is useful since it takes into account the size of the population and the distribution that most accurately represents the data to determine the B-basis and therefore, a good estimate of this parameter can be obtained using a small number of data points.

In Fig. 9 the B-basis allowable for OH strength determined using the CMH-17 methodology for different sample sizes is shown and is compared with the value obtained using MCS. For each sample size, 100 simulations were performed based on different randomly generated samples, to get not only an average value for the B-basis but also to determine its dispersion for each sample size.

As the sample size increases, the B-value determined with the CMH-17 approach becomes less conservative and the confidence interval is reduced, as bigger samples are considered more representative of the population. In Table 6 the results of the B-value are also shown for different sample sizes. In addition, the methodologies from the CMH-17 that were applied for each sample are shown, as different distributions were seen to best fit the data depending on the sample considered.

For a sample size of 30 it is seen that the variability of the calculated B-basis increases. This increase in variability with increased sample size can be justified with the fact that for the mentioned sample size, there was an increase in the number of samples that could not be represented by a Weibull distribution (see Table 6) and, therefore, a different distribution had to be used, or even the non-parametric methodology, which increased the dispersion in the determination of the B-basis.

In the remainder of this study, a sample size of 25 is considered when determining the B-basis with the CMH-17 methodology, as it is seen to be a reasonable sample size, which might be used in experimental campaigns, that ensures a good B-basis estimation.

5.3. Validation of the UQ&M framework

A comparison between the experimental results presented in Ref. [18] and the predictions using the proposed framework is shown in Fig. 10. Both the OH strengths computed using the nominal values of the material and geometrical properties and the results obtained when these properties are considered stochastic are included. The latter methodology allows not only to obtain the average value for OH strength for each geometry but also the expected variability.

As expected, using the nominal values of the geometrical and material parameters results in approximately the same open hole strength as the average of the stochastic results, ensuring the consistency of the uncertainty quantification framework developed. The results shown in Fig. 10 indicate that the proposed framework is capable of accurate predictions of the open-hole tension strength. The maximum error obtained for this case study was 12% which, taking into account that this is an analytical formulation with very reduced computational cost, is very reasonable.

As the developed framework is aimed at the determination of the B-basis allowable for open hole strength, the comparison between the B-basis obtained analytically, with the two presented methods, and

Table 6
Results for the B-basis determination using the CMH-17 methodology.

Samples, n	Weibull	Normal	Lognormal	Non parametric	$\bar{B}$ [MPa]	s_B [MPa]	IC_B [± MPa]	error %
5	92	8	0	0	411.35	17.992	3.5696	6.858
10	93	3	0	0	428.77	9.5808	1.9008	2.9152
15	88	3	0	0	431.84	8.0774	1.6026	2.2193
20	94	2	0	0	434.78	4.2685	0.84686	1.553
25	94	2	0	0	435.92	4.3825	0.86948	1.2953
30	91	4	0	5	438.17	7.051	1.3989	0.78675
40	94	3	0	3	437.74	3.4001	0.67458	0.88285
50	92	5	0	3	437.24	3.2488	0.64456	0.99621
100	78	5	0	17	438.76	2.7482	0.54525	0.65224
150	91	1	0	8	439.43	1.5205	0.30167	0.50112

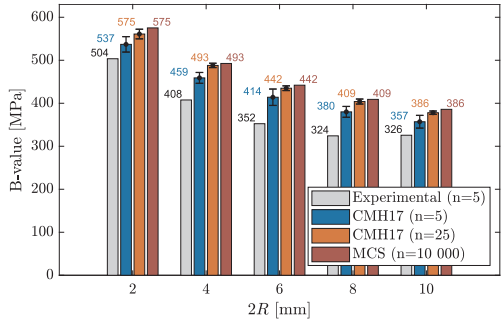

Fig. 11. Comparison between the B-value obtained experimentally ($n = 5$), with the CMH-17 ($n = 5$ and $n = 25$) and with the MCS method ($n = 10, 000$).

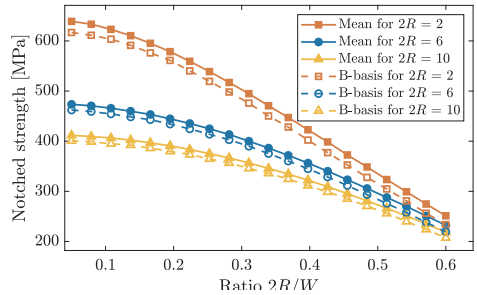

Fig. 12. Design chart of the mean and B-basis value of the open hole strength calculated by means of MCS for different $2R$ and $2R/W$ ratios.

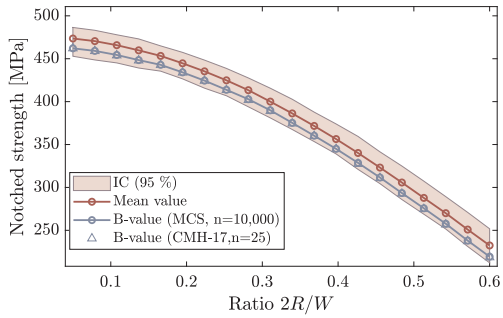

Fig. 13. Design chart of the notched strength for $2R = 6$ mm.

experimentally is shown in Fig. 11. For consistency, as the experimental sample size used was 5 specimens [18], the same sample size was considered when computing the B-value with the CMH-17 approach. This allows a direct comparison between the experimental B-basis and the one obtained numerically. Nevertheless, the results with a sample size of 25 are also shown. To ensure that the results obtained did not result in outliers, 10 B-basis calculations were performed for each geometry. For the Monte Carlo simulations approach a larger number of simulations is always required to ensure the representativeness of the population, therefore, the sample size was kept at 10,000.

Observing the previous results it is concluded that the B-value determined with the CMH-17 approach is similar to that obtained experimentally, for the same sample size ($n = 5$), which reflects not only the ability of the framework to accurately compute the open hole strength of a given configuration, but also its ability to propagate the uncertainty of the input parameters to the open hole strength. The B-basis obtained with the MCS approach is always less conservative than the one obtained with the CMH-17 approach due to the larger sample size, which is reflected in the results of Fig. 11 and was also obtained in the numerical comparison provided in Fig. 9. The same sample size effect can be observed comparing the CMH-17 approach with $n = 5$ and $n = 25$. Nevertheless, the results obtained are consistent with the experimental ones.

6. Applications

6.1. Design charts for open hole tension

Taking into account that the analytical UQ&M framework developed enables the quick estimation of the notched strength of laminated composites and the respective B-basis allowables, it can be used to generate design charts and compare the performance of different layups and materials in a preliminary stage of the design process.

Following Camanho et al. [9], design charts that relate the diameter-to-width ratio to the notched tensile strength of specimens with diameters 2, 6 and 10 mm were generated. Monte Carlo simulations with $n = 10, 000$ were used to generate the average notched strength distribution of each point and compute the mean value and respective B-basis allowable, as defined in Section 5.1 (Fig. 12). To calculate the B-value, the CMH-17 approach could also have been used without significant loss of accuracy as shown in Fig. 13 for a specimen with a hole radius of 6 mm, however, given the computational efficiency of the model, performing Monte Carlo simulations is not a particularly limiting approach.

Experimentally generating statistically representative design charts is unreasonable given the number of specimens, specimen configurations, layups and materials required to populate them. The analytical UQ&M framework here proposed can help overcome this limitation and assist engineers during the design process given its simplicity and efficiency.

6.2. Influence of the load direction on the open hole strength

The framework was developed to work as a fast design tool that is capable to predict the notched strength of a laminate in the most varied cases. In this section, the variation of the loading direction and its effect on the open hole tensile strength is explored. The design of a laminate for a given structure is usually optimized for a given load direction, however, it is not acceptable to have a laminate whose strength is very high in one direction but any misalignment in the load, which most certainty occurs in real usage, leads to a high reduction of its strength. Therefore, being able to rapidly predict the notched strength in a multitude of loading directions is an useful design tool. The variation of the mean open hole strength as a function of the load direction and the respective 95% confidence interval and predicted B-basis value based on MCS ($n = 10, 000$) and on the CMH-17 ($n = 25$) are shown in Fig. 14. This analysis was done for the baseline configuration of a width of 36 mm and a radius of 6 mm.

Due to the fact that the laminate in study is quasi isotropic (Section 3), the notched strengths at 0, 45 and 90° are equal. However the strength is reduced for any other load direction. From the shown results it is possible to conclude that with the given laminate the reduction of strength due to changing the load direction is small, being the lowest value equal to 377.1 MPa, while the maximum (for 0, 45 and 90°) is equal to 455.0 MPa. Additionally, it is observed that small variations around the principal load direction (0°) have only a small effect on the notched strength. Regarding the B-basis allowable it is seen that for the

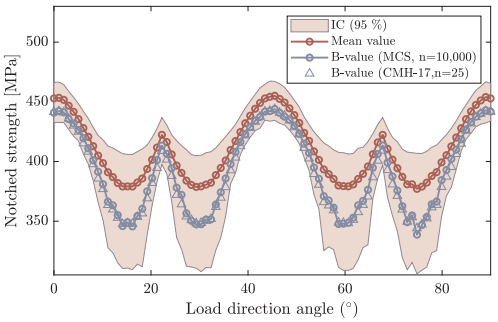

Fig. 14. Notched strength variation with the load direction.

analysed cases the results from the CMH-17 and MCS approach are similar. It is interesting to note that the difference between the B-basis and the mean value for the open hole strength is not constant throughout the angle space. This difference is highest when the average strength is lowest, which creates a wider span of the B-basis allowable between its maximum and minimum. This can be explained by the fact that at these load angles the variability of the material and geometrical parameters leads to a higher variability of the notched strength and, therefore, a reduced B-basis allowable.

6.3. Large damage capability

The proposed framework was developed with the aim of predicting the open-hole strength of laminate structures, however, it is general enough to be able to predict the strength of different notched geometries, provided the stress distribution and energy release rate are known for those geometries and loading conditions. As it is well known, the tensile strength of composite laminates in the presence of through-the-thickness notches is significantly affected by size, being the smallest geometries strength-dominated and large ones toughness-dominated [19]. Therefore, the analysis tools must be able to account this distinct material behaviours when computing the notched strength. Following Arteiro et al. [19] the developed framework is used to predict the large damage capability of the laminate in study, considering a centre notched plate under tension loading (Fig. 15).

In Fig. 16, the mean notched strength and respective B-basis allowable of centre notched plates with a constant plate width-to-notch length ratio ($W/2a$) equal to 7.5 with different notch sizes are shown. The notches were considered to have a constant tip radius of 0.5 mm ($h = 1$ mm). For the smaller geometries the traditional methods that only consider the steady state value of the fracture toughness in their formulation are able to predict the notched strength, however, for larger specimens and large damage capability analysis the introduction of the R-curve in the modelling strategy is of utmost importance [19]. This is taken into account in the present framework, which increases the reliability of the modelling strategy. It is possible to see in Fig. 16 that both the mean notched strength and its respective B-basis allowable follow the same trends, being the difference between both parameters similar throughout the analysed space.

In this study, two notched geometries are analysed, open-hole tension and centre-notched tension, however the framework is generic enough to take into account other geometries such as open-hole compression and bolted joints failing by net-tension [20], given that the stress concentration factors and energy release rates of the configuration in study are known.

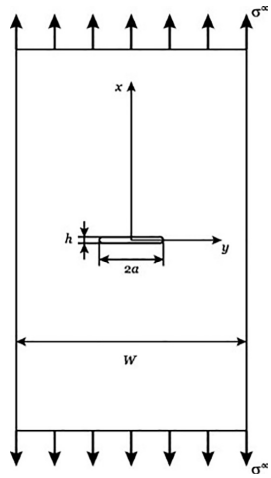

Fig. 15. Centre notched plate configuration [19].

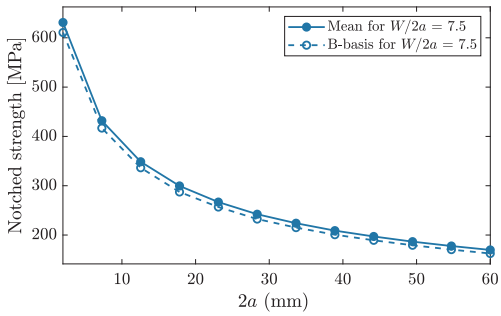

Fig. 16. Design chart of the mean and B-basis value of the notched strength calculated by means of MCS ($n = 10,000$) for centre notched plates.

7. Conclusions

The current approach to determine the design allowables in the aeronautical industry relies in extensive testing based on the building block approach, which makes the selection and certification of composite materials expensive and time consuming. To increase the efficiency of material and laminate selection during preliminary design, there is a need to reduce the number of experimental tests required during this process, and replace or complement them with accurate modelling strategies coupled with the statistical tools to account for material, manufacturing and geometrical variability.

In this work an UQ&M framework was developed to estimate the B-basis design allowable for notched components. This framework is based on the analytical model developed by Furtado et al. [8] that only requires three lamina level material properties to estimate the notched strength of a laminate, given that the stress distribution and energy release rate are known for the geometries and loading conditions in study. This model is coupled with the statistical tools required to take into account the variability of both the material and geometrical parameters and propagate this uncertainty to the notched strength, therefore allowing the quick estimation of B-basis allowable.

The developed framework allows the computation of the B-basis

allowable based on Monte Carlo simulations and on the approach proposed in the CMH-17, which requires a lower number of samples. Both approaches are compared and it is concluded that the CMH-17 gives a more conservative estimation of the B-basis allowable due to the lower number of samples usually used. Given that the current modelling strategy is computationally efficient, the usage of Monte Carlo simulations allows the estimation of a less conservative B-basis as a large number of samples can be computed in a reasonable time frame. This makes the proposed framework specially interesting in the preliminary design and selection of materials and layups.

The proposed framework is validated successfully with the open-hole tension experimental campaign for the IM7/8552 material [18], ensuring a maximum error around 10%, which is very reasonable given the analytical formulation of the model.

Additionally, the framework is used to develop design charts for notched specimens, tools that are useful for design engineers and would otherwise be infeasible to attain as they require a large number of testing or time consuming simulations to be performed.

Note that in this paper, the methodology is applied to open hole tension and center notched specimens, but the framework can be enriched with other notched configurations, provided the stress distribution and energy release rate are known for those geometries and loading conditions.

Acknowledgements

OV acknolwedges the support of the Catalan Government, under the Grant 2018FI_B_00904 CF and RT acknowledge the support of the Portuguese Government's Fundação para a Ciência e Tecnologia, under the Grants SFRH/BD/115859/2016 and SFRH/BD/115872/2016. AA would like to thank the financial support provided by FCT – Fundação para a Ciência e a Tecnologia through National Funds in the scope of project MITP-TB/PFM/0005/2013. PC gratefully acknowledges the funding of Project PTDC/EMS-PRO/4732/2014, cofinanced by Programa Operacional Competitividade e Internacionalização and Programa Operacional Regional de Lisboa, through Fundo Europeu de Desenvolvimento Regional (FEDER) and by National Funds through FCT – Fundação para a Ciência e Tecnologia. AT gratefully acknowledgeshe the funding of the Project TRA2015-71491-R, cofinanced by the Spanish Government (Ministerio de Economia y Competitividad) and the European Social Fund.

References

[1] CMH-17, Composites material handbook 17g. vol. 1 guidelines for characterization of structural materials (2012).
[2] Rousseau C. How various uncertainties and assumptions affect b-basis allowables development. Lockheed Martin Corporation; 2013.
[3] Spendley PR. Design allowables for composite aerospace structures Ph.D thesis University of Surrey; 2012.
[4] Abdi F, Clarkson E, Godines C, DorMohammadi S. Ab basis allowable test reduction approach and composite generic basis strength values. 2016. p. 0951.
[5] Zhang Y, Schutte J, Meeker J, Palliyaguru U, Kim NH, Haftka RT. Predicting b-basis allowable at untested points from experiments and simulations of plates with holes. 2017. URL https://www.researchgate.net/publication/318909364.
[6] Abumeri G, Abdi F, Raju K, Housner J, Bohner R, McCloskey A. Cost effective computational approach for generation of polymeric composite material allowables for reduced testing. Advances in Composite Materials-Ecodesign and Analysis. InTech; 2011.
[7] Nam K, Park KJ, Shin S, Kim SJ, Choi I-H. Estimation of composite laminate design allowables using the statistical characteristics of lamina level test data. Int J Aeronaut Space Sci 2015;16(3):360–9.
[8] Furtado C, Arteiro A, Bessa M, Wardle B, Camanho PP. Prediction of size effects in open-hole laminates using only the Young's modulus, the strength, and the R-curve of the 0° ply. Compos Part A: Appl Sci Manuf 2017;101(AAA):306–17.
[9] Camanho PP, Erçin G, Catalanotti G, Mahdi S, Linde P. A finite fracture mechanics model for the prediction of the open-hole strength of composite laminates. Compos Part A: Appl Sci Manuf 2012;43(8):1219–25.
[10] Tsai SW, Melo JDD. An invariant-based theory of composites. Compos Sci Technol 2014;100:237–43.
[11] Tsai SW, Melo JDD. A unit circle failure criterion for carbon fiber reinforced polymer composites. Compos Sci Technol 2016;123:71–8.
[12] Camanho PP, Catalanotti G. On the relation between the mode i fracture toughness of a composite laminate and that of a 0 ply: analytical model and experimental validation. Eng Fract Mech 2011;78(13):2535–46.
[13] Catalanotti G, Arteiro A, Hayati M, Camanho PP. Determination of the mode i crack resistance curve of polymer composites using the size-effect law. Eng Fract Mech 2014;118:49–65.
[14] Catalanotti G, Xavier J, Camanho PP. Measurement of the compressive crack resistance curve of composites using the size effect law. Compos Part A: Appl Sci Manuf 2014;56:300–7.
[15] Bazant ZP, Planas J. Fracture and size effect in concrete and other quasibrittle materials Vol. 16. CRC Press; 1997.
[16] Chakraborti S, Li J. Confidence interval estimation of a normal percentile. Am Statist 2007;61(4):331–6.
[17] W.C. (PA), A.S. for Testing, M. (ASTM), Standard test method for open hole tensile strength of polymer matrix composite laminates, ASTM D 5766/D 5766M–02a.
[18] Camanho PP, Maimí P, Dávila C. Prediction of size effects in notched laminates using continuum damage mechanics. Compos Sci Technol 2007;67(13):2715–27.
[19] Arteiro A, Catalanotti G, Xavier J, Camanho P. Large damage capability of non-crimp fabric thin-ply laminates. Compos Part A: Appl Sci Manuf 2014;63:110–22.
[20] Catalanotti G, Camanho P. A semi-analytical method to predict net-tension failure of mechanically fastened joints in composite laminates. Compos Sci Technol 2013;76:69–76.

A.2 Paper B – A methodology to obtain material design allowables from high-fidelity compression after impact simulations on composite laminates

The paper has been published in *Composites Part A: Applied Science and Manufacturing* 139 (2020) 106069.

Composites Part A 139 (2020) 106069

Contents lists available at ScienceDirect

Composites Part A

journal homepage: www.elsevier.com/locate/compositesa

A methodology to obtain material design allowables from high-fidelity compression after impact simulations on composite laminates

I.R. Cózar*, A. Turon, E.V. González, O. Vallmajó, A. Sasikumar

AMADE, Polytechnic School, University of Girona, Campus Montilivi s/n, 17071 Girona, Spain

ARTICLE INFO

Keywords:
B. Strength
C. Statistical properties
C. Statistical method
C. Numerical analysis

ABSTRACT

Aeronautical industries address the structural reliability of designs by defining design allowables that account for any uncertainties. The Composite Materials Handbook-17 proposes A/B-basis values as design allowables. In this study, a new methodology to estimate the design allowables of the Compression After Impact (CAI) strength is presented. The CAI strength is predicted with high-fidelity simulations using finite element models featuring in-house constitutive damage models. The uncertainty associated to parameters of the model is defined and propagated to obtain the CAI strength distribution. To efficiently estimate this distribution, a Monte Carlo simulation is carried out employing a response surface previously calibrated with a reduced number of high-fidelity simulations. The A/B-basis values for the CAI strength are estimated from the strength distribution obtained and then compared with experimental results. The methodology proposed allows to reduce the number of experimental tests associated with generating design allowables, thus leading to an optimised cost-effective design.

1. Introduction

The design allowables most widely used in the aeronautic sector are the A/B-basis values, which are defined as 95% of the lower one-sided confidence bound of the 1st and 10th percentiles of the population measured [1], respectively. Consequently, if the load or stress in the part is greater than the allowable design value, then the design criteria is not fulfilled. Current industry practice uses experimental tests that generally adhere to the Composites Materials Handbook-17 (CMH-17 approach) [1] to determine design allowables (as in Laurin et al. [2]). According to the CMH-17 approach, design allowables are approximated by using the localisation and scale parameters of the results (i.e. mean value and standard deviation, respectively, in a normal distribution) and a coefficient factor according to the distribution of the results and the number of samples. To obtain accurate design allowables, the population distribution of the parameter must be measured, which implies a large number of laboratory tests and, therefore, the associated increase in time and economic costs.

Alternatively, the basis values can be obtained using advanced models and an appropriate methodology to quantify and manage uncertainty. The uncertainty associated to the analysis method can be grouped into two types: (i) uncertainty associated to the repeatability of the model or (ii) uncertainty due to the intrinsic variability of the parameters of the model. The uncertainty associated to the repeatability of the model does not apply to this study because the prediction from the high-fidelity model will only change if the parameters of the model are changed. Hence, the variability in the output results is caused by the uncertainty associated to the input parameters. This uncertainty can derive from different sources such as the manufacturing process, batch-to-batch variability of raw materials, the test method used to characterize the material, or the intrinsic variability of the material [1]. In addition, it can also be uncertainty associated to the boundary conditions (e.g. a misalignment in the applied load) and to the geometry of the specimen.

Therefore, to determine the design allowable values from high-fidelity simulations, the uncertainty associated to the different input parameters must be quantified. This uncertainty is propagated into the model to obtain the population of the output results. Further, the design allowables are estimated using a proper statistical analysis.

One way to propagate the uncertainty is to use the Stochastic Finite Element Method (SFEM) [3], which is based on the random variation of the input parameters of the model according to their distribution. Meanwhile, the easy-to-implement Crude Monte Carlo Simulations (CMCS) makes it a widely-used method for uncertainty propagation analysis. Vallmajó et al. [4] proposed a new methodology for estimating the B-basis value of notched composite laminates by means of CMCS using an analytical framework. The authors demonstrated that, for large sample sizes ($>10^4$), the B-value can be estimated to the 10th

* Corresponding author.
E-mail address: ivan.ruiz@udg.edu (I.R. Cózar).

https://doi.org/10.1016/j.compositesa.2020.106069
Received 7 April 2020; Received in revised form 14 July 2020; Accepted 3 August 2020
Available online 14 August 2020
1359-835X/ © 2020 Elsevier Ltd. All rights reserved.

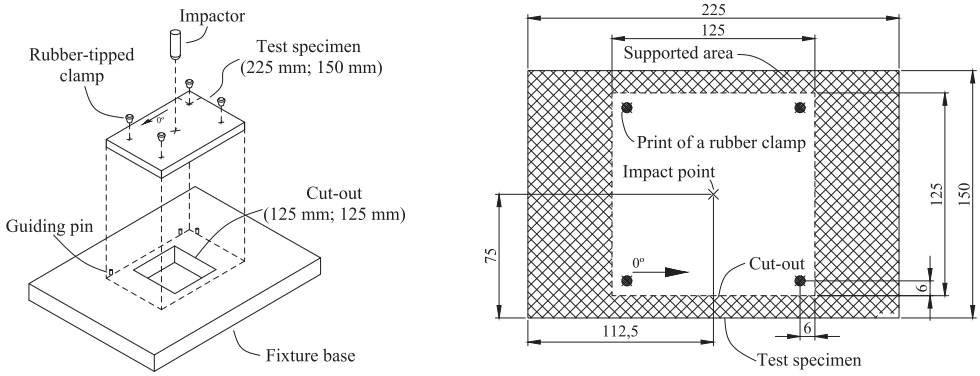

Fig. 1. Schematic representation of the LVI test: assembly (left) and general dimensions of the specimen in mm (right).

percentile. However, as the CMCS requires a large number of results, this is not feasible for simulations that require high computational times (e.g. FE analysis), thus, more economic methods, in terms of computational time, need to be employed.

The First Order Reliability Method (FORM) and the Second Order Reliability Method (SORM) are used in some applications to approximate the probability of a function with random input parameters. They are based on a Taylor series assuming that the output results follow a normal distribution and, therefore, require a small number of simulations. Gosling et al. [5] presented a methodology to estimate the reliability of a complex shear-deformable composite laminate using FORM, while Delbariani-Nejad et al. [6] studied the reliability of the delamination growth under mode I, mode II and mixed mode in composite laminates applying the FORM and SORM methods. According to their results, FORM provides a good balance between accuracy and economic cost in terms of computational time. Hussein at el. [7] used the First Order Second Moment (FOSM) method to maximize plate stiffness using the minimum carbon reinforcement polymer volume fraction in a plate under uniform pressure loading. The authors concluded, however, that these methods are not suitable when the model has non-linearities.

Nowadays, a large number of numerical works addresses the simulation of Low-Velocity Impact (LVI) and Compression After Impact (CAI) tests on composite structures [8–17]. The interest in simulating the CAI test has grown considerably, as CAI strength is a design-driver for some aeronautical components. The prediction of CAI strength is quite complex and challenging as it is based on the previous impact simulation and involves complex contact interactions and progressive material degradation and the interaction of several failure mechanisms. For airworthiness certification, the analysis must be supported by test. For this study, the analysis of the CAI strength is performed in sub-element-level and, hence, the input parameters that feed the model have been experimentally tested.

English et al. [18] used the SFEM approach to simulate an LVI test on a laminate. The authors used the Latin Hypercube Sampling (LHS) technique to define an input test matrix. Afterwards, the results from the FE simulations were compared with experimental data to adjust and validate the FE model. Patel et al. [19,20] performed a probabilistic analysis using a Gaussian response surface method in an LVI test by SFEM. The authors estimated the probability of the failure criteria for the matrix cracking and the delamination with different impacted energies by taking into account the uncertainty of the material properties. A sensitivity analysis was performed to determine which input parameters had a greater influence on the probability of failure.

Despite the large amount of published works, there is hardly any work that addresses determining design allowables directly from damage tolerance simulations using advanced constitutive models. This work proposes a cost-effective methodology to estimate the A/B-basis values for the CAI strength of laminated composites using high-fidelity FE simulations and statistical analysis. The main objective of this study is to present the methodology in detail, followed by the accurate design allowables. Nevertheless, the authors would like to remark that the methodology presented in this study to obtain the design allowables of the LVI & CAI test can reduce the number of tests to be performed but, it will not ever completely replace the experimental tests. Details of the modelling approach used to simulate the LVI and CAI experimental tests performed by Airbus and the post-processing of the results are presented in Section 2. Section 3 details the methodology used to obtain the A/B-basis values, while the results and discussion are presented in Section 4. All the data shown in this study is normalized, due to confidentiality and data rights from Airbus. The paper ends with concluding remarks in Section 5.

2. Damage tolerance simulation

The aeronautical industry judges CAI strength to be a damage tolerance design allowable. CAI strength is measured using a standard test where a laminate, after having been impacted, is subjected to compression loading to evaluate its residual strength. By repeating the test for different levels of impact energy, a correlation between the impact energy level and CAI strength is thus obtained.

In the present work, the LVI and CAI tests are simulated using economical FE models and advanced in-house constitutive damage models. The LVI and CAI experimental tests were performed by Airbus following an internal procedure based on the AITM-1.0010 standard [21]. The specimen is positioned over a metal frame and constrained by four fixture rubber pads (see Fig. 1). Using a drop-tower, the specimen is then impacted. After the impact, the specimen is loaded under in-plane compression to obtain its residual strength. The laminate thickness used in this study is very low, around 1.8 mm. Thin laminates are subjected to global buckling when tested under CAI [22] and hence a strategy is used in this study to avoid this phenomenon. The impacted specimen and a pristine specimen (with of the same laminate as that of the impacted one) are glued to both sides of a honeycomb specimen to prevent failure due to buckling. Fig. 2 illustrates the assembly of the above-mentioned specimens. Finally, the assembled sandwich specimen is loaded under compression to measure the CAI strength.

The LVI and CAI tests considered here meet the AITM 1.0010 standard [21], despite the dimensions of the specimen, the size of the LVI window, and the position of the fixture rubber pads being slightly

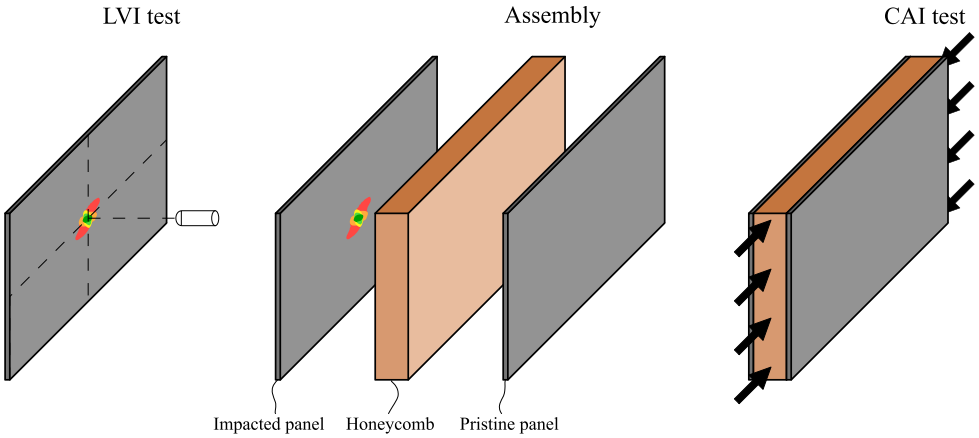

Fig. 2. Schematic representation of the LVI test, the assembly of the panels to be tested and the CAI test. (For interpretation of the references to colour in this figure legend, the reader is referred to the web version of this article.)

Table 1
Technical characteristics of the LVI and CAI laboratory test.

Material type	UD tape - CFRP	
Stacking sequence	$[45/135/90/0/0]_s$	
Specimen dimensions	225 × 150	mm
Thickness of the laminate	1.84	mm
LVI test window	125 × 125	mm
Impact energy	25	J
Impactor mass	3.2	kg
Honeycomb type	HRH-10–6.0–0.96	
Thickness of the honeycomb	30	mm

different. Specimen geometry and details of the LVI test configuration are summarised in Table 1.

2.1. High-fidelity model

The simulation of the LVI and CAI events on composite materials relies on selecting a suitable modelling strategy. This means selecting an appropriate element type and interaction technology for ply and delamination modelling, respectively. Also, it is important to decide on the number of potential interfaces susceptible to delamination.

It was recently demonstrated that the use of conventional shell elements is a suitable choice, resulting in reasonable time analysis and accurate predictions [23–25]. In this work, the modelling strategy presented by Soto et al. [23] is applied, in which conventional shell elements are used together with zero-thickness cohesive elements. All the interfaces with mismatch oriented surrounding plies are considered for delamination and the kinematics of the shell elements are transferred to the cohesive elements using tie constraints, thus allowing two different surfaces, without relative motion between them, to be joined. Fig. 3 illustrates the modelling approach used [23].

For successful simulations, there are some key numerical parameters that must be well defined, for example, a criterion to avoid excessive finite element distortion, the mass distribution between shell and cohesive elements, and the mesh size.

The criterion selected to avoid excessive distortion of degraded shell (intralaminar) elements is based on considering a residual stress in each material loading direction. The residual stress is calculated as the stress associated to the corresponding damage variable equal to 0.99 (i.e. for the fibre (d_1), for the matrix (d_2) and for the in-plane shear degradation (d_6)). Therefore, the damage increases while the residual stress is kept

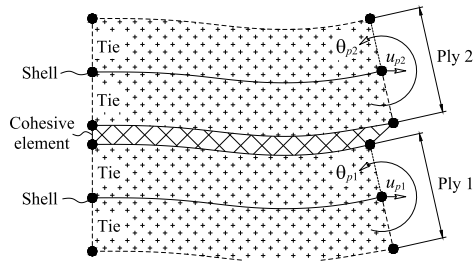

Fig. 3. FE modelling strategy based on using conventional shell elements, cohesive elements and tie connections. Note: although the cohesive element is sketched with thickness, they are modelled with zero-thickness elements.

constant.

For cohesive elements, the same strategy as in [23] is used, the isotropic damage variable of the cohesive (interlaminar) elements is limited to a value of 0.9999, so that a residual stiffness remains constant at any propagation mode once the element is degraded. No element deletion criteria is considered. In-house constitutive models featuring intra- [26,27] and interlaminar [28] damage are also used. Both models were implemented in a VUMAT user-written subroutine.

The simulations are run in an explicit solver. Therefore, the density of each element type, including cohesive elements, must be defined. The whole mass of the structure is distributed between the shell and cohesive elements. As performed in [23], the density of the shell elements and the surface density of zero-thickness cohesive elements are defined so that the corresponding stable time increment associated to shell elements, cohesive elements and contact interactions are similar.

As outlined earlier, a pristine panel and a honeycomb are bonded to the impacted panel after impact. For this step, the *import* option of ABAQUS is used, since it allows an FE model with previously simulated and non-simulated parts to be built. The strategy followed is: (i) an LVI is performed on a single panel, (ii) the impacted panel is imported to a new model and bonded to a honeycomb and a pristine laminate and (iii) the sandwich structure is loaded under compression to determine the CAI strength. The honeycomb is bonded to the panels by tie constraints on the corresponding interaction surfaces. An area 25 mm in diameter at the centre of the impacted panel is not glued to the honeycomb,

following the same procedure used for the physical specimens. To simplify the model, the honeycomb is defined using linear elastic solid elements and no damage is modelled for this part. It is assumed that it will fail after the first load drop of the load–displacement curve (CAI strength), see Section 2.2. The total number of elements for the LVI FE model is 114692 and for the CAI model is 340830.

2.2. Post-processing output results of the FE models

The main output result from the LVI model is the projected delaminated area. In the experimental LVI test, the projected delaminated area is measured by performing an ultrasonic C-Scan analysis. In the LVI FE model, the projected delaminated area can be estimated from the damaged cohesive elements. However, there is no general rule to compare the projected delaminated area from the test with the one numerically obtained from the cohesive damage variable. In this work, the numerical projected delaminated area is estimated spanning over all the cohesive elements with a damage variable larger than the damage corresponding to the dissipation of the visual onset mode II interlaminar fracture toughness ($\mathcal{G}_{IIc,vis}$). Two mode II interlaminar fracture toughness are obtained from the laboratory test: visual onset value ($\mathcal{G}_{IIc,vis}$) and crack propagation value ($\mathcal{G}_{IIc}$). According to the constitutive model, the relation between the energy dissipated during the damage development ($\mathcal{G}$)and the damage variable (d) is [29]:

$$\mathcal{G} = \frac{\mathcal{G}_{IIc}\tau_{II}^2 d}{2K\mathcal{G}_{IIc}(1-d) + \tau_{II}^2 d} \tag{1}$$

where K is the penalty stiffness and τ_{II} is the mode II interlaminar strength. Therefore, when the energy dissipated is equal to the visual onset value of the fracture toughness the damage variable reads:

$$d_{vis} = \frac{2\mathcal{G}_{IIc}\mathcal{G}_{IIc,vis}K}{\mathcal{G}_{IIc}\tau_{II}^2 - \mathcal{G}_{IIc,vis}\tau_{II}^2 + 2\mathcal{G}_{IIc}\mathcal{G}_{IIc,vis}K} \tag{2}$$

and the delaminated area is computed with all the elements with a damage variable higher than d_{vis}. The numerical simulation under predicted the projected delaminated by 10.63% compared to the mean experimental value.

The output result of the CAI simulation is the CAI strength. This is obtained when the load–displacement curve (adding the contributions of the impacted and the pristine panel and the honeycomb) presents the first load drop (as is schematically shown in Fig. 4). In the numerical simulations, this first load drop takes place when the impacted laminate fails. It is assumed the same behaviour in the experimental test.

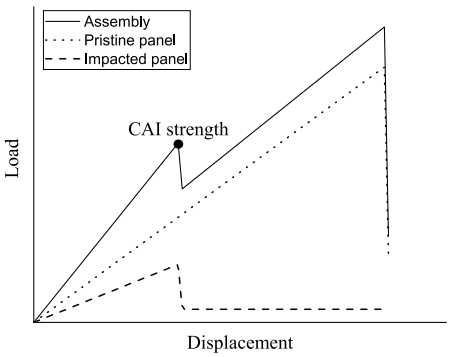

Fig. 4. Schematic representation of the load vs displacement curve obtained from the CAI FE model.

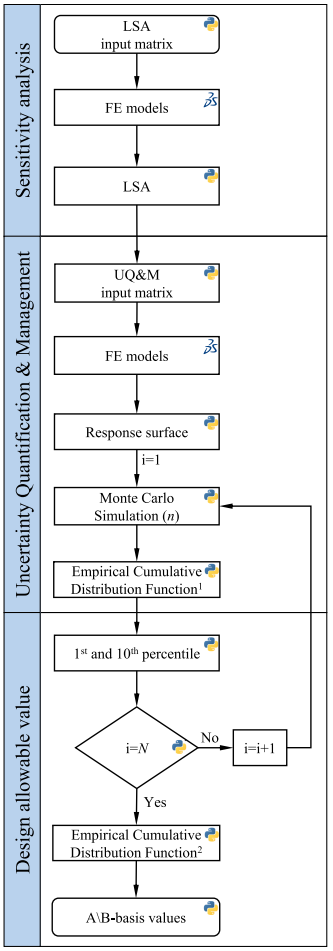

Fig. 5. Flowchart of the methodology to estimate the A/B-basis values. (For interpretation of the references to colour in this figure legend, the reader is referred to the web version of this article.)

3. Methodology to obtain A/B-basis values

The A-basis value of the CAI strength is defined as the 5th percentile of the distribution of the 1st percentile of the CAI strength distribution. The B-basis value is the 5th percentile of the distribution of the 10th percentile of the CAI strength distribution, according to the definition from [1]. The methodology followed in this study to estimate the design allowables is as follows (see Fig. 5): (i) a Local Sensitivity Analysis (LSA) is performed to identify the input parameters (independent variables X) that have a greater impact on the output results (dependent variables Y), defined as key parameters; (ii) an input test matrix for the FE models is created varying only the key parameters, submitted and post-processed to obtain the output results; (iii) using the inputs and outputs of the previous analyses, a Response Surface (RS) of the CAI FE model is created; (iv) Monte Carlo Simulations (MCS) with a size of n cases using the previous RS is applied and the Empirical Cumulative

Table 2
Input parameters used for the LSA.

Symbol	Input parameter
m_{imp}	Impactor mass
μ	Friction coefficient
$\mathcal{G}_{Ic}$	Mode I interlaminar fracture toughness
$\mathcal{G}_{IIc}$	Mode II interlaminar fracture toughness
BK_{η}	B-K exponent parameter for mixed mode propagation
τ_{II}	Mode II interlaminar strength
ρ	Density
E_{11}	Young Modulus in fibre direction
E_{22}	Young Modulus in matrix direction
ν_{12}	Major Poisson ratio
ν_{23}	Transverse Poisson ratio
G_{12}	Shear modulus
X_T	Fibre tensile strength
X_C	Fibre compression strength
f_{XC}	Portion of X_T
f_{XC}	Portion of X_C
Y_T	Matrix tensile strength
Y_C	Matrix compression strength
S_L	Matrix shear strength
S_{LP}	Matrix shear yield stress
K_P	Shear plasticity parameter
$\mathcal{G}_{XT}$	Tensile fibre fracture toughness
$\mathcal{G}_{XC}$	Compression fibre fracture toughness
$f_{\mathcal{G}XT}$	Portion of $\mathcal{G}_{XT}$ dissipated by the first branch
$f_{\mathcal{G}XC}$	Portion of $\mathcal{G}_{XC}$ dissipated by the first branch
E_{33_H}	Longitudinal Young Modulus of the honeycomb
ν_{12_H}	Transverse Poisson ratio of the honeycomb
C_H	Coefficient of the honeycomb[1]
G_{12_H}	Shear modulus of the honeycomb
G_{13_H}	Shear modulus of the honeycomb
G_{23_H}	Shear modulus of the honeycomb

[1] C_H is a parameter to estimate the Young Modulus in the transverse direction and the longitudinal Poisson ratio of the honeycomb by means of empirical equations provided by Airbus.

Distribution Function (ECDF) of the CAI strength is calculated; (v) the 1st and 10th percentile from the ECDF are obtained; (vii) steps iv and v are repeated N times; (viii) the ECDF of the 1st and 10th percentiles are calculated and the A/B-basis values, respectively, are estimated.

The whole procedure is automated by a Python script which generates the input test matrix for the FE simulation, submits them to ABAQUS and performs the post processing. The script also automatically computes the LSA, the UQ&M and the calculus of the design allowables.

The input parameters of the FE models can be grouped into: material properties, specimen dimensions, impact energy, position of impactor/load and supports, and stacking sequence. In this work, only the material properties required for the FE models are varied to estimate the design allowables. Hence, the LSA and the UQ&M are performed considering only the variability of the material properties. The variation of the mode II interlaminar fracture toughness requires redefining the mesh element size to properly capture the interlaminar behaviour. However, in the current study, the element size was decided to be kept constant to simplify the modelling strategy. The list of the material properties used as input parameters in the LSA are summarised in Table 2.

The following subsections describe the LSA, the UQ&M analysis and the procedure with which to estimate the design allowables.

3.1. Local sensitivity analysis

The LSA is performed to select the input parameters that have the greatest influence on the output results (key parameters). In this study, the independent variables are varied within their 95.4% confidence interval (i.e. ± 2 standard deviations for a normal distribution) to establish their influence on the output results within their probable values because in the MCS the input parameters will be also varied within their probability range. This range has been considered to have enough distance between the bounds of each input variable to capture its influence on the model, but also, to have physically meaningful, but avoiding potential numerical errors caused by extreme values.

The LSA is applied before the UQ&M analysis, thus allowing the number of the independent variables of the UQ&M analysis to be reduced and, as such, reduce the total computational time. Thus, in the UQ&M analysis only the key parameters selected in the LSA are used to propagate their uncertainty into the model.

The LSA is performed using a one-at-a-time analysis, because the main objective of the study is to describe a new methodology to obtain the design allowables. This approach is based on the variation of only one parameter for each simulation and helps to analyse the relative contribution the different input parameters have on the output of the model. However, this approach will not capture any possible interaction between the parameters and it can be non-conservative. Therefore, a global sensitivity analysis should be carried out to account for the interaction between parameters.

In this work, two cases per independent variable are studied in the LSA. The variation of the independent variables is defined by the limits of the 95.4% confidence interval of each parameter, while the rest of the parameters are fixed to their mean values. The LSA test matrix is schematically displayed in Table 3. The first case (first row in Table 3) has all the parameters equal to the corresponding mean value (all the input variables are distributed by means of a normal distribution, in the same way as in [6] [19]).

The cases of the test matrix in Table 3 are calculated using the methodology presented in Section 2. Then, the first-order sensitivity index is calculated as:

$$S_j = E\left(\left|\frac{\partial Y}{\frac{\partial X_j}{\hat{s}_j}}\right|\right) \tag{3}$$

where j refers to the input parameters and $\hat{s}_j$ is the sample standard deviation. The derivative in Eq. (3) is normalised by $\hat{s}_j$, as the objective is to determine the input parameters that generate more dispersion on the output results of the model within their probable values. On the contrary, if the derivative is not normalised by the sample standard deviation, the correct dispersion of the results in the MCS will not be obtained.

The comparison between an index calculated using only the derivative $E\left(\left|\frac{\partial Y}{\partial X_j}\right|\right)$ or using Eq. (3) is shown in Fig. 6 together with the variability of the output results. The scatter data and the error bars are the mean value and one standard deviation of the output results, respectively. They are obtained when an MCS is performed only with the X_j input parameter and the rest of parameters are kept constant. Each bar represents the sensitivity index calculated by the corresponding equation. The input parameter $|\overline{X_j}| \ll 1$ has an absolute value of the

Table 3
Schematic representation of the LSA test matrix, where m refers to the number of independent variables. The values are normalised as $\frac{X_j - \bar{X}_j}{\hat{s}_j}$, where j refers to the input parameters, X_j is the lower/upper value, $\bar{X}_j$ is the mean value and $\hat{s}_j$ is the sample standard deviation.

No.	X_1	X_2	$\cdots$	X_m
1	0	0	$\cdots$	0
2	-2	0	$\cdots$	0
3	2	0	$\cdots$	0
4	0	-2	$\cdots$	0
$\vdots$	$\vdots$	$\vdots$	$\ddots$	$\vdots$
$2m+1$	0	0	$\cdots$	2

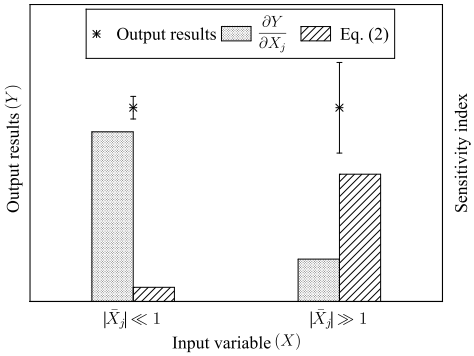

Fig. 6. Schematic representation of the sensitivity index calculated by the derivative of the output results with respect to the input parameters, and by Eq. (3). The input parameter $|\overline{X}_j| \ll 1$ has an absolute value of the mean less than 1 and the input parameter $|\overline{X}_j| \gg 1$ has an absolute value of the mean greater than 1. The scatter data and the error bar are the mean value and the one standard deviation, respectively, of the output results when an MCS is performed only with X_j.

mean value less than 1 (e.g. Poisson ratio) and the input parameter $|\overline{X}_j| \gg 1$ has an absolute value of the mean value greater than 1 (e.g. Young's modulus of elasticity). In this case, the input parameter $|\overline{X}_j| \ll 1$ produces a dispersion in the output results lower than that obtained by $|\overline{X}_j| \gg 1$. However, the sensitivity index of the $|\overline{X}_j| \ll 1$ calculated by the derivative is greater than that obtained by Eq. (3). Therefore, if the parameter $|\overline{X}_j| \ll 1$ is used to compute the MCS, the variability of the output results will not be properly captured. On the other hand, if the sensitivity index calculated by Eq. (3) is used, the input parameter selected will be the one that generates the correct dispersion on the results when the MCS is applied. In the case in Fig. 6, the input parameter selected will be $|\overline{X}_j| \gg 1$.

Finally, the sensitivity index for each input parameter is calculated using its expected value. The absolute values are used as in Campolongo et al. [30] who estimated the mean value of each sensitivity index to prevent opposing components being cancelled. The input parameters with the greater S_j in both models (LVI and CAI FE models) are selected as the key parameters.

3.2. Uncertainty quantification and management analysis

An RS is adjusted for the CAI FE model to obtain the correlation between the key parameters and the CAI strength. This allows the total computational time of the UQ&M analysis to be reduced because the RS makes it possible to estimate the results of several cases in a few seconds. The design of experiment used to create the UQ&M test matrix is the LHS technique; it is not fully random sampling because it avoids the clustering of samples. After the test matrix is defined, it is submitted to the FE models, and then the CAI strength is obtained for each case. Next, the Kriging algorithm is used to create the RS. Finally, the accuracy of the RS is estimated with the coefficient of determination (R^2) and the Root Mean Square Error (RMSE) of the goodness-of-fit plot. In addition, a chi-squared test is applied to determine if there is any statistical evidence that the predicted values from the RS are reproducible from the observed values from the FE models. The Pearson goodness-of-fit statistic is defined as:

$$\chi^2 = \sum \frac{(Observed - Predicted)^2}{Predicted} \tag{4}$$

where the *Observed* and the *Predicted* values are the data used to create a goodness-of-fit plot. If an improvement in the accuracy of the RS is required, new cases should be added to the UQ&M test matrix in the region needing to be improved.

Next, a large number of MCS (N) are performed using the RS, where the size of each MCS is n. Finally, the ECDF of each previous MCS is calculated, thus obtaining N ECDF from the distribution of the CAI strength (see Fig. 7).

3.3. Determining the A/B-basis value

The 1st and 10th percentiles of the CAI strength are obtained from each previously calculated ECDF. Thus, N values of the 1st and also the 10th percentile are provided. Next, the ECDF for both percentiles are calculated. Finally, the 5th percentile of the ECDF from the distribution of the 1st percentile is the A-basis value. Likewise, the B-basis value is the 5th percentile of the ECDF from the distribution of the 10th percentile (see Fig. 8).

4. Results and discussion

First, the CAI strength from the deterministic FE result using the mean input values is obtained following the FE methodology described

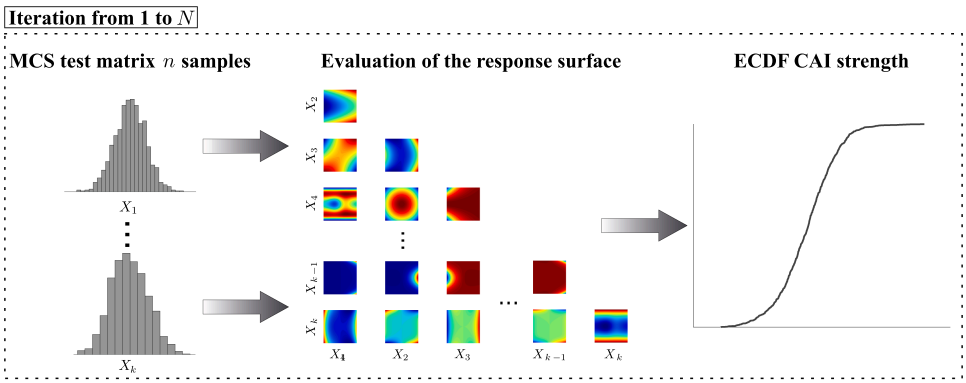

Fig. 7. Schematic representation of the loop of the UQ&M. In accordance with the Fig. 5 flowchart, the left and centre parts correspond to the "Monte Carlo Simulation (n)" box and the right to the first "Empirical Cumulative Distribution Function" box. (For interpretation of the references to colour in this figure legend, the reader is referred to the web version of this article.)

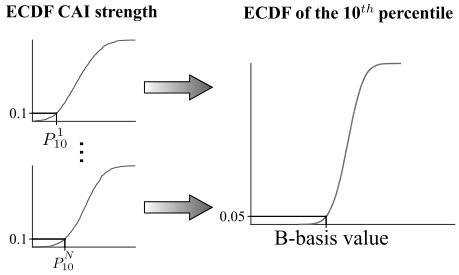

Fig. 8. Schematic representation of the steps to estimate the B-basis value. In accordance with the Fig. 5 flowchart, the left part corresponds to the last "Empirical Cumulative Distribution Function" box and the right part corresponds to the "A/B-basis value" box. P_{10} is the 10th percentile from the ECDF of the CAI strength of iteration ith.

Table 4
Comparison of the experimental CAI strength values with the one obtained using the deterministic FE model. The values are normalised with respect to the mean value of the experimental CAI strength.

	Experimental	Deterministic
mean	1.000	1.096
median	0.957	
Percentile 5	0.847	
Percentile 95	1.193	

in Section 2 and the prediction is compared with those obtained from the laboratory test (see Table 4). The FE model over predicts the median CAI strength by 14.6% and the mean value by 9.6% and it falls within the 90% confidence bound of the experimental data. These over predictions are in concordance with the results obtained in previous works [10,15] and are considered acceptable, given the complexity of the simulations. The difference can be attributed to some of the simplifications done in the modelling approach such as assuming linear elastic behaviour of the honeycomb or possible loading misalignments.

Once the damage tolerance simulation methodology is validated, an LSA is launched and then, using the procedure of Section 3.2, the UQ&M results are analysed. Finally, the A/B-basis value results estimated with the methodology proposed in this work are discussed. A comparison with the results obtained using a replication of the CMH-17 approach [1] is also given. It is worth mentioning that the results from the LSA and the design allowables obtained in this section are only valid for this particular case. If the input parameters change, a new analysis must be carried out.

The computational time for the deterministic LVI and CAI FE models is around 29 h and 10 h, respectively, with 8 cpus (3.1 GHz CPU and 32 GB RAM for each CPU). However, the computational time for the LVI and CAI FE models used in the UQ&M analysis is in average around 39 h (from 21 h to 96 h) and 14 h (from 5 h to 44 h), respectively. The difference in computational time is due to the variation in the different values of the input parameters. For example, for a higher value of $\mathcal{G}_{Xc}$, the CAI strength and ultimate strain also increase which leads to a large computational time.

4.1. Local sensitivity analysis

The sensitivity indices using Eq. (3) for the LVI and CAI FE models are presented in Fig. 9. The indices are normalised with respect to the highest sensitivity index for each FE model. The LVI sensitivity index is calculated since the UQ&M analysis takes into account the projected delaminated area as an input variable for the creation of the RS of the CAI model. Therefore, the parameters of the model that generate the highest dispersion in the LVI results and the CAI strength are selected as key parameters. In this case, the key parameters are: $\mathcal{G}_{IIc}$ for the LVI and $\mathcal{G}_{XC}$ for the CAI strength. The large influence of $\mathcal{G}_{IIc}$ on the projected delamination area is explained because it is the interlaminar fracture toughness in mode II that corresponds to the delamination damage mechanism. In addition, the high impact of $\mathcal{G}_{XC}$ on the CAI strength is plausible because it is the longitudinal compression fracture toughness linked with the fibre kinking damage mechanism. Moreover, $\mathcal{G}_{XC}$ is also the second independent variable that generates the most dispersion in the LVI index (projected delaminated area). For the CAI strength, $\mathcal{G}_{IIc}$ also has a high sensitivity index.

Out of the 31 input parameters analysed, the LVI FE model has 19 input parameters with a sensitivity index greater than 0.2. This indicates that the LVI results are sensitive to several input parameters and, therefore, this model demands a more accurate calibration of a larger number of input parameters than the CAI strength, since the latter has only four input parameters greater than 0.2. To fully capture the influence of all the input parameters, a global sensitivity analysis with interactions should be carried out.

4.2. Response surface analysis

Firstly, the UQ&M test matrix is created with 80 FE models defined by means of the LHS method. The cases are distributed following a uniform distribution narrowed to $\pm 3\hat{s}_i$ for each key parameter to obtain an RS within the range described. Therefore, the probability of evaluating the RS by means of MCS outside the previous range is 0.26%. In addition, 20 more FE models are defined with the normal LHS method. These cases follow a normal distribution to obtain a more accurate RS in the centre range of each key parameter; because the RS will be more thoroughly evaluated in the centre range of each key parameter in the MCS. Therefore, the total number of cases for the UQ&M test matrix is 100.

Then, the test matrix is submitted to the FE models and the projected delaminated area and the CAI strength are obtained for each case. Further, the RS is generated by randomly selecting 90 cases (out of the total 100 cases) from the UQ&M test matrix as explained below. The input variables of the CAI RS are the key parameters and the projected delaminated area obtained from the LVI simulations. Finally, the accuracy factors presented in Section 3.2 are calculated using the remaining ten cases for validation. The most accurate RS is obtained using an optimisation algorithm to maximize the accuracy factors. .

Two different RSs for the CAI model are used to determine the influence accuracy of the RS has on the design allowables. CAI90A and CAI90I are the RSs for the CAI strength generated with 90 randomly selected cases from the UQ&M test matrix. The accuracy of CAI90A (RS of CAI model with 90 cases and Accurate) is greater than CAI90I (RS of CAI model with 90 cases and Inaccurate).

In addition, the effect of using or not the projected delaminated area as an input of the CAI RS on the design allowables is analysed by comparing the results between CAI90A and CAI90AnD. The input parameters of CAI90AnD are only the key parameters but not the projected delaminated area.

The configuration of each RS analysed and the accuracy analysis results are summarised in Table 5. The CAI90A and CAI90AnD R^2 coefficients are very close - 0.97 and 0.98 respectively. In addition, they have the same p-value for the Pearson goodness-of-fit statistic analysis (p-value equal to 0.98). Therefore, there is not enough evidence to reject the hypothesis that the RSs fit the CAI strength. However, the RMSE coefficient has significant differences for these two surfaces, with CAI90AnD having the best accuracy factors. Meanwhile, CAI90I has the poorest accuracy factors, and from a statistical point of view does not fit the CAI strength.

Fig. 10 compares the goodness-of-fit plot for each RS in Table 5. The values are normalised with respect to the mean value of the 100 FE

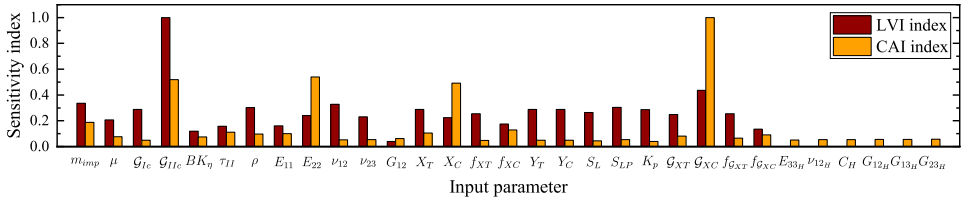

Fig. 9. Sensitivity index of each input parameter for the LVI FE model and for the CAI FE model. The indices are normalised with respect to the highest sensitivity index for each FE model. (For interpretation of the references to colour in this figure legend, the reader is referred to the web version of this article.)

Table 5
Statistics of the RS for the CAI FE model created to estimate the design allowables. AD refers to the projected delaminated area.

Nomenclature	Samples	Input parameter	R^2	RMSE	p-value
CAI90A	90	AD, $\mathcal{G}_{IIc}$ and $\mathcal{G}_{XC}$	0.97	7.13	0.98
CAI90I	90	AD, $\mathcal{G}_{IIc}$ and $\mathcal{G}_{XC}$	0.84	12.91	0.32
CAI90AnD	90	$\mathcal{G}_{IIc}$ and $\mathcal{G}_{XC}$	0.98	5.87	0.98

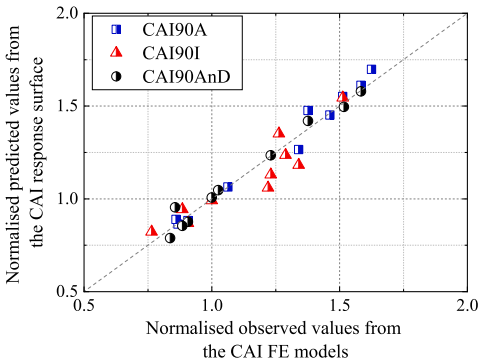

Fig. 10. Goodness-of-fit plot for each RS in Table 5. The values are normalised with respect to the mean value of the CAI strength obtained from the 100 FE models used to create the RS. (For interpretation of the references to colour in this figure legend, the reader is referred to the web version of this article.)

models used to create the RSs. Data comparison confirms the accuracy coefficients in Table 5, where the more accurate RSs are CAI90A and CAI90AnD, because the R^2 and the p-value from the chi-squared test are close to 1 and the RMSE is small.

4.3. Design allowables

The A/B-basis values of the CAI strength obtained from each RS in Table 5 are displayed in Fig. 11. The results are represented as a function of n and N. They are normalised with respect to the mean value of the CAI strength obtained from the CAI90A RS with the maximum sample size ($n = 10^5$ and $N = 10^5$). The percentage difference between the mean value from $n = 10^2$ and $N = 10^2$ with respect to the one obtained from $n = 10^5$ and $N = 10^5$ is equal to 0.11%. The normalisation allows the design allowables to be compared with the mean value.

The results obtained from the CAI90A and CAI90I RSs are lower than the mean value of the CAI strength from the CAI90A RS, whereas the values obtained from CAI90AnD are higher. This indicates that CAI90AnD overestimated the A/B-basis values since the 5th percentile of the distribution of the 1st percentile and the 10th percentile, respectively, must be lower than the mean value of the measured population. Hence, the results obtained from CAI90AnD are rejected. It can be concluded that the projected delaminated area must be an input of the CAI RS to estimate the design allowables. In addition, the results obtained from CAI90I are close to those obtained from CAI90A and the sample size n of the MCS has a greater influence on the results than the number of repetitions N of the MCS.

The comparison of the design allowables obtained from CAI90A and CAI90I as a function of n shows the biggest discrepancies for small values of n (see Fig. 12). The maximum percentage differences for the design allowables between both RSs are lower than 7.7% and 3.5% for the A-basis value and the B-basis value, respectively. As expected, the calculus in the tail of a distribution requires a large sample size and, since the CAI90I RS is less accurate, the discrepancies between both RS for small sample size are higher. The A-basis values are almost constant when $n > 5{\cdot}10^6$. Using CAI90A RS, the A-value is 0.732 and using CAI90I it is 0.725. The B-basis value is almost constant when $n > 5{\cdot}10^5$ and it is 0.938 using CAI90A and 0.937 using CAI90I.

The influence of sample size n and the number of repetitions N on the design allowables is also described in Fig. 13. The ECDF for different values of n and N of the 1st and 10th percentile distributions are represented by CAI90A RS. For $n = 10^2$ and $N = 10^2$, the dispersion of each percentile distribution is greater than the rest of the ECDFs. The difference for the A-basis value between the cases with $n = 10^2$ and $N = 10^2$ and $n = 10^4$ and $N = 10^2$ is equal to 21.5%. For the B-basis value it is equal to 5.9%. However, the results from $n = 10^4$ and $N = 10^2$ and those from $n = 10^4$ and $N = 10^5$ (with the same n and different N) are almost identical. Similarly, the results from $n = 10^5$ and $N = 10^2$ and those from $n = 10^5$ and $N = 10^5$ are also close.

The difference between the A-basis value and the mean of the 1st percentile when $n = 10^5$ and $N = 10^5$ is 0.67%, and for the B-basis value the difference of the mean value of the 10th percentile is 0.11%. This results suggest that the A-basis and B-basis values can be approximated using the 1st and 10th percentile, respectively, when n is sufficiently higher. This is in line with the conclusion of Vallmajó et al. [4].

The design allowables selected from the MCS approach are those obtained from CAI90A with $n = 10^4$ and $N = 10^2$; since, from CAI90A a good compromise between the stabilisation of the results and the computational time is obtained. This refers to a reduction in the computational effort by 7.5×10^3 times, whereas the percentage difference of the design allowables is lower than 1.2%, compared with respect to those obtained with $n = 10^5$ and $N = 10^5$. In addition, the best accuracy coefficients are obtained with the CAI90A RS.

The experimental data are compared with the numerical results in Fig. 14. The grey area is the 90% confidence bound of the experimental data. The values are normalised with respect to the mean value of the experimental CAI strength. The deterministic value is obtained using the FE models with the mean value of the input parameters. Ten samples randomly selected from the 20 normal LHS samples used to create the RSs are selected. The difference between the mean from the previous ten samples and the one obtained from the experimental data is equal to 6.1% and the difference of the median is equal to 10.9%. Both values (mean and median) from the ten random samples are within the 50% confidence bound of the experimental data. This demonstrates that

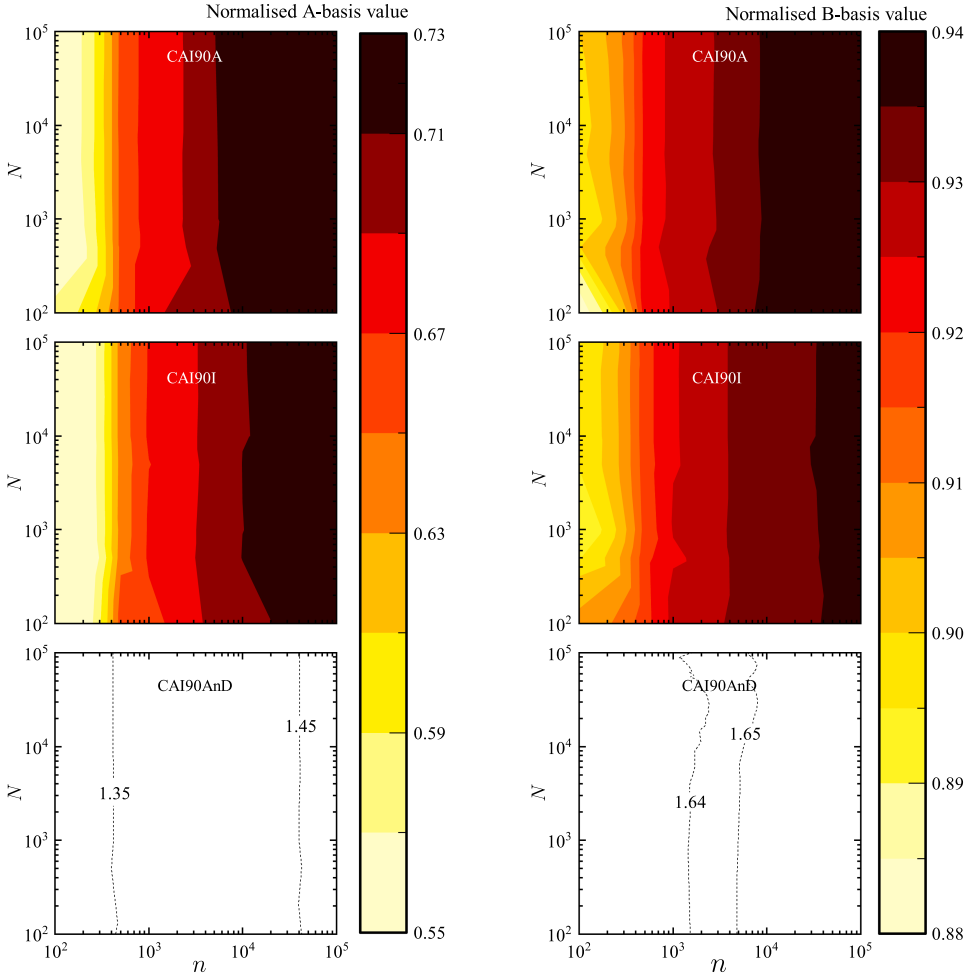

Fig. 11. Comparison of the A-basis value (left) and the B-basis value (right) of the CAI FE model estimated with different sizes of the MCS (n) and with different repetition numbers of the MCS (N). Results obtained using the CAI90A RS (top), the CAI90I (centre) and the CAI90AnD RS (bottom). The values are normalised with respect to the mean value of the CAI strength obtained from the CAI90A RS with $n = 10^5$ and $N = 10^5$. (For interpretation of the references to colour in this figure legend, the reader is referred to the web version of this article.)

the validation of a numerical model by comparing the deterministic numerical result with the mean from the experimental data is not a good procedure. The input variability of a numerical model is required for its validation. The mean and median values obtained from the MCS with $n = 10^4$ and $N = 10^2$ are within the 90% confidence bound of the experimental data and their difference is equal to 10.5% and 17.7%, respectively.

The accuracy of the CAI90A RS can be also observed in Fig. 14. The mean and median values from the MCS are within the outlier bounds of the ten randomly selected FE results. In addition, the difference of the mean and median values between these two approaches are equal to 6.0% and 5.1%, respectively. Thus is, in concordance with the results obtained in the accuracy analysis of the RSs. The differences between the experimental data and the numerical results can be associated to the same sources of the deterministic model, but also, due to the mesh size kept constant despite varying the $\mathcal{G}_{IIc}$ and the assumption on the statistical distributions of the input parameters.

The dispersion of the results of the experimental data is greater than that obtained numerically (from the FE models and the RS). This could imply that there are other input parameters that generate dispersion on the results apart from the key parameters ($\mathcal{G}_{IIc}$ and $\mathcal{G}_{XC}$). Another possibility is that the uncertainty of the key parameters are not properly defined (i.e. the coefficient of variation of the key parameters can be greater than those used in the analysis).

4.4. CMH-17 approach vs. present methodology

The A/B-basis values obtained using the methodology presented in

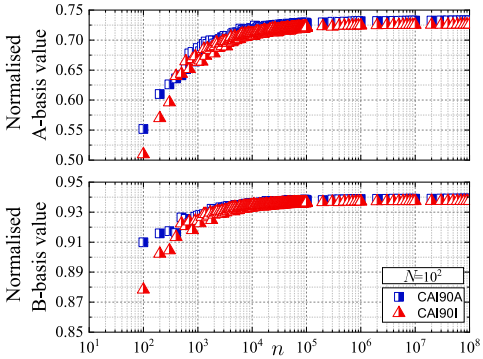

Fig. 12. Comparison of the A-basis value (top) and the B-basis value (bottom) vs. the size of the MCS (n) repeated 10^2 times ($N = 10^2$), from the CAI90A and CAI90I RS. The values are normalised with respect to the mean value of the CAI strength obtained from the CAI90A RS with $n = 10^5$ and $N = 10^5$. (For interpretation of the references to colour in this figure legend, the reader is referred to the web version of this article.)

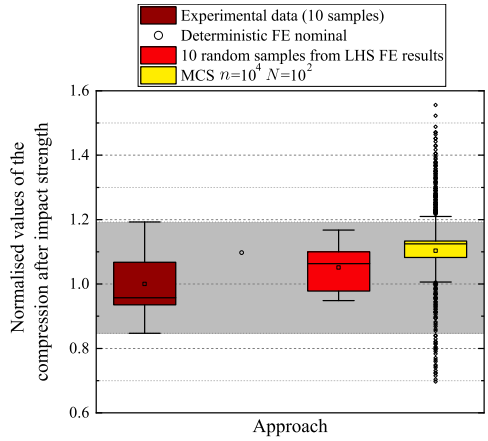

Fig. 14. Comparison of the CAI strength values obtained for the different approaches. The grey area is the 90% confidence bound of the experimental data. The values are normalised with respect to the mean value of the experimental CAI strength. (For interpretation of the references to colour in this figure legend, the reader is referred to the web version of this article.)

the previous section is also compared with the basis values obtained by a direct replication of the procedure used for the experimental results, i.e., following the CMH-17 guidelines (see Fig. 15). The values of the figure are normalised with respect to the mean value of the corresponding group. The values summarised in this figure are obtained from the ten experimental samples using the CMH-17 approach ($n = 10$ and $N = 1$), the ten samples randomly selected from the 20 normalised LHS FE models used to create the RSs and using the CMH-17 approach, and the CAI90A RS using the ECDF with $n = 10^4$ and $N = 10^2$. It is worth mentioning that, although the number of laboratory tested specimens is small, the sample size meets the requirements of the CMH-17 approach, because specimens from four different batches were tested to obtain the experimental data (more than the three batches required by CMH-17 approach).

The design allowables obtained from the experimental data are lower than those obtained from the ten samples randomly selected from the normal LHS FE models. This trend is explained by the results in Fig. 14. Although the mean values of these two cases are closer, the dispersion of the experimental data is greater. Therefore, the 1st and the 10th percentiles obtained from the experimental data are lower than those estimated from the numerical results. Consequently, the design allowables of the experimental data are lower than those calculated from the numeric results. This is in agreement with the results obtained by Laurin et al. in [2].

The difference between the values calculated by the CMH-17 approach and those estimated using the CAI90A RS is explained in Fig. 16. It is created by computing the B-basis value for a different number of specimens using the CAI90A RS and (i) the guidelines given in the CMH-17 and (ii) using ECDF with $N = 1$ (i.e. the 10th percentile). The red dashed line is the B-basis value obtained with $n = 10^4$ and $N = 10^2$. The values are normalised with respect to the mean value of the CAI strength obtained from CAI90A RS with $n = 10^5$ and $N = 10^5$. The B-basis values calculated with the CMH-17 approach are more conservative than the theoretical B-basis value (red dashed line). In addition, these values do not show a clear trend for small sample size ($n < 90$). However, the 10th percentiles estimated with the ECDF are closer to the theoretical B-basis value and there is no significant dispersion in function of n. In addition, when n increases, the difference in the values from the two approaches decreases, but the CMH-17 values

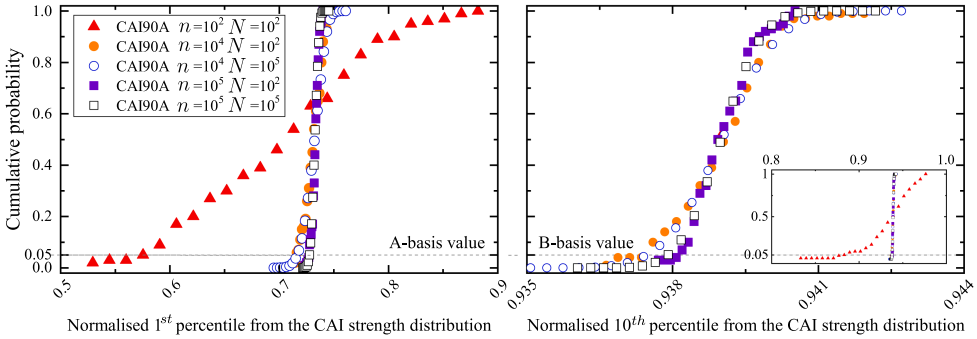

Fig. 13. Comparison of the ECDF of the 1st percentile (left) and the 10th percentile (right) of the CAI strength for different sizes of the MCS (n) and for different repetition numbers of the MCS (N) from the CAI90A RS. The percentile values are normalised with respect to the mean value of the CAI strength obtained from CAI90A RS with $n = 10^5$ and $N = 10^5$. (For interpretation of the references to colour in this figure legend, the reader is referred to the web version of this article.)

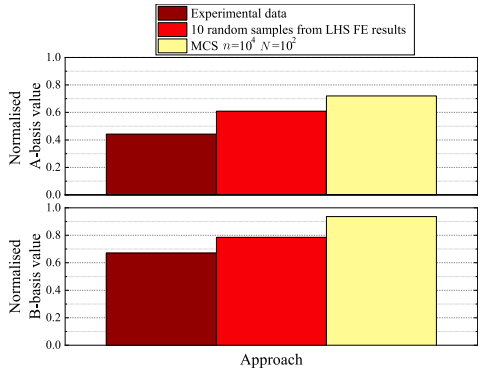

Fig. 15. Comparison of the A-basis value (top) and B-basis value (bottom) obtained from ten experimental samples using the CMH-17 approach [1], from ten randomly selected samples from the 20 normalised LHS FE models used to create the response surfaces using the CMH-17 approach [1] and from the MCS (MCS) and ECDF function approach with a size of the MCS of 10^4 samples ($n = 10^4$) and 10^2 repetitions ($N = 10^2$) using the CAI90A RS. The values are normalised with respect to their mean value of the corr.esponding group. (For interpretation of the references to colour in this figure legend, the reader is referred to the web version of this article.)

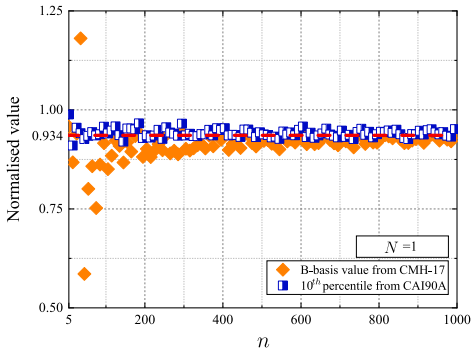

Fig. 16. B-basis value estimated by means of the CMH-17 approach [1] and the 10th percentile estimated by means of ECDF function from the CAI90A RS with n samples repeated once ($N = 1$). The red dashed line is the B-basis value obtained with $n = 10^4$ and $N = 10^2$. The values are normalised with respect to the mean value of the CAI strength obtained from the CAI90A RS with $n = 10^5$ and $N = 10^5$. (For interpretation of the references to colour in this figure legend, the reader is referred to the web version of this article.)

remain more conservative.

5. Conclusions

A methodology to obtain the design allowables using high-fidelity models is proposed. The methodology is based on generating a Response Surface (RS) from a reduced number of high-fidelity simulations. Using the RS, an empirical cumulative density function is determined and used to obtain the basis value. The methodology was applied to the A/B-basis value calculation of the compression after impact strength of thin laminates. The experimental procedure used relies on first impacting a laminate, then gluing this impacted laminate to a honeycomb core and another pristine laminate, and finally loading the sandwich structure under compression. The same procedure was used for the high-fidelity simulations. The model strategy used was validated by comparing the distribution of the numerical results with the one obtained from the experimental data.

Next, several simulations were performed to generate the RS and apply the proposed methodology to obtain the A/B-basis values. When creating the RS, if the selection of the input parameters for the RS is not appropriate, good statistical coefficients in the accuracy analysis may not guarantee a proper reproduction of the model behaviour. Moreover, the A/B-basis values obtained with a less accurate RS are very close to those obtained from a more accurate RS if the sample size is large. As the A-basis value is more towards the left tail of the distribution, it is more sensitive to the accuracy of the RS than the B-basis value. It has also been demonstrated that, when performing the Monte Carlo simulations, the sample size has more influence on the design allowables than the number of repetitions does. Hence, the A/B-basis value can be numerically estimated using a single Monte Carlo simulation provided a large sample size.

The methodology presented has the potential to reduce non-recurring certification cost provided the reduction on the test cost and/or design span time is higher than the cost associated to perform the numerical simulations and to obtain the design allowables. The approach followed in this work, where the UQ&M methodology presented has been implemented using python scripts that automate all the process (including the generation and post-process the finite element models), reduces the engineering labour associated to obtain the design allowables.

CRediT authorship contribution statement

Ivan R. Cózar: Conceptualization, Methodology, Validation, Investigation, Formal analysis, Writing - original draft, Writing - review & editing, Visualization. **A. Turon:** Conceptualization, Methodology, Validation, Investigation, Formal analysis, Writing - original draft, Writing - review & editing, Visualization. **E.V. Gonzólez:** Methodology, Software, Investigation, Formal analysis, Writing - original draft, Writing - review & editing, Visualization. **O. Vallmajó:** Writing - review & editing. **A. Sasikumar:** Writing - review & editing.

Declaration of Competing Interest

The authors declare that they have no known competing financial interests or personal relationships that could have appeared to influence the work reported in this paper.

Acknowledgements

The authors would like to acknowledge Philippe Peters from Airbus for the discussions held and the input provided to perform this study. The first author would like to acknowledge the support of the Catalan Government (Agència de Gestió d'Ajuts Universitaris i de Recerca), through Grant 2019FI_B_01117. O. Vallmajó acknowledges the support of the Catalan Government, under the Grant 2018FI_B_00904. This work has been partially funded by the Spanish Government (Ministerio de Economia y Competitividad) under contract RTI2018-099373-B-I00, partially funded by the European Social Fund.

References

[1] Composite Materials Handbook, Vol. 1. Polymer matrix composites guidelines for characterization of structural materials, SAE International on behalf of CMH-17, a division of Wichita State University; March 2012.
[2] Laurin F, Paulmier P, Irisarri F-X. Determination of the longitudinal compressive strength of a cfrp ply through a tensile test on a laminate. Compos Part A: Appl Sci Manuf 2018;113:209–19.
[3] Arregui-Mena JD, Margetts L, Mummery PM. Practical application of the stochastic finite element method. Arch Comput Methods Eng 2016;23(1):171–90.
[4] Vallmajó O, Cózar I, Furtado C, Tavares R, Arteiro A, Turon A, et al. Virtual

calculation of the b-value allowables of notched composite laminates. Compos Struct 2019;212:11–21.
[5] Gosling PD, Polit O, et al. A high-fidelity first-order reliability analysis for shear deformable laminated composite plates. Compos Struct 2014;115:12–28.
[6] Delbariani-Nejad A, Farrokhabadi A, Jafari SR. An energy based approach for reliability analysis of delamination growth under mode I, mode II and mixed mode I/II loading in composite laminates. Int J Mech Sci 2018;145:287–98.
[7] Hussein OS, Mulani SB. Reliability analysis and optimization of in-plane functionally graded cnt-reinforced composite plates. Struct Multidiscip Optim 2018;58(3):1221–32.
[8] Bogenfeld R, Kreikemeier J, Wille T. Review and benchmark study on the analysis of low-velocity impact on composite laminates. Eng Fail Anal 2018;86:72–99.
[9] González E, Maimí P, Camanho P, Turon A, Mayugo J. Simulation of drop-weight impact and compression after impact tests on composite laminates. Compos Struct 2012;94(11):3364–78.
[10] Rivallant S, Bouvet C, Hongkarnjanakul N. Failure analysis of cfrp laminates subjected to compression after impact: Fe simulation using discrete interface elements. Compos Part A: Appl Sci Manuf 2013;55:83–93.
[11] Caputo F, De Luca A, Lamanna G, Borrelli R, Mercurio U. Numerical study for the structural analysis of composite laminates subjected to low velocity impact. Compos Part B: Eng 2014;67:296–302.
[12] Tan W, Falzon BG, Chiu LN, Price M. Predicting low velocity impact damage and compression-after-impact (cai) behaviour of composite laminates. Compos Part A: Appl Sci Manuf 2015;71:212–26.
[13] Abdulhamid H, Bouvet C, Michel L, Aboissière J, Minot C. Numerical simulation of impact and compression after impact of asymmetrically tapered laminated cfrp. Int J Impact Eng 2016;95:154–64.
[14] Perillo G, Jørgensen JK, Cristiano R, Riccio A. A numerical/experimental study on the impact and cai behaviour of glass reinforced composite plates. Appl Compos Mater 2018;25(2):425–47.
[15] Sun X, Hallett S. Failure mechanisms and damage evolution of laminated composites under compression after impact (cai): Experimental and numerical study. Compos Part A: Appl Sci Manuf 2018;104:41–59.
[16] Liu H, Falzon BG, Tan W. Predicting the compression-after-impact (cai) strength of damage-tolerant hybrid unidirectional/woven carbon-fibre reinforced composite laminates. Compos Part A: Appl Sci Manuf 2018;105:189–202.
[17] Sasikumar A, Costa J, Trias D, González E, García-Rodríguez S, Maimí P. Unsymmetrical stacking sequences as a novel approach to tailor damage resistance under out-of-plane impact loading. Compos Sci Technol 2019;173:125–35.
[18] English SA, Briggs TM, Nelson SM. Quantitative validation of carbon-fiber laminate low velocity impact simulations. Compos Struct 2016;135:250–61.
[19] Patel S, Soares CG. System probability of failure and sensitivity analyses of composite plates under low velocity impact. Compos Struct 2017;180:1022–31.
[20] Patel S, Soares CG. Reliability assessment of glass epoxy composite plates due to low velocity impact. Compos Struct.
[21] AITM, Airbus Test Method. Fibre Reinforced Plastics: Determination of Compression Strength after Impact, Tech. rep., Blagnac Cedex, France; 2005.
[22] Sasikumar A, Trias D, Costa J, Blanco N, Orr J, Linde P. Effect of ply thickness and ply level hybridization on the compression after impact strength of thin laminates. Compos Part A: Appl Sci Manuf 2019;121:232–43.
[23] Soto A, González E, Maimí P, Mayugo J, Pasquali P, Camanho P. A methodology to simulate low velocity impact and compression after impact in large composite stiffened panels. Compos Struct 2018;204:223–38.
[24] González E, Maimí P, Martín-Santos E, Soto A, Cruz P, de la Escalera FM, de Aja JS. Simulating drop-weight impact and compression after impact tests on composite laminates using conventional shell finite elements. Int J Solids Struct 2018;144:230–47.
[25] Soto A, González E, Maimí P, De La Escalera FM, De Aja JS, Alvarez E. Low velocity impact and compression after impact simulation of thin ply laminates. Compos Part A: Appl Sci Manuf 2018;109:413–27.
[26] Maimí P, Camanho PP, Mayugo J, Dávila C. A continuum damage model for composite laminates: Part I–constitutive model. Mech Mater 2007;39(10):897–908.
[27] Maimí P, Camanho PP, Mayugo J, Dávila C. A continuum damage model for composite laminates: Part II–computational implementation and validation. Mech Mater 2007;39(10):909–19.
[28] González E, Maimí P, Turon A, Camanho P, Renart J. Simulation of delamination by means of cohesive elements using an explicit finite element code. Comput, Mater Continua (CMC) 2009;9(1):51.
[29] Turon A, Camanho P, Costa J, Renart J. Accurate simulation of delamination growth under mixed-mode loading using cohesive elements: definition of interlaminar strengths and elastic stiffness. Compos Struct 2010;92(8):1857–64.
[30] Campolongo F, Cariboni J, Saltelli A. An effective screening design for sensitivity analysis of large models. Environ Model Software 2007;22(10):1509–18.

A.3 Paper D – Micromechanical analysis of composite materials considering material variability and microvoids

The paper has been published in *International Journal of Mechanical Sciences.* 108781 (2023).

International Journal of Mechanical Sciences 263 (2024) 108781

Contents lists available at ScienceDirect

International Journal of Mechanical Sciences

journal homepage: www.elsevier.com/locate/ijmecsci

Micromechanical analysis of composite materials considering material variability and microvoids

O. Vallmajó [a,*], A. Arteiro [b,c], J.M. Guerrero [a], A.R. Melro [d], A. Pupurs [e], A. Turon [a]

[a] AMADE, Polytechnic School, University of Girona, C/Universitat de Girona 4, 17003 Girona, Spain
[b] DEMec, Faculdade de Engenharia, Universidade do Porto, Rua Dr. Roberto Frias, 4200-465 Porto, Portugal
[c] INEGI, Rua Dr. Roberto Frias, 400, 4200-465 Porto, Portugal
[d] Bristol Composites Institute (ACCIS), University of Bristol, Queen's Building, BS8 1TR, UK
[e] Laboratory of Experimental Mechanics of Materials, Riga Technical university, Riga, LV 1048, Latvia

ARTICLE INFO

Keywords:
Fiber reinforced polymers (FRP)
Microvoids
Mechanical properties
Micro-mechanics

ABSTRACT

One of the main challenges for fiber-reinforced polymers (FRP) is the difficulty to predict their mechanical behavior. At the microscale, the properties of the constituents, their spatial distribution and the defects arising from manufacturing affect the mechanical behavior. In this work, statistically representative volume elements (SRVEs) are proposed based on a micromechanical finite element model to determine the effect of content, distribution and size of microstructural defects and, material uncertainties on the elastic mesoscale properties of FRPs. To that end, different cylindrical void sizes are considered as well as irregular shaped voids between fiber tows (inter-fiber voids). Fibers and voids are randomly distributed in a SRVE. An uncertainty quantification and management analysis is employed to obtain statistical descriptors of the effective mesoscale mechanical properties of FRPs. The results obtained are compared with analytical models. It is demonstrated that, for carbon fiber/epoxy composites, SRVEs with lateral dimensions equivalent to 15 times the average fiber diameter and a length of 0.01 mm along the longitudinal direction remain statistically representative with or without the presence of voids. The results show that the presence of voids reduces the transverse and shear elastic properties of FRPs. The smaller the voids are, the bigger is the reduction. Regarding the presence of inter-fiber voids, the reduction is lower. This trend is well predicted by the Mori–Tanaka mean field theory. However, the relative difference between the numerical and the analytical predictions increases for high void volume fractions. Regarding the effective longitudinal Young's modulus, the rule of mixtures, the Mori–Tanaka mean field theory and the concentric cylinder assembly model provide similar predictions for the mean value, but the uncertainty is overestimated by the analytical models because the properties of the fibers take a single value for each calculation with the analytical model, while they more realistically change from fiber to fiber in the numerical SRVEs.

1. Introduction

Composite materials are of special interest in modern industry due to their excellent specific mechanical properties. However, the brittle nature of polymer composites means that failure initiates from a stress raiser. This can be a geometrical feature, e.g., a hole, damage, e.g., impact on a surface, or the presence of defects, e.g., the existence of voids. In fiber-reinforced polymers (FRPs) there are many defects related to the constituents: fiber defects, such as fiber degradation or in-plane misalignment, matrix defects, such as porosity or contaminants, and fiber–matrix defects, such as debonding or poor wetting of the fibers [1]. Voids are among the most important defects since they affect a wide range of composite properties and they tend to be common in many different manufacturing techniques [2,3].

Voids can usually be defined as cylindrical branch-type defects generally aligned with the fiber direction [4]. The main sources of porosity in composite materials are air entrapment during the initial manufacturing stage and volatile components or contaminants generated during curing [5]. Voids may be present in a composite with different sizes, shapes and content. When studying macrovoids in carbon/carbon composites, Drach et al. [6] showed that, in unidirectional composites, assuming voids aligned with the fibers and extending continuously with constant cross-section may significantly overestimate the longitudinal and slightly underestimate the transverse stiffness of the material when compared with irregularly shaped macrovoids. On the other hand, parallel 2:1 spheroidal voids randomly distributed in the same transversely

* Corresponding author.
E-mail address: oriol.vallmajo@udg.edu (O. Vallmajó).

https://doi.org/10.1016/j.ijmecsci.2023.108781
Received 14 April 2023; Received in revised form 21 September 2023; Accepted 24 September 2023
Available online 4 October 2023
0020-7403/© 2023 The Authors. Published by Elsevier Ltd. This is an open access article under the CC BY license (http://creativecommons.org/licenses/by/4.0/).

isotropic matrix result in closer predictions of the effective moduli. In the present study, however, focus will be given to the presence of voids at the level of the constituents, linked to the occurrence of porosity at the microscale. Most of the authors found, by 3D micro-CT scanning, that microvoids have a rod-like geometry oriented along the fiber direction [7–18]. Regarding the cross-section, some microvoids present an irregular shape which, for the sake of simplicity, can be fitted into a circle [17–19], whereas others are almost circular [15,20]. These microvoids typically have an equivalent diameter of 3 to 20 μm [13–16] even for thermoplastic matrices [21]. Vajari et al. [15], Hyde et al. [20] and Daggumati et al. [22] concluded that, microvoids whose size is comparable with the fiber diameter are present in a composite between fiber clusters with an irregular shape, since the matrix cannot easily flow-in during manufacturing. They also concluded that microvoids can be present as small air bubbles being trapped in the matrix.

Several studies have been focused on the effect voids have on the mechanical properties of FRPs. Experimentally, Almeida and Neto [23] determined that voids have a high detrimental effect on the fatigue life of composite structures. Chambers et al. [16] found that an increasing void content reduces the flexural strength and the fatigue performance acting on the initiation and propagation of failure mechanisms. Zhu et al. [11] concluded that cracks emanate from the voids and so both tensile strength and modulus decrease. Finally, Chu et al. [24] also observed that porosity have a detrimental effect on the transverse and shear moduli, whereas the effect on the longitudinal properties is much lower.

Accurate numerical simulations, with advanced constitutive models, can help understand the mechanical behavior at the microscale (constituents level) and their effect on the mesoscale properties (ply level). Melro et al. [25] defined a methodology to generate a micromechanical 3D representative volume element (RVE) containing randomly distributed fibers in accordance to the fiber volume fraction. Tavares et al. [26] extended this version of the random fiber generator to obtain the microstructure of a composite material with different types of fibers, i.e., a fiber-hybrid composite. In the present work, this methodology is further extended to take into account the presence of voids. To that end, an RVE of the composite material with defects needs to be defined. That is, a sample that is structurally entirely typical of the whole mixture on average and contains a sufficient number of inclusions to be effectively independent, so that the results are macroscopically uniform [27].

The analysis of the effect of matrix voids using computational micro-mechanics is not new. Previous studies include the work of Vajari et al. [15], where 2D numerical simulations were performed considering elongated voids parallel to the fiber direction with a circular cross section. Inter-fiber voids with an irregular shape were also considered. Dong [28] studied the effect of randomly distributed voids on the stiffness and strength of FRP also comparing the results with analytical models. Mehdikhani et al. [2,18] also simulated the effect of microvoids on the elastic moduli of carbon fiber reinforced polymers considering a single ellipsoidal void embedded in the matrix. These voids will be simply referred to as “matrix voids”. Hyde et al. [14,20] used a micromechanics-based finite element modeling strategy to study the effect of a single matrix or inter-fiber void on the strength of composite structures. Sharifpour et al. [29] developed a 2D micromechanical model to assess the effect of microvoids on the local stress state, with a circular shape, in a cross-ply laminate. Chu et al. [24] studied the influence of voids on the stiffness properties of unidirectional FRPs, considering very small spherical voids. More recently, Daggumati et al. [22] checked the effect of matrix and inter-fiber voids, as well as other geometrical and material features such as thermal residual stresses and the random spatial distribution of the reinforcements, in a 2D cell under a transverse loading state. Vinot et al. [30] developed a model to quantify uncertainties, e.g., porosity, in continuous unidirectional composites and evaluate their influence on the mechanical properties of the material. However, to the authors’ best knowledge, all the current literature studies have not taken into account simultaneously the random spatial distribution of the constituents, the variability in their properties and the variability of the characteristics of microvoids in the definition of statistically representative volume elements (SRVEs) for fiber-reinforced polymers.

In the design of composite structures it is also important to take into account the uncertainties in the design parameters, arising, for example, from the scatter in the material properties. Vallmajó et al. [31] defined a methodology to account for the uncertainty of an open-hole specimen by calculating analytically B-value design allowables through Monte Carlo simulation (MCS). The B-value is a statistically-based design allowable, recommended by the Composite Materials Handbook (CMH-17) [32], and defined as the 95% lower confidence bound on the tenth percentile of a specified population of measurement. Cózar et al. [33] also created a methodology to calculate the B-value from a high-fidelity numerical model creating a response surface of the results and, afterwards, performing a MCS. These strategies rely on input material properties at the ply level, and their uncertainties, characterized by experimental results to, finally, obtain the B-value allowables. However, contribution to uncertainty is not only based on the scatter in the material properties, but also from the presence of defects and their characteristics. Currently, there is a lack of studies considering the definition of SRVEs that, besides the random distribution of the reinforcements, also take into account the uncertainty of the material properties as well as the presence of defects. Therefore, SRVEs are generated herein that account for the effect of the uncertainties related to void content, distribution and size, and for the effect of the uncertainties of material properties on the elastic mesoscale properties of a carbon fiber reinforced polymer (CFRP). The methodology proposed in this work can be used to guide the quantification of uncertainties at the micro-scale, for example, to help defining knock-down factors for the effect of voids and void content, or to generate statistically representative material allowables to be used in analysis methods at the meso and macroscales. Rather than simply providing deterministic predictions of effective properties (and strengths), this methodology will enable the calculation of reliable statistical descriptors, herein focused on the effective elastic properties, but with the possibility to be extended to the stochastic prediction of damage initiation and propagation. This first step considering only the effective elastic properties will allow the assessment of the proposed approach with alternative methods, incl. well established analytical models.

The paper is organized as follows: Section 2 shows the methodology followed to generate, simulate and post-process the results from an RVE with the presence of defects; Section 3 describes the composite material and defects considered in this study; Section 4 presents the results and their discussion; finally, Section 5. summarizes the conclusions of this work.

2. Methodology

In this work, an exhaustive methodology is proposed to define SRVEs and determine the elastic properties of FRPs accounting for the uncertainty due to the material and geometric variability in the constituents, their spatial distribution and the presence of defects, in the form of matrix and inter-fiber voids. The flow chart in Fig. 1 shows the uncertainties propagation procedure followed in this study, as described in the following sections.

2.1. Composite microscopic uncertainties

In previous studies addressing the effect of the presence of microvoids on fiber-reinforced composite systems [2,8,22,24,34], the determination of the elastic properties did not account for the uncertainties associated with the intrinsic variability of the constituent properties, their spatial distribution and the characteristics of this class of defects.

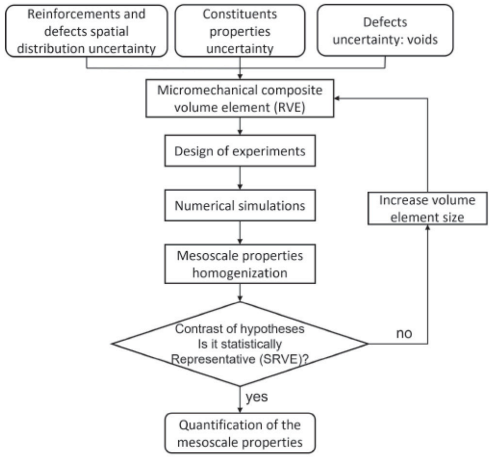

Fig. 1. Flow chart of the propagation of the uncertainties related to a composite structure to quantify their effect on the elastic mesoscale properties of the composite.

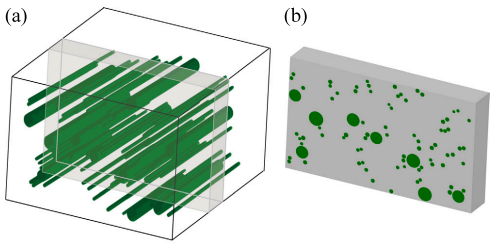

Fig. 2. A schematic 3D representation of voids inside a unidirectional ply obtained from micro-computed tomography in the literature [7,17,18,21] (a) and the corresponding representative volume element considered in this study (b).

2.1.1. Reinforcement and defects spatial distribution uncertainty

The reinforcements of FRPs are randomly distributed inside a ply. In addition, the distribution of the defects also does not follow a deterministic dispersion. Therefore, their random spatial distribution is taken into account in this study when generating the micromechanical model.

2.1.2. Constituent properties uncertainty

The different materials present in a composite system exhibit an intrinsic variability in their properties. Moreover, the size of the fibers are not constant. Therefore, the variability in the properties of the constituents and in their geometrical parameters, such as the fiber diameter, is taken into account in this study to quantify the elastic material properties of the composite.

2.1.3. Defects uncertainty: Voids

In the present work, following the data available from the literature (see Section 1), all voids are assumed to be aligned with the fiber direction (see Fig. 2).

Looking to the literature, most authors agree that voids can be represented with a circular cross-section. Moreover, in this study optical microscopy images were analyzed to characterize typical voids in glass/epoxy cross-ply laminates manufactured using pre-preg lay-up. Optical microscopy images were taken observing polished specimen edges with magnification of 200x. It is assumed that the typically observed shape and distribution of voids in glass/epoxy composite shown in Fig. 3a also applies for carbon/epoxy composites analyzed in this study. The images support that porosity appears as voids with a circular shape entrapped in matrix-rich regions or as voids with an irregular shape within the fiber tows. Therefore, this study is focused on these two types of voids: matrix voids and inter-fiber voids. Moreover, in addition to the position of the voids, the effect of their size is also considered. According to the size, voids could be classified as voids with a diameter smaller than the fibers (small matrix voids) or voids with a larger diameter (large matrix voids), as shown in Fig. 3b. It is important to note that, in this study, "small" and "large" voids (Fig. 3b) refer simply to the relative size of the voids when studying the influence of their size (considering the relative size of the fibers just as a reference), and not to an absolute measure.

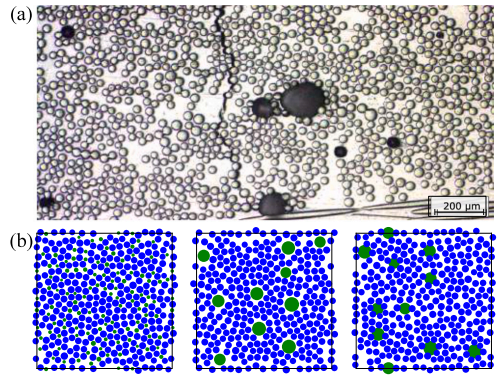

Fig. 3. (a) Image from optical microscopy with the presence of voids in dark color and (b) the corresponding RVEs (in blue the fibers and the white region is the matrix) with the presence of three types of voids (in green). From left to right: matrix voids with a diameter smaller than the fibers ("small" matrix voids), matrix voids with a larger diameter ("large" matrix voids) and voids that intersect with the fibers (inter-fiber voids). (For interpretation of the references to color in this figure legend, the reader is referred to the web version of this article.).

Void content is calculated as the void volume fraction in FRPs, e.g., following the ASTM D2734 standard that compares the theoretical and the measured composite density [35]. Although porosity should not exceed 1% for high-performance laminates and a void content greater than 5% for a composite is not acceptable in most industries, this work addresses void contents ranging up to 10% to characterize their effect in a wider range, including some of its highest and critical values reported in the literature [14,17,24,36].

2.2. Micromechanical model with voids

In the following, the approach followed to generate the micromechanical finite element model including all uncertainties taken into account in this study, described in Section 2.1, is summarized.

Generation of an RVE. The micromechanical model proposed by Melro et al. [25] to randomly distribute the fibers in an RVE and extended by Tavares et al. [26] to be able to define different types of fibers was modified to accurately represent an RVE with voids. The algorithm has been enhanced to generate voids with cylindrical shape parallel to the fiber direction, randomly distributed in the RVE. Two different populations are defined. The first one represents the fibers with its own geometrical properties, uncertainties and volume fraction. The second

population includes the voids, which also have their own properties and uncertainties.

The algorithm consists of the following steps:

1. Hard-core model to randomly distribute the constituents in the RVE. Therefore, in this first step, the model simply generates randomly new fibers and voids in the RVE. These are accepted on the RVE depending on a distance criterion that checks if these overlap with other fibers or voids. This criterion is different for fibers and voids as will be clarified later.
2. First Heuristic to move closer the fibers and voids between them to gain more empty areas to fill afterwards.
3. Second Heuristic to move the constituents on the outskirts towards the center of the RVE and compact them for generating matrix-rich regions.

The use of the heuristics allows reaching fiber volume fractions over 65% [25]. After these steps, the model starts a new iteration and repeats all the steps to add more fibers and voids until the desired volume fraction is achieved. In-deep details about these steps can be found in Ref. [25]. Overall, the model has the following abilities:

- Adding either fibers or voids according to the RVE size and their volume fractions.
- Defining a mean value and standard deviation for the diameters of the fibers and voids to account for the uncertainties related to their size.
- Defining three different minimum distances while placing the fibers and voids. One between fibers, another between fibers and voids and, finally, between voids. Thus, the algorithm can generate different types of voids: voids embedded in matrix-rich regions or inter-fiber voids which overlap with the fibers. These distances are defined as the mean radius of two consecutive circles of radius r_i and r_{i+1}, respectively, multiplied by a different constant value (k) for each minimum distance previously described ($k_{\text{fiber-fiber}}$, $k_{fiber-void}$ and $k_{void-void}$, respectively). Hence, the minimum distance between two of these features is calculated as $k \times (r_i + r_{i+1})/2$. For the case of inter-fiber voids, the distance between fiber and void is negative to allow the overlap between them, thus $k_{fiber-void} < 0$. Instead, for the matrix voids, this distance must be larger than 0 since no overlap is permitted.
- Generating fiber-rich regions (fiber clusters) where fibers are more compacted.

Thus, different categories of RVEs with voids can be generated (see Fig. 3) to assess the effect of shape and size of the voids, for example: (i) matrix voids with a diameter smaller than the fibers (small matrix voids); (ii) matrix voids with a diameter larger than the fibers (large matrix voids); (iii) voids that intersect the fibers (inter-fiber voids).

To avoid the appearance of zero-volume elements when meshing the RVE, the algorithm was modified to force that fibers and voids close to the boundaries of the RVE remain, at least, at a distance from the boundaries equal to the average size of the matrix finite elements. Likewise, the fibers and voids cut by the RVE boundaries are cut, at least, at a section as large as their corresponding mesh size.

Modeling strategy. Once the RVE is generated according to the size, fiber volume fraction, void volume fraction and their respective diameters and variation, it needs to be discretized and analyzed using the Finite Element Method (FEM). Fig. 4 shows the sequence of steps used to generate the FEM model of the RVE. It can be summarized as follows:

(a) Creation of each part, i.e., each fiber, each void and the matrix, independently as a plate, i.e., in two dimensions (2D).
(b) Assembly of all the plates and mesh of the whole model, with the possibility of defining a different mesh size for each constituent (fiber, matrix and defect). The element mesh shape is defined as quad-dominated. Thus, almost all the elements are quadrangular except in some regions where triangular elements are included. Linear elements with reduced integration are used.

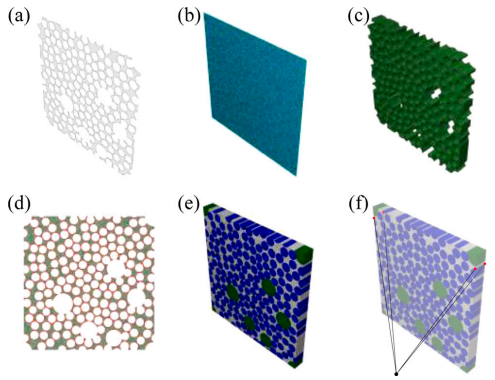

Fig. 4. Steps to model the RVE: (a) creation of each part as a plate, (b) assembly of all the parts and meshing, (c) extrusion of the mesh and conversion to 3D parts, (d) creation of each surface to define the contacts between materials, (e) assembly of all 3D parts, and (f) example of application of the periodic boundary conditions in a specific node linked with the dummy node where the far-field strains are applied.

(c) Extrusion of the mesh to convert each plate to a three-dimensional (3D) part. This strategy is followed to ensure that there is a mesh continuity in the longitudinal direction as done in previous works [34]. Hence, the periodic boundary conditions can be implemented afterwards without any problem. After the extrusion, the majority of the elements are C3D8R which correspond to linear brick elements with reduced integration, whereas in some regions the elements are C3D6 which correspond to linear triangular prism elements.
(d) Determination of each surface from each 3D part to define the constraints between the materials.
(e) Assembly of all 3D parts. The fibers and the matrix are connected with contact interactions, which adds the possibility of representing fiber–matrix debonding by employing cohesive surfaces, while the voids are assumed to be perfectly bonded to the matrix and fibers by defining contact interactions with a high penalty stiffness. It should be noted that tie constraints cannot be used since this would lead to over-constraining some nodes (the ones in the boundaries) with more than one equation: one for the periodic boundary conditions and another for the tie constraints.
(f) Implementation of the periodic boundary conditions (PBC) to link nodes in opposite faces, edges or vertices, while the micromechanical model is generated to guarantee that the RVE is geometrically and materially periodic [37]. In other words, if a fiber crosses the boundary of an RVE, the external part must be cut and moved to the opposite side keeping the same material properties. Thus, the periodicity of stress/strain field is ensured. A set of constraint equations is defined between all the nodes at the boundaries of the RVE along all degrees of freedom, through a dummy node where the far-field strain is applied (see Fig. 4f). For the complete set of equations defining the PBC, the reader is referred to Ref. [37]. To prevent rigid body motion (RBM) a random node in the middle of the RVE is fixed.

2.3. Design of experiments

Once the micromechanical RVE is created, the uncertainty of the input parameters, i.e., the variability in the constituents, the random spatial distribution and the presence of voids, is propagated to the mesoscale elastic properties (engineering constants) to quantify their

effect. To that end, an MCS is carried out. The MCS relies on the repetition of random samples to obtain statistically relevant results. In other words, a sample with n RVEs is created, where each RVE has different material properties, random spatial distribution of the constituents and random distribution of the different types of voids, and it is analyzed to obtain the distribution of the homogenized elastic material properties. The constituent properties are generated following a statistical distribution. In each RVE, the fibers are generated with different dimensions and properties according to their input distributions. The matrix properties also change, but from RVE to RVE, according to their corresponding input distributions.

2.4. Numerical simulation

The micromechanical model is simulated using the finite element software ABAQUS/Standard 6.14–2 [38]. To determine the effective elastic properties of the composite system, far-field strains of 0.001% were applied, and the stress and strain fields in the RVE post-processed (see Section 2.5).

2.5. Mesoscale properties homogenization

The uncertainties present in composite systems may be taken into account while predicting the elastic properties. According to the CMH-17 [32], the elastic properties should be defined with its mean and standard deviation. Therefore, from each simulation, the elastic properties of a composite material and their corresponding uncertainty are determined using a first-order homogenization technique (more details in Appendix A).

The results of the computational micromechanics model obtained from first-order homogenization are compared with the results calculated analytically using the rule of mixtures (RoM), the Mori–Tanaka theory and the concentric cylinder assembly (CCA) model. The RoM provides reasonable values for the longitudinal stiffness assuming that the fibers and the matrix are working in parallel, and assuming that the fibers and matrix are working as springs in series for the transverse and shear properties (more details in Appendix B). However, the predictions using the RoM for the transverse and shear stiffness are not accurate. Therefore, other micromechanical models have been proposed in the literature to determine these properties, such as the Halpin–Tsai [39] model. But to account for the presence of multiple types of inclusions (here fibers and voids), the elastic properties are better estimated using the Mori–Tanaka mean field theory [40] (more details in Appendix C). Finally, the CCA model [41] is also checked since it also allows the presence of multiple phases (more details in Appendix D).

The uncertainty quantification analyses performed numerically using computational micromechanics and analytically following the RoM, the Mori–Tanaka mean field theory, and the CCA model are compared, in terms of the obtained mean values and STDVs. The comparison considers the constituent properties variability in all cases, and includes the spatial distribution of the reinforcements and of the defects in the case of computational micromechanics (the only one herein that can account for these effects).

2.6. Definition of statistically representative volume elements (SRVEs)

The definition of an RVE implies that the results obtained are macroscopically uniform. That is, the RVE must be large enough to be representative of the continuum at a higher scale. Thus, an infinitesimal RVE may be used. However, in numerical analysis a finite size is required [42]. On the other hand, SRVEs must reproduce the same statistics related to the stress and strain fields of the macroscopic material. To account for the spatial distribution of constituents and defects and the possible material variation, a number of samples (n) is analyzed to determine these statistics.

To determine the minimum size of the SRVE, the mean values of the properties of interest obtained with volume elements of different size and discretization options (type and size of the finite elements) are determined and compared. A contrast of hypotheses is performed to check if two means can be assumed to be equal:

$$\begin{aligned} H_0 &: \bar{x_1} = \bar{x_2} \\ H_1 &: \bar{x_1} \neq \bar{x_2} \end{aligned} \tag{1}$$

where H_0 and H_1 are the null and alternative hypotheses assuming that $\bar{x_i}$ is the mean value of each sample. A pooled standard deviation, S_p, is used as an estimator of common population standard deviation:

$$S_p = \sqrt{\frac{(n_1-1)s_1^2 + (n_2-1)s_2^2}{n_1+n_2-2}} \tag{2}$$

where n_i is the sample size and s_i the standard deviation of each sample. Using the S_p and the $\bar{x_i}$ of the main data set and the ones to be compared, the test statistic

$$t_0 = \frac{\bar{x_1} - \bar{x_2}}{S_p - \sqrt{\frac{1}{n_1} + \frac{1}{n_2}}} \tag{3}$$

is used to determine if the null hypothesis can be accepted or if it must be rejected. Since this is a two-sided t-test, the required t value to accept the null hypothesis, i.e., the mean values are equal, is:

$$t_{a,n} = t_{\frac{\alpha}{2}, n_1+n_2-2} \tag{4}$$

where α is the probability of rejecting the null hypothesis when it is true. Finally, the p-value, which is the probability of obtaining test results outside the results observed under the assumption that the null hypothesis is true, is calculated. Therefore, the p-value to accept H_0 must satisfy that:

$$\text{p-value} = P(t_0 \leq t_{n_1-n_2-2}) \geq \alpha \tag{5}$$

Moreover, in this study, the variance in the results due to the uncertainty of the input parameters, such as the material variability, the spatial distribution and the presence of defects, is an important parameter that must be independent of the SRVE size and discretization. Thus, to determine the parameters for generation of SRVEs, a contrast of hypotheses is also performed to ensure that the standard deviations (STDVs) are independent of the modeling options:

$$\begin{aligned} H_0 &: s_1 = s_2 \\ H_1 &: s_1 \neq s_2 \end{aligned} \tag{6}$$

The test statistic used to determine if the null hypothesis can be accepted is F_0 defined as:

$$F_0 = \frac{s_1^2}{s_2^2} \tag{7}$$

Since this is an F-test, the F_{n_1-1,n_2-1} statistic is used to accept the null hypothesis, i.e., that the STDVs are equal. Thus, the p-value can be calculated as:

$$\text{p-value} = P(F_0 \leq F_{n_1-1,n_2-1}) \geq \alpha \tag{8}$$

So, the minimum size of the SRVE is determined by the one that provides the same mean values and STDVs of a larger one.

3. Composite material selection and effect of defects

This section describes the properties of the constituents, i.e., fibers and matrix, and the characteristics of the defects, i.e., voids, which will be used to determine the effect of defects on FRPs.

Table 1
Mean values of the elastic properties of the constituents and assumed standard deviations (STDVs).

Constituent	E_1 [MPa]		E_2, E_3 [MPa]		ν_{12}, ν_{13}		ν_{23}		G_{12}, G_{13} [MPa]		G_{23} [MPa]	
	Mean	STDV	Mean	STDV	Mean	STDV	Mean	STDV	Mean	STDV	Mean	STDV
Carbon fiber AS4	225 000	11 250	15 000	750	0.2	0.01	0.07	0.0035	15 000	750	7000	350
Epoxy matrix 3501/6	4200	210	–	–	0.34	0.017	–	–	1567	78.35	–	–

Table 2
Mean and STDV of the void diameter and the distance between fibers and voids, defined as $k_{void-fiber}$ multiplied by the mean radius, for each type of void analyzed in this study.

Void type	Mean diameter [mm]	STDV diameter [mm]	$k_{fiber-void}$ [–]
Small matrix voids	0.004	0.0004	0.1
Large matrix voids	0.014	0.001	0.1
Inter-fiber voids	0.014	0.001	−0.05

3.1. Properties of the constituents

The proposed methodology can be applied to any FRP. In this study, the material system considered is composed of AS4 carbon fibers embedded in a 3501-6 epoxy matrix. The properties of the constituents are summarized in Table 1 [43]. However, the material properties variability has not been previously reported. Other studies, such as [44], which accounted for the uncertainty in the predicted mechanical properties and the failure strengths of composite laminates, also assumed a variation equivalent to 5% of the mean value for the properties of the constituents. Moreover, the CMH-17 [32] suggests defining the elastic properties with its mean and standard deviation. So, in this analysis, a normal distribution of the material properties is considered, with a coefficient of variation of 5%.

In this study, the fiber–matrix interface is assumed to be perfectly bonded. Thus, using the interaction properties in ABAQUS/Standard, a surface interaction between fibers and matrix is used with a high penalty stiffness and without taking damage into account (i.e., without interface degradation).

The fibers have a cylindrical shape with a mean diameter of 0.007 mm and a STDV of 0.0003 mm according to Ref. [45]. The minimum distance between them ($k_{\text{fiber-fiber}}$) is defined as 0.1 times the mean radius of the two adjacent fibers. Due to the presence of voids, the fiber volume fraction (V_f) tends to be lower than usual. Therefore, the fiber volume fraction considered in this study is 55%, i.e., it is kept constant with a value of 55% while the matrix volume fraction (V_m) is reduced according to the void volume fraction (V_v).

The dimensions of the RVE and the mesh size are determined according to the statistical analysis explained in Section 2.6 and developed in Section 4.1.

3.2. Distribution and discretization of defects

As discussed previously (see Sections 1 and 2.1.3), at the microscale, voids can be represented with a cylindrical shape parallel to the fiber direction (longitudinal direction) with a circular cross-section (matrix voids), whereas inter-fiber voids present an irregular shape due to their intersection with the fibers.

The generation of voids in the finite element model is performed according to the assigned diameter and void content. Although most industries do not allow void contents above 5%, the void volume fraction considered in this study is 7% to promote a greater influence and characterize more clearly their effect, a similar approach to previous studies [14,24,28]. The characteristics of each type of voids analyzed in this study is summarized in Table 2. The minimum distance between voids ($k_{void-void}$) is two times the mean radius of two consecutive voids to allow to have fiber bundles around them.

For the sake of simplicity, and since all the SRVEs analyzed in this study are only a small portion of the whole ply (see Fig. 2b), voids represented in this micromechanical model extend along the length the SRVE, although it is recognized that, unlike the fibers, voids are not continuous. Yet, given their rod-like geometry, this is considered a suitable approximation.

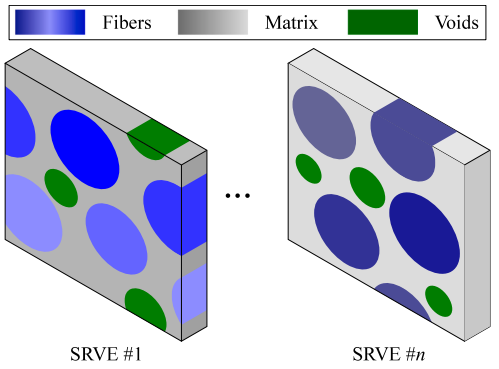

Fig. 5. Illustration of two SRVEs containing small matrix voids. The different grades of the colors show the material variability of the matrix between samples and of the fibers in each sample. Material periodicity is ensured. Geometrical variability of the fibers and voids is also represented. (For interpretation of the references to color in this figure legend, the reader is referred to the web version of this article.).

Voids dummy material. Voids represent air entrapped in the composite system. To avoid numerical problems and account for the volume variation of the RVE due to the elastic deformations, in this study voids are characterized using an isotropic dummy material [2]. A parametric analysis was conducted to assess the effect of the dummy material properties on the resulting homogenized composite properties. Finally, a value equal to 0.001 MPa for the Young's modulus and 0.001 for the Poisson's ratio resulted in no effect on the homogenized composite properties.

4. Results and discussion

This section presents, the statistical analysis to determine the SRVE, the effect of voids on FRPs and the discussion of the results obtained in this study.

4.1. Determination of the minimum size of the SRVE

A sample size n of 20 samples is analyzed. In each sample, all different fibers have random material and geometric properties according to their respective normal distribution, whereas voids have different dimensions according to their associated uncertainty. Each model also has different material properties for the matrix and a random spatial distribution of the fibers and of the defects. Therefore, each sample takes into account the material variability, the geometrical uncertainties, the effect of voids and the random spatial position of the fibers and defects (see Fig. 5).

To determine the minimum size of the SRVE and its most efficient discretization, a contrast of hypotheses for the means and the STDVs with a significance level of 5% ($\alpha = 5\%$) is performed. The parameters studied in this statistical analysis are:

Table 3
Contrast of hypotheses of the mean value ($H_{0,mean}$) and the STDV ($H_{0,STDV}$) of a 15 × 15 model to determine the minimum mesh size for discretization of fibers and matrix. The values in **bold** are the reference values used for the contrast of hypotheses.

Matrix finite element size	Fiber finite element size	
	0.00035 [mm]	0.00070 [mm]
0.00035 [mm]	**Ref value**	$H_{0,mean}$: False for E_1 $H_{0,STDV}$: False for G_{23}
0.00070 [mm]	$H_{0,mean}$: True $H_{0,STDV}$: True	$H_{0,mean}$: False for E_1, E_2, G_{12}, G_{23} $H_{0,STDV}$: True

1. The length on the longitudinal direction of the SRVE.
2. The mesh size. The fibers and the matrix can have different mesh sizes.
3. The size of the SRVE (width and height) considering a square cross-section. The SRVE size is determined relative to the fiber diameter, i.e., if the SRVE width is 20, that means that the width and height will be 20 times the mean fiber diameter (0.007 mm).
4. The presence of defects, i.e., whether the size of the SRVE is affected by the presence of voids.

Determination of the minimum length. To determine the minimum length of the SRVE, three different lengths are analyzed: 0.1 mm, 0.05 mm and 0.01 mm, in line with previous numerical studies [46]. Moreover, three model sizes were analyzed: $5 \times 5, 10 \times 10$ and 15×15, corresponding to a width and height 5, 10 and 15 times the mean fiber diameter (0.007 mm), respectively. For this analysis, the size of the finite elements was 0.0007 mm. The RVE with a length equal to 0.1 mm is taken as the reference.

The contrast of hypotheses, for the mean and STDV, were true for all the cases analyzed. It can be concluded that the length has no effect when determining the elastic properties since, for any length and size, the mean value and the STDV can be assumed to be equal to the reference value (0.1 mm long RVE). SRVEs with a length of 0.01 mm are, therefore, chosen, discretized by 5 elements, leading to a mesh size in the longitudinal direction of 0.002 mm.

Determination of the mesh size. To perform the mesh convergence study, four different mesh sizes according to the fiber diameter were evaluated in an RVE with a model cross-section of 15 × 15 fibers. The reference one is the finest, which has an element size of 0.00035 mm for both the matrix and the fibers. This leads to approximately 20 elements across the fiber diameter. Moreover, different combinations of mesh sizes for the matrix and the fibers are considered. Fig. 6 shows the results for the four different mesh size combinations normalized by the reference value. Table 3 summarizes the results of the contrast of hypotheses for the mean values and the STDVs for the mesh convergence study.

From the results of the contrast of hypotheses, the fibers will be discretized by finite elements with 0.00035 mm whereas the matrix will be discretized by finite elements with 0.00070 mm, very close to the values obtained by Li et al. [47], without compromising the accuracy of the results. The use of a heterogeneous mesh enables reducing the total number of elements and the computational cost with respect to the finest mesh attempted.

Determination of the SRVE size. Once the length of the SRVE has been determined to be 0.01 mm and the mesh size 0.00035 mm for the fibers and 0.00070 mm for the matrix, finally, the cross-section size of the SRVE is studied. Four possible SRVE sizes were studied. The reference has 20 × 20 fibers. The results are shown in Fig. 7. The study of the contrast of hypotheses is summarized in Table 4.

From this statistical analysis, it can be concluded that the reference value previously selected (20 × 20) is representative since the contrast of hypotheses demonstrate that there is a smaller RVE (15 × 15) with the same mean and STDV for all the elastic properties. So, a convergence of the results is achieved. Therefore, to not compromise the computational time and resources needed, the SRVEs with a cross-section size of 15 × 15 fibers, i.e., 0.105 mm width and 0.105 mm height, are selected. These values are in good agreement with some other studies available in the literature. For example, Trias et al. [42] determined that the minimum size should be between 5 × 5 and 25 × 25 fiber diameters. Moreover, it is also in good agreement with González and Llorca [48] who predicted that an RVE with 30 fibers is representative of the macroscopic material. In the present study, with a 15 × 15 cross-section, the number of fibers is much larger than 30.

Table 4
Contrast of hypotheses of the mean value ($H_{0,mean}$) and the STDV ($H_{0,STDV}$) for different model dimensions to determine the smallest SRVE assuming a length of 0.01 mm and a mesh size of 0.00035 mm for the fibers and 0.00070 mm for the matrix. The values in **bold** are the reference values used for the contrast of hypotheses.

SRVE	$H_{0,mean}$	$H_{0,STDV}$
Cross-section size 20 × 20	**Ref value**	**Ref value**
Cross-section size 15 × 15	True	True
Cross-section size 10 × 10	True	False for E_1
Cross-section size 5 × 5	False for G_{12}, G_{23}	False for E_1

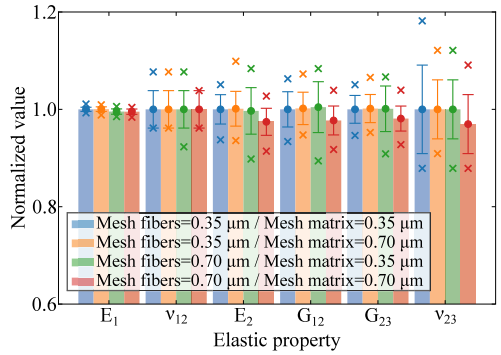

Fig. 6. Normalized elastic properties from a cross-section size 15 × 15 with four different mesh sizes for the fibers and the matrix. The crosses are the minimum and maximum values, and the circle the mean value with an error bar equal to one STDV. (For interpretation of the references to color in this figure legend, the reader is referred to the web version of this article.).

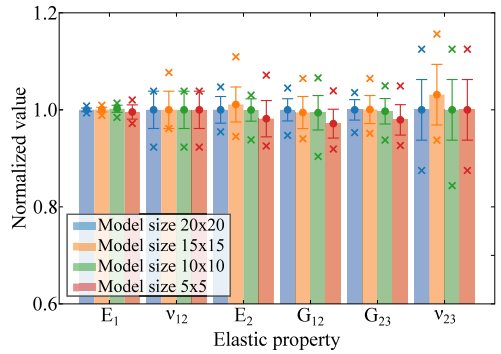

Fig. 7. Normalized elastic properties from $5 \times 5, 10 \times 10, 15 \times 15$ and 20 × 20 cross-section size to determine the minimum size. The crosses are the minimum and maximum values, and the circle the mean value with an error bar equal to one STDV. (For interpretation of the references to color in this figure legend, the reader is referred to the web version of this article.).

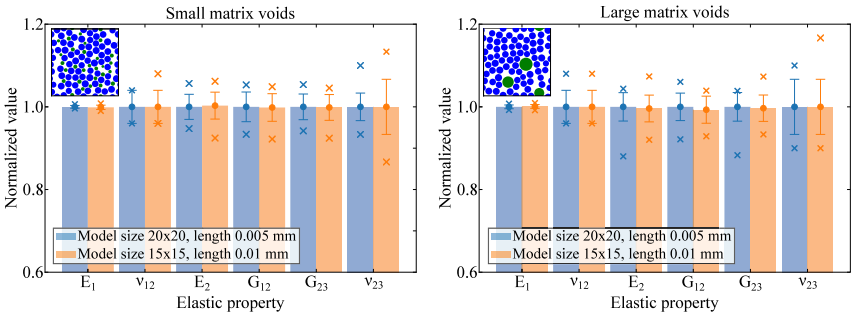

Fig. 8. Normalized elastic properties with the presence of matrix voids. The crosses are the minimum and maximum values, and the circle the mean value with an error bar equal to one STDV. (For interpretation of the references to color in this figure legend, the reader is referred to the web version of this article.).

Table 5
Contrast of hypotheses of the mean value ($H_{0,mean}$) and the STDV ($H_{0,STDV}$) to determine the effect of the presence of voids on the model size. Two RVEs with voids have been analyzed: small matrix voids and large matrix voids. The values in **bold** are the reference values used for the contrast of hypotheses.

SRVE	20 × 20 in plane size L = 0.05 mm	15 × 15 in plane size L = 0.01 mm
Small matrix voids	**Ref value**	$H_{0,mean}$: True $H_{0,STDV}$: False for ν_{23}
Large matrix voids	**Ref value**	$H_{0,mean}$: True $H_{0,STDV}$: True

To sum up, for a sample size of 20 SRVEs, the minimum lateral dimensions are 15 × 15 fibers, with a mesh size of 0.00035 mm for the fibers and 0.00070 mm for the matrix and a length in the longitudinal direction of 0.01 mm. With this combination, the number of finite elements for each SRVE is around 450 000.

Verification of the SRVE size with the presence of voids. The previous analyses, performed on "pristine" microstructures, is now repeated considering the presence of voids. The 20 × 20 RVEs with a length of 0.05 mm and matrix voids are taken as reference and compared with the previously determined: 15 × 15 fiber diameters cross-section and a length of 0.01 mm. In both cases, the mesh size for the fibers is 0.00035 mm, whereas for the matrix and the voids the mesh size is 0.00070 mm, which correspond to the best mesh combination found previously. The results of the elastic properties normalized by the reference values are shown in Fig. 8, while Table 5 summarizes the results from the contrast of hypotheses for the mean values and the STDVs.

From the contrast of hypotheses, independently of the size of the matrix voids, the mean values can be considered statistically equivalent, while for small matrix voids the STDV of ν_{23} cannot. This is explained by the presence of two extremely high values (see the corresponding minimum and maximum value in Fig. 8) in two of the 20 samples with small matrix voids. Neglecting these two extreme results, the STDVs turn out statistically equivalent.

Based on these results, it can be concluded that the size of the SRVE previously selected is practically independent of the presence of voids.

4.2. Effect of voids on the elastic properties

Finally, once the characteristics of the SRVE have been determined, the elastic engineering constants are calculated with the presence of voids. Different types of voids are analyzed, including matrix voids and inter-fiber voids to assess the effect of voids shape and size. For reference, SRVEs without defects or material variability and SRVEs without defects and material and geometric variability are also considered. The results are shown in Fig. 9.

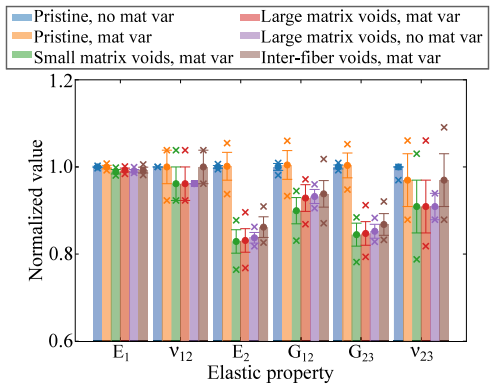

Fig. 9. Normalized engineering constants obtained from six different SRVEs: (i) without defects (pristine) and without material variability, (ii) without defects (pristine) but with material variability, (iii) with small matrix voids and material variability, (iv) with large matrix voids and material variability, (v) with large matrix voids but without material variability and (vi) with inter-fiber voids and material variability. All models account for the spatial variability of the fibers (and voids). The crosses are the minimum and maximum values, and the circle the mean value with an error bar equal to one STDV. (For interpretation of the references to color in this figure legend, the reader is referred to the web version of this article.).

As expected, the presence of voids implies a reduction of the elastic properties, and the transverse and shear properties experience the highest reductions. Pristine SRVEs without material or geometrical variability exhibit very low variability of their elastic properties since they only account for the random spatial distribution of reinforcements. However, when introducing material and geometrical variability, the STDV increases without major changes in the mean values of the elastic properties. Interestingly, the presence of voids reduced the mean value of the elastic properties, but the variability (STDV) is barely affected. To check the effect of voids on the STDV, a set of analyses with large matrix voids but without material variability was performed. The results show that the mean value is almost the same, whereas the variability is smaller when only taking into account the uncertainty

Table 6
Effect of the presence of voids on the elastic properties of a composite system. The cases with voids include material variability.

Elastic property		No material variability No defects	Material variability No defects	Small matrix voids	Large matrix voids	Large matrix voids No material variability	Inter-fiber voids
E_1 [MPa]	Mean	125 760	125 714	124 385	124 853	124 560	124 848
	STDV	182	511	651	577	471	842
	Rel. dif.	–	−0.04%	−1.09%	−0.72%	−0.95 %	−0.73%
ν_{12} [–]	Mean	0.26	0.26	0.25	0.25	0.25	0.26
	STDV	0.0	0.01	0.01	0.01	0.01	0.01
	Rel. dif.	–	0%	−3.85%	−3.85%	−3.85 %	0%
E_2 [MPa]	Mean	8 464	8 477	7 016	7 035	7 087	7 294
	STDV	27	271	228	229	103	201
	Rel. dif.	–	0.15%	−17.11%	−16.88%	−16.27 %	−13.82%
G_{12} [MPa]	Mean	4 336	4 355	3 900	4 026	4 042	4 068
	STDV	35	143	131	133	70	132
	Rel. dif.	–	0.44%	−10.06%	−7.15%	−6.82 %	−6.18%
G_{23} [MPa]	Mean	3 193	3 204	2 696	2 705	2 721	2 771
	STDV	15	91	84	87	51	80
	Rel. dif.	–	0.34%	−15.57%	−15.28%	−14.78 %	−13.21%
ν_{23} [–]	Mean	0.33	0.32	0.30	0.30	0.30	0.32
	STDV	0.0	0.02	0.02	0.02	0.01	0.02
	Rel. dif.	–	−3.03%	−9.09%	−9.09%	−9.09 %	−3.03%

on the voids size and not the variability on the material properties. Therefore, for a fixed void content, the uncertainty is mainly related to the material variability whereas the knock-down factor of the mean properties comes from the presence of voids.

Table 6 shows the results for the pristine SRVE and the relative difference, i.e., the knock down factor, with respect to the models considering material variability and the presence of voids.

The longitudinal Young's modulus, E_1, suffers a reduction of around 1% when the void content increases to 7% and the fiber volume fraction remains the same. This is expected, since E_1 is mostly governed by the longitudinal Young's modulus of the fibers and the fiber volume fraction which is not affected by the presence of voids, as in [47]. However, all the other elastic properties suffer a non-negligible reduction with the presence of voids, which leads to a reduction of the matrix volume fraction. For example, the reduction of the transverse Young's modulus, E_2, is around 17%.

Comparing the results between large matrix voids and inter-fiber voids, although both have similar diameter, it observed that the reduction with inter-fiber voids is lower than with matrix voids, except for E_1. To assess the effect of fiber-void intersection, a model allowing larger intersections was created. The results show lower knock-down factors for the properties dominated by the matrix, in particular E_2 and G_{23}, including a very small decrease for G_{12}, and a higher knock-down factor for E_1. Thus, it can be concluded that the position of the voids, in particular how much intersection is allowed with the fibers, affects the global elastic response of the composite. If the voids are intersected by the fibers, instead of being completely embedded in the matrix, the transverse properties are less affected, whereas the longitudinal properties dominated by the fibers, suffer a higher reduction. Interestingly, in Ref. [14] it is shown that the effect of the position of the voids on the strength of FRPs is the opposite, i.e., the strength in the presence of inter-fiber voids tends to be lower because the intersection between fiber and voids implies higher stress concentration which induce the strength reduction.

Regarding the comparison between small and large matrix voids, there is also a clear trend that the smaller the voids are, the bigger is the reduction in the mechanical properties.

The effect of voids on the elastic properties is also compared with three analytical models. To determine the minimum number of samples, n_{anal}, to run the analytical models used in this study, a contrast of hypotheses was conducted comparing different number of samples from 20 to 50 000, with $n_{anal} = 50\,000$ used as the reference value. The contrast of hypotheses showed that with a 95% of confidence it can be assumed that the mean and the STDV for all the elastic properties with 20 samples are equal to the reference value. Thus, a number of samples $n_{anal} = 20$, which is the same sample size used for the numerical analyses, is used.

Fig. 10 shows a comparison between the results obtained from computational micromechanics and the predictions of the RoM, the Mori–Tanaka mean field theory, and the CCA model for the same fiber volume fraction. Two SRVEs are considered: a pristine SRVE without defects and only considering material variability, and an SRVE with defects. The presence of voids with the RoM model can only be evaluated reducing the V_m whereas for the Mori–Tanaka and the CCA model they are assumed as a new inclusion with a dummy material. Because the analytical models do not account for the void size, the numerical results of the SRVEs with large matrix voids are selected for comparison.

For the pristine SRVE, while the predictions of the longitudinal properties are in good agreement with the numerical results (except for ν_{12} using the CCA model), the RoM, as expected, does not properly predict the transverse and shear properties, whereas the Mori–Tanaka mean field theory provides good predictions of the transverse and shear properties. Finally, the results from the CCA model are worse than the ones from Mori–Tanaka but still in good agreement with the numerical predictions except for G_{12} and ν_{12}.

Considering the presence of defects, firstly, it is important to mention that Eqs. (B.3) and (B.4) (series model) for the prediction of the transverse Young's modulus and shear modulus of the composite using the RoM are not valid in the presence of voids, as the results would lead to higher stiffness since V_m is in the denominator. In other words, with a lower V_m, which means a higher V_i, a higher E_2 or G_{12} would be obtained. Nevertheless, the predictions of the longitudinal properties remain in good agreement with the numerical results, using either the RoM, the Mori–Tanaka mean field theory or the CCA model. For the transverse and shear properties, the Mori–Tanaka mean field theory still provides the best predictions compared to the numerical model, but with a higher difference compared to the pristine results.

The CCA model is also able to capture the effect of having the voids in the matrix or within the fibers by changing the position of each phase. In that case, 3-phase CCA model is considered with the voids in the middle, embedded by the fibers, and the matrix as the outer surface. Therefore, the effect of inter-fiber voids, in that case voids completely inside the fibers, can be also considered. Using this analytical model, the same trend observed in the numerical predictions was obtained: a lower reduction of the transverse properties and a significant effect on the longitudinal properties.

Regarding the uncertainty, which is mainly dominated by the variation of the material properties, both analytical models present similar

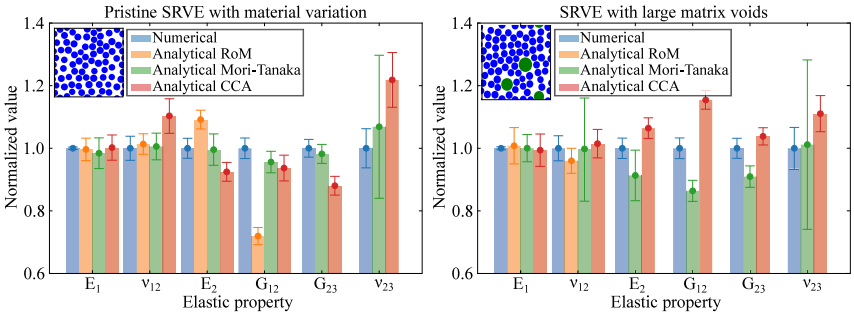

Fig. 10. Normalized elastic properties from the numerical analysis, the rule of mixtures (RoM), the Mori–Tanaka mean field theory, and the concentric cylinder assembly (CCA) of a pristine SRVE and an SRVE with large matrix voids. The error bar corresponds to one STDV. (For interpretation of the references to color in this figure legend, the reader is referred to the web version of this article.).

predictions except for E_1 and ν_{23}. Regarding E_1, the STDV obtained analytically without or with defects is much higher (more than 10 times) than the one obtained with the micromechanical model. Taking into account that E_1 is mainly dominated by the fiber properties, a higher STDV can be explained because in the micromechanical model each SRVE has different material properties for each fiber according to their corresponding normal distribution (variability from fiber to fiber as shown in Fig. 5). Thus, the different properties from fiber to fiber tends to cancel out in each SRVE. However, in the analytical models, the fiber properties only change from sample to sample inducing a higher variability between samples and, consequently, a higher STDV. A numerical analysis replicating the same conditions of the analytical models, i.e., with all fibers of each SRVE having the same randomly assigned material properties, was conducted and the STDV obtained was similar to the analytical one. Finally, it is important to note that, although there is no quantitative comparison with experimental results, the computational micromechanics modeling strategy employed here to predict the elastic properties of fiber reinforced polymers has been previously validated, e.g., Ref. [46]. Moreover, the results obtained with the presence of voids are in good agreement with the analytical models that have been already validated, incl. Mori–Tanaka mean field theory in Ref. [40] and the concentric cylinder assembly model in Ref. [41]. However, computational micromechanics provides higher flexibility in the parametrization of the SRVEs for uncertainty quantification analyses.

4.3. Parametric study of the influence of fiber and void content

The presented methodology can be used to study the influence of the input parameters (the geometry, the material variability and the presence of voids) on the mesoscale properties. This influence can be easily represented with a response surface which is a useful tool to compare the homogenized elastic properties obtained varying two of the input parameters. The previous discussed results (see Section 4.2) show that the highest effect of voids is in the transverse and shear properties. Since E_1 mainly depends on the longitudinal Young's modulus of the fibers and the fiber volume fraction, E_1 is almost independent of the V_v. Thus, Fig. 11 shows the prediction of the elastic transverse and shear moduli for different fiber (V_f) and void volume fractions (V_v) obtained numerically with the presence of large matrix voids and the relative difference between numerical predictions and analytical ones using the Mori–Tanaka mean field theory, which has been demonstrated to be the analytical model with closer predictions.

As expected, the elastic moduli are reduced with decreasing V_f. The elastic moduli governed mainly by the matrix, E_2 and G_{23}, show a pronounced reduction while increasing the V_v. However, as predicted by Tai et al. [49] in their micromechanical model with the presence of matrix microvoids, the reduction of G_{23} is more affected by the V_f rather than higher V_v. Regarding the longitudinal shear modulus G_{12}, which is more affected by the V_f rather than the V_v, the reduction due to a greater V_v is less noticeable.

The relative difference between the numerical results and the analytical Mori–Tanaka mean field theory increases with higher V_v. Regarding the V_f, the relative difference also increases with increasing V_f, although the increasing difference is less pronounced. For all the transverse and shear properties the analytical model underpredicts the elastic moduli. Nevertheless, the analytical model is able to capture the same trend obtained numerically for all the elastic properties.

The same analysis has been performed to check the effect of V_f and V_v on the uncertainty. However, no trend on the evolution of the STDV of the elastic properties with void and fiber volume fractions has been identified.

5. Conclusions

In this study, the definition of SRVEs to account for the effect of defects on the elastic properties of composite systems, including their uncertainty, is presented. An enhanced algorithm to generate the spatial distribution of the constituents in an RVE has been implemented with the ability of adding voids which have been represented as cylindrical branch-type defects aligned with the fiber direction. This RVE has been numerically simulated with a well parameterized modeling strategy, which accounts for different types of voids and materials. SRVEs are then determined for the uncertainty quantification and management of the mechanical response of composite systems with defects at the micro-scale.

Based on the elastic response of the constituents, and through the analysis of contrast of hypotheses, it is demonstrated that, as expected, the presence of voids reduces the transverse and shear elastic properties. However, for the same fiber and void volume fractions, voids completely embedded in the matrix (matrix voids) lead to higher reductions in elastic properties than inter-fiber voids of similar size, except for E_1, showing that the position of the voids affects how detrimental is their effect on the elastic properties. On the other hand, the smaller the matrix voids, the larger is the reduction in the elastic properties of the composite. Regarding the effect on the uncertainties of the meso-scale properties, it is clear that, for a fixed void content, material variability has a larger effect than the presence of voids. The material variability, in this case, is responsible for the uncertainties at the meso-scale level, while the voids are mainly responsible for the reduction of the predicted elastic properties, in particular the transverse and shear ones. Finally, the comparison with analytical models shows that the Mori–Tanaka mean field theory provides the same trends of

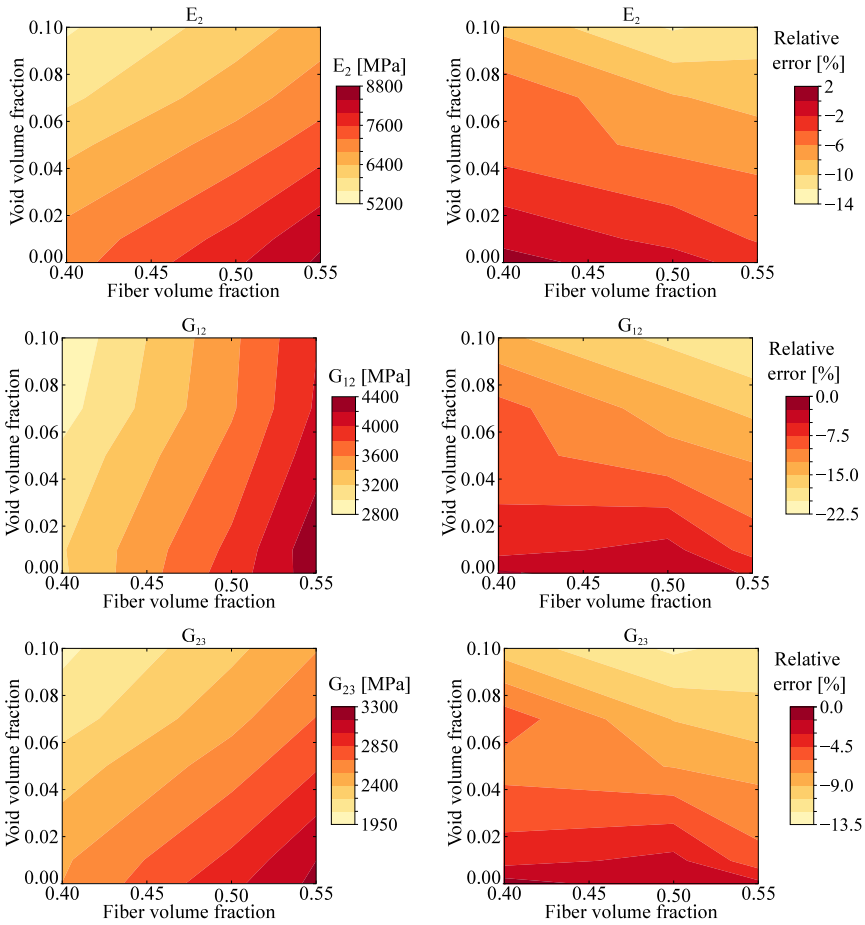

Fig. 11. Prediction of the elastic transverse and shear moduli obtained numerically with the presence of large matrix voids and the relative difference between numerical results and the analytical ones from Mori–Tanaka mean field theory. (For interpretation of the references to color in this figure legend, the reader is referred to the web version of this article.).

the numerical results for the transverse properties as a function of fiber and void volume contents. However, the relative difference between the numerical and the analytical predictions increases for high void volume fractions.

To sum up, this study shows how the added flexibility provided by computational micromechanics can aid in assessing the effect of material variability, geometric variability, as well as other microstructural effects, such as the presence of defects. Accounting for all these effects will be key in enabling multiscale reliability-based design of composite structures, linking the microstructural features with the macroscopic response and uncertainty management. Moreover, the methodology proposed herein can be extended to include the effects of other uncertainties, such as the presence of clusters of fibers or voids, and other types of defects.

CRediT authorship contribution statement

O. Vallmajó: Conceptualization, Methodology, Software, Validation, Formal analysis, Investigation, Data curation, Writing – Original Draft. **A. Arteiro:** Conceptualization, Validation, Formal analysis, Data curation, Writing – Review & Editing, Supervision. **J.M. Guerrero:** Software, Formal analysis, Writing – Review & Editing. **A.R. Melro:** Software, Formal analysis, Writing – Review & Editing. **A. Pupurs:** Conceptualization, Software, Writing – Review & Editing. **A. Turon:** Conceptualization, Validation, Formal analysis, Writing – Review & Editing, Supervision, Project administration, Funding acquisition.

Declaration of competing interest

The authors declare that they have no known competing financial interests or personal relationships that could have appeared to influence the work reported in this paper.

Data availability

No data was used for the research described in the article

Acknowledgments

OV acknowledges the support of the Catalan Government, under the Grant 2020FI B2 00110. AT and OV gratefully acknowledge the funding of the Project RTI, United States 2018-099373-B-100, co-financed by the Spanish Government (Ministerio de Economia y Competitividad) and the European Social Fund. AT acknowledges the Generalitat de Catalunya for the ICREA Academia prize 2022. This work has been conducted within the framework of the CAELESTIS project, funded by the European Climate, Infrastructure and Environment Executive Agency (CINEA) under grant agreement No. 101056886. Views and opinions expressed are however those of the author(s) only and do not necessarily reflect those of CINEA. Neither the European Union nor the granting authority can be held responsible for them. J.M. Guerrero would also like to acknowledge the funding of the post-doc grant Margarita Salas with reference REQ2021-A-15, financed by the Spanish "Ministerio de Universidades" and the European Union - Next GenerationEU.

Appendix A. First-order homogenization

The elastic properties of a composite material can be determined using a first-order homogenization technique. The Hooke's law for transversely isotropic materials can be defined as:

$$\begin{Bmatrix} \bar{\sigma}_{11} \\ \bar{\sigma}_{22} \\ \bar{\sigma}_{33} \\ \bar{\sigma}_{12} \\ \bar{\sigma}_{13} \\ \bar{\sigma}_{23} \end{Bmatrix} = \begin{bmatrix} C_{1111} & C_{1122} & C_{1122} & 0 & 0 & 0 \\ C_{1122} & C_{2222} & C_{2233} & 0 & 0 & 0 \\ C_{1122} & C_{2233} & C_{2222} & 0 & 0 & 0 \\ 0 & 0 & 0 & C_{4444} & 0 & 0 \\ 0 & 0 & 0 & 0 & C_{4444} & 0 \\ 0 & 0 & 0 & 0 & 0 & \frac{C_{2222}-C_{2233}}{2} \end{bmatrix} \begin{Bmatrix} \bar{\epsilon}_{11} \\ \bar{\epsilon}_{22} \\ \bar{\epsilon}_{33} \\ \bar{\epsilon}_{12} \\ \bar{\epsilon}_{13} \\ \bar{\epsilon}_{23} \end{Bmatrix} \tag{A.1}$$

where $\bar{\sigma}_{ij}$ represents the volume average of the ij stress component, C_{ijj} are the stiffness tensor components and $\bar{\epsilon}_{ij}$ is the volume average of the ij strain component. From the stiffness tensor components, the five independent engineering constants and the transverse Poisson's ratio, can be calculated as:

$$\begin{aligned} E_1 &= C_{1111} - \frac{2C_{1122}^2}{C_{2222}+C_{2233}} \\ \nu_{12} &= \frac{C_{1122}}{C_{2222}+C_{2233}} \\ E_2 &= C_{2222} + \frac{C_{1122}^2(C_{2233}-C_{2222}) + C_{2233}(C_{1122}^2 - C_{1111}C_{2233})}{C_{1111}C_{2222} + C_{1122}^2} \\ G_{12} &= C_{4444} \\ G_{23} &= \frac{C_{2222}-C_{2233}}{2} \\ \nu_{23} &= \frac{C_{1111}C_{2233} - C_{1122}^2}{C_{1111}C_{2222} - C_{1122}^2} \end{aligned} \tag{A.2}$$

where E_1 and E_2 are the longitudinal and transverse Young's moduli, G_{12} and G_{23} are the longitudinal and transverse shear moduli, ν_{12} is the major Poisson's ratio, and ν_{23} is the transverse Poisson's ratio. For a given applied far-field strain ϵ_{ij}^0, the volume average strain components can be calculated as:

$$\bar{\epsilon}_{ij} = \frac{1}{V}\int_V \epsilon_{ij} dV = \epsilon_{ij}^0 \tag{A.3}$$

and the volume average stress field as:

$$\bar{\sigma}_{ij} = \frac{1}{V}\int_V \sigma_{ij} dV \tag{A.4}$$

Therefore, since the stiffness tensor is symmetric (Eq. (A.1)), and taking into account Eq. (A.2), applying ϵ_{11}^0, ϵ_{22}^0 and ϵ_{12}^0 far-field strains is sufficient to determine the components of the stiffness tensor and, consequently, all the homogenized elastic material properties.

Appendix B. The rule of Mixtures

The Rule of Mixtures (RoM) provides reasonable values for the longitudinal stiffness (E_1) assuming that the fibers and the matrix are working in parallel:

$$E_1 = V_f E_{1f} + V_m E_m \tag{B.1}$$

where V_f is the fiber volume fraction and V_m is the matrix volume fraction, and $V_f + V_m + V_v = 1$, where V_v is the void volume fraction. E_{1f} is the longitudinal Young's modulus of the fibers, assumed transversely isotropic, and E_m is the Young's modulus of the matrix, assumed isotropic. The major Poisson's ratio (ν_{12}) can be estimated following the same assumption, as:

$$\nu_{12} = V_f \nu_{12f} + V_m \nu_m \tag{B.2}$$

where ν_{12f} is the major Poisson's ratio of the fibers and ν_m the Poisson's ratio of the matrix.

The transverse Young's modulus (E_2) can be calculated assuming that the fibers and matrix are working as springs in series:

$$E_{2,RoM} = \frac{E_m E_{2f}}{E_m V_f + E_{2f} V_m} \tag{B.3}$$

where E_{2f} is the transverse Young's modulus of the fibers. Finally, the shear modulus can be calculated as:

$$G_{12,RoM} = \frac{G_m G_{12f}}{G_m V_f + G_{12f} V_m} \tag{B.4}$$

where G_{12f} is the longitudinal shear modulus of the fibers and G_m is the shear modulus of the matrix.

Appendix C. The Mori–Tanaka mean field theory

The Mori–Tanaka mean field theory [40] account for the presence of multiple types of inclusions (here fibers and voids). In that case, for a system with unidirectional fibers with a transversely isotropic behavior and with more than one inclusion (fibers and voids), the overall elastic moduli and Poisson's ratio can be calculated as [50]:

$$\begin{aligned} p^* &= \frac{\sum_{i=1}^n \frac{V_i p_i}{p_m + p_i}}{\sum_{i=1}^n \frac{V_i}{p_m + p_i}} = G_{12} \\ \gamma_m &= \left(\frac{1}{m_m} + \frac{2}{k_m}\right)^{-1} \\ m^* &= \frac{\sum_{i=1}^n \frac{V_i m_i}{m_i + \gamma_m}}{\sum_{i=1}^n \frac{V_i}{m_i + \gamma_m}} = G_{23} \\ k^* &= \frac{\sum_{i=1}^n \frac{V_i k_i}{m_m + k_i}}{\sum_{i=1}^n \frac{V_i}{m_m + k_i}} = -\left(\frac{1}{G_{23}} - \frac{4}{E_2} + \frac{4\nu_{12}^2}{E_1}\right)^{-1} \\ l^* &= \frac{\sum_{i=1}^n \frac{V_i l_i}{m_m + k_i}}{\sum_{i=1}^n \frac{V_i}{m_m + k_i}} = 2k^* \nu_{12} \\ n^* &= \sum_{i=1}^n V_i n_i - \sum_{i=1}^n V_i \frac{(l_i - l_m)^2}{m_m + k_i} + \frac{\left[\sum_{i=1}^n V_i \frac{(l_i - l_m)}{m_m + k_i}\right]^2}{\sum_{i=1}^n \frac{V_i}{m_m + k_i}} = E_1 + 4k^* \nu_{12}^2 \end{aligned} \tag{C.1}$$

where k^*, l^*, m^*, n^* and p^* are Hill's elastic moduli [50], and the index i refers to each inclusion (i.e., fibers and voids) and m to the matrix.

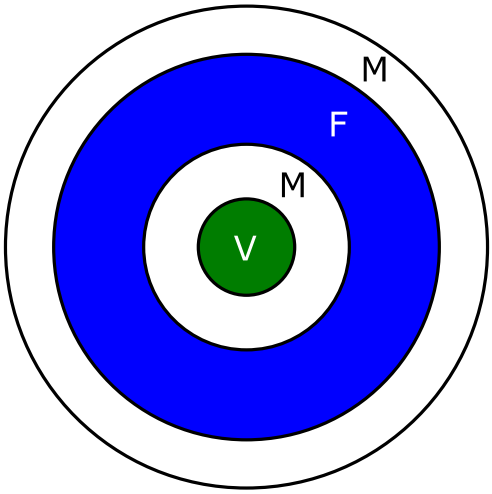

Fig. D.1. 4-phase CCA model representing UD composite with voids in the matrix phase: V – void, M – matrix, F – fiber.

The Hill's elastic moduli for an isotropic material, such as the matrix, are:

$$\begin{aligned} m_m &= p_m = G_m \\ l_m &= 2k_m\nu_m \\ n_m &= E_m + 4k_m\nu_m^2 \\ k_m &= \frac{-1}{\frac{1}{G_m} - \frac{4}{E_m} + \frac{4\nu_m^2}{E_m}} \end{aligned} \tag{C.2}$$

whereas for a transversely isotropic reinforcement, such as the fibers, they are described as:

$$\begin{aligned} m_i &= G_{i,23} \\ p_i &= G_{i,12} \\ l_i &= 2k_i\nu_{i,12} \\ n_i &= E_{i,1} + 4k_i\nu_{i,12}^2 \\ k_i &= \frac{-1}{\frac{1}{G_{i,23}} - \frac{4}{E_{i,2}} + \frac{4\nu_{i,12}^2}{E_{i,1}}} \end{aligned} \tag{C.3}$$

Appendix D. The concentric cylinder assembly model

The concentric cylinder assembly (CCA) model [41] also allows the presence of multiple phases. The micromechanical model is a straightforward extension of Hashin's [51] and Christensen and Lo's [52] models with the main novelty of its applicability to multilayered (N-phased) inclusions with transversely isotropic material properties. The composite consists of N-cylinders perfectly bonded together in which each phase (k) is homogeneous, linear elastic and with a transversely isotropic behavior. The outer (r_k) and inner radius (r_{k-1}) of each cylinder, i.e., the thickness, is determined according to each corresponding volume fraction (V_k) as:

$$V_k = \frac{r_k^2 - r_{k-1}^2}{r_N^2} \tag{D.1}$$

where $r_N = 1$ since the calculated effective elastic properties depend only on the relative dimensions of constituents. Thus, macroscopically, the composite is transversely isotropic. The problem of radial loading is solved to find the bulk modulus K_{23}, of axial loading to find E_1 and ν_{12}, of in-plane shear loading to find G_{12} and of shear loading in the plane transverse to the fibers to find G_{23}. Finally, E_2 and ν_{23} are determined using:

$$\begin{aligned} E_2 &= \frac{1}{\frac{1}{4K_{23}} + \frac{1}{4G_{23}} + \frac{\nu_{12}^2}{E_1}} \\ \nu_{23} &= \frac{E_2}{2G_{23}} - 1 \end{aligned} \tag{D.2}$$

In the present study, to account for the presence of voids, a first phase representing the voids with near zero elastic properties is embedded inside a cylinder representing the matrix. The void and matrix unit is surrounded by a cylinder which represents fibers. Finally, the final outer phase in the 4 cylinder model represents the matrix. It was found that such 4-phase CCA model (see Fig. D.1) is a more realistic representation of UD composite with voids in matrix compared to a similar 3-phase CCA model with outer phase being the fiber cylinder as the latter leads to underestimation of transverse modulus and a large overestimation of in-plane shear modulus.

References

[1] Greenhalgh E. Failure analysis and fractography of polymer composites. Woodhead, Cambridge; 2009.
[2] Mehdikhani M, Petrov NA, Straumit I, Melro AR, Lomov SV, Gorbatikh L. The effect of voids on matrix cracking in composite laminates as revealed by combined computations at the micro-and meso-scales. Composites A 2019;117:180–92.
[3] Zhou X-Y, Qian S-Y, Wang N-W, Xiong W, Wu W-Q. A review on stochastic multiscale analysis for FRP composite structures. Compos Struct 2022;284:115132.
[4] Yang P, Elhajjar R. Porosity content evaluation in carbon-fiber/epoxy composites using X-ray computed tomography. Polym-Plast Technol Eng 2014;53(3):217–22.
[5] Thomason J. The interface region in glass fibre-reinforced epoxy resin composites: 2. Water absorption, voids and the interface. Composites 1995;7(26):477–85.
[6] Drach B, Tsukrov I, Gross T, Dietrich S, Weidenmann K, Piat R, Böhlke T. Numerical modeling of carbon/carbon composites with nanotextured matrix and 3D pores of irregular shapes. Int J Solids Struct 2011;48(18):2447–57.
[7] Tserpes K, Stamopoulos A, Pantelakis SG. A numerical methodology for simulating the mechanical behavior of CFRP laminates containing pores using X-ray computed tomography data. Composites B 2016;102:122–33.
[8] Matveeva A, Garoz D, Sevenois R, Zhu M, Pyl L, Van Paepegem W, et al. Effect of intra-ply voids on the homogenized behavior of a ply in multidirectional laminates. In: IOP conference series: Materials science and engineering, vol. 406, no. 1. IOP Publishing; 2018, 012009.
[9] Stamopoulos A, Tserpes K, Prucha P, Vavrik D. Evaluation of porosity effects on the mechanical properties of carbon fiber-reinforced plastic unidirectional laminates by X-ray computed tomography and mechanical testing. J Compos Mater 2016;50(15):2087–98.
[10] Huang H, Talreja R. Effects of void geometry on elastic properties of unidirectional fiber reinforced composites. Compos Sci Technol 2005;65(13):1964–81.
[11] Zhu H, Wu B, Li D, Zhang D, Chen Y. Influence of voids on the tensile performance of carbon/epoxy fabric laminates. J Mater Sci Technol 2011;27(1):69–73.
[12] Yang P, El-Hajjar R. Porosity defect morphology effects in carbon fiber–epoxy composites. Polym-Plast Technol Eng 2012;51(11):1141–8.
[13] Scott A, Sinclair I, Spearing SM, Mavrogordato MN, Hepples W. Influence of voids on damage mechanisms in carbon/epoxy composites determined via high resolution computed tomography. Compos Sci Technol 2014;90:147–53.
[14] Hyde A, He J, Cui X, Lua J, Liu L. Effects of microvoids on strength of unidirectional fiber-reinforced composite materials. Composites B 2020;187(107844).
[15] Vajari DA, Gonzalez C, Llorca J, Legarth BN. A numerical study of the influence of microvoids in the transverse mechanical response of unidirectional composites. Compos Sci Technol 2014;97:46–54.
[16] Chambers A, Earl J, Squires C, Suhot M. The effect of voids on the flexural fatigue performance of unidirectional carbon fibre composites developed for wind turbine applications. Int J Fatigue 2006;28(10):1389–98.
[17] Hernández S, Sket F, Molina-Aldaregui J, González C, LLorca J, et al. Effect of curing cycle on void distribution and interlaminar shear strength in polymer-matrix composites. Compos Sci Technol 2011;71(10):1331–41.

[18] Mehdikhani M, Nguyen NQ, Straumit I, Gorbatikh L, Lomov SV. Analysis of void morphology in composite laminates using micro-computed tomography. In: IOP conference series: Materials science and engineering, vol. 406, no. 012010. IOP Publishing; 2018.
[19] Bodaghi M, Cristóvão C, Gomes R, Correia N. Experimental characterization of voids in high fibre volume fraction composites processed by high injection pressure RTM. Composites A 2016;82:88–99.
[20] Hyde A, Liu L, Cui X, Lua J. Micromechanics-enriched finite element modeling of composite structures with fiber waviness and void defects. In: AIAA scitech 2019 forum. 2019, p. 0694.
[21] Zhang D, Heider D, Advani SG, Gillespie J. Out of autoclave consolidation of voids in continuous fiber reinforced thermoplastic composites. In: SAMPE 2013-Long Beach. 2013, p. 16.
[22] Daggumati S, Sharma A, Van Paepegem W. Synergistic effects of microscale variabilities on the thermo-mechanical behavior of a UD CFRP ply. Int J Mech Sci 2023;242:108004.
[23] de Almeida SFM, Neto ZdSN. Effect of void content on the strength of composite laminates. Compos Struct 1994;28(2):139–48.
[24] Chu Y, Sun L, Yang X, Wang J, Huang W. Multiscale simulation and theoretical prediction for the elastic properties of unidirectional fiber-reinforced polymer containing random void defects. Polym Compos 2021;42(6):2958–72.
[25] Melro A, Camanho P, Pinho S. Generation of random distribution of fibres in long-fibre reinforced composites. Compos Sci Technol 2008;68(9):2092–102.
[26] Tavares RP, Melro AR, Bessa MA, Turon A, Liu WK, Camanho PP. Mechanics of hybrid polymer composites: analytical and computational study. Comput Mech 2016;57(3):405–21.
[27] Hill R. Elastic properties of reinforced solids: some theoretical principles. J Mech Phys Solids 1963;11(5):357–72.
[28] Dong C. Effects of process-induced voids on the properties of fibre reinforced composites. J Mater Sci Technol 2016;32(7):597–604.
[29] Sharifpour F, Montesano J, Talreja R. Assessing the effects of ply constraints on local stress states in cross-ply laminates containing manufacturing induced defects. Composites B 2020;199:108227.
[30] Vinot M, Liebold C, Usta T, Holzapfel M, Toso N, Voggenreiter H. Stochastic modelling of continuous glass-fibre reinforced plastics–considering material uncertainty in microscale simulations. J Compos Mater 2023;57(1):133–45.
[31] Vallmajó O, Cózar I, Furtado C, Tavares R, Arteiro A, Turon A, et al. Virtual calculation of the B-value allowables of notched composite laminates. Compos Struct 2019;212:11–21.
[32] Military Handbook. MIL-HDBK-17-1F: Composite materials handbook, volume 1-polymer matrix composites guidelines for characterization of structural materials. US Department of Defense.
[33] Cózar I, Turon A, González E, Vallmajó O, Sasikumar A. A methodology to obtain material design allowables from high-fidelity compression after impact simulations on composite laminates. Composites A 2020;139:106069.
[34] Tavaf V, Saadatzi M, Banerjee S. Quantification of degraded constitutive coefficients of composites in the presence of distributed defects. J Compos Mater 2019;53(18):2517–29.
[35] Mehdikhani M, Gorbatikh L, Verpoest I, Lomov SV. Voids in fiber-reinforced polymer composites: A review on their formation, characteristics, and effects on mechanical performance. J Compos Mater 2019;53(12):1579–669.
[36] Bowles KJ, Frimpong S. Relationship between voids and interlaminar shear strength of polymer matrix composites. In: International SAMPE symposium and exhibition, no. E-5825. 1991.
[37] Melro A, Camanho P, Pires FA, Pinho S. Numerical simulation of the non-linear deformation of 5-harness satin weaves. Comput Mater Sci 2012;61:116–26.
[38] ABAQUSInc. User's manual, 6.14-2. Pawtucket, RI, USA; 2014.
[39] Arteiro A, Pereira L, Bessa M, Furtado C, Camanho P. A micro-mechanics perspective to the invariant-based approach to stiffness. Compos Sci Technol 2019;176:72–80.
[40] Mori T, Tanaka K. Average stress in matrix and average elastic energy of materials with misfitting inclusions. Acta Metall 1973;21(5):571–4.
[41] Marklund E, Varna J, Neagu RC, Gamstedt EK. Stiffness of aligned wood fiber composites: effect of microstructure and phase properties. J Compos Mater 2008;42(22):2377–405.
[42] Trias D, Costa J, Turon A, Hurtado J. Determination of the critical size of a statistical representative volume element (SRVE) for carbon reinforced polymers. Acta Mater 2006;54(13):3471–84.
[43] Soden PD, Hinton MJ, Kaddour A. Lamina properties, lay-up configurations and loading conditions for a range of fibre reinforced composite laminates. In: Failure criteria in fibre-reinforced-polymer composites. Elsevier; 2004, p. 30–51.
[44] Sotiropoulos DG, Tserpes K. Interval-based computation of the uncertainty in the mechanical properties and the failure analysis of unidirectional composite materials. Math Comput Appl 2022;27(3):38.
[45] Breite C, Melnikov A, Turon A, de Morais A, Le Bourlot C, Maire E, et al. A synchrotron computed tomography dataset for validation of longitudinal tensile failure models based on fibre break and cluster development. Data Brief 2021;39:107590.
[46] Melro A, Camanho P, Pinho S. Influence of geometrical parameters on the elastic response of unidirectional composite materials. Compos Struct 2012;94(11):3223–31.
[47] Li Y, Zhou L, Zhang M, Song C. Study on the effect of void defect on mechanical properties of carbon fiber composites by finite element method. J Inst Eng (India) Ser C 2022;103(6):1433–46.
[48] González C, LLorca J. Mechanical behavior of unidirectional fiber-reinforced polymers under transverse compression: Microscopic mechanisms and modeling. Compos Sci Technol 2007;67(13):2795–806.
[49] Tai J-H, Kaw A. Transverse shear modulus of unidirectional composites with voids estimated by the multiple-cells model. Composites A 2018;105:310–20.
[50] Chen T, Dvorak GJ, Benveniste Y. Mori–Tanaka estimates of the overall elastic moduli of certain composite materials. ASME J Appl Mech 1992;59(3):539–46.
[51] Hashin Z. Analysis of composite materials—a survey. J Appl Mech 1983;50(3):481–505.
[52] Christensen R, Lo K. Solutions for effective shear properties in three phase sphere and cylinder models. J Mech Phys Solids 1979;27(4):315–30.


AMADE
Universitat de Girona